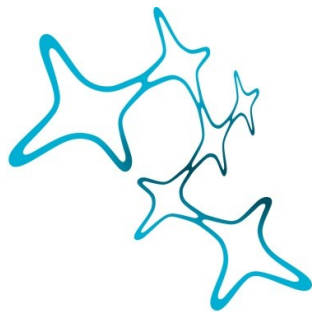

CONTEXTUAL MODULATION OF STIMULUS PROCESSING IN THE MOUSE VISUAL THALAMUS

Davide Crombie



Graduate School of
Systemic Neurosciences

LMU Munich



Dissertation der
Graduate School of Systemic Neurosciences der
Ludwig-Maximilians-Universität München

March 2024

Supervisor
Prof. Dr. Laura Busse
Department of Biology II – Neurobiology
Ludwig Maximilian University of Munich

First Reviewer: Prof. Dr. Laura Busse
Second Reviewer: Prof. Dr. Christian Leibold

Date of Submission: March 14, 2024
Date of Defense : July 11, 2024

Acknowledgements

My supervisor, Laura Busse deserves thanks not only for her invaluable and direct involvement in the scientific work presented here, but also for her general commitment to higher education. It is rare to encounter anyone so unrelenting in their dedication to the profession, and so genuine in their desire to provide students with knowledge and guidance. Laura, much like your brilliant scientific research, this aspect of work will have lasting impact.

I would also like to extend my gratitude to all of my supervisors – official and unofficial. Martin Spacek for collecting such high quality data, and for transforming me into someone who genuinely enjoys coding. Steffen Katzner for making my first teaching experience so enjoyable, and for enthusiastically sharing your musings against reductionism in neuroscience. Christian Leibold for your refreshingly candid approach to research, and for inspiring confidence in my rudimentary mathematical abilities. And lastly, my thesis advisory committee, which includes Laura, Christian, and Jakob Macke, for their advice, and for their flexibility during a time when in-person communication was restricted.

Trying to completing one's doctoral studies during a global pandemic has its challenges, especially away from home where access to support is limited. I would like to thank all the members of the Vision Circuits Lab for their continuous positivity and engagement, and everyone in the LMU neurobiology department for providing such a pleasant working environment. Thank you to the Graduate School of Systemic Neuroscience, not only for providing the academic infrastructure in which this work was completed, but also, to the administrative team for keeping everyone on track during these difficult years.

Outside of the academic sphere, I need to thank two dear friends, Carlos Muñoz Ferrandis and Xiao-Xiong Lin, without whom there wouldn't have been nearly as much laughter accompanying this work. To my teammates at Rugby Club Unterföhring and Touch München: thank you for your uplifting attitudes on and off the pitch. Following my father, I should also express my appreciation to the Canadian and German taxpayers for funding high-quality education and research.

Finally, thank you to my family. Dad, for instilling me with the attitude that everything worth doing is worth doing right. My sister, for her unconditional friendship and understanding. And Mom, for teaching me to always question the prevailing narrative.

I would like to dedicate this work to my grandparents: Grandma, Grandpa, Nonna, and Nonno. Your pride is the object of my motivation. *Il vostro orgoglio è l'oggetto della mia motivazione.* And to my partner, Bethan Joy Jenkins. *Tu sei il mondo per me.*

Abstract

In order to appropriately utilize visual signals from the environment, the brain needs to place this information into a context. Contexts are multifaceted, and can refer to the overall nature of the visual landscape, as well as the goals and behaviours of the animal. The behavioural context can determine the type of visual signals that the animal is likely to encounter, and, simultaneously, the type of behaviours the animal is likely to perform on a moment-to-moment basis. These behaviours may be used to explore the visual scene, and can themselves generate certain types of visual signals. It is therefore unsurprising that visual systems in the brain account for context at the earliest stages of sensory processing. One of these initial processing stages in the mammalian brain is the visual thalamus. This dissertation presents the results of three investigations on the contextual modulation of neural activity in the dorsal lateral geniculate nucleus (dLGN) of the thalamus. To conclude, novel results involving the ventral lateral geniculate nucleus of the thalamus in setting a behavioural context are synthesized. Taken together, it is hoped that these works will contribute to an acknowledgement of the *diversity* of contextual modulations in vision, and lead to a better understanding of how the brain constructs its own sensory world.

Until the last decade, investigations of sensory processing in the mammalian brain were typically carried out in anaesthetized animals using simple artificial stimuli. However, brains have evolved to process complex natural environments while the animal is awake and behaving. These factors must therefore be taken into account when investigating the function of a certain piece of neural circuitry. The research presented in Chapter 2 examines the role of feedback from the visual cortex to the dLGN in awake animals viewing naturalistic video stimuli. The work reveals a robust effect of this feedback on dLGN neurons in the presence of naturalistic stimulation. Furthermore, it was found that cortical feedback produces effects that are similar to locomotion, but that the two influences are statistically independent, suggesting that locomotion operates on dLGN neurons through a different mechanism.

Researchers use behavioural signals like locomotion to infer that the animal is in a behavioural state termed “arousal”. Another external marker for arousal is pupil dilation. Previous work examined the effects of arousal on sensory systems by partitioning neural activity into two mutually exclusive groupings based on the level of arousal. The work in Chapter 3, however, extends the notion of behavioural state by showing relationships between dLGN activity and pupil dilation over multiple, nested temporal scales. Some of these modulations, especially at faster timescales, were related to specific behaviours such as locomotion and eye movement. Overall, despite the presence of a robust neural activity pattern characterizing these modulations across temporal scales, there was a diversity in the strength with which individual neurons coupled to a certain temporal component. This pattern of results indicates that, rather than operating in two distinct modes, dLGN neurons are under the continuous influence of a multitude of arousal-related factors.

Modelling plays an important role in neuroscience, allowing the translation between conceptual and quantitative understanding. In Chapter 4, a descriptive model is introduced to assess the additive contributions of locomotion, pupil size, and cortical feedback to the stimulus responses of individual dLGN neurons. This work

not only utilizes a novel efficient and robust method for assessing responses to naturalistic visual stimuli, but also provides a unified quantitative account of the various modulatory influences acting on dLGN neurons.

The enclosed research primarily provides *descriptive* accounts of contextual modulation of activity in the early visual system of mammals. Where it is limited is in the discussion of mechanisms and functional roles. Chapter 5 reviews two findings from other research groups uncovering a novel mechanism, involving the ventral lateral geniculate nucleus (vLGN) of the thalamus, by which mammals might control behavioural responses to visual stimuli. These novel findings highlight the usefulness of asking “how” and “why” in neurobiological research. Thus, in the final chapter, the potential mechanisms underlying dLGN modulations uncovered in Chapters 2 through 4 are discussed, and various proposals for their teleological functions in vision are made.

Contents

1	Introduction	1
1.1	The dynamic brain	1
1.2	Thalamic circuits for vision	3
1.3	Modulation of dLGN activity	6
1.4	Objectives and key questions	9
2	Exploring the effects of feedback and locomotion in the dLGN	12
2.1	Front matter & contributions	12
2.2	Robust effects of corticothalamic feedback and behavioral state on movie responses in mouse dLGN	13
3	On the temporal structure of modulation in the mouse dLGN	45
3.1	Front matter & contributions	45
3.2	Spiking activity in the visual thalamus is coupled to pupil dynamics across temporal scales . . .	46
4	A unified model of dLGN stimulus-responses and modulation	82
4.1	Front matter & contributions	82
4.2	The combination of stimulus-driven and modulatory inputs in visual thalamus depend on visual responsiveness and stimulus type	83
5	A transthalamic pathway for visual control of fear behaviour	114
5.1	Front matter & contributions	114
5.2	Should I stay or should I go? A thalamic circuit for modulating behavioral responses to visual threat	115
6	Discussion	118
6.1	Summary	118
6.2	Modulatory mechanisms	120
6.3	Visual processing	125
6.4	Partitioning neural activity and behaviour	131
7	References	136
8	Appendix	164
8.1	List of publications	164
8.2	Curriculum vitae	164
8.3	Author contributions	165
8.4	Affidavit	169

1 Introduction

1.1 The dynamic brain

Information coming from the environment is processed in the brain by sensory systems that are adaptive, shaping sensory signal processing to meet the needs of the animal at any given moment. This sculpting of the animal’s sensory world is a multifaceted process, involving active behaviours used to explore the environment, and distinct patterns of neural activity used to meet cognitive demands. These factors are inextricably linked through the conceptual framework of “internal states”, where latent processes simultaneously influence the expression of exploratory behaviours and neuronal modes of operation, both of which result in measurable modulations of neural activity in sensory systems.

Vision in action

Animals do not experience the visual world passively, but rather use behaviours such as locomotion and eye movements to actively explore visual scenes. These behaviours, in turn, result in changes to sensory input that need to be accounted for by the brain in order to distinguish self-generated changes in input from those that originate in the environment (Von Holst and Mittelstaedt, 1950). Furthermore, through these exploratory behaviours, animals will encounter diverse environmental statistics. As the animal begins to move, a largely static world is transformed into one where the flow of objects from the centre of the visual field to the periphery is expected (Gibson, 1950). Eye movements can transition the visual world of the animal from the relative uniformity of the sky to the fine textures of landscapes below the horizon. Sensory input that does not fit the patterns expected from the movements may be a sign of food or danger. The result is that the study of the neural circuits involved in visual perception cannot only consider the effects of passive visual stimulation, but needs to consider visual input in the context of active behaviours (Busse et al., 2017; Cullen, 2004). In addition to this “active sensing”, the visual system needs to orchestrate other functions such as vigilance, attention, learning, and memory consolidation. Vision is thus fundamentally multi-functional, and the integration of this type of contextual information with visual signals leads to distinct regimes of operation and dynamic input-output mapping at the earliest stages of visual processing in the brain.

The dorsal lateral geniculate nucleus (dLGN) of the thalamus is an integrative hub for all of the above considerations. Although it is far from the only structure directly receiving input from the retina (Morin and Studholme, 2014; Martersteck et al., 2017), it is the initial node for what is known as “image-forming vision” – so called because the thalamocortical visual system extracts fine detail from visual scenes, contributing to object recognition and conscious vision (Seabrook et al., 2017). Thus, the dLGN sits at the bottom of an important hierarchy (Siegle et al., 2021), with the potential to influence much upstream visual processing in the brain.

Neurons of the dLGN are embedded in a complex circuit, suggesting that their role in transmission of visual signals is dynamic, although a precise functional description of this dynamism has proven difficult to articulate. Beyond transmitting retinal signals to the visual cortex, the dLGN also receives re-entrant

input from the visual cortex and is reciprocally connected to a sheet of inhibitory neurons known as the thalamic reticular nucleus (TRN; Sherman and Guillery, 2004; Kerschensteiner and Guido, 2017), also known as “guardian of the gateway to the cortex” Crick (1984) as it is thought to influence thalamocortical activity based on cognitive states. Meanwhile, behavioural signals can reach the dLGN via projections from various brainstem nuclei (McCormick, 1992; Sherman and Guillery, 2004; Kerschensteiner and Guido, 2017) involved in coordinating behaviours and brain states (Steriade and McCarley, 1990; Mena-Segovia and Bolam, 2017). Thus, while still being a relatively simple piece of brain circuitry – in the sense that the dLGN has one strong driving input and one clear output – the integration of diverse modulatory inputs make the dLGN a key structure in which to study dynamic sensing.

Behaviour and brain states

One of the most obvious distinctions between operating modes in the brain is the partitioning of sleep and wakefulness. These two states can be distinguished using the collective electrical activity of large populations of cortical neurons, which can even be measured using electrodes placed outside the skull (Berger, 1929; Adrian and Matthews, 1934). During certain stages of sleep, the electrical potentials generated by cortical activity display large, slow oscillations (Steriade et al., 1993). This state is often referred to as *synchronized* (Harris and Thiele, 2011) because these high-amplitude oscillations arise largely from coordinated, simultaneous inputs to a neuronal population (Buzsáki et al., 2012; Einevoll et al., 2013). In contrast, wakefulness is generally characterized by smaller, faster oscillations. While some degree of transient synchronization can occur in this state, it is generally characterized by the independent firing of cortical neurons, and therefore referred to as *desynchronized* or *activated* (Harris and Thiele, 2011). These two oscillatory states are thought to have functional importance, with the synchronous state decoupling neural activity from external drive and supporting the coordinated activity necessary for offline memory consolidation (Steriade, 2006), and the activated state allowing for the more complex activity patterns required for stimulus encoding (Harris and Thiele, 2011; Zgha and McCormick, 2014; Haider et al., 2013).

The transition from a synchronous to an activated cortex involves the coordinated activity of a group of brainstem nuclei historically referred to as the *ascending reticular activating system* or *midbrain reticular formation* (Moruzzi and Magoun, 1949; Munk et al., 1996). This system contains nuclei that convey a variety of modulatory neurotransmitters, including norepinephrine (NE) and acetylcholine (ACh), to the thalamus and cortex (Steriade and McCarley, 1990). This control system has more recently been expanded to include other nuclei, such as the basal forebrain (Buzsáki et al., 1988; Xu et al., 2015). Nonetheless, the activity of these systems promotes wakefulness through their coordinated actions on the thalamocortical system (Lee and Dan, 2012; Scammell et al., 2017). The thalamus, while not the driver in transitions between brain states (Fuller et al., 2011), plays an integral role in their expression (Hirata and Castro-Alamancos, 2010; Poulet et al., 2012; Nestvogel and McCormick, 2022) and determines the representational content of sensory cortices during wakefulness. Thalamic relay nuclei provide strong, driving input to both sensory and association regions of the cortex (Sherman and Guillery, 2002; Bruno and Sakmann, 2006). Furthermore, the motif of recurrent

connectivity between the thalamus and cortex, together with the intrinsic properties of thalamic and cortical cells, is thought to cause and sustain state-related activity patterns (Steriade et al., 1993; Hill and Tononi, 2005; Crunelli and Hughes, 2010; McCormick et al., 2015; Neske, 2016).

Brain state transitions similar to those described above have also been observed during wakefulness, and are often related to the ongoing behaviour of the animal. In the whisker-associated somatosensory cortex of mice, it was observed that cortical states resembling those associated with sleep arose when the animal stopped moving its whiskers, while whisker motion brought about an activated state (Crochet and Petersen, 2006; Poulet and Petersen, 2008). Subsequently, locomotion was also shown to modulate activity patterns in a similar manner in the primary visual cortex (V1; Niell and Stryker, 2010). Later investigations revealed a substantial impact of locomotion on thalamic activity as well (Erisken et al., 2014), and even uncovered a driving role for the thalamus in promoting an activated cortical state during whisking (Poulet et al., 2012).

Movements such as whisking and locomotion are almost invariably accompanied by pupil dilation (Erisken et al., 2014; Vinck et al., 2015; Petty et al., 2021). Historically, however, pupil dilation was measured in response to the viewing of “interesting visual stimuli” (Hess and Polt, 1960), or while performing an effortful task (Hess and Polt, 1964; Kahneman and Beatty, 1966). More recently, spontaneous pupil dilation – in the absence of locomotion or “interesting” stimuli – has been linked to cortical activation (Reimer et al., 2014), improved sensory processing (McGinley et al., 2015a), and to the activity of neuromodulatory systems responsible for cortical activation such as the locus coeruleus norepinephrine system (LC-NE; Aston-Jones and Cohen, 2005; Joshi et al., 2016; Reimer et al., 2014) and the basal forebrain cholinergic system (BF-ACh; Nelson and Mooney, 2016; Reimer et al., 2016). For these reasons, modulations of thalamocortical activity during pupil dilation in the awake animal, beyond the effects attributable to specific behaviours (Poulet and Petersen, 2008; Vinck et al., 2015; Petty et al., 2021), are thought to reflect a unified internal state: *arousal*.

1.2 Thalamic circuits for vision

The dLGN as a relay for visual information

One of the initial nodes of visual information processing in the mammalian brain is the dorsal lateral geniculate nucleus of the thalamus (dLGN). Here, incoming visual signals from retinal ganglion cells (RGCs) in the eye are passed on to the primary visual cortex (V1; Sherman and Guillery, 2004). In early recordings from the visual system of cats, Hubel (1960) observed that RGCs and dLGN neurons had similar response properties, and concluded that “complex integrative [visual] function” must occur in the cortex. This observation continues to be made in more modern investigations (e.g. Rathbun et al., 2010), where receptive fields (RFs) of monosynaptically connected RGC-dLGN cell pairs, measured under anaesthesia and using white noise stimulation were found to be nearly identical. This type of observation has led to the textbook labelling of dLGN thalamocortical (TC) neurons as “relays”, implying that no transformation of visual information occurs as it passes through the dLGN (Casanova and Chalupa, 2023). While the evidence against this idea is substantial, this simple description of the dLGN remains, perhaps due to the lack of a unifying framework for the mosaic

of observations made in the dLGN (Casanova and Chalupa, 2023).

But what exactly is the nature of the visual information available to dLGN neurons? The apparent simplicity of the RFs measured using noise stimuli tends to obscure the fact that the circuitry of the retina does not generate pixel-like output, but decomposes the image into behaviourally-relevant feature channels representing complex spatio-temporal visual features (Masland, 2012; Kerschensteiner, 2022). These response types can be robustly detected with the use of a rich visual stimulus (i.e. one with a variety of spatial and temporal patterns), together with a modern unsupervised clustering method, revealing the presence of >30 functional RGC sub-types (Baden et al., 2016). These included classes of RGCs representing simple pixel-like spots of light and dark (ON and OFF types), but with diverse temporal response patterns, and representing additional features of visual stimuli such as edge orientation, movement, and movement direction. This type of investigation confirmed and expanded upon functional classes which had been previously discovered using targeted visual stimuli and analyses (e.g. Barlow and Hill, 1963; Weng et al., 2005). Further investigations uncovered that, in addition to linear stimulus filtering properties, RGS can have non-linear response properties dependent on the illumination context (Pearson and Kerschensteiner, 2015) and, interestingly, also the context provided by naturalistic visual stimuli (Goldin et al., 2022; Karamanlis et al., 2022). Indeed, the spatial distribution of RGCs types reflects the statistics of natural visual scenes (Gupta et al., 2023). These results strongly suggests that visual encoding functions of later processing stages such as the dLGN cannot be easily inferred from investigations using a limited set of parametric stimuli, but rather should be studied under naturalistic stimulation conditions.

The older, simplified understanding of RGC response types, combined with the observation that dLGN neurons in cats and monkeys only require one retinal input spike to themselves spike (Bishop et al., 1958; Cleland et al., 1971; Usrey et al., 1999; Sincich et al., 2007), has led to the idea that dLGN stimulus responses should also be simple. Stimulus responses in the dLGN are thought to have a pixel-like center-surround organization, and often descriptively modelled using a simple “difference of Gaussians” model (Rodieck, 1965; Grubb and Thompson, 2003; Einevoll and Plesser, 2012). However, even under anaesthesia, it has been reported mouse dLGN neurons represent more complex visual features such as orientation and direction of movement (Piscopo et al., 2013). Indeed, taking an empirical modelling approach to quantifying dLGN stimulus-responses, Rosón et al. (2019) revealed that multiple complex RGC response types are required to capture dLGN stimulus responses to a rich visual stimulus. One of the differences separating studies measuring simple dLGN receptive fields and those revealing complexities could be the use of anesthesia (e.g. Rathbun et al., 2010), which may limit the degree to which top-down and behaviour-related modulatory inputs influence the RFs of dLGN neurons. In addition, the use of naturalistic stimuli with higher-order structure could further improve our understanding of how dLGN circuitry shapes its stimulus-responses. Studies that use stimulus-response kernels derived from artificial stimuli to obtain a good prediction (~25-60% of response variance explained) of dLGN responses to naturalistic stimuli have only been performed in anaesthetized animals (Dan et al., 1996; Lesica and Stanley, 2004; Mante et al., 2008). Interestingly, one particular situation in which these models fail is for rapid transient increases in firing rate linked to burst firing (Lesica and Stanley, 2004;

Mante et al., 2008), the occurrence of which has been linked to particular brain states in the awake animal (Bezdudnaya et al., 2006).

Two firing modes in the dLGN

One of the most prominent features of dLGN activity was recorded by Hubel, who observed that, when cats entered into periods of quiescence or sleep, dLGN neurons began to fire more sparsely, but in clusters of several spikes at firing rates sometimes exceeding 500 Hz (Hubel, 1960). These bursts of spikes, a feature of all thalamocortical relay neurons (Sherman, 2001), are generated by a cell-intrinsic mechanism: prolonged hyperpolarization de-inactivates T-type calcium channels, which, together with a depolarizing input or intrinsic depolarization driven by a hyperpolarization-activated cation current, produces a prolonged calcium-dependent depolarization known as a low threshold spike and subsequent sodium action potentials at high rates (Jahnsen and Llinás, 1984; Crunelli et al., 1989; Llinás and Steriade, 2006). Importantly, the presence of the intrinsic hyperpolarization-activated cation current can lead to rhythmic bursting (McCormick and Pape, 1990; Llinás and Steriade, 2006). As already noted by Hubel, these bursts preferentially occur during sleep (Livingstone and Hubel, 1981; McCarley et al., 1983), but their occurrence in the dLGN during wakefulness was later emphasized (Guido and Weyand, 1995), specifically during periods of visual inattention (Weyand et al., 2001) and with a synchronized hippocampal LFP (Bezdudnaya et al., 2006). Indeed, thalamic bursting is thought to play a crucial role in the expression of slow cortical rhythms during sleep (Steriade et al., 1993) as well as quiescent wakefulness (Nestvogel and McCormick, 2022). However, the counter-intuitive observation that thalamic bursting also occurs in conjunction with exploratory behaviours such as eye movements (Guido and Weyand, 1995; Ramcharan et al., 2000) and whisker twitches (Fanselow et al., 2001) led to the hypothesis that bursting may also play a role in stimulus encoding. For example, because bursts strongly activate cortical neurons (Swadlow and Gusev, 2001), stimulus-driven bursting may facilitate stimulus detection, while regular “tonic” spiking is better suited to encode stimulus detail (Sherman, 2001; Nicolelis and Fanselow, 2002). However, it has also been observed that bursts may carry *more* information per unit than tonic spikes (Reinagel et al., 1999), and have the potential for multiplexed stimulus encoding, conveying distinct information through burst timing, intra-burst spike rate, and intra-burst spike timing (Mease et al., 2017). Furthermore, naturalistic stimulus sequences regularly elicit bursts from dLGN neurons (Lesica and Stanley, 2004), and may serve to encode low-frequency information and transitions from non-preferred to preferred stimuli (Lesica and Stanley, 2004; Alitto et al., 2005). Thus, rhythmic bursting during periods of quiescence plays a role in driving brain states that are de-coupled from the environment, while bursting during periods of arousal may play a role in altering stimulus encoding.

Retinotectal and vLGN pathways

The thalamocortical pathway is, however, only one of the many visual pathways in the brain. The retina projects to more than fifty brain areas, including a prominent projection to the superior colliculus (SC; Martersteck et al., 2017). While the SC receives visual information from the retina, it has long been thought

that the SC does not participate in “image-forming” vision, but rather coordinates “reflexive” behaviours (Ramón Y Cajal et al., 1995). Some characteristics of the SC anatomy and stimulus responses would appear to support this view. For example, the SC has two output pathways that respectively cause orienting or avoidance behaviours (Dean et al., 1989; Isa et al., 2020), and contains neurons that respond to behaviourally relevant visual features, such as small moving stimuli resembling potential prey (Hoy et al., 2019), or rapidly expanding dark discs known as “looming” stimuli resembling potential predators (Shang et al., 2015). These visual feature representations may even simply be inherited from retinal outputs representing looming (Kim et al., 2020), rather than computed *de novo* in SC. However, it is clear that the SC is involved in multiple visual functions beyond reflex orchestration, perhaps orchestrated by its wide-spread ascending projections (Basso et al., 2021). Furthermore, the types of behaviours orchestrated by the SC are not invariably elicited by visual stimulation, but are subject to contextual modulation (Evans et al., 2019). One potential substrate for this could be gain control of SC visual responses by descending projections from the visual cortex (Zhao et al., 2014).

While the cortex provides excitatory gain control, inhibitory control may be provided by a thalamic structure called the ventral lateral geniculate nucleus (vLGN). Unlike the dLGN, the vLGN is composed of predominantly inhibitory neurons (Sabbagh et al., 2021), and appears to be involved in visuomotor transformation and other non-image-forming visual functions such as circadian rhythms (Harrington, 1997). The vLGN is highly integrative, with inputs from a wide variety of brain regions (Harrington, 1997). The vLGN may be partitioned into two subdivisions; the inner portion receiving brainstem neuromodulatory input but lacking visual responses, and the external portion receiving top-down input from visual cortex as well as direct retinal input (Harrington, 1997; Kolmac and Mitrofanis, 2000). The visual stimulus responses of the rodent vLGN are arranged retinotopically, and appear to be simple: predominantly sustained responses to light increments (ON responses) with lower spatial specificity than dLGN neurons (Harrington, 1997). A subset of vLGN neurons project to SC (Moore et al., 2000), and, interestingly, this SC-projecting population of neurons overlaps with the visually responsive retinorecipient neurons (Hayashi and Nagata, 1981). Thus, the vLGN contains the anatomical and functional prerequisites to exert inhibitory control of SC depending on visual context.

1.3 Modulation of dLGN activity

Modulation of the dLGN by behaviour

Although some studies have found that almost all dLGN spikes can be associated with a single retinal EPSP in anaesthetized animals (Sincich et al., 2007), RGC axon terminals only account for around 10% of synapses on dLGN neurons (Van Horn et al., 2000; Bickford et al., 2010). One additional major source of input are neuromodulatory axons, which account for 30-35% of synapses (Erişir et al., 1997; Sherman and Guillery, 2002). The majority of these are cholinergic fibres arising from the pedunculopontine tegmental nucleus (PPN; Hallanger et al., 1987; Huerta-Ocampo et al., 2020; Sokhadze et al., 2022), a part of the reticular activating system, and the parabigeminal nucleus, a structure involved in the coordination of targeted eye movements

(Cui and Malpeli, 2003; Ma et al., 2013). Acetylcholine may also influence the dLGN via projections from the basal forebrain (BF) to the TRN (Hallanger et al., 1987; Sokhadze et al., 2022), which exerts tight inhibitory control over thalamic relay nuclei (Pinault, 2004). Additional direct neuromodulatory inputs to the dLGN transmit norepinephrine from the locus coeruleus (Lindvall et al., 1974; Mackay-Sim et al., 1983), and serotonin from the dorsal raphe (Moore et al., 1978; Mackay-Sim et al., 1983). Thus, while RGCs represent “driver” inputs to dLGN thalamocortical neurons, these other “modulator” inputs are prevalent (Sherman and Guillery, 1998), and provide a means by which information related to arousal and even specific behaviours can sculpt dLGN stimulus-responses.

It is therefore not surprising that signatures of ongoing behaviour and brain state are reflected in the spiking output of dLGN neurons. For example, during locomotion dLGN neurons decrease their bursting and increase their baseline and evoked firing rates (Erisken et al., 2014; Aydın et al., 2018). Locomotion also influences the spatial and temporal integration properties of the dLGN. During locomotion dLGN neurons tend to have reduced surround suppression and prefer larger stimuli (Erisken et al., 2014), as well as particularly strong enhancement of responses to high temporal frequency stimuli (Aydın et al., 2018; Reinhold et al., 2023), which was also observed in state transitions demarcated by the hippocampal LFP (Bezdudnaya et al., 2006). This running-related response enhancement in dLGN neurons could be mediated either by direct depolarization via cholinergic signalling from the PPN, or by disinhibition via BF-GABA input to the TRN (McKenna et al., 2013; Erisken et al., 2014). While locomotion is a behaviour that changes visual input, whisking does not. Yet, Petty et al. (2021) found that whisking, like locomotion, increases activity in the lateral posterior nucleus (LP) of the thalamus, a higher-order visual thalamic relay. Furthermore, even in somatosensory thalamic nuclei this modulation was not related to specific whisker movements, and was unchanged after elimination of both sensory reafference from the somatosensory cortex, as well movement-related input from motor cortex and SC (Petty et al., 2021). These results would suggest that the modulated activity of thalamic relay nuclei during behaviour is more related to the overall context or state than moment-to-moment changes in behaviour, and that neuromodulatory nuclei are mediators, but both of these hypotheses remain to be confirmed for the dLGN. However, these conjectures do not eliminate the possibility that different types of contextual modulation, or the sculpting of modulation beyond a general increase in firing rate, may still be provided by diverse modulatory input sources.

Modulation of the dLGN by corticothalamic feedback

Corticofugal inputs to the dLGN from layer 6 of the primary visual cortex (V1-L6) account for almost half of all inputs to dLGN neurons (40-50%; Erişir et al., 1997; Van Horn et al., 2000; Sherman and Guillery, 2002). This corticothalamic feedback (CT-FB) arises from a specific sub-population of V1-L6 excitatory pyramidal neurons (Bourassa and Deschênes, 1995; Olsen et al., 2012; Whilden et al., 2021). The precise function of these neurons has been difficult to discern due to their inaccessible location, their intermingling with other pyramidal projection and inhibitory neurons, and their complex axonal arborization to other cortical layers (Thomson, 2010). In the cortex, CT neurons appear to exert a largely inhibitory role within their cortical column by

recruiting local interneurons (Olsen et al., 2012; Bortone et al., 2014), while providing strong excitation to L5 pyramidal projection neurons (Kim et al., 2014). Similarly, these CT neurons also have a dual influence in their thalamic projections. They provide direct modulatory excitation to thalamic neurons via their contacts to the distal dendrites of thalamic relay neurons (Wilson et al., 1984; Erişir et al., 1997) and recruitment of slow-acting NMDAR glutamate receptors (Scharfman et al., 1990; Jones et al., 1998; Alexander et al., 2006; Augustinaite et al., 2014), with fast-acting AMPARs contributing mainly at hyperpolarized membrane potentials (Crandall et al., 2015). The relatively prolonged depolarizations caused by NMDAR activation can contribute to switching thalamic neurons from burst to tonic mode (Scharfman et al., 1990; McCormick and von Krosigk, 1992). However, CT-FB also provides indirect inhibition through local interneurons and axon collaterals in the TRN (Bourassa and Deschênes, 1995; Olsen et al., 2012), making its overall effects on the dLGN difficult to discern.

The direct projection from V1-L6 to the dLGN is spatially localized and roughly topographical (Tsumoto et al., 1978; Born et al., 2021), conferring a functional role for CT-FB in spatial integration in the dLGN. Thalamic neurons with spatial RF centres matching those of the V1-L6 neurons providing feedback show response enhancement, while those with displaced RF centres are suppressed (Tsumoto et al., 1978; Eyding et al., 2003; Jones et al., 2012; Born et al., 2021). Thus, one function of CT-FB in vision is to sharpen spatial responses in dLGN neurons (Alitto and Usrey, 2003; Andolina et al., 2013), though a combination of targeted direct excitation and wide-spread inhibition through recruitment of the TRN (Born et al., 2021). Importantly, uncovering this result required the use of spatially localized visual stimuli (*c.f.* Denman and Contreras, 2015), but it is consistent with a primarily suppressive effect of CT-FB measured using full-field stimuli (Olsen et al., 2012). Interestingly, the spatial sharpening effect of CT-FB was inconsistent when measured using white noise stimulation (Denman and Contreras, 2015), which might be due to the specific orientation tuning of corticothalamic V1-L6 neurons (Vélez-Fort et al., 2014; Stoelzel et al., 2017).

While CT-FB is not required for dLGN orientation tuning (Zhao et al., 2014), it is likely that oriented stimuli – or, more generally, stimuli with a variety of visual features – are required in order to properly drive CT-FB under control conditions. For this same reason, it is also likely that global activation of CT-FB produces uninterpretable results, as it is functionally equivalent to presenting a visual stimulus with every orientation present at all locations in space. Therefore suppression of CT-FB together with stimuli that properly engage V1-L6 is more likely to produce interpretable results. Furthermore, it has been shown that the overall effect of CT-FB is dependent on stimulus contrast (Denman and Contreras, 2015) and the frequency of optogenetic V1-L6 activation (Kirchgessner et al., 2020), due to the differential plasticity of L6-dLGN and L6-TRN synapses (Crandall et al., 2015). Perhaps related to this, there is also evidence that CT-FB has complex temporal effects, primarily affecting the sustained component of stimulus responses (Eyding et al., 2003; De Labra et al., 2007), leading to better tracking of temporal modulations with CT-FB intact (Andolina et al., 2007), and that CT-FB has temporally modulated – even biphasic – effects on thalamic relays (Mease et al., 2014). Thus, while the overall function of CT-FB remains unclear, it is clear that the circuit is sensitive to the fine-grained spatial and temporal characteristics of the visual stimulus.

Beyond modulating dLGN activity depending on the context provided by the visual stimulus, there is also substantial evidence that CT-FB modulates dLGN activity depending on contextual cues provided by brain state and behaviour. Indeed, there is evidence that almost half of thalamic-projecting V1-L6 neurons may not be visually responsive at all (Stoelzel et al., 2017; Augustinaite and Kuhn, 2020). This corticothalamic population receives a large proportion of its inputs from higher-order visual and association areas of the cortex (Vélez-Fort et al., 2014), such as vestibular inputs from the retrosplenial cortex, which allow encoding of head rotations (Vélez-Fort et al., 2018). CT-FB may also convey a more generalized notion of behavioural state, displaying a brain state-dependent increase in responses to drifting grating stimuli (Stoelzel et al., 2017). Using behavioural arousal (pupil size and locomotion) as a measure of state, Augustinaite and Kuhn (2020) found that visually activated V1-L6 CT-FB neurons increased their visual responses during arousal (while maintaining a stable baseline), whereas visually suppressed V1-L6 CT-FB neurons decreased their baseline activity (effectively reducing modulation depth during visual stimulation). These state-related signals may be conveyed by acetylcholine: V1-L6 CT-FB neurons were found to increase their input resistance and firing rates in response to ACh application via nicotinic and muscarinic receptors (as opposed to network effects; Sundberg et al., 2018). This state-dependence of L6 activity could contribute to state-related switches between burst and tonic mode in the thalamus (McCormick and von Krosigk, 1992; Wang et al., 2006; Augustinaite et al., 2014; Mease et al., 2014). Furthermore, CT-FB has been implicated in attentional modulation of sensory processing in the dLGN (Montero, 2000; Saalman and Kastner, 2011), although emphasis has so far been placed on cross-modal attention via the TRN (McAlonan et al., 2008; Wimmer et al., 2015). Nonetheless, CT-FB from V1-L6 neurons has the potential to convey both generalized (cognitive or behavioural state) and specific (feature-based attention) contextual information to the dLGN.

1.4 Objectives and key questions

The retino-geniculo-cortical pathway is the most thoroughly studied visual pathways in mammals, and yet the apparent simplicity of visual processing through this circuit is challenged by observations collected in the awake and behaving animal, and with the use of spatio-temporally complex naturalistic stimuli. The convergence of many different modulatory inputs onto single dLGN neurons suggests that they are a hub for diverse influences, and likely participate in multiple functions related to active vision during behaviour as well as cognitive processes orchestrated by top-down signalling. Furthermore, the tuning of RGCs, dLGN neurons, and V1-L6 neurons to complex visual features implies that these circuit elements are sensitive to multiple dimensions of visual stimuli, and may be best probed with naturalistic stimuli.

One specific case that requires the use of naturalistic stimuli is during investigation of corticothalamic feedback. The use of simple, artificial stimuli has yielded conflicting results in many respects, which might result from the failure of these stimuli to appropriately drive activity in V1-L6. Related to this, the direction of manipulation of V1-L6 is important. Because the activity of V1-L6 in response to naturalistic stimulation is largely unknown, it is unclear how the CT-FB projection should be manipulated to probe its endogenous effects. Consequently, a strategy for the *suppression* of V1-L6 should be employed, such that endogenous activity

patterns remain intact, but can be selectively eliminated. Finally, because the dynamic regime of cortical activity is strongly dependent on the behavioural state of the animal, the use of anaesthesia could eliminate V1-L6 dynamics that are essential to CT-FB function in an awake and perceiving animal. Furthermore, V1-L6 activity is dependent on active behaviours, and this might be a channel through which behavioural signals reach the dLGN that can only be revealed during awake recordings. Thus, Spacek et al. (2022, Chapter 2) presents the first investigation of the functional effects of CT-FB in awake animals with all of these factors taken into consideration. It was hypothesized that naturalistic stimuli would be particularly effective in revealing a robust effect of CT-FB in dLGN neurons, and the interaction of these effects with a behavioural state defined by locomotion was also investigated.

While locomotion provides a powerful index for the behavioural state-related activity in sensory systems, dLGN neurons are, anatomically speaking, a hub for the convergence of many modulatory inputs. It is therefore unlikely that one single factor can capture all of the modulation in dLGN neurons. Given the multifaceted links between pupil size changes and behavioural and cognitive factors, Crombie et al. (2024, Chapter 3) departs from the hypothesis that diverse aspects of pupil size dynamics can explain spiking modulations in the dLGN. Specifically, it was observed that pupil size changes occur over a multitude of timescales, all of which were hypothesized to be relevant for activity modulation in the dLGN. From previous results it was hypothesized that pupil dilation should be linked to an increase in firing rate, while pupil contraction should be linked to “offline” activity patterns such as thalamic bursting. Furthermore, because pupil size changes are linked to behaviours with visual consequences, the contributions of locomotion and eye movements were separated from those captured by pupil size dynamics. Finally, it was hypothesized that the modulations linked to pupil dynamics should have consequences for how dLGN neurons encode naturalistic visual stimuli.

It should already be clear that a multitude of factors can influence the activity of dLGN neurons: visual stimulation, feedback from the visual cortex, and behaviours such as locomotion and/or a generalized state of arousal. Yet there is no unified modelling framework that captures all of these influences together. Schmors et al. (2023, Chapter 4) introduces a generalized linear model including terms for spatio-temporally extended effects of a visual stimulus, CT-FB, locomotion, and pupil size. Critically, the typical GLM was made more efficient by fitting response kernels as a combination of spline basis functions rather than individual pixels or time-points (Huang et al., 2021). This adjustment was also hypothesized to help the model fit sparse receptive fields in the presence of the spatiotemporal correlations present in natural visual scenes, which were used in the experiment to elicit visually-driven dLGN activity. Furthermore, CT-FB was manipulated using an optogenetic suppression approach, rather than artificial activation, in order to assess its endogenous contributions. Once the model has been fit to the spiking activity of a dLGN neuron, it can be used as an *in silico* version of the neuron that can be used to probe how the neuron would respond in the presence of experimental manipulations, such as the artificial elimination of cortical feedback.

Finally, despite decades of continuous interest in the visual pathway through the dLGN, it is still unclear how dynamic visual feature extraction through this pathway contributes to guiding the behaviour of animals. However, there are other visual pathways that have been more closely linked to behavioural consequences.

One example is the pathway through the retino-recipient SC, which links relatively simple visual features to stereotyped responses. Even this pathway is subject to modulation by cognitive factors, and two recent, independent reports converge on a function for long-range inhibitory projections from the vLGN to the SC in this modulation. Crombie and Busse (2021, Chapter 5) summarizes the findings of these reports, and places their contribution in the broader literature of visually-guided behavioural responses.

2 Exploring the effects of feedback and locomotion in the dLGN

The following chapter is reproduced from an article originally published in *eLife*:

Martin A Spacek, Davide Crombie, Yannik Bauer, Gregory Born, Xinyu Liu, Steffen Katzner, Laura Busse (2022). Robust effects of corticothalamic feedback and behavioral state on movie responses in mouse dLGN. *Elife*, 11, e70469. DOI: <https://doi.org/10.7554/eLife.70469>.

Author contributions

The study was conceptualized by MAS and LB. MAS and YB performed the experiments, with the assistance of XL. The data was curated by MAS, DC, GB, SK, and LB. The methodology was developed by MAS and DC. The formal statistical analysis was performed by SK. MAS, DC, YB, XL, and SK all contributed to developing the software infrastructure supporting the investigation. Data visualization was performed by MAS, YB, GB, and SK. GB and LB wrote the original draft. MAS, DC, SK, and LB contributed to reviewing and editing the manuscript. LB was responsible for project administration, supervision, and funding acquisition. DC, YB, and GB contributed equally to the work.

Personal contributions

DC wrote the software used to perform video-based eye tracking and curated the eye tracking data that was used in Figure 1 – supplement 2, Figure 1 – supplement 6, Figure 5 – supplement 1, and Figure 5 – supplement 2. The code for the analyses involving eye tracking data in Figure 5 – supplement 1h and i, and Figure 5 – supplement 2 was written by DC. DC also contributed substantially to developing the software infrastructure supporting the investigation. Furthermore, DC regularly participated in project meetings to decide on methodology, wrote the methods section pertaining to eye tracking, and contributed to the editing and review process.

Copyright

This article was published under the CC-BY 4.0 International licence.

Robust effects of corticothalamic feedback and behavioral state on movie responses in mouse dLGN

Martin A Spacek^{1*}, Davide Crombie^{1,2†}, Yannik Bauer^{1,2†}, Gregory Born^{1,2†}, Xinyu Liu^{1,2}, Steffen Katzner¹, Laura Busse^{1,3*}

¹Division of Neurobiology, Faculty of Biology, LMU Munich, Planegg-Martinsried, Germany; ²Graduate School of Systemic Neurosciences, LMU Munich, Munich, Germany; ³Bernstein Centre for Computational Neuroscience, Munich, Germany

Abstract Neurons in the dorsolateral geniculate nucleus (dLGN) of the thalamus receive a substantial proportion of modulatory inputs from corticothalamic (CT) feedback and brain stem nuclei. Hypothesizing that these modulatory influences might be differentially engaged depending on the visual stimulus and behavioral state, we performed in vivo extracellular recordings from mouse dLGN while optogenetically suppressing CT feedback and monitoring behavioral state by locomotion and pupil dilation. For naturalistic movie clips, we found CT feedback to consistently increase dLGN response gain and promote tonic firing. In contrast, for gratings, CT feedback effects on firing rates were mixed. For both stimulus types, the neural signatures of CT feedback closely resembled those of behavioral state, yet effects of behavioral state on responses to movies persisted even when CT feedback was suppressed. We conclude that CT feedback modulates visual information on its way to cortex in a stimulus-dependent manner, but largely independently of behavioral state.

*For correspondence:
m.spacek@lmu.de (MAS);
busse@bio.lmu.de (LB)

†These authors contributed
equally to this work

Competing interest: The authors
declare that no competing
interests exist.

Funding: See page 26

Preprinted: 19 September 2019

Received: 18 May 2021

Accepted: 13 March 2022

Published: 22 March 2022

Reviewing Editor: Tatyana
O Sharpee, Salk Institute for
Biological Studies, United States

© Copyright Spacek et al. This
article is distributed under the
terms of the [Creative Commons
Attribution License](#), which
permits unrestricted use and
redistribution provided that the
original author and source are
credited.

Editor's evaluation

This paper will be of interest to neuroscientists interested in understanding the role of corticothalamic feedback in coding of sensory inputs. The authors show that feedback is stronger for natural stimuli compared to artificial stimuli. Surprisingly, the feedback from the cortex works in parallel with other modulatory influences reflecting changes in the arousal (measured here with pupil size) or changes in locomotion.

Introduction

Mammalian vision is based on a hierarchy of processing stages that are connected by feedforward circuits projecting from lower to higher levels, and by feedback circuits projecting from higher to lower levels. Feedforward processing is thought to create feature selectivity (*Lien and Scanziani, 2018; Hubel and Wiesel, 1962*) and invariance to low-level stimulus features (*Hubel and Wiesel, 1962; Chance et al., 1999; Riesenhuber and Poggio, 1999; Riesenhuber and Poggio, 2000*), to ultimately enable object recognition (*DiCarlo et al., 2012*). Hypotheses about the functional role of feedback circuits include top-down attention, working memory, prediction, and awareness (*Squire et al., 2013; Roelfsema and de Lange, 2016; Bastos et al., 2012; Lamme and Roelfsema, 2000; Takahashi et al., 2016; Larkum, 2013*). Compared to theories of feedforward processing, however, there is little consensus on the specific function of feedback connections (*Heeger, 2017; Gilbert and Li, 2013*).

Feedback in the mammalian visual system targets brain areas as early as the dorsolateral geniculate nucleus (dLGN) of the thalamus, where up to 30% of synaptic connections onto relay cells are established by corticothalamic (CT) feedback (Sherman and Guillery, 2002). Direct CT feedback is thought to arise from V1 layer 6 (L6) CT pyramidal cells (Briggs, 2010; Sillito and Jones, 2002), which are known for their notoriously low firing rates (Vélez-Fort et al., 2014; Stoelzel et al., 2017; Crandall et al., 2017; Oberlaender et al., 2012; Swadlow, 1989; Pausin and Krieger, 2018), their sharp tuning for orientation (Vélez-Fort et al., 2014; Liang et al., 2021), and their diverse signaling of behavioral state (Augustinaite and Kuhn, 2020; Liang et al., 2021). The action of CT feedback on dLGN activity is generally considered modulatory rather than driving (Sherman and Guillery, 1998), as CT feedback inputs contact the distal dendrites of relay cells via NMDA glutamate (Augustinaite et al., 2014) or mGluR1 metabotropic receptors (Godwin et al., 1996), implying rather slow and long-lasting effects on dLGN activity. Similar to other depolarizing inputs to dLGN, such as neuromodulatory brain stem inputs (McCormick, 1992), CT feedback has been linked to promoting switching from burst to tonic firing mode, and to facilitating transmission of retinal signals (Augustinaite et al., 2014; de Labra et al., 2007; Wang et al., 2006; Dossi et al., 1992). However, since L6 CT pyramidal cells provide both direct excitation and indirect inhibition of dLGN via the thalamic reticular nucleus (TRN) and dLGN inhibitory interneurons (Sillito and Jones, 2002; Usrey and Sherman, 2019), the effects of CT feedback are expected to be complex and dependent on temporal and spatial aspects of the stimulus (Crandall et al., 2015; Born et al., 2021; Murphy and Sillito, 1987; McClurkin and Marrocco, 1984; Jones et al., 2012; Hasse and Briggs, 2017).

Most of the previous in vivo studies have probed the functional role of CT feedback with artificial stimuli, and often in anesthetized animals; CT feedback, however, might be most relevant for processing of dynamic naturalistic information and during wakefulness. From a conceptual perspective, if the role of feedback was to provide context based on an internal model built from the statistics of the world (Berkes et al., 2011; Lee and Mumford, 2003; Rao and Ballard, 1999; Clark, 2013), natural stimuli would be expected to best comply with this model, and hence better drive these feedback mechanisms. Indeed, it has previously been suggested that CT feedback might be more strongly engaged for moving compared to stationary stimuli (Sillito and Jones, 2002), and for complex dynamic noise textures than simple moving bars (Gulyás et al., 1990), consistent with a potential role in figure-ground processing (Poltoratski et al., 2019; Sillito et al., 1993; Cudeiro and Sillito, 1996). Furthermore, since the responsiveness of feedback projections (Makino and Komiyama, 2015; Keller et al., 2020), including those originating from V1 CT neurons (Briggs and Usrey, 2011), seem to be strongly reduced by anesthesia, it is critical to examine CT feedback effects in awake animals. Indeed, L6CT neurons have recently been found to have diverse response modulations according to pupil-indexed behavioral state (Augustinaite and Kuhn, 2020).

Here, we recorded spiking activity in dLGN of awake mice and investigated how CT feedback affected dLGN responses to naturalistic movie clips. Suppressing CT feedback either via photostimulation of V1 parvalbumin-positive (PV+) inhibitory interneurons or via direct photosuppression of L6CT neurons, we found that CT feedback had consistent modulatory effects on dLGN responses to movie clips, which could largely be captured by an increase in gain. Effects of CT feedback on dLGN responses to grating stimuli were more diverse, highlighting the stimulus-dependency of CT feedback effects. Finally, while geniculate responses to movies during V1 suppression resembled those during quiescence, we found effects of CT feedback and behavioral state to be largely independent. Overall, our results demonstrate that neural responses to naturalistic movies en route to cortex can be robustly modulated by extra-retinal influences such as cortical feedback and behavioral state, which seem to be largely conveyed via different modulatory pathways.

Results

CT feedback robustly modulates dLGN responses to naturalistic movie clips

To investigate the impact of CT feedback on visual processing of naturalistic stimuli, we presented to head-fixed mice full-screen movie clips and compared responses of dLGN neurons during optogenetic suppression of V1 activity to a control condition with CT feedback left intact (Figure 1 and -Supplement 1). The responses of individual dLGN neurons to naturalistic movie clips were characterized by distinct

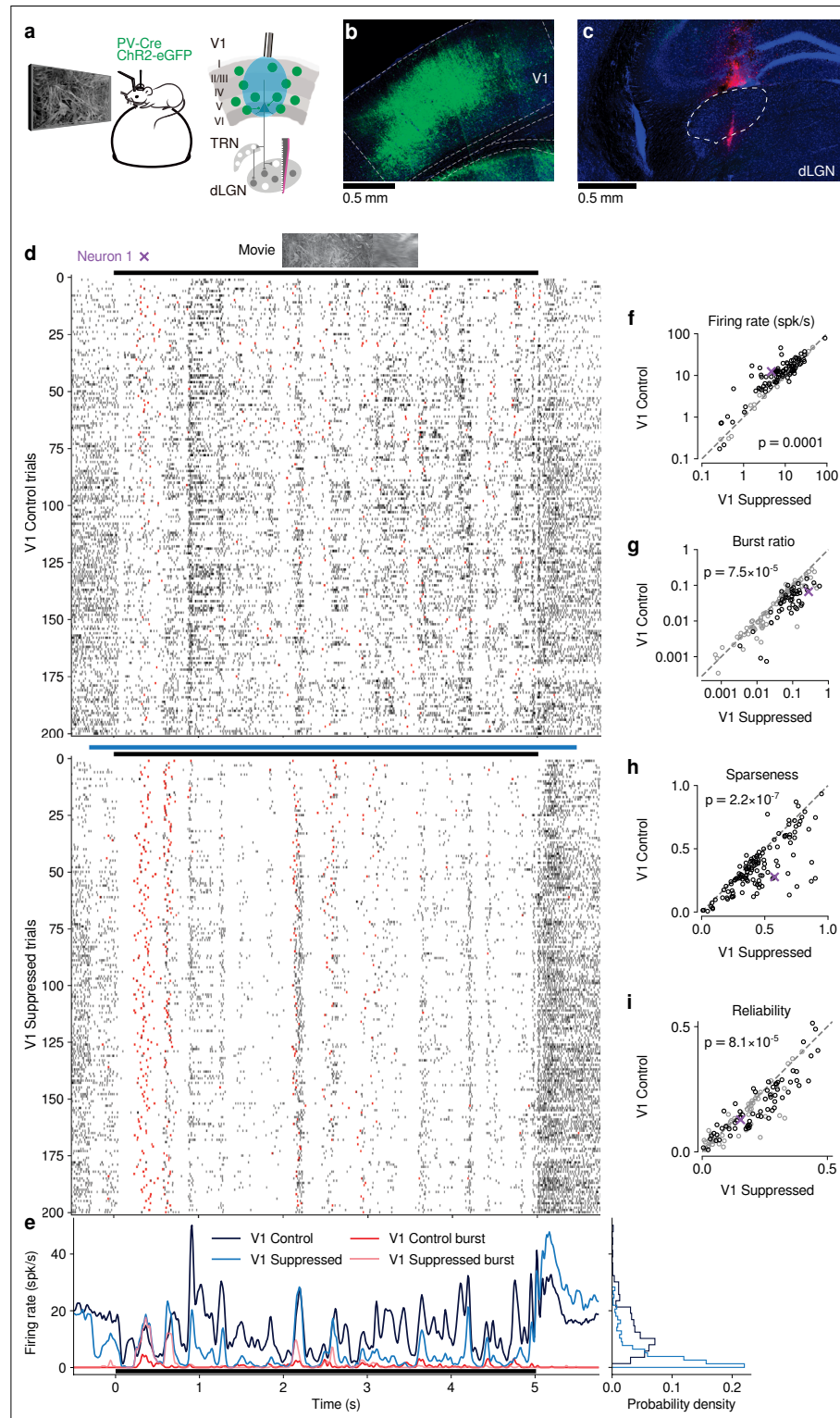


Figure 1. CT feedback modulates dLGN responses to full-screen naturalistic movie clips. (a) *Left:* Schematic of experimental setup. Head-fixed mice were placed on a floating Styrofoam ball and visual stimuli were presented on a screen located ~25 cm away from the animal. *Right:* ChR2 was conditionally expressed in PV + inhibitory interneurons (green) in all layers of V1 using a viral approach. Extracellular silicon electrode recordings were

Figure 1 continued on next page

Figure 1 continued

performed in dLGN with and without optogenetic suppression of V1. **(b)** Coronal section close to the V1 injection site for an example PV-Cre mouse (blue: DAPI; green: eYFP; Bregma: -3.4 mm). **(c)** Coronal section at the dLGN (white outline) recording site, same animal as in **(b)**. For post-mortem confirmation of the electrode position, the back of the probe was stained with Dil (magenta) for one of the recording sessions (blue: DAPI; Bregma: -1.82 mm). **(d)** Raster plots of an example neuron for 200 presentations of a 5 s naturalistic movie clip, with CT feedback intact (control condition, top) and during V1 suppression (bottom). Red: burst spikes; black bar: movie clip presentation; light blue bar: V1 suppression. **(e)** Left: PSTHs for both the control (dark blue) and V1 suppression (light blue) conditions. Superimposed are PSTHs of burst spikes only, separately for control (red) and V1 suppression (pink) conditions. Right: Corresponding instantaneous firing rate distributions. **(f–i)** Comparison of control vs. V1 suppression conditions for mean firing rate **(f)**, burst ratio **(g)**, temporal sparseness **(h)**, and response reliability **(i)**, all calculated for the duration of the movie clip. Sparseness captures the activity fraction of a neuron, re-scaled between 0 and 1 (Vinje and Gallant, 2000). Response reliability is defined as the mean Pearson correlation of all single trial PSTH pairs (Goard and Dan, 2009). For sample sizes, see Table 1. Purple: example neuron. Black markers in **(f,g,i)** indicate neurons with individually significant effects (Welch's t-test). See also Figure 1—figure supplement 1 to Figure 1—figure supplement 6.

The online version of this article includes the following video and figure supplement(s) for figure 1:

Figure supplement 1. Confirmation of optogenetic suppression of V1 responses and targeting dLGN for recordings.

Figure supplement 2. Effects of CT feedback on additional parameters of responses to naturalistic movies and their relationship with firing rate.

Figure supplement 3. Feedback effects during movie presentation are largely independent of functional cell type classification.

Figure supplement 4. Selective optogenetic suppression of L6 CT feedback in Ntsr1-Cre yielded similar results as global V1 suppression via PV + activation.

Figure supplement 5. Photostimulation in an Ntsr1- control mouse injected with cre-dependent stGtACR2 had no effect on neural responses.

Figure supplement 6. Effects of photostimulation on pupil size were unrelated to CT feedback effects on dLGN neuronal activity.

Figure 1—video 1. First example 5 s movie clip used for visual stimulation.

<https://elifesciences.org/articles/70469/figures#fig1video1>

Figure 1—video 2. Second example 5 s movie clip used for visual stimulation.

<https://elifesciences.org/articles/70469/figures#fig1video2>

response events that were narrow in time and reliable across trials (Figure 1d, top, example neuron). Consistent with the notion that CT feedback has a modulatory rather than driving role (Sherman, 2016), even during V1 suppression this temporal response pattern remained somewhat preserved (Pearson correlation $r = 0.54$, $p < 10^{-6}$, Figure 1d and e). Yet, as illustrated in the example neuron, with CT feedback intact, firing rates were higher and burst spikes were less frequent (Figure 1e, left). Accordingly, the distributions of instantaneous firing rates in the two conditions were significantly different (KS test, $p < 10^{-6}$), and were more skewed during V1 suppression than with CT feedback intact ($\gamma = 2.02$ vs 1.22; Figure 1e, right).

We observed similar effects in the recorded population of dLGN neurons, where CT feedback enhanced overall responses and promoted tonic firing mode. Indeed, while mean firing rates varied almost 4 orders of magnitude across the population (~ 0.1–100 spikes/s), they were higher in control conditions with CT feedback intact than during V1 suppression (13.7 vs 10.5 spikes/s; linear multilevel-model (LMM): $F_{1,63.2} = 17.1$, $p = 0.0001$; Figure 1f). In addition, CT feedback also influenced more fine-grained properties of geniculate responses. First, with CT feedback, the mean proportion of spikes occurring as part of a burst event was about half of what we observed during suppression (0.05 vs 0.09; LMM: $F_{1,64.0} = 17.9$, $p = 7.5 \times 10^{-5}$; Figure 1g). Second, consistent with the distributions of firing rate for the example neuron (Figure 1e, right), responses to the naturalistic movie clips with CT feedback intact were, on average, less sparse (0.35 vs 0.45; LMM: $F_{1,63.0} = 33.7$, $p = 2.2 \times 10^{-7}$; Figure 1h), indicating that neurons fired less selectively across the frames of the movie. Finally, we also examined the effect of CT feedback on response reliability. To quantify reliability, we computed the Pearson correlation coefficient of a neuron's responses between each pair of the 200 stimulus repeats

per condition, and averaged the correlation coefficients over all pair-wise combinations (Goard and Dan, 2009). With CT feedback intact, mean response reliability was lower than without feedback (0.15 vs 0.18; LMM: $F_{1,63.1} = 17.8, p = 8.1 \times 10^{-5}$; Figure 1i). Except for the effects on sparseness, the feedback effects on responses to naturalistic movies were unrelated to changes in firing rates (Figure 1—figure supplement 2c-g). The increased trial-to-trial reliability during V1 suppression could not be explained by higher stability in eye positions, because variability in eye position was slightly larger with CT feedback intact vs. suppressed (Figure 1—figure supplement 2h), and effects of CT feedback on neural reliability were unrelated to changes in variability of eye position (Figure 1—figure supplement 2i). Splitting the dLGN population into putative cell types according to several functional characteristics and location within dLGN revealed few differences in how global V1 suppression affected firing rates and bursting (Figure 1—figure supplement 3). As V1 suppression by PV + activation is robust, yet lacks selectivity (Wiegert et al., 2017), we repeated our experiments while directly photo-suppressing L6CT neurons. To this end, we expressed the inhibitory opsin stGtACR2 (Mahn et al., 2018) in V1 Ntsr1+ neurons, which correspond to $\geq 90\%$ to L6 CT neurons (Bortone et al., 2014; Kim et al., 2014, Figure 1—figure supplement 4). These experiments with specific suppression of L6 CT neurons during viewing of naturalistic movies yielded identical conclusions (Figure 1—figure supplement 4a-h).

Lastly, we performed two additional controls to rule out that photostimulation *per se* caused our findings. First, we repeated our experiments on an Ntsr1- control mouse, which was injected and underwent the same visual and photostimulation protocol. This negative control mouse did not show any effects of photostimulation on dLGN responses (Figure 1—figure supplement 5a-d). Second, we identified those experiments (14/31 for PV + activation, 0/10 for Ntsr1 + suppression experiments), where photostimulation decreased pupil size, indicative of light leakage into the retina. Even with these sessions removed, we found that our results remained qualitatively unchanged (Figure 1—figure supplement 6a-f). Finally, considering again all recordings, the effects of CT feedback on neuronal activity were unrelated to light-induced changes in pupil size (Figure 1—figure supplement 6g-j). Together, these results rule out that photostimulation *per se* led to the modulation of dLGN responses during naturalistic movie viewing.

Taken together, our results indicate that CT feedback can robustly modulate responses of dLGN neurons to naturalistic movie clips. The modulations are consistent with a net depolarizing effect, which supports higher firing rates and more linear, tonic firing mode with higher dynamic range, at the expense of sparseness, trial-to-trial reliability, and signal-to-noise.

V1 suppression decreases dLGN responses to naturalistic movies by reducing response gain

To better understand the effects of V1 suppression on dLGN firing rate, we next asked whether the observed reduction in responsiveness could be explained by a divisive and/or subtractive change (Figure 2). Using repeated random subsampling cross-validation, we fit a simple threshold linear model (Figure 2a, inset) to timepoint-by-timepoint responses in suppression vs. feedback conditions, and extracted the slope and threshold of the fit for each subsample (Figure 2b and d). In the two example neurons shown in Figure 2a-d, the fitted slope was significantly smaller than 1 (neuron 2: median slope of 0.66, 95% CI: 0.63–0.69, Figure 2b; neuron 1: median slope of 0.37, 95% CI: 0.32–0.41, Figure 2d), while the threshold (x -intercept) was either small or not significantly different from 0 (neuron 2: median of 1.58, 95% CI: 0.39–2.91; neuron 1: median of -0.14 , 95% CI: -1.49 – 0.89). We obtained similar results for the population of recorded neurons, where V1 suppression decreased the neurons' responses to naturalistic movie clips via a substantial change in response gain (slope of 0.75 ± 0.1 ; LMM) without a significant shift in baseline (threshold of -0.19 ± 1.15 ; LMM; Figure 2e). This demonstrates that V1 suppression influences responses in dLGN to naturalistic movie clips predominantly via a divisive effect.

We noticed that the threshold linear model could predict the effects of V1 suppression better for some neurons than for others. We therefore explored whether poor fits of the model might be related to our finding that V1 suppression can trigger non-linear, burst-mode firing. For instance, the threshold-linear model accurately captured the responses of example neuron 2 (median $R^2 = 0.90$, cross-validated; Figure 2a and b), which exhibited little bursting during V1 suppression (burst ratio: 0.007). Neuron 1, in contrast, had a higher burst ratio during suppression (0.28) and the prediction

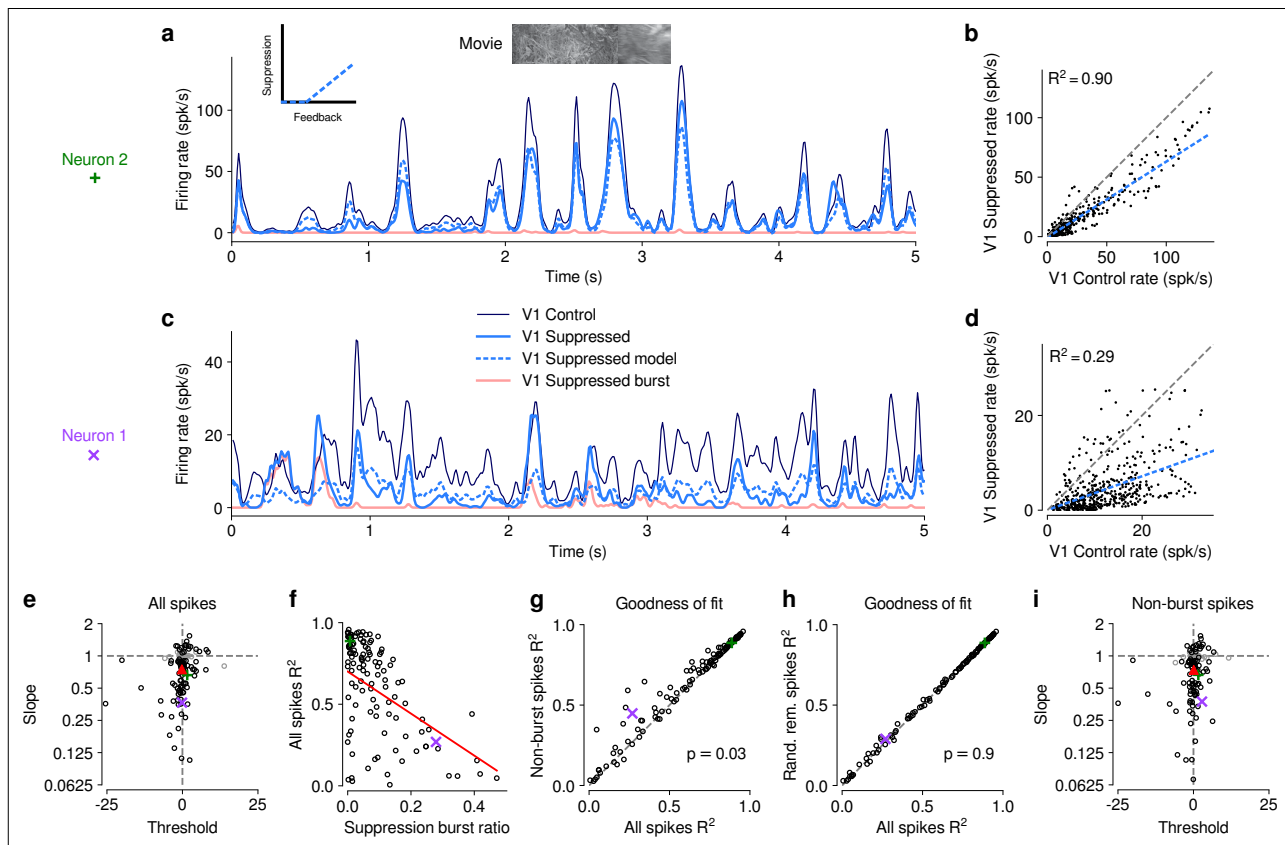


Figure 2. The effect of V1 suppression on dLGN responses to naturalistic movie clips is predominantly divisive. **(a)** PSTHs of an example neuron during control (dark blue) and V1 suppression (light blue) conditions, for a random subset of 50% of trials per condition not used for model fitting. Responses during the V1 suppression condition are approximated by the threshold linear model (dashed light blue) based on responses during the control condition. Pink: PSTH during V1 suppression for burst spikes only. Inset: cartoon of threshold linear model. **(b)** Timepoint-by-timepoint comparison of instantaneous firing rates of the PSTHs (derived from the 50% of trials not used for fitting) during the suppression vs. feedback conditions. PSTH data points are plotted at 0.01ms resolution. Dashed light blue line: threshold linear model fit. **(c,d)** Same as **(a,b)** for a second example neuron (same as in **Figure 1d and e**). **(a,b)** and **(c,d)** each contain data from 1 representative subsample. **(e)** Slope and threshold parameters for all neurons. Each point represents the median for each neuron across 1000 random subsamples of trials. Black points indicate neurons with slopes significantly different from 1 (95% CI). **(f)** Cross-validated model prediction quality (median R^2) vs. burst ratio during V1 suppression. Red line: LMM fit. **(g)** Model prediction quality R^2 with and without removal of burst spikes. **(h)** Model prediction quality with and without removal of an equivalent number of tonic spikes. **(i)** Same as **(e)** but with burst spikes removed. **(e–h)** Purple, green: example neurons; red triangle: LMM estimate of the mean.

sometimes overestimated or underestimated peaks in the actual response, such that the percentage of explained variability was rather low (median $R^2 = 0.29$, cross-validated, **Figure 2c and d**).

Indeed, across the population of recorded neurons, the model goodness of fit (median R^2 , cross-validated) during V1 suppression was inversely related to the burst ratio (slope of -1.29 ± 0.5 ; LMM; **Figure 2f**), consistent with the notion that the highly non-linear, all-or-none-like burst mode firing (**Sherman, 2001**) cannot be captured by the threshold-linear model (see also **Lesica and Stanley, 2004**). To further investigate the impact of bursting on response transformations by CT feedback, we re-computed the PSTHs for each neuron during V1 suppression after removing all burst spikes. Removal of burst spikes allowed our model to capture the effects of V1 suppression even better (all spikes: mean $R^2 = 0.58$; non-burst spikes: mean $R^2 = 0.61$; LMM: $F_{1,160.8} = 4.8$, $p = 0.03$; **Figure 2g**). Importantly, this increase in model performance was not simply a consequence of removing a certain proportion of spikes that originally needed to be predicted: discarding an equivalent number of randomly selected tonic spikes did not yield improved fit quality (random tonic spikes removed: mean $R^2 = 0.58$; LMM: $F_{1,162} = 0.005$, $p = 0.9$; **Figure 2h**). While burst spikes cannot be captured by the threshold-linear model, removing burst spikes, however, did not change our conclusion that the

effect of V1 suppression on movie responses was predominantly divisive (slope: 0.74 ± 0.09 ; threshold: 0.09 ± 1.3 ; LMM; **Figure 2i**), likely because burst events were much rarer than tonic spikes (see also **Figure 1g**). Indeed, firing mode (all spikes vs. non-burst spikes) had no effect on either slope (LMM: $F_{1,162.7} = 0.6$, $p = 0.4$) or threshold estimates (LMM: $F_{1,157.3} = 0.2$, $p = 0.7$) of the simple linear model. Together, these results show that V1 suppression decreases dLGN responses to naturalistic movies mostly by reducing response gain.

CT feedback modulates dLGN responses evoked by drifting gratings

Previous studies have investigated the effects of CT feedback using artificial stimuli, such as gratings and bars (**Olsen et al., 2012; Denman and Contreras, 2015; Wang et al., 2006; Murphy and Sillito, 1987**). To relate our findings to these studies, and to investigate the role of stimulus type, we next examined the effects of V1 suppression during the presentation of drifting gratings (**Figure 3**). To approximate the visual stimulus configuration used for naturalistic movie clips, we presented full-screen gratings drifting in one of 12 different orientations, and selected a pseudo-random subset of trials for V1 suppression. As expected, we found that many single dLGN neurons in the control condition with CT feedback responded at the temporal frequency (TF, 4 cyc/s) of the drifting grating (**Figure 3a and b**). Similar to previous studies in mouse dLGN (**Piscopo et al., 2013; Román Rosón et al., 2019; Marshel et al., 2012**), we also encountered some dLGN neurons with tuning for grating orientation or direction (**Figure 3, a2, b**).

Contrary to the robust effects of CT feedback on movie responses, V1 suppression had mixed effects on dLGN responses to drifting gratings. Example neuron 1, for instance, had lower firing rates with CT feedback intact, both in the orientation tuning (**Figure 3, a₂**) and the cycle-averaged response to the preferred orientation (**Figure 3a3**). In addition, in control conditions with CT feedback intact, there were markedly fewer burst spikes. In contrast, example neuron 3 responded more strongly with CT feedback intact (**Figure 3, b_{2,3}**). Such diverse effects of CT feedback, as reported before for anesthetized mice (**Denman and Contreras, 2015**), were representative of the recorded population (**Figure 3c**): V1 suppression during grating presentation significantly reduced responses for some neurons, but significantly increased responses for others, such that the average firing rates in the two conditions were almost identical (control: 14.5 spikes/s, V1 suppression: 15.0 spikes/s) and statistically indistinguishable (LMM: $F_{1,43.0} = 0.15$, $p = 0.70$). In contrast to these diverse effects on firing rate, but similar to our findings for naturalistic movie clips, intact CT feedback was consistently associated with less bursting (burst ratios of 0.043 vs 0.15; LMM: $F_{1,43.0} = 25.3$, $p = 9.2 \times 10^{-6}$; **Figure 3d**). Also similar to our findings for movies, there was no relationship between the strength of feedback effects on firing rate and on bursting (LMM: slope 0.029 ± 0.41 , **Figure 4—figure supplement 1a**).

Beyond studying overall changes in responsiveness and firing mode, we next asked how CT feedback affected the tuning for grating orientation of dLGN neurons. It is known from previous studies (**Piscopo et al., 2013; Cruz-Martín et al., 2014; Marshel et al., 2012; Zhao et al., 2013; Scholl et al., 2013**) that mouse dLGN neurons show various degrees of orientation tuning, ranging from few strongly tuned neurons, potentially relaying tuned input from the retina (**Cruz-Martín et al., 2014**), to a larger group with orientation bias (**Piscopo et al., 2013; Scholl et al., 2013**). We computed orientation tuning curves separately for control conditions with CT feedback and V1 suppression conditions. For neuron 1, intact CT feedback was associated not only with lower average firing rates, but also poorer selectivity (OSIs of 0.14 vs 0.25; **Figure 3, a₂**). In contrast, for neuron 3, orientation selectivity was similar during control and V1 suppression conditions (OSIs of 0.1 vs 0.09; **Figure 3, b₂**). These results were representative of the population, where CT feedback affected orientation selectivity in diverse ways, with virtually no difference in population means (control OSI: 0.13; V1 suppression: 0.12; LMM: $F_{1,88.7} = 0.31$, $p = 0.58$; **Figure 3e**; see also **Scholl et al., 2013; Li et al., 2013; Lien and Scanziani, 2013; Denman and Contreras, 2015**). For neurons with OSI > 0.02 and well-fit orientation tuning curves ($R^2 > 0.5$), preferred orientation during feedback and suppression conditions was largely similar, except for some cases where it shifted (**Figure 3f**). As was the case for movies, splitting the dLGN population into putative cell types according to several functional characteristics and their location within dLGN revealed few consistent differences in how global V1 suppression during gratings affected firing rates and bursting (**Figure 3—figure supplement 1**). Taken together, although effects of V1 suppression on firing rate were more diverse in magnitude and sign for grating stimuli, the similarity of orientation

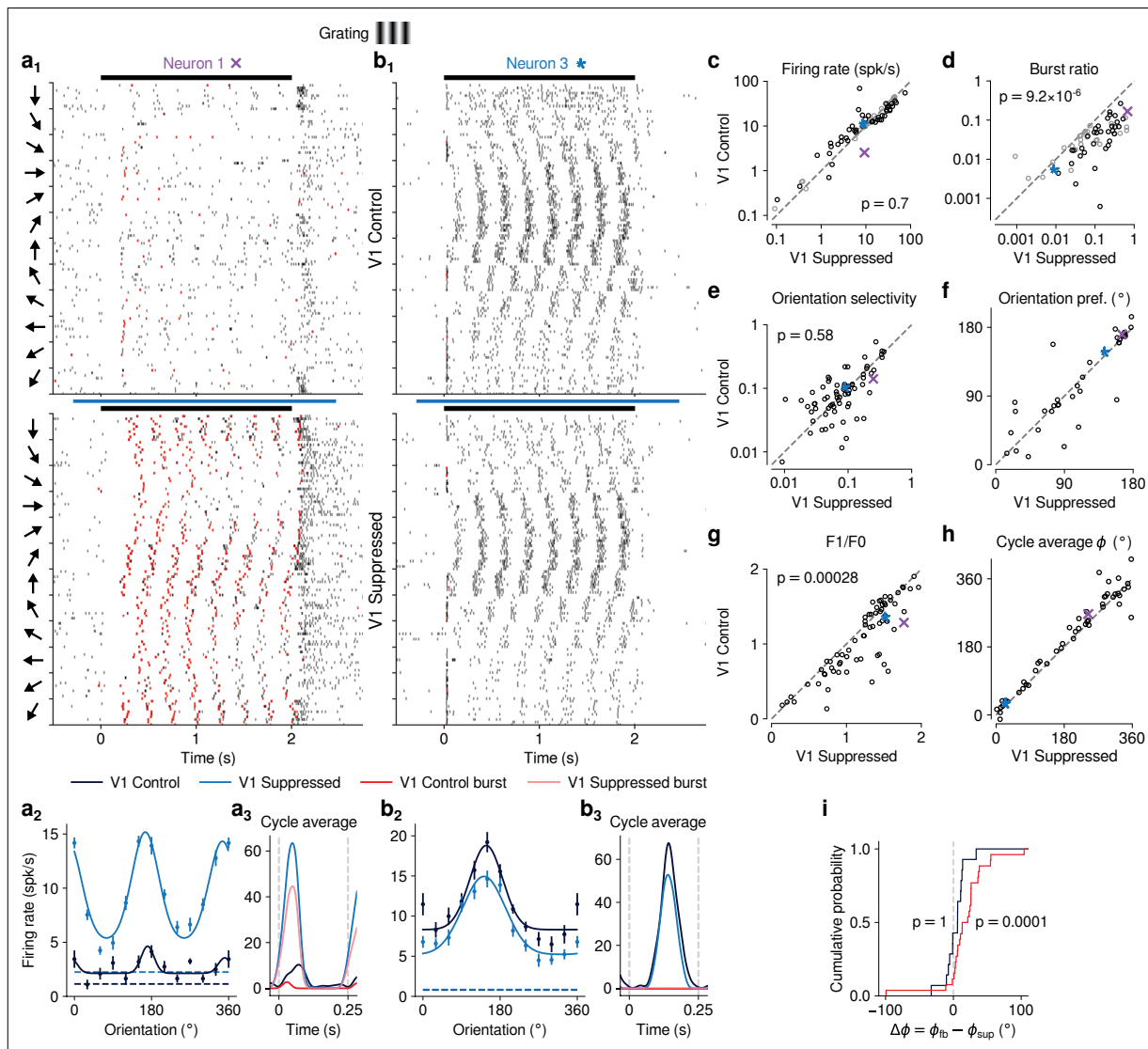


Figure 3. CT feedback modulates dLGN responses to drifting gratings. **(a)** Responses of example neuron 1 (same as in **Figures 1d, e, 2c and d**) to full-screen, drifting gratings. **(a₁)** Raster plot in response to drifting gratings, with trials sorted by grating orientation (10 trials per orientation, 30° steps). Red: burst spikes; black bar: grating stimulation; light blue bar: V1 suppression. **(a₂)** Corresponding orientation tuning curve. Dashed lines represent spontaneous firing rates in response to medium gray screen. Error bars: standard error of the mean. **(a₃)** Cycle average response to preferred orientation. Dark blue, light blue: cycle average constructed from all spikes. Red, pink: cycle average constructed from burst spikes only. Dark blue, red: Control condition with CT feedback intact; light blue, pink: V1 suppression. **(b)** Same as **(a)**, for another example neuron (example neuron 3). **(c–h)** Comparison of the control condition with CT feedback intact vs. V1 suppression, for mean firing rate **(c)**, burst ratio **(d)**, orientation selectivity index (OSI) **(e)**, preferred orientation θ **(f)**, F_1/F_0 **(g)**, and cycle average phase ϕ **(h)**. Purple, blue: example neurons. Black markers in **(c,d)** indicate neurons with individually significant effects (Welch’s t-test). **(i)** Cumulative distribution of cycle average phase differences between control and V1 suppression conditions. Dark blue: neurons with little burst spiking (ratio of cycle average peak for burst spikes to cycle average peak for all spikes < 0.1); red: neurons with substantial burst spiking (ratio of cycle average peak for burst spikes to cycle average peak for all spikes ≥ 0.1).

The online version of this article includes the following figure supplement(s) for figure 3:

Figure supplement 1. As for movies (**Figure 1—figure supplement 3**), feedback effects during grating presentation are largely independent of functional cell type classification.

selectivity between CT feedback conditions suggests underlying changes in gain, in accordance with what we observed for naturalistic movies.

Inspecting the spike rasters at different orientations, we realized that dLGN neurons appeared to have a stronger response component at the grating's temporal frequency during V1 suppression than when feedback was intact (**Figure 3, a₁**). To test whether V1 suppression affected the ability of dLGN to respond at the gratings' temporal frequency, for each neuron we computed the amplitude of the response at the stimulus frequency (F_1 component) relative to the mean response (F_0 component) (**Skottun et al., 1991; Carandini et al., 1997**) and found that F_1/F_0 ratios were indeed lower when feedback was intact (1.08 vs 1.22; LMM: $F_{1,43.5} = 15.6$, $p = 0.00028$; **Figure 3g**). To explore the impact of CT feedback on the F_1 response component in more detail, we examined the cycle average responses to the preferred orientation, and asked how CT feedback affected response phase. Similar to the results obtained for the example neurons (**Figure 3, a₃, b₃**), we found that V1 suppression could advance response phase (**Figure 3h**). This phase advance occurred more often for neurons whose responses during V1 suppression included a substantial proportion of burst spikes (**Figure 3i, red**; 25 of 29 neurons showed phase advance, $p = 0.0001$, binomial test) than for neurons which during V1 suppression burst little or not all (**Figure 3i, dark blue**; 11 of 21 neurons advanced, $p = 1$, binomial test). In agreement with earlier findings from intracellular recordings in anesthetized cats (**Lu et al., 1992**), these analyses demonstrate that the phase advance is driven by the dynamics of burst spiking. Finally, as for our re-assessment of CT feedback effect on responses to naturalistic movies, our conclusions regarding the effects of CT feedback on grating responses did not change when we repeated our experiments using a selective suppression of Ntsr1 + neurons with stGtACR2 (**Mahn et al., 2018, Figure 1—figure supplement 4i-o**). Also, during grating experiments, the Ntsr1- mouse controlling for effects of photostimulation per se showed no effects on neural responses to gratings (**Figure 1—figure supplement 5e-i**).

Effects of CT feedback on dLGN firing rates are more consistent and stronger overall for full-screen movies than full-screen gratings

Our analyses suggest that the impact of CT feedback on firing rates might be stronger overall for naturalistic movie stimuli than for gratings. To test this hypothesis, we focused on the subset of neurons recorded with both types of stimuli. Indeed, when we compared feedback modulation indices (FMIs), i.e. the difference between feedback conditions over their sum of firing rates, we found that FMI was

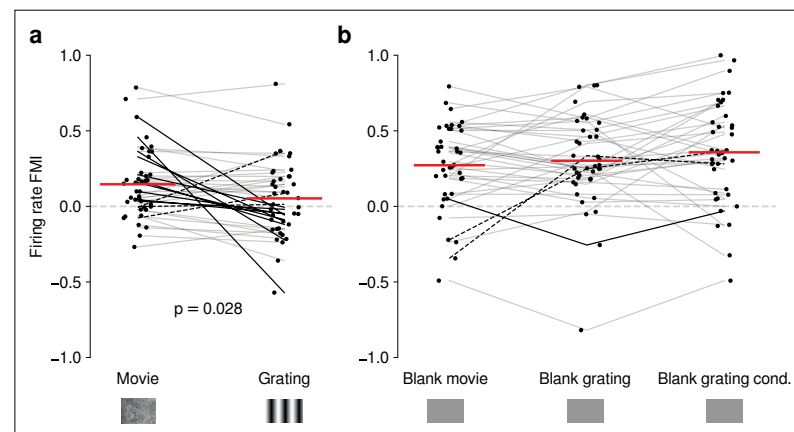


Figure 4. Effects of CT feedback on dLGN firing rate depend on stimulus type. **(a)** Comparison of the strength of CT feedback effects on firing rate (feedback modulation index, FMI) during presentation of full-screen movie clips and gratings. **(b)** Comparison of the strength of CT feedback effect on firing rate for blank stimuli interleaved with movies or gratings. Red: mean (LMM), dark lines: changes in sign of feedback modulation effect with stimulus type from positive for movies to negative for gratings (solid) and vice versa (dashed). For **(a)** and **(b)**, we randomly jittered the horizontal position of the points to avoid overlap; lines connecting the paired samples still end at the central position to represent change. See also **Figure 4—figure supplement 1**.

The online version of this article includes the following figure supplement(s) for figure 4:

Figure supplement 1. Control analyses assessing the difference in CT feedback effects for gratings and movies.

on average more positive for movies than for gratings (0.15 vs 0.053; LMM: $F_{1,38} = 5.21$, $p = 0.028$; **Figure 4a**). Remarkably, in 10/39 neurons (**Figure 4a**, dark lines) V1 suppression decreased firing rates for movies (positive movie FMI), but increased firing rates for gratings (negative grating FMI). The opposite effect only occurred in 3/39 neurons (dark dashed lines). These findings were not a consequence of differences in firing rates that might have already been present in control conditions with CT feedback intact (**Figure 4—figure supplement 1b**), and were also not a consequence of the longer duration of V1 suppression during movie clips (**Figure 4—figure supplement 1c, d**).

The differences in the effects of CT feedback on firing rates during full-screen gratings vs. movies might be related to feedback-induced changes in bursting, which might be stimulus-dependent (**Lu et al., 1992; Grubb and Thompson, 2005**) and can drive high-frequency firing. To test this hypothesis, we compared CT feedback modulation of burst ratio for gratings vs. movie clips, and found that V1 suppression indeed induced stronger bursting for gratings than for movies (**Figure 4—figure supplement 1e**). However, for both movies (**Figure 1—figure supplement 2c**) and gratings (**Figure 4—figure supplement 1a**), CT feedback effects on firing rates were unrelated to those on bursting. Thus, while suppression of CT feedback engages bursting overall more strongly for gratings than movies, this differential recruitment does not seem to account for differences in CT feedback-related modulations of firing rates for movies vs. grating stimuli.

Differences in CT feedback effects between firing rates to full-screen gratings and movies might instead be related to differences in longer-lasting, systematic changes in neural activity, which might occur due to differential adaptation or differences in behavioral state induced by the two stimulus types. To address this possibility, we focused on periods of blank screen, which were contained in both stimulus types. These were short (~0.3 s) periods directly preceding each full-screen movie and grating trial (see e.g., **Figures 1d and 3a**), as well as blank trials interleaved as one condition in the grating experiments. Applying our analyses to these various blank stimuli (**Figure 4b, Figure 4—figure supplement 1g-i**), we found that CT feedback enhanced mean firing rates regardless of blank type or blank period duration (positive firing rate FMIs, mean FMIs: 0.27 vs. 0.30 vs. 0.36; LMM: $F_{2,76} = 1.69$, $p = 0.19$; **Figure 4b**). This CT feedback-related average enhancement for blank stimuli was even stronger than the enhancement observed during movie presentation (LMM: $F_{1,116} = 15.1$, $p = 0.0002$), and stronger than the mixed effects during grating presentation (LMM: $F_{1,116} = 34.9$, $p = 3.6 \times 10^{-8}$). Since the CT feedback effects on these various blank stimuli did not depend on blank period duration or whether blanks were embedded in grating or movie experiments (see also **Figure 4—figure supplement 1f-i**), we conclude that differences in longer lasting changes in neural activity or behavioral state did not underlie the differential effect of CT feedback for full screen movies vs. gratings. Instead, we interpret these findings to highlight that CT feedback modulates dLGN responses in a stimulus-dependent way. In particular, the strength and sign of CT feedback gain might be sensitive to features of the visual stimulus, such as the contrast, the dynamics, or the statistics of the center and the surround stimulation.

Effects of behavioral state on dLGN responses resemble effects of CT feedback, but are largely independent

Previous studies have reported that responses of mouse dLGN neurons to grating stimuli are modulated by behavioral state as inferred by locomotion (**Erskens et al., 2014; Aydın et al., 2018; Williamson et al., 2015**). To assess how these findings extend to more complex stimuli, we separated the trials with CT feedback intact according to the animals' locomotion behavior. We considered trials as 'run trials' if the animal's speed exceeded 1 cm/s for at least 50% of the stimulus presentation and as 'sit trials' if the animal's speed fell below 0.25 cm/s for at least 50% of the stimulus presentation. When we examined the spike rasters and PSTHs of example neuron 1 in control conditions with CT feedback intact (**Figure 5a and b**), we found that, despite preserved temporal features of the responses (Pearson correlation $r = 0.72$ between run and sit PSTHs, $p < 10^{-6}$), firing rates were higher overall during locomotion than stationary periods. Additionally, during locomotion, the distribution of firing rates was less skewed ($\gamma = 1.15$ vs 1.45 during stationary trials), with a decrease of low and an increase of medium firing rates (KS test, $p < 10^{-6}$). This pattern was also observed in the population of dLGN neurons, where firing rates were consistently higher for trials with locomotion compared to trials when the animal was stationary (11.9 vs 8.9 spikes/s; LMM: $F_{1,63,9} = 94.1$, $p = 3.5 \times 10^{-14}$; **Figure 5c**). Similar to previous reports using gratings (**Niell and Stryker, 2010; Erskens et al., 2014**), we found that

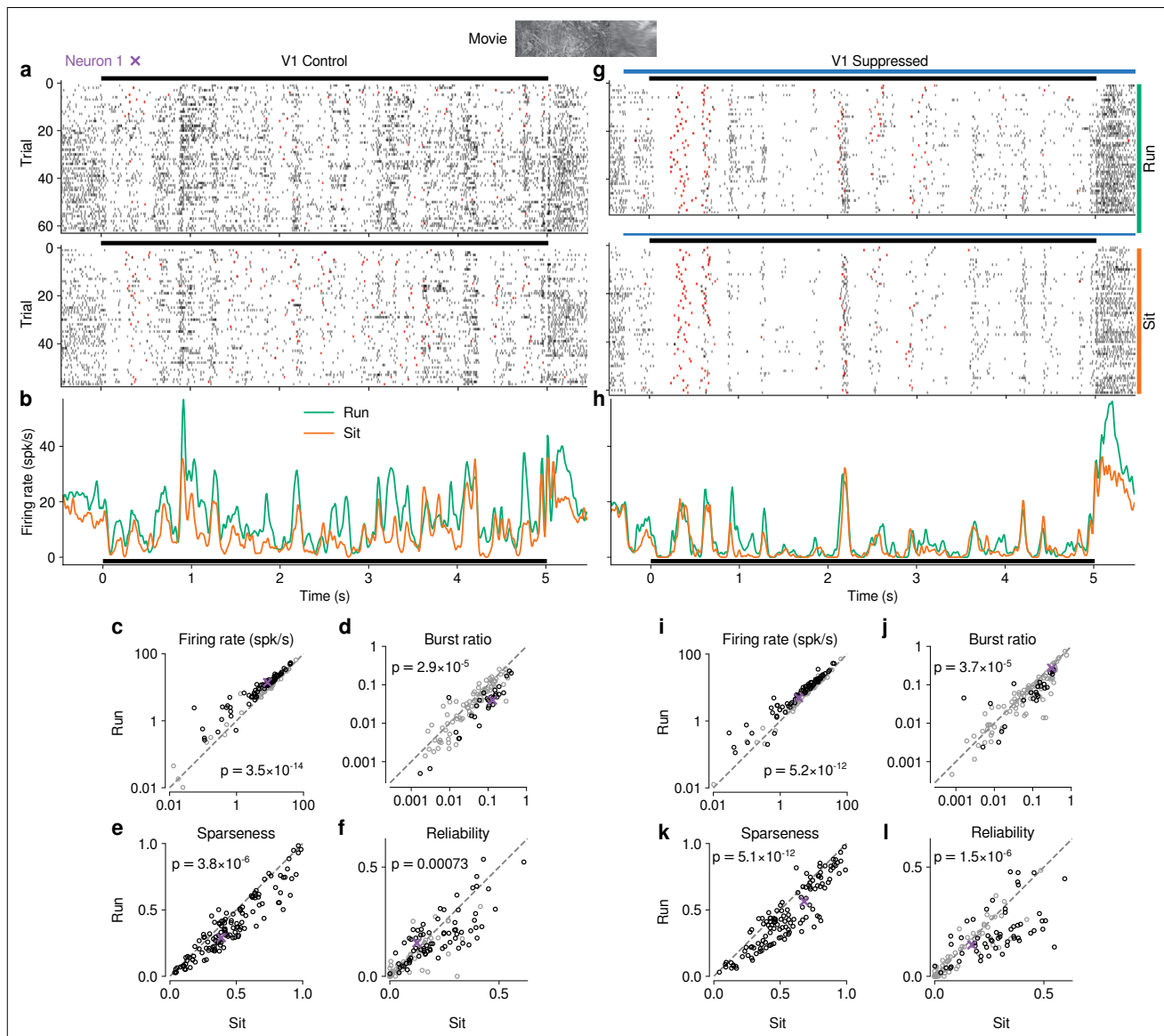


Figure 5. Effects of locomotion on dLGN responses resemble those of CT feedback, but persist even during V1 suppression. **(a)** Spike raster of example neuron 1 (same as **Figure 1d**) in response to a naturalistic movie clip during locomotion and stationary trials with CT feedback intact. *Top*: trials with run speed > 1 cm/s; *bottom*: trials with run speed < 0.25 cm/s, both for at least > 50% of each trial. *Red*: burst spikes. **(b)** Corresponding PSTHs. *Green*: locomotion, *orange*: stationary; *black bar*: duration of movie clip. **(c–f)** Comparison of firing rates **(c)**, burst ratio **(d)**, sparseness **(e)**, and trial-to-trial reliability **(f)** during locomotion and stationary trials. Black markers in **(c,d,f)** correspond to individually significant observations (Welch's t-test). **(g–l)** Same as **(a–f)**, for locomotion and stationary trials during V1 suppression. *Light blue bar*: V1 suppression. See also **Figure 5—figure supplement 1**.

The online version of this article includes the following figure supplement(s) for figure 5:

Figure supplement 1. Effects of locomotion on additional parameters of responses to naturalistic movie clips and relationship with firing rate.

Figure supplement 2. Effects of pupil-indexed arousal on dLGN responses to movies.

bursting was lower during locomotion than stationary periods (0.035 vs 0.063; LMM: $F_{1,66.7} = 20.2$, $p = 2.9 \times 10^{-5}$; **Figure 5d**). Beyond these established measures, using movie clips allowed us to test the effects of locomotion on additional response properties: trials with locomotion were associated with lower sparseness (0.40 vs 0.47; LMM: $F_{1,181.9} = 22.8$, $p = 3.8 \times 10^{-6}$; **Figure 5e**) and lower trial-to-trial reliability (0.13 vs 0.16; LMM: $F_{1,176.1} = 11.8$; **Figure 5f**). This locomotion-related decrease of reliability could be related to, but is likely not fully explained by, the increase in eye movements typically

associated with running (**Figure 5—figure supplement 1h, i**; **Erisken et al., 2014**; **Bennett et al., 2013**). These analyses demonstrate that in dLGN, processing of naturalistic movie clips is robustly modulated by locomotion. Curiously, in all aspects tested, these modulations by locomotion had the same signatures as those of CT feedback: increased firing rates, reduced bursting, and decreased sparseness and trial-to-trial reliability.

Since the effects of CT feedback and locomotion closely resembled each other, and since L6CT neurons themselves are modulated by locomotion (**Augustinaite and Kuhn, 2020**), are the effects of locomotion on dLGN responses inherited via feedback from cortex? To test this hypothesis, we next focused on only those movie trials in which feedback was suppressed by V1 PV+ photostimulation and repeated the separation according to locomotion (**Figure 5g–h**). These analyses revealed that effects of locomotion on the responses to our movies persisted, even if CT feedback was suppressed (**Figure 5i–l**; firing rate: 9.7 vs 7.6 spikes/s; LMM: $F_{1,64.8} = 71.1$, $p = 5.2 \times 10^{-12}$; burst ratio: 0.081 vs 0.11 spikes/s; LMM: $F_{1,68.1} = 19.5$, $p = 3.7 \times 10^{-5}$; sparseness: 0.47 vs 0.56; LMM: $F_{1,179.5} = 54.7$, $p = 5.1 \times 10^{-12}$; reliability: 0.14 vs 0.18; LMM: $F_{1,175.7} = 24.9$, $p = 1.5 \times 10^{-6}$).

Besides running, another often-used indicator for behavioral state is pupil size (**Reimer et al., 2014**; **Vinck et al., 2015**; **Erisken et al., 2014**). Indexing arousal via pupil size, however, is challenging for movie stimuli, whose fluctuations in luminance will themselves drive changes in pupil size (**Figure 5—figure supplement 2a**). To test whether locomotion-independent, pupil-indexed arousal also modulates dLGN responses and whether this modulation depends on CT feedback, we exploited methods initially proposed by **Reimer et al., 2014**, focusing on periods within the movie when the animal was sitting and assuming that the average change in pupil size over multiple movie repetitions was due to luminance changes in the movie, while the variability around this average reflected trial-by-trial differences in behavioral state (**Figure 5—figure supplement 2b–g**). Recapitulating our running-related results, we found that both with CT feedback intact and during V1 suppression, response periods with faster than average pupil dilation (or slower than usual constriction; top quartile pupil change) were associated with higher firing rates, while periods with faster than usual pupil constriction (or slower than usual dilation; bottom quartile pupil change) were associated with lower firing rates (**Figure 5—figure supplement 2b–c**). In contrast, response reliability and SNR were not significantly different during periods of rapid dilation vs. rapid constriction, regardless of photostimulation condition (**Figure 5—figure supplement 2d–g**).

Finally, to further test the relationship between effects of behavioral state and CT feedback, we directly compared CT feedback and running-related modulations on a neuron-by-neuron basis. We focused on experiments with naturalistic movies, because this was the condition in which we observed robust effects of both CT feedback and behavioral state (for a related analysis with gratings and qualitatively similar results, see **Figure 6—figure supplement 1a**). First, we hypothesized that if effects of locomotion on dLGN responses were inherited from primary visual cortex, such effects should vanish during V1 suppression (**Figure 6, a₀**). However, consistent with the observations shown in **Figure 5i–l**, even during V1 suppression, running-related modulations were significantly different from 0 (firing rate run modulation index (RMI): 0.18 ± 0.06 ; burst ratio: -0.17 ± 0.1 ; sparseness: -0.12 ± 0.04 ; reliability: -0.11 ± 0.09 ; **Figure 6, a_{1–4,4}**). In fact, the degree of running modulation was correlated between control conditions with feedback intact and V1 suppressed (firing rate: slope of 0.51 ± 0.12 ; burst ratio: slope of 0.38 ± 0.2 ; sparseness: slope of 0.44 ± 0.14 ; reliability: slope of 0.50 ± 0.15 ; **Figure 6, a_{1,4}**). Interestingly, for firing rates and burst ratios, locomotion effects were slightly stronger, on average, with CT feedback intact compared to V1 suppression (firing rate RMI: 0.23 vs 0.20; LMM: $F_{1,168.3} = 4.3$, $p = 0.04$, **Figure 6, a₁**; burst ratio RMI: -0.25 vs. -0.17 ; LMM: $F_{1,154.7} = 6.3$, $p = 0.013$, **Figure 6, a₂**), indicating that these two modulatory influences likely interact.

We next tested the hypothesis that CT feedback might have a stronger impact during active behavioral states than during quiescence. Indeed, it has previously been shown that during brain states associated with anesthesia, the responsiveness of feedback circuits is particularly reduced (**Briggs and Usrey, 2011**; **Makino and Komiyama, 2015**; **Keller et al., 2020**). One might therefore predict that during quiescence, if feedback circuits were already completely disengaged, we should not be able to observe further effects of V1 suppression (**Figure 6, b₀**). This was clearly not the case, because CT feedback effects were correlated across behavioral states (firing rate: slope of 0.72 ± 0.10 ; burst ratio: slope of 0.34 ± 0.15 ; sparseness: slope of 0.85 ± 0.12 ; reliability: slope of 0.43 ± 0.14 ; **Figure 6, b_{1–4}**). In addition, and similar to the slightly stronger run modulation with feedback left intact, we discovered

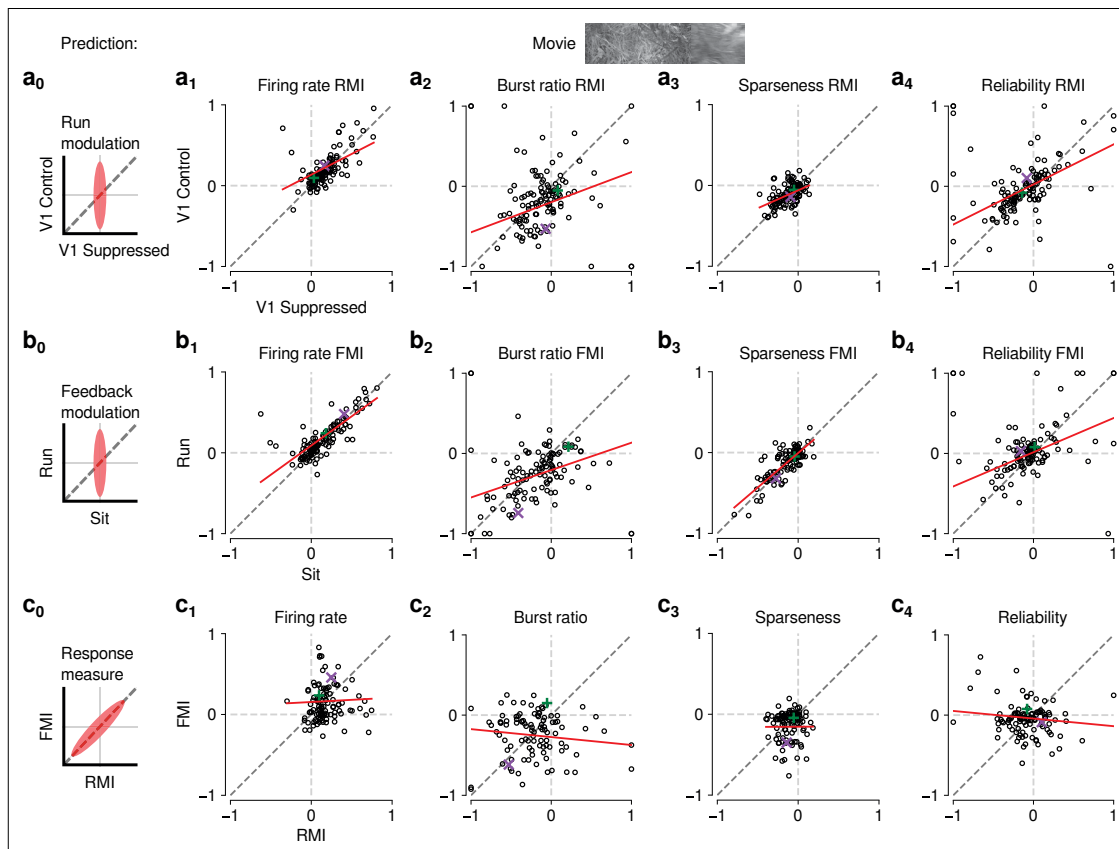


Figure 6. The effects of CT feedback and locomotion on movie responses are largely independent. (**a**₀–**c**₀) Predicted relationships between modulation indices and response measures in different conditions, assuming dependence in the effects of CT feedback and locomotion. (**a**) Comparison of modulation by running (RMI) during CT feedback intact and V1 suppression for firing rates (**a**₁), burst ratio (**a**₂), sparseness (**a**₃), and reliability (**a**₄). Running effects were quantified with a run modulation index (RMI), where $RMI = (\text{running} - \text{sitting}) / (\text{running} + \text{sitting})$. (**b**) Comparison of modulation by CT feedback (FMI) during locomotion and stationary periods for firing rates (**b**₁), burst ratio (**b**₂), sparseness (**b**₃), and reliability (**b**₄). (**c**) Comparison of modulation by feedback (FMI) and modulation by running (RMI) for firing rates (**c**₁), burst ratio (**c**₂), sparseness (**c**₃), and reliability (**c**₄). Red: LMM fit. Green, purple: example neurons from **Figure 2a and b**.

The online version of this article includes the following figure supplement(s) for figure 6:

Figure supplement 1. The effects of CT feedback and locomotion on responses to gratings are also largely independent.

a locomotion-dependent CT feedback effect for firing rates and burst ratios: CT feedback effects were slightly stronger, on average, during locomotion than during quiescence (firing rate FMI: 0.18 vs 0.15; LMM: $F_{1,172.8} = 3.5$, $p = 0.065$; **Figure 6**, **b**₁; burst ratio FMI: -0.27 vs. -0.19 ; LMM: $F_{1,166.9} = 6.8$, $p = 0.0097$; **Figure 6**, **b**₂). This subtle interaction between behavioral state and CT feedback effects might relate to a previous finding, where careful dissection of brain states by depth of anesthesia had already suggested that the effects of transient cortical inactivation on dLGN responses were more evident during lighter anesthesia, that is, during desynchronized cortical activity (**Wörgötter et al., 2002**). However, our ability to observe effects of V1 suppression in dLGN while the animal was stationary suggests that CT feedback circuits are engaged even under conditions of behavioral quiescence.

Finally, if modulations by CT feedback and behavioral state exploited the same circuitry, neurons experiencing strong modulation by V1 suppression should also be strongly affected by locomotion (**Figure 6**, **c**₀). Contrary to this prediction, we found that effects of CT feedback (FMI) and behavioral state (RMI) were uncorrelated (firing rate: slope of 0.054 ± 0.13 ; burst ratio: slope of -0.1 ± 0.13 ; sparseness: slope of 0.005 ± 0.23 ; reliability: slope of -0.095 ± 0.12 ; **Figure 6c**_{1–4}). Together, these comparisons demonstrate that effects of behavioral state associated with locomotion and effects of CT feedback are largely independent.

Discussion

In this study, we used naturalistic movies to reveal that corticothalamic feedback and behavioral state can have robust effects on dLGN responses. We found that V1 suppression during movie presentation reduces the gain of time-varying dLGN firing rates, and leads to increases in bursting, sparseness and trial-to-trial reliability. The effects of CT feedback seem to be stimulus-specific, as V1 suppression led to more consistent and therefore stronger overall effects on firing rates for naturalistic movies than for gratings. Interestingly, the signatures of CT feedback closely resembled those of behavioral state. However, we found their effects during movie viewing to be largely independent, demonstrating that behavioral modulations of dLGN activity are not simply inherited from cortex. Overall, our findings highlight that dLGN responses to naturalistic movies can be reliably modulated by two extra-retinal sources – cortical feedback and behavioral state – which likely exert their influences via largely separate neural circuits.

Manipulation of CT feedback

To manipulate CT feedback, we chose a potent, yet global, V1 suppression approach based on optogenetic activation of ChR2 expressed in local PV+ inhibitory interneurons (*Lien and Scanziani, 2013; Li et al., 2013; King et al., 2016; Olsen et al., 2012; Wiegert et al., 2017*). While silencing by excitation of inhibitory interneurons can exploit the robust effects of GABA-mediated inhibition in cortical circuits, it comes with a limitation in specificity. Hence, in addition to the direct L6 → thalamus circuit, indirect polysynaptic effects might be exerted via alternative routes. One example is L5 corticofugal pyramidal cells projecting to the superior colliculus (SC), where tectogeniculate neurons in the superficial layers provide retinotopically organized, driving inputs to the dorsolateral shell region of the dLGN (*Bickford et al., 2015*). To address this lack of specificity, in control experiments, we replaced photoactivation of PV +neurons with direct, selective suppression of V1 Ntsr1 +neurons, encompassing the population of L6 CT pyramidal cells (*Kim et al., 2014; Bortone et al., 2014*). Since photosuppression via the light-gated chloride channel stGtACR2 (*Mahn et al., 2018*) did not alter any of our conclusions regarding the effects of CT feedback on dLGN responses, we assume that the effects of V1 suppression to a large degree reflect the specific impact of the L6 CT circuit. L6 CT neurons, however, have an intracortical axon collateral making privileged connections with a translaminal PV +interneuron subtype in L6 (*Frndolig et al., 2019; Bortone et al., 2014*), which in turn strongly regulates the gain of the entire V1 column (*Olsen et al., 2012; Bortone et al., 2014; Frndolig et al., 2019*), so that even with such specific suppression, polysynaptic effects cannot be excluded. However, since suppression of L6 CT neurons increases the gain in V1 (*Olsen et al., 2012*), and since this is the opposite of the global effects of V1 suppression via PV +activation, L6 CT gain modulation of V1 seems unlikely to drive our effects. Nevertheless, decisively ruling out alternative circuits would require the selective suppression of L6 CT axon terminals at the thalamic target.

Cortical layer 6 is well known for its particularly high diversity of neuronal cell types (*Briggs, 2010*). Even within the population of L6 CT pyramidal cells there is heterogeneity, with at least two subtypes defined by morphology (*Frndolig et al., 2019; Tasic et al., 2016; Gouwens et al., 2019; Augustinaite and Kuhn, 2020*), three subtypes defined by electrophysiology and morphology (*Gouwens et al., 2019*), and four major subtypes defined by transcriptomics (*Tasic et al., 2016; Gouwens et al., 2019*). Whether these subtypes mediate different aspects of feedback modulations is currently unknown. In the visual system of primates and carnivores, CT feedback circuits seem to be organized into distinct streams (*Briggs et al., 2016; Hasse et al., 2019; Briggs and Usrey, 2009*) whose functional organization mimics that of the feedforward streams. Whether the known subtypes in mice can convey independent, stream-specific information is currently unknown, partly because already at the level of feedforward processing, the notion of streams in mouse dLGN is a matter of ongoing debate (*Chen et al., 2016; Denman and Contreras, 2016; Morgan et al., 2016; Chen et al., 2016; Zhuang et al., 2019*), and dLGN response properties are diverse (*Piscopo et al., 2013; Román Rosón et al., 2019; Liang et al., 2018*). Our own assessment of CT feedback effects revealed few systematic differences for various dLGN cell-type classifications. Such an absence of differences, however, is not surprising, because our optogenetic circuit manipulations non-specifically suppressed all L6 CT neuron subtypes. Once genetic targeting of L6 CT subtypes will become possible, it will be important to test the stream-specificity of CT feedback in the mouse.

CT feedback effects on gain, reliability, and bursting

Our analyses of the time-varying firing rates in response to naturalistic movies revealed that V1 suppression results in a robust decrease of geniculate response gain. Divisive effects of CT feedback suppression have also been previously reported for contrast response functions of parvocellular dLGN neurons in anesthetized macaques (*Przybylski et al., 2000*). A crucial element to produce gain modulations seems to be changes in the level of synaptically driven V_m fluctuations, often called 'synaptic noise' (*Hô and Destexhe, 2000; Shu et al., 2003; Chance et al., 2002*). Indeed, in vivo V1 recordings suggest that the combined impact of changes in V_m fluctuations, input resistance, and depolarization is needed to produce gain changes (*Cardin et al., 2008*). These cellular properties are altered by both feedback (*Chance et al., 2002*) and neuromodulation (*Disney et al., 2007*), not only in cortex (*Ferguson and Cardin, 2020*) but also in the corticothalamic system (*Béhuret et al., 2015; Augustinaite et al., 2014*). Here, 'synaptic noise' together with varying degrees of T-type channel recruitment has been shown to change the slope of the input-output function and alter the temporal filtering characteristics of thalamic relay cells (*Wolfart et al., 2005; Béhuret et al., 2015*). Thus, by providing variable synaptic input and affecting membrane depolarization, for example, through NMDA plateau potentials (*Augustinaite et al., 2014*), CT feedback might be in a prime position to dynamically tune the gain of the thalamic relay.

In addition to potentially contributing to the observed gain modulations, 'synaptic noise' from CT feedback may also help explain the less precise and less reliable dLGN responses we observed when feedback was left intact. Specifically, V1 neurons are known to exhibit about double the trial-to-trial variability of simultaneously recorded dLGN neurons (*Kara et al., 2000*), and eliminating variable cortical input might unmask the even greater reliability of feed-forward retinal inputs (*Kara et al., 2000*).

Our analyses of movie and grating response characteristics showed that V1 suppression robustly and consistently biased geniculate activity toward burst firing mode. Burst firing mode occurs when dLGN neurons undergo sustained (≥ 100 ms) hyperpolarization (*Sherman, 2001*), which allows for the de-inactivation of low-threshold T-type calcium channels abundant in thalamus (*Jahnsen and Llinás, 1984*). Such 'calcium bursts' can only be unequivocally separated from high-frequency firing in intracellular recordings or calcium imaging, but can be inferred in extracellular recordings, such as ours, by imposing a minimum duration of 100 ms of silence preceding a high-frequency (< 4 ms ISI) firing event (*Lu et al., 1992*). Previous in vivo intracellular recordings in cat dLGN have revealed that cortical ablation can hyperpolarize the resting membrane potential of dLGN relay cells by ~ 9 mV, enough to push them into burst-firing mode (*Dossi et al., 1992*). Conversely, direct optogenetic activation of L6 CT neurons in primary somatosensory cortex has been shown to decrease burst mode firing (*Mease et al., 2014*), potentially mediated by NMDA plateau potentials as observed in slice recordings (*Augustinaite et al., 2014*). In burst firing mode, reminiscent of the effects we observed during V1 suppression, dLGN spontaneous activity is low (*Sherman, 2001*), stimulus-evoked responses show phase-advance (*Lu et al., 1992; Alitto et al., 2005*) and high trial-to-trial reliability (*Alitto et al., 2005*). The increase in trial-to-trial response reliability we observed during V1 suppression might therefore be explained not only by the removal of a more variable input as mentioned above (*Kara et al., 2000*), but also by a shift towards burst mode, where retinogeniculate communication efficacy is elevated (*Alitto et al., 2019*).

Theories about the function of thalamic firing modes can provide a useful framework for interpreting the effects of CT feedback we observed here, in particular since the greater precision and trial-to-trial reliability of responses during V1 suppression might be unexpected at first glance. Thalamic burst mode is often linked with 'inattentive states', where the sudden appearance or change of a visual stimulus from non-preferred to preferred RF contents (*Lesica and Stanley, 2004; Lesica et al., 2006; Wang et al., 2007*) can reliably trigger a thalamic burst. Bursting is associated with high signal-to-noise, well-suited for stimulus detection (*Sherman, 2001; Whitmire et al., 2016*). In addition, thalamic burst mode is known to augment the efficacy of retinal input to drive spiking in dLGN (*Alitto et al., 2019*), and increases the probability of relay between thalamus and cortex (*Swadlow and Gusev, 2001*). This in turn might lead to depolarizing CT feedback, switching the thalamus to tonic mode and allowing more faithful, linear relay of information with a higher dynamic range, better suited for encoding of more finely graded details (*Sherman, 2001; Béhuret et al., 2015*). Such a 'wake-up-call' for cortex (*Sherman, 2001; Lesica and Stanley, 2004*) could represent a neural implementation

of bottom-up attention in dLGN (*Hochstein and Ahissar, 2002*). To understand if CT feedback is indeed recruited for detailed perceptual analyses, an essential next step would be to measure the activity of L6 CT neurons under behaviorally relevant conditions. Interestingly, in the auditory system, activation of L6 CT feedback has been shown to influence sound perception, with enhancements of sound detection or discrimination behavior, depending on the relative timing between CT spiking and stimulus onset (*Guo et al., 2017*). Beyond having a broad impact on coding regimes and transmission, bursting in thalamus is also known to have specific computational properties, such as efficiently encoding high- and low-frequency information in parallel (*Mease et al., 2017*).

Stimulus-dependence of CT feedback effects

So far, most studies using naturalistic stimuli to probe dLGN responses have been performed in anesthetized animals and have not considered CT feedback (*Dan et al., 1996; Lesica and Stanley, 2004; Lesica et al., 2006; Lesica et al., 2007; Wang et al., 2007; Mante et al., 2005*). Similarly, most studies investigating the impact of CT feedback have relied on artificial stimuli (*Olsen et al., 2012; Denman and Contreras, 2015; Wang et al., 2006; Murphy and Sillito, 1987*). Comparing the effects of CT feedback during naturalistic movies and gratings, we found evidence that CT feedback modulates firing rates at the geniculate level in a stimulus-dependent fashion. What could be the relevant difference? For artificial stimuli, such as gratings and bars, it has long been known that CT feedback can enhance dLGN surround suppression by increasing responses to small stimuli and reducing responses to large stimuli (*Born et al., 2021; McClurkin and Marrocco, 1984; Murphy and Sillito, 1987; Jones et al., 2012; Wang et al., 2018; Cudeiro and Sillito, 1996; Andolina et al., 2013; Hasse and Briggs, 2017; Webb et al., 2002*). Such CT feedback-mediated enhancement of surround suppression might result from recruitment of a more narrow direct excitatory and a wider indirect inhibitory CT feedback component according to grating size (*Born et al., 2021*), with the balance shifting more towards direct excitation for small gratings and more towards indirect inhibition for large gratings. Size, however, is likely not the only determinant of relative recruitment of CT feedback circuits: for instance, V1 ablation or pharmacological suppression in anesthetized cats leads to more prominent reductions of dLGN surround suppression for iso- vs. cross-oriented gratings (*Cudeiro and Sillito, 1996; Sillito et al., 1993*), suggesting an additional role of stimulus context. For naturalistic stimuli with complex context, measurements in area V1 have already demonstrated that surround suppression is generally lower than for iso-oriented gratings, and is flexibly invoked depending on the specific statistics in the RF center and surround (*Coen-Cagli et al., 2015*). The differential effect of CT feedback on dLGN firing rates for full-screen naturalistic movies and iso-oriented gratings observed in our study might therefore be parsimoniously explained by differences in the relative strength of direct excitatory and indirect inhibitory CT feedback. It would be of prime interest to measure, in future experiments, size tuning curves with and without CT feedback using different stimuli, such as naturalistic movies, iso- and cross-oriented gratings. Given our results, we predict that CT feedback would affect firing rate responses to full-screen cross-oriented gratings more similarly to full-screen naturalistic movies than would iso-oriented gratings. Alternatively, CT feedback might change firing rates more consistently for lower contrast stimuli, such as our movies, where additional top-down inputs might be helpful for detection or discrimination.

Relationship between CT feedback and behavioral state

By measuring the effects of V1 suppression on movie responses during different behavioral states, and by measuring effects of behavioral state with and without CT feedback, we found that behavioral state and CT feedback had similar effects on dLGN responses, but seemed to operate via largely separate circuits. The lack of substantial dependence between effects of CT feedback and behavioral state on responses to our naturalistic movies is remarkable: neuromodulation accompanying changes in behavioral state will affect cortical layer 6, which receives dense cholinergic afferents from basal forebrain (*Radnikow and Feldmeyer, 2018*). Accordingly, in slice recordings, upon bath application of ACh, mouse V1 L6 CT neurons increase action potential firing (*Sundberg et al., 2018*). Potentially related, many V1 L6 CT neurons themselves increase activity during locomotion or arousal (*Augustinaite and Kuhn, 2020; Swadlow and Weyand, 1987*). Together, these studies would predict that effects of behavioral state should be augmented during CT feedback. Indeed, two recent studies investigating the interactions between CT feedback and arousal reported, during suppression of CT feedback,

less correlation between dLGN firing and pupil size (Molnár et al., 2021), and a loss of effects of behavioral state on dLGN tuning curves for temporal and spatial frequency, but not for spontaneous activity (Reinhold et al., 2021). Together with other findings more consistent with our results (Murata and Colonnese, 2018; Nestvogel and McCormick, 2022; Schröder et al., 2020), this discrepancy suggests that the degree to which effects of behavioral state in dLGN might be dependent on cortex is not fully understood.

If not inherited from CT feedback, which alternative circuits could mediate the effects of behavioral state in dLGN (Erisken et al., 2014; Aydın et al., 2018; Williamson et al., 2015)? Locomotion is accompanied by arousal (Vinck et al., 2015), which in turn involves various neuromodulatory influences [reviewed in Zaghera and McCormick, 2014]. For instance, norepinephrine from the locus coeruleus (LC) and acetylcholine (ACh) from the midbrain are known to act directly on the thalamus [reviewed in McCormick, 1992; Lee and Dan, 2012] and could drive some of the arousal-related depolarizing effects on firing rate independent of cortical feedback, for instance by blocking a long-lasting Ca^{2+} -dependent K^+ current (Sherman and Koch, 1986). In addition, electrical stimulation of the LC (Holdefer and Jacobs, 1994) and the parabrachial region (PBR) (Lu et al., 1993) within the mesencephalic locomotor region (MLR), and direct application of noradrenergic (Funke et al., 1993) and cholinergic (McCormick, 1992; Sillito et al., 1983) agonists within dLGN, are sufficient to reduce thalamic burst mode firing. Finally, at least part of the locomotion effects in dLGN might also be related to modulations of retinal output (Schröder et al., 2020; Liang et al., 2020). Indeed, two-photon calcium imaging of retinal ganglion cell boutons in dLGN (Liang et al., 2020) and SC (Schröder et al., 2020) revealed that their activity can be modulated by locomotion, albeit with an overall suppressive effect. In future studies, it will be key to further dissect the contributions of retinal, cortical and potentially collicular modulations, and the different neuromodulatory sources of behavioral state-related modulations in thalamic targets.

Materials and methods

Key resources table

Reagent type (species) or resource	Designation	Source or reference	Identifiers	Additional information
Recombinant DNA reagent	pAAV EF1a.DIO.hChr2(H134R)- eYFP.WPRE.hGH	Addgene	#20298-AAV9	
Recombinant DNA reagent	pAAV hSyn1-SIO-stGtACR2- FusionRed	Addgene	#105,677	
Strain, strain background (<i>Mus musculus</i>)	B6;129P2-Pvalb ^{tm1(cre)Abr/J}	Jackson Laboratory	#008069	PV-Cre, Pvalb-Cre
Strain, strain background (<i>Mus musculus</i>)	B6.FVB(Cg)-Tg(Ntsr1-cre) GN220Gsat/Mmcd	MMRRC	#030648-UCD	Ntsr1-Cre
Chemical compound, drug	Metamizole	MSD Animal Health	Vetalgin	200 mg/kg
Chemical compound, drug	Buprenorphine	Bayer	Buprenovet	0.1 mg/kg
Chemical compound, drug	Lidocaine hydrochloride	bela-pharm		2 %
Chemical compound, drug	Meloxicam	Böhringer Ingelheim	Metacam	2 mg/kg
Chemical compound, drug	Isoflurane	CP Pharma		in oxygen
Chemical compound, drug	Bepanthen	Bayer		eye ointment
Chemical compound, drug	DAPI-containing mounting medium	Vector Laboratories Ltd		
Chemical compound, drug	Vectashield DAPI H-1000	Vector Laboratories Ltd		
Chemical compound, drug	Dil	Invitrogen		electrode stain
Software, algorithm	Python 3.6	http://python.org	RRID:SCR_008394	
Software, algorithm	R	R Core Team, 2017	RRID:SCR_001905	
Software, algorithm	MATLAB R2019b	Mathworks	RRID:SCR_001622	
Software, algorithm	EXPO	https://sites.google.com/a/nyu.edu/expo/home		visual stimulus display

Continued on next page

Continued

Reagent type (species) or resource	Designation	Source or reference	Identifiers	Additional information
Software, algorithm	Kilosort	<i>Pachitariu et al., 2016</i>	RRID:SCR_016422	
Software, algorithm	Spyke	<i>Spacek et al., 2009</i>		
Software, algorithm	Fiji/ImageJ	NIH	RRID:SCR_003070	
Software, algorithm	DataJoint	<i>Yatsenko et al., 2018</i>	RRID:SCR_014543	

Surgical procedures

Experiments were carried out in 6 adult PV-Cre mice (median age at first recording session: 23.5 weeks; B6;129P2-Pvalb^{tm1(cre)Arbr/J}; #008069, Jackson Laboratory) and 3 adult Ntsr1-Cre mice (median age: 29.4 weeks; B6.FVB(Cg)-Tg(Ntsr1-cre)GN220Gsat/Mmcd; #030648-UCD, MMRRC) of either sex. Thirty minutes prior to the surgical procedure, mice were injected with an analgesic (Metamizole, 200 mg/kg, sc, MSD Animal Health, Brussels, Belgium). To induce anesthesia, animals were placed in an induction chamber and exposed to isoflurane (5% in oxygen, CP-Pharma, Burgdorf, Germany). After induction of anesthesia, mice were fixated in a stereotaxic frame (Drill & Microinjection Robot, Neurostar, Tuebingen, Germany) and the isoflurane level was lowered (0.5–2% in oxygen), such that a stable level of anesthesia could be achieved as judged by the absence of a pedal reflex. Throughout the procedure, the eyes were covered with an eye ointment (Bepanthen, Bayer, Leverkusen, Germany) and a closed loop temperature control system (ATC 1000, WPI Germany, Berlin, Germany) ensured that the animal's body temperature was maintained at 37 °C. At the beginning of the surgical procedure, an additional analgesic was administered (Buprenorphine, 0.1 mg/kg, sc, Bayer, Leverkusen, Germany) and the animal's head was shaved and thoroughly disinfected using iodine solution (Braun, Melsungen, Germany). Before performing a scalp incision along the midline, a local analgesic was delivered (Lidocaine hydrochloride, sc, bela-pharm, Vechta, Germany). The skin covering the skull was partially removed and cleaned from tissue residues with a drop of H₂O₂ (3%, AppliChem, Darmstadt, Germany). Using four reference points (bregma, lambda, and two points 2 mm to the left and to the right of the midline respectively), the animal's head was positioned into a skull-flat configuration. The exposed skull was covered with OptiBond FL primer and adhesive (Kerr dental, Rastatt, Germany) omitting three locations: V1 (AP: -2.8 mm, ML: -2.5 mm), dLGN (AP: -2.3 mm, ML: -2 mm), and a position roughly 1.5 mm anterior and 1 mm to the right of bregma, designated for a miniature reference screw (00–96 X 1/16 stainless steel screws, Bilaney) soldered to a custom-made connector pin. Two µL of the adeno-associated viral vector rAAV9/1. EF1a.DIO.hChr2(H134R)-eYFP.WPRE.hGH (Addgene, #20298-AAV9) was dyed with 0.3 µL fast green (Sigma-Aldrich, St. Louis, USA). After performing a small craniotomy over V1, in PV-Cre mice a total of ~ 0.5 µL of this mixture was injected across the entire depth of cortex (0.05 µL injected every 100 µm, starting at 1000 µm and ending at 100 µm below the brain surface), using a glass pipette mounted on a Hamilton syringe (SYR 10 µL 1701 RN no NDL, Hamilton, Bonaduz, Switzerland). In V1 of Ntsr1-Cre mice, we injected 0.35 µL of stGtACR2 (pAAV_hSyn1-SIO-stGtACR2-FusionRed, Addgene, #105677; 0.05 µL injected every 100 µm, starting at 1000 µm and ending at 500 µm below the brain surface). A custom-made lightweight stainless steel head bar was positioned over the posterior part of the skull such that the round opening in the bar was centered on V1/dLGN. The head bar was attached with dental cement (Ivoclar Vivadent, Ellwangen, Germany) to the primer/adhesive. The opening was later filled with the silicone elastomer sealant Kwik-Cast (WPI Germany, Berlin, Germany). At the end of the procedure, an antibiotic ointment (Imex, Merz Pharmaceuticals, Frankfurt, Germany) or iodine-based ointment (Braunodivon, 10%, B. Braun, Melsungen, Germany) was applied to the edges of the wound and a long-term analgesic (Meloxicam, 2 mg/kg, sc, Böhringer Ingelheim, Ingelheim, Germany) was administered and for 3 consecutive days. For at least 5 days post-surgery, the animal's health status was assessed via a score sheet. After at least 1 week of recovery, animals were gradually habituated to the experimental setup by first handling them and then simulating the experimental procedure. To allow for virus expression, neural recordings started no sooner than 3 weeks after injection. On the day prior to the first day of recording, mice were fully anesthetized using the same procedures as described for the initial surgery, and

a craniotomy (ca. 1.5 mm²) was performed over dLGN and V1 and re-sealed with Kwik-Cast (WPI Germany, Berlin, Germany). As long as the animals did not show signs of discomfort, the long-term analgesic Metacam was administered only once at the end of surgery, to avoid any confounding effect on experimental results. Recordings were performed daily and continued for as long as the quality of the electrophysiological signals remained high.

Electrophysiological recordings, optogenetic suppression of V1, perfusion

Head-fixed mice were placed on an air-cushioned Styrofoam ball, which allowed the animal to freely move. Two optical computer mice interfaced with a microcontroller (Arduino Duemilanove) sampled ball movements at 90 Hz. To record eye position and pupil size, the animal's eye was illuminated with infrared light and monitored using a zoom lens (Navitar Zoom 6000) coupled with a camera (Guppy AVT camera; frame rate 50 Hz, Allied Vision, Exton, USA). Extracellular signals were recorded at 30 kHz (Blackrock microsystems). For each recording session, the silicon plug sealing the craniotomy was removed. For V1 recordings, a 32- or 64 channel silicon probe (Neuronexus, A1 × 32-5 mm-25-177, A1 × 32Edge-5mm-20-177 A32 or A1 × 64-Poly2-6mm-23s-160) was lowered into the brain to a median depth of 1025 μm. For dLGN recordings, a 32-channel linear silicon probe (Neuronexus A1 × 32Edge-5mm-20-177 A32) was lowered to a depth of ~2300–3611 μm below the brain surface. We judged recording sites to be located in dLGN based on the characteristic progression of RFs from upper to lower visual field along the electrode shank (Piscopo *et al.*, 2013, *Figure 1—figure supplement 1b*), the presence of responses strongly modulated at the temporal frequency of the drifting gratings (F1 response), and the preference of responses to high temporal frequencies (Grubb and Thompson, 2003; Piscopo *et al.*, 2013). For *post hoc* histological reconstruction of the recording site, the electrode was stained with Dil (Invitrogen, Carlsbad, USA) for one of the final recording sessions.

For photostimulation of V1 PV +inhibitory interneurons or photosuppression of V1 L6CT neurons, an optic fiber (910 μm diameter, Thorlabs, Newton, USA) was coupled to a light-emitting diode (LED, center wavelength 470 nm, M470F1, Thorlabs, Newton, USA; or center wavelength 465 nm, LEDC2_465/635_SMA, Doric Lenses, Quebec, Canada) and positioned with a micromanipulator less than 1 mm above the exposed surface of V1. A black metal foil surrounding the tip of the head bar holder prevented most of the photostimulation light from reaching the animal's eyes. To ensure that the photostimulation was effective, the first recording session for each mouse was carried out in V1. Only if the exposure to light reliably induced suppression of V1 activity was the animal used for subsequent dLGN recordings. For gratings, photostimulation started either 0.1 s before stimulus onset and ended 0.1 s after stimulus offset (2 experiments), or photostimulation started 0.3 s before stimulus onset and ended 0.2 s after stimulus offset (11 experiments), or photostimulation started 0.3 s before stimulus onset and ended 0.45 s after stimulus offset (12 experiments). For movie clips, photostimulation started either 0.1 s before stimulus onset and ended 0.1 s after stimulus offset (2 experiments), or photostimulation started 0.3 s before stimulus onset and ended 0.45 s after stimulus offset (45 experiments). LED light intensity was adjusted on a daily basis to evoke reliable effects (median intensity: 13.66 mW/mm² for activating ChR2 in PV-Cre mice, and 10.84 mW/mm² for activating stGtACR2 in Ntsr1-Cre mice, as measured at the tip of the optic fiber). Since the tip of the fiber never directly touched the surface of the brain, and since the clarity of the surface of the brain varied (generally decreasing every day following the craniotomy), the light intensity delivered even to superficial layers of V1 was inevitably lower. Importantly, changes in dLGN firing rates induced by V1 suppression (FMI, see below) did not differ, on average, from those induced by behavioral state (RMI, see below) (firing rate: FMI 0.20 vs. RMI 0.15, LMM: $F_{1,145.7} = 3.02$, $p = 0.08$; burst ratio: FMI -0.27 vs. RMI -0.28, $F_{1,124.0} = 0.002$, $p = 0.97$; sparseness: FMI -0.12 vs. RMI -0.14, $F_{1,144.9} = 1.03$, $p = 0.31$; reliability: FMI -0.084 vs. -0.037, $F_{1,183.0} = 1.96$, $p = 0.16$; *Figure 6c*), indicating that optogenetic stimulation effects were not outside the physiological range.

After the final recording session, mice were first administered an analgesic (Metamizole, 200 mg/kg, sc, MSD Animal Health, Brussels, Belgium) and following a 30 min latency period were transcardially perfused under deep anesthesia using a cocktail of Medetomidin (Domitor, 0.5 mg/kg, Vetoquinol, Ismaning, Germany), Midazolam (Climasol, 5 mg/kg, Ratiopharm, Ulm, Germany) and Fentanyl (Fentadon, 0.05 mg/kg, Dechra Veterinary Products Deutschland, Aulendorf, Germany) (ip). A few animals, which were treated according to a different license, were anesthetized with sodium

pentobarbital (Narcofen, 400 mg/kg, ip, Böhringer Ingelheim, Ingelheim, Germany). Perfusion was first done with Ringer's lactate solution followed by 4% paraformaldehyde (PFA) in 0.2 M sodium phosphate buffer (PBS).

Histology

To verify recording site and virus expression, we performed histological analyses. Brains were removed, postfixed in PFA for 24 hr, and then rinsed with and stored in PBS at 4 °C. Slices (40 µm) were cut using a vibratome (Leica VT1200 S, Leica, Wetzlar, Germany), stained with DAPI solution before (DAPI, Thermo Fisher Scientific; Vectashield H-1000, Vector Laboratories) or after mounting on glass slides (Vectashield DAPI), and coverslipped. A fluorescent microscope (BX61, Olympus, Tokyo, Japan) was used to inspect slices for the presence of yellow fluorescent protein (eYFP) and Dil. Recorded images were processed using FIJI (Rueden et al., 2017; Schindelin et al., 2012).

Visual stimulation

Visual stimuli were presented on a liquid crystal display (LCD) monitor (Samsung SyncMaster 2233RZ, 47 × 29 cm, 1680 × 1050 resolution at 60 Hz, mean luminance 50 cd/m²) positioned at a distance of 25 cm from the animal's right eye (spanning ~ 108 × 66°, small angle approximation) using custom written software (EXPO, <https://sites.google.com/a/nyu.edu/expo/home>). The display was gamma-corrected for the presentation of artificial stimuli, but not for movies (see below).

To measure receptive fields (RFs), we mapped the ON and OFF subfields with a sparse noise stimulus. The stimulus consisted of nonoverlapping white and black squares on a square grid, each flashed for 200ms. For dLGN recordings, the square grid spanned 60° on a side, while individual squares spanned 5° on a side. For a single experiment, the vertical extent was reduced to 50°. For subsequent choices of stimuli, RF positions and other tuning preferences were determined online after each experiment based on multiunit activity, that is high-pass filtered signals crossing a threshold of 4.5–6.5 SD.

We measured single unit orientation preference by presenting full-screen, full-contrast drifting sinusoidal gratings of either 12 (23 experiments) or 8 (2 experiments) different, pseudo-randomly interleaved orientations (30° or 45° steps). For dLGN recordings, spatial frequency was either 0.02 cyc/° (17 experiments) or 0.04 cyc/° (8 experiments) and temporal frequency was either 2 Hz (2 experiments) or 4 Hz (23 experiments). One blank condition (i.e. mean luminance gray screen) was included to allow measurements of spontaneous activity. The stimulus duration was either 2 s (23 experiments) or 5 s (2 experiments), with an interstimulus interval (ISI) of 2.4 s (21 experiments) or 1.25 s (2 experiments). For two Ntsr1-Cre experiments, ISIs varied and were either 0.58 s or 1.09 s.

For laminar localization of neurons recorded in V1, we presented a full-screen, contrast-reversing checkerboard at 100% contrast, with a spatial frequency of either 0.01 cyc/° (2 experiments) or 0.02 cyc/° (5 experiments) and a temporal frequency of 0.5 cyc/s.

Movies were acquired using a hand-held consumer-grade digital camera (Canon PowerShot SD200) at a resolution of 320 × 240 pixels and 60 frames/s. Movies were filmed close to the ground in a variety of wooded or grassy locations in Vancouver, BC, and contained little to no forward/backward optic flow, but did contain simulated gaze shifts (up to 275°/s), generated by manual camera movements (for example movies, see *Figure 1—video 1* and *Figure 1—video 2*). Focus was kept within 2 m and exposure settings were set to automatic. The horizontal angle subtended by the camera lens was 51.6°. No display gamma correction was used while presenting movies, since consumer-grade digital cameras are already gamma corrected for consumer displays (Poynton, 1998). For presentation, movies were cut into 5 s clips and converted from color to grayscale. Movie clips were presented full-screen with an ISI of 1.25 s (43 experiments). For two Ntsr1-Cre experiments, ISIs varied and were either 0.58 s or 1.08 s.

Spike sorting

To obtain single unit activity from extracellular recordings, we used the open source, Matlab-based, automated spike sorting toolbox Kilosort (Pachitariu et al., 2016). Resulting clusters were manually refined using Spyke (Spacek et al., 2009), a Python application that allows the selection of channels and time ranges around clustered spikes for realignment, as well as representation in 3D space using dimension reduction (multichannel PCA, ICA, and/or spike time). In 3D, clusters were then further split

via a gradient-ascent based clustering algorithm (GAC) (Swindale and Spacek, 2014). Exhaustive pairwise comparisons of similar clusters allowed the merger of potentially over-clustered units. For subsequent analyses, we inspected autocorrelograms and mean voltage traces, and only considered units that displayed a clear refractory period and a distinct spike waveshape. All further analyses were carried out using the DataJoint framework (Yatsenko et al., 2018) with custom-written code in Python.

Response characterization

We used current source density (CSD) analysis for recordings in area V1 to determine the laminar position of electrode contacts. To obtain the LFP data we first down-sampled the signal to 1 kHz before applying a bandpass filter (4–90 Hz, 2nd-order Butterworth filter). We computed the CSD from the second spatial derivative of the local field potentials (Mitzdorf, 1985), and assigned the base of layer 4 to the contact that was closest to the earliest CSD polarity inversion. The remaining contacts were assigned to supragranular, granular and infragranular layers, assuming a thickness of ~1 mm for mouse visual cortex (Heumann et al., 1977).

In recordings targeting dLGN, we used the envelope of multi-unit spiking activity (MUAe) (van der Togt et al., 2005) to determine RF progression (Figure 1—figure supplement 1b). Briefly, we full-wave rectified the high-pass filtered signals (cutoff frequency: 300 Hz, 4th-order non-causal Butterworth filter) before performing common average referencing by subtracting the median voltage across all channels in order to eliminate potential artifacts (e.g. movement artifacts). We then applied a low-pass filter (cutoff frequency: 500 Hz, Butterworth filter) and down-sampled the signal to 2 kHz. Recording sessions for which RFs did not show the retinotopic progression typical of dLGN (Figure 1—figure supplement 1b; Piscopo et al., 2013) were excluded from further analysis.

Each unit's peristimulus time histogram (PSTH, i.e. the response averaged over trials) was calculated by convolving a Gaussian of width $2\sigma = 20$ ms with the spike train collapsed across all trials, separately for each condition.

We defined bursts according to Lu et al., 1992, which required a silent period of at least 100ms before the first spike in a burst, followed by a second spike with an interspike interval < 4 ms. Imposing the silent period was found to be crucial for separating dLGN 'low threshold calcium bursts' from high-frequency firing in extracellular recordings (Lu et al., 1992); note however, that 'low-threshold calcium bursts' can only be unequivocally detected in intracellular recordings or calcium imaging. Any subsequent spikes with preceding interspike intervals < 4ms were also considered to be part of the burst. All other spikes were regarded as tonic. We computed a burst ratio (the number of burst spikes divided by the total number of spikes) and compared this ratio in conditions with CT feedback intact vs. V1 suppression or during locomotion vs. stationary conditions. PSTHs for burst spikes were calculated by only considering spikes that were part of bursts before collapsing across trials and convolving with the Gaussian kernel (see above). PSTHs for non-burst spikes were calculated in an analogous way.

To quantify the effect of V1 suppression on various response properties, we defined the feedback modulation index (FMI) as

$$\text{FMI} = \frac{\text{feedback} - \text{suppression}}{\text{feedback} + \text{suppression}} \quad (1)$$

Characterization of responses to naturalistic movie clips

Signal to noise ratio (SNR) was calculated according to Baden et al., 2016 by

$$\text{SNR} = \frac{\text{Var}\langle C_r \rangle_t}{\langle \text{Var}\{C\}_t \rangle_r} \quad (2)$$

where C is the T by R response matrix (time samples by stimulus repetitions) and $\langle \rangle_x$ and $\text{Var}[\]_x$ denote the mean and variance across the indicated dimension, respectively. If all trials were identical such that the mean response was a perfect representative of the response, SNR would equal 1.

The sparseness S of a PSTH was calculated according to Vinje and Gallant, 2000 by

$$S = \left(1 - \frac{\left(\sum_{i=1}^n r_i/n \right)^2}{\sum_{i=1}^n r_i^2/n} \right) \left(\frac{1}{1-1/n} \right) \quad (3)$$

where $r_i \geq 0$ is the signal value in the i^{th} time bin, and n is the number of time bins. Sparseness ranges from 0 to 1, with 0 corresponding to a uniform signal, and 1 corresponding to a signal with all of its energy in a single time bin.

Response reliability was quantified according to **Goard and Dan, 2009** as the mean pairwise correlation of all trial pairs of a unit's single-trial responses. Single-trial responses were computed by counting spikes in 20ms, overlapping time bins at 1ms resolution. Pearson's correlation was calculated between all possible pairs of trials, and then averaged across trials per condition.

To detect response peaks in trial raster plots and measure their widths, clustering of spike times collapsed across trials was performed using the gradient ascent clustering (GAC) algorithm (**Swindale and Spacek, 2014**), with a characteristic neighborhood size of 20ms. Spike time clusters containing less than 5 spikes were discarded. The center of each detected cluster of spike times was matched to the nearest peak in the PSTH. A threshold of $\theta = b + 3$ Hz was applied to the matching PSTH peak, where $b = 2 \text{ median}(x)$ is the baseline of each PSTH x . Peaks in the PSTH that fell below θ were discarded, and all others were kept as valid peaks. Peak widths were measured as the temporal separation of the middle 68% (16th to 84th percentile) of spike times within each cluster.

To determine whether V1 suppression changes dLGN responses in a divisive or subtractive manner, we fit a threshold-linear model using repeated random subsampling cross-validation. To this end, we first selected a random set of 50% of the trials for each condition for fitting to the timepoint-by-

timepoint responses a threshold linear model given by $R_{supp} = s R_{fb} + b$, where $R_{supp} > 0$, with s repre-

senting the slope and b the offset. Fitting was done using non-linear least squares (scipy.optimize.curve_fit). Throughout **Figure 2**, we report the resulting x -intercept as the threshold. We evaluated goodness of fit (R^2) for the other 50% of trials not used for fitting. We repeated this procedure 1000 times and considered threshold and slope as significant if the central 95% of their distribution did not include 0 and 1, respectively.

Characterization of responses to drifting gratings

For display of spike rasters (**Figure 3**), trials were sorted by condition. We computed orientation tuning curves by fitting a sum of two Gaussians of the same width with peaks 180° apart:

$$R(\theta) = R_0 + R_p e^{-\frac{(\theta - \theta_p)^2}{2\sigma^2}} + R_n e^{-\frac{(\theta - \theta_p + 180)^2}{2\sigma^2}} \quad (4)$$

In this expression, θ is stimulus orientation (0–360°). The function has five parameters: preferred orientation θ_p , tuning width σ , baseline response (offset independent of orientation) R_0 , response at the preferred orientation R_p , and response at the null orientation R_n .

Orientation selectivity was quantified according to **Bonhoeffer et al., 1995; Olsen et al., 2012** as

$$OSI = \frac{\sqrt{(\sum R_k \sin(2\theta_k))^2 + (\sum R_k \cos(2\theta_k))^2}}{\sum R_k} \quad (5)$$

where R_k is the response to the k th direction given by θ_k . We determined OSI for each unit during both feedback and suppression conditions.

We computed the first harmonic of the response R from the spike trains according to **Carandini et al., 1997** to obtain the amplitude and phase of the best-fitting sinusoid, which has the same temporal frequency as the stimulus. For each trial, we calculated

$$R = (1/D) \sum_k \cos(2\pi f t_k) + i \sin(2\pi f t_k) \quad (6)$$

where D is the stimulus duration, f is the temporal frequency of the stimulus, and the t_k are the times of the individual spikes. We excluded the first cycle to avoid contamination by the onset

response. For (Figure 3g), we calculated average amplitude F_1 by obtaining the absolute value of the complex number R on each trial, before averaging across trials, to avoid potential confounds due to differences in response phase across conditions. For the comparison of response phase, we focused on the orientation which elicited the maximal cycle average response across both feedback and suppression conditions.

Cell typing

Units were classified as suppressed by contrast (SbC) or not suppressed by contrast (non-SbC) by comparing their mean firing rates during full-screen drifting grating presentation to their mean firing rates during blank-screen presentation. Units were classified as SbC if they were visually responsive to gratings (see below) and had a median z-scored response across orientation conditions of ≤ -3 during at least one grating experiment. Otherwise, units were classified as non-SbC. SbC units seem to constitute a sizeable fraction in our dataset, which is similar to our previous results (Román Rosón et al., 2019), where SbC was also found to be among the overrepresented retinal ganglion cell (RGC) types providing input to dLGN.

To identify electrode channels within the dLGN, and their relative depth, which could be useful to distinguish between shell and core, we concentrated on the RF progression as assessed with MUAe maps that were constructed using sparse noise experiments. Because RF progression is mainly along elevation, amplitudes of MUAe for each channel were collapsed across azimuth and then range normalized. Channels with normalized amplitudes higher than an empirically set threshold (0.4) were considered part of dLGN. Non-detected channels located between detected channels were also included.

Direction selectivity index (DSI, Niell and Stryker, 2008) was calculated for each unit as

$$DSI = \frac{R_p - R_n}{R_p + R_n + 2R_0} \quad (7)$$

where R_p and R_n are the firing rates in the preferred and null directions, respectively, extracted from tuning curves fit to drifting grating responses (see above), and R_0 is baseline firing rate independent of orientation.

The RF distance from the center of the screen was calculated for each unit by finding the position of the MUAe RF for the channel on which the unit's mean spike waveform had the largest amplitude.

Exclusion criteria

Neurons with mean evoked firing rates < 0.01 spikes/s were excluded from further analysis. For movie clips, only neurons with $SNR \geq 0.015$ in at least one of the conditions in an experiment were considered. Of this population, 2 neurons were excluded from the analysis of the parameters returned by the threshold linear model, because their R^2 was lt_0 . For gratings, we converted firing rates in response to each orientation to z-scores relative to responses to the mean luminance gray screen. We only considered visually responsive neurons, with an absolute z-scored response ≥ 2.5 to at least 1 orientation. For the analysis of response phase, we only considered neurons with a peak of the cycle average response of at least 10 Hz in both feedback and suppression conditions, and an F_1/F_0 ratio of at least 0.25.

Locomotion

We used the Euclidean norm of three perpendicular components of ball velocity (roll, pitch, and yaw) to compute animal running speed. For the analysis of neural responses as a function of behavioral state, locomotion trials were defined as those for which speed exceeded 1 cm/s for at least 50% of the stimulus presentation, and stationary trials as those for which speed fell below 0.25 cm/s for at least 50% of the stimulus presentation. To quantify the effect of running vs. sitting on various response properties, the run modulation index (RMI) was defined as

$$RMI = \frac{\text{running} - \text{sitting}}{\text{running} + \text{sitting}} \quad (8)$$

Eye tracking

The stimulus viewing eye was filmed using an infrared camera under infrared LED illumination. Pupil position was extracted from the videos using a custom, semi-automated algorithm. Briefly, each video

frame was equalized using an adaptive bi-histogram equalization procedure, and then smoothed using median and bilateral filters. The center of the pupil was detected by taking the darkest point in a convolution of the filtered image with a black square. Next, the peaks of the image gradient along lines extending radially from the center point were used to define the pupil contour. Lastly, an ellipse was fit to the contour, and the center of this ellipse was taken as the position of the pupil. A similar procedure was used to extract the position of the corneal reflection (CR) of the LED illumination. Eye blinks were automatically detected and the immediately adjacent data points were excluded. Adjustable algorithm parameters were set manually for each experiment. Output pupil position time-courses were lightly smoothed, and unreliable segments were automatically removed according to a priori criteria. Finally, the CR position was subtracted from the pupil position to eliminate translational eye movements, and pupil displacement in degrees relative to the baseline (median) position was determined by

$$\theta = 2 \frac{\arcsin(d/2)}{r} \tag{9}$$

where d is the distance between the pupil and the baseline position, and $r = 1.25$ mm is the radius of the eye (Remtulla and Hallett, 1985). Angular displacement was computed separately for x and y directions.

Eye position standard deviation was computed by first taking the standard deviation of the horizontal eye position at each time point across trials, and then averaging over the 5 s during which the visual stimulus was presented. We focused on horizontal eye position because horizontal and vertical eye movements tend to occur in tandem under head-fixed conditions, and the horizontal position variance is larger (Sakatani and Isa, 2007), thus serving as a better proxy for variance in 2D. For each experiment, trials were sorted either by the presence of optogenetic suppression of CT feedback (Figure 1—figure supplement 2h), or by the behavioral state of the animal as described above (Figure 5—figure supplement 1h). The eye position standard deviation FMI and RMI (Figure 1—figure supplement 2i and Figure 5—figure supplement 1i) were calculated in the same manner as for the neural response properties.

Table 1. Breakdown of sample sizes (N) for the analyses of neural data. See text for details.

	Neurons	Mice
Figure 1f–i	65	6
Figure 2e–i	63	6
Figure 3c–e and g	44	4
Figure 3f	28	4
Figure 3h–i	35	3
Figure 4a–b	39	4
Figure 5c–f,i–l	66	6
Figure 6, a _{1,3}	64	6
Figure 6, a ₂	58	6
Figure 6, a ₄	63	6
Figure 6, b ₁ and b ₃	63	6
Figure 6, b ₂	58	6
Figure 6, b ₄	62	6
Figure 6, C _{1,3} and 4	59	6
Figure 6, C ₂	56	6
Figure 1—figure supplement 2a	65	6
Figure 1—figure supplement 2b,g	57	6
Figure 1—figure supplement 2c	63	6
Figure 1—figure supplement 2d–f, i	64	6
Figure 1—figure supplement 2h		6
Figure 1—figure supplement 3a,c	39	4
Figure 1—figure supplement 3b,j	63	6
Figure 1—figure supplement 3d	54	6
Figure 1—figure supplement 3e	64	6
Figure 1—figure supplement 3f, h	38	4
Figure 1—figure supplement 3g	62	6
Figure 1—figure supplement 3i	53	6
Figure 1—figure supplement 4e–h	62	3
Figure 1—figure supplement 4l–n	73	3
Figure 1—figure supplement 5c,d,h,i	19	1
Figure 1—figure supplement 6c–f	35	5
Figure 1—figure supplement 6g	65	6
Figure 1—figure supplement 6h	56	3
Figure 1—figure supplement 6i	64	6
Figure 1—figure supplement 6j	54	3
Figure 3—figure supplement 1a,c,e	44	4
Figure 3—figure supplement 1b,f,h,i	42	4
Figure 3—figure supplement 1d	36	4
Figure 3—figure supplement 1g	40	4

Table 1 continued on next page

Table 1 continued

	Neurons	Mice
Figure 3—figure supplement 1i	35	4
Figure 4—figure supplement 1a	42	4
Figure 4—figure supplement 1b,k,i	43	4
Figure 4—figure supplement 1c-d,g,i	65	6
Figure 4—figure supplement 1e	36	3
Figure 4—figure supplement 1f	29	3
Figure 4—figure supplement 1h, i	44	4
Figure 5—figure supplement 1a	66	6
Figure 5—figure supplement 1g	56	6
Figure 5—figure supplement 1c	57	6
Figure 5—figure supplement 1d-f, i	65	6
Figure 5—figure supplement 1h		6
Figure 5—figure supplement 2d-g	57	6
Figure 6—figure supplement 1, a ₁ , b ₁ , c ₁	37	4
Figure 6—figure supplement 1, a ₂ , c ₂	34	3
Figure 6—figure supplement 1, b ₂	33	3

Analysis of pupil dilation during movies

Following (Reimer et al., 2014), changes in pupil area collected during movie clip presentation (e.g. Figure 5—figure supplement 2a) were measured at 20ms resolution. Spiking responses were binned to match the temporal resolution of the pupil change signal, masked to exclude periods of locomotion (> 0.25 cm/s), and then further masked to only include bins corresponding to the top or bottom quartiles (dilation or constriction) of the pupil area dynamics. Neural responses (firing rate, reliability, and SNR) were then calculated separately for the remaining unmasked top or bottom pupil quartile bins. To make our analyses comparable to those obtained for V1 by Reimer et al., 2014, we considered pupil-related response modulations as a function of instantaneous firing rate. For Figure 5—figure supplement 2c, we therefore separated each time point of the PSTH, determined without taking pupil size into account, into firing rate quartiles. We then computed, for each neuron, the % change in median firing rates between top and bottom pupil quartiles in each of the four firing rate quartiles. While Reimer et al., 2014 observed a multi-

plicative effect of pupil size change on V1 responses to movies, our results for dLGN rather resemble an inverted U-shape pattern.

Statistical methods

To assess statistical significance, we fitted and examined multilevel linear models (Gelman and Hill, 2007). Such models take into account the hierarchical structure present in our data (i.e. neurons nested in experiments, experiments nested in recording sessions, recordings sessions nested in animals), and eliminate the detrimental effect of structural dependencies on the likelihood of Type I errors (false positive reports) (Aarts et al., 2014). By considering the nested structure of the data, multilevel models also eliminate the need for 'pre-selecting' data sets, such as one out of several experiments repeatedly performed on the same neurons. Whenever we have several experiments per neuron, we include all of them, and also show them in the scatter plots ('observations'). We provide the sample size for each analysis in Table 1. To account for repeated measurements, we fitted by-neuron random intercepts and random slopes over measurement conditions (V1 control vs V1 suppressed). By-neuron random intercepts model, the difference between neurons in overall firing rates, while by-neuron random slopes model between-neuron differences in how they responded to V1 suppression. Where possible, we included random intercepts for experiments nested in recording sessions, nested in mice, and random intercepts and slopes for neurons partially crossed in experiments. In cases where the model structure was too complex for a given data set (i.e. did not converge, or gave singular fits), we simplified the random effects structure by removing one or more terms. We fit these models in R (R Core Team, 2017), using the lme4 package (Bates et al., 2015). We estimated F-values, their degrees of freedom, and the corresponding p-values using the Satterthwaite approximation (Luke, 2017) implemented by the lmerTest package (Kuznetsova et al., 2017). For each analysis, we provide the exact model specification and the complete output of the model (see Data and code availability).

Throughout the manuscript, uncertainty in estimated regression slopes is represented as $slope \pm x$, where x is $2 \times$ the estimated standard error of the slope.

Acknowledgements

This research was supported by the German Research Foundation (DFG) SFB 870 TP 19, project number 118803580 (LB), DFG BU 1808/5-1 (LB), DFG SFB 1233, Robust Vision: Inference Principles and Neural Mechanisms, TP 13, project number: 276693517 (LB), and by an add-on fellowship of the Joachim Herz Stiftung (GB). We thank D Metzler for discussions regarding the multi-level modeling, M Sotgia for lab management and support with animal handling and histology, S Schörnich for IT support, and B Grothe for providing excellent research infrastructure.

Additional information

Funding

Funder	Grant reference number	Author
Deutsche Forschungsgemeinschaft	SFB 1233, Robust Vision: Inference Principles and Neural Mechanisms, TP 13, project number: 276693517	Laura Busse
Deutsche Forschungsgemeinschaft	SFB 870, TP 19, project number: 118803580	Laura Busse
Deutsche Forschungsgemeinschaft	DFG BU 1808/5-1	Laura Busse
Joachim Herz Stiftung	add-on fellowship	Gregory Born

The funders had no role in study design, data collection and interpretation, or the decision to submit the work for publication.

Author contributions

Martin A Spacek, Conceptualization, Data curation, Investigation, Methodology, Software, Visualization, Writing – review and editing; Davide Crombie, Data curation, Methodology, Software, Writing – review and editing; Yannik Bauer, Investigation, Software, Visualization; Gregory Born, Data curation, Software, Visualization, Writing - original draft, Writing – review and editing; Xinyu Liu, Investigation, Software; Steffen Katzner, Data curation, Formal analysis, Software, Visualization, Writing – review and editing; Laura Busse, Conceptualization, Data curation, Funding acquisition, Project administration, Supervision, Writing - original draft, Writing – review and editing

Author ORCIDs

Martin A Spacek <http://orcid.org/0000-0002-9519-3284>

Yannik Bauer <http://orcid.org/0000-0003-2613-6443>

Gregory Born <http://orcid.org/0000-0003-0430-3052>

Steffen Katzner <http://orcid.org/0000-0002-4424-2197>

Laura Busse <http://orcid.org/0000-0002-6127-7754>

Ethics

All procedures complied with the European Communities Council Directive 2010/63/EU and the German Law for Protection of Animals, and were approved by local authorities, following appropriate ethics review.

Decision letter and Author response

Decision letter <https://doi.org/10.7554/eLife.70469.sa1>

Author response <https://doi.org/10.7554/eLife.70469.sa2>

Additional files

Supplementary files

- Transparent reporting form

Data availability

Data and source code used to generate the figures in the manuscript has been made available on G-Node (<https://doi.org/10.12751/g-node.58bc8k>).

The following dataset was generated:

References

- Aarts E, Verhage M, Veenvliet JV, Dolan CV, van der Sluis S. 2014. A solution to dependency: using multilevel analysis to accommodate nested data. *Nature Neuroscience* **17**:491–496. DOI: <https://doi.org/10.1038/nn.3648>
- Alitto HJ, Weyand TG, Usrey WM. 2005. Distinct properties of stimulus-evoked bursts in the lateral geniculate nucleus. *The Journal of Neuroscience* **25**:514–523. DOI: <https://doi.org/10.1523/JNEUROSCI.3369-04.2005>
- Alitto H, Rathbun DL, Vandeleest JJ, Alexander PC, Usrey WM. 2019. The Augmentation of Retinogeniculate Communication during Thalamic Burst Mode. *The Journal of Neuroscience* **39**:5697–5710. DOI: <https://doi.org/10.1523/JNEUROSCI.2320-18.2019>
- Andolina IM, Jones HE, Sillito AM. 2013. Effects of cortical feedback on the spatial properties of relay cells in the lateral geniculate nucleus. *Journal of Neurophysiology* **109**:889–899. DOI: <https://doi.org/10.1152/jn.00194.2012>
- Augustinaite S, Kuhn B, Helm PJ, Heggelund P. 2014. NMDA spike/plateau potentials in dendrites of thalamocortical neurons. *The Journal of Neuroscience* **34**:10892–10905. DOI: <https://doi.org/10.1523/JNEUROSCI.1205-13.2014>
- Augustinaite S, Kuhn B. 2020. Complementary Ca²⁺ Activity of Sensory Activated and Suppressed Layer 6 Corticothalamic Neurons Reflects Behavioral State. *Current Biology* **30**:3945–3960. DOI: <https://doi.org/10.1016/j.cub.2020.07.069>
- Aydın Ç, Couto J, Giugliano M, Farrow K, Bonin V. 2018. Locomotion modulates specific functional cell types in the mouse visual thalamus. *Nature Communications* **9**:4882. DOI: <https://doi.org/10.1038/s41467-018-06780-3>
- Baden T, Berens P, Franke K, Román Rosón M, Bethge M, Euler T. 2016. The functional diversity of retinal ganglion cells in the mouse. *Nature* **529**:345–350. DOI: <https://doi.org/10.1038/nature16468>
- Bastos AM, Usrey WM, Adams RA, Mangun GR, Fries P, Friston KJ. 2012. Canonical microcircuits for predictive coding. *Neuron* **76**:695–711. DOI: <https://doi.org/10.1016/j.neuron.2012.10.038>
- Bates D, Mächler M, Bolker B, Walker S. 2015. Fitting Linear Mixed-Effects Models Using lme4. *Journal of Statistical Software* **67**:1. DOI: <https://doi.org/10.18637/jss.v067.i01>
- Béhuret S, Deleuze C, Bal T. 2015. Corticothalamic Synaptic Noise as a Mechanism for Selective Attention in Thalamic Neurons. *Frontiers in Neural Circuits* **9**:80. DOI: <https://doi.org/10.3389/fncir.2015.00080>
- Bennett C, Arroyo S, Hestrin S. 2013. Subthreshold mechanisms underlying state-dependent modulation of visual responses. *Neuron* **80**:350–357. DOI: <https://doi.org/10.1016/j.neuron.2013.08.007>
- Berkes P, Orbán G, Lengyel M, Fiser J. 2011. Spontaneous cortical activity reveals hallmarks of an optimal internal model of the environment. *Science (New York, N.Y.)* **331**:83–87. DOI: <https://doi.org/10.1126/science.1195870>
- Bickford ME, Zhou N, Krahe TE, Govindaiah G, Guido W. 2015. Retinal and Tectal “Driver-Like” Inputs Converge in the Shell of the Mouse Dorsal Lateral Geniculate Nucleus. *The Journal of Neuroscience* **35**:10523–10534. DOI: <https://doi.org/10.1523/JNEUROSCI.3375-14.2015>
- Bonhoeffer T, Kim DS, Malonek D, Shoham D, Grinvald A. 1995. Optical imaging of the layout of functional domains in area 17 and across the area 17/18 border in cat visual cortex. *The European Journal of Neuroscience* **7**:1973–1988. DOI: <https://doi.org/10.1111/j.1460-9568.1995.tb00720.x>
- Born G, Schneider-Soupiadis FA, Erisken S, Vaiceliunaite A, Lao CL, Mobarhan MH, Spacek MA, Einevoll GT, Busse L. 2021. Corticothalamic feedback sculpts visual spatial integration in mouse thalamus. *Nature Neuroscience* **24**:1711–1720. DOI: <https://doi.org/10.1038/s41593-021-00943-0>
- Bortone DS, Olsen SR, Scanziani M. 2014. Translaminar inhibitory cells recruited by layer 6 corticothalamic neurons suppress visual cortex. *Neuron* **82**:474–485. DOI: <https://doi.org/10.1016/j.neuron.2014.02.021>
- Briggs F, Usrey WM. 2009. Parallel processing in the corticogeniculate pathway of the macaque monkey. *Neuron* **62**:135–146. DOI: <https://doi.org/10.1016/j.neuron.2009.02.024>
- Briggs F. 2010. Organizing principles of cortical layer 6. *Frontiers in Neural Circuits* **4**:3. DOI: <https://doi.org/10.3389/fncir.2010.0003.2010>
- Briggs F, Usrey WM. 2011. Corticogeniculate feedback and visual processing in the primate. *The Journal of Physiology* **589**:33–40. DOI: <https://doi.org/10.1113/jphysiol.2010.193599>
- Briggs F, Kiley CW, Callaway EM, Usrey WM. 2016. Morphological Substrates for Parallel Streams of Corticogeniculate Feedback Originating in Both V1 and V2 of the Macaque Monkey. *Neuron* **90**:388–399. DOI: <https://doi.org/10.1016/j.neuron.2016.02.038>
- Carandini M, Heeger DJ, Movshon JA. 1997. Linearity and normalization in simple cells of the macaque primary visual cortex. *The Journal of Neuroscience* **17**:8621–8644. DOI: <https://doi.org/10.1523/JNEUROSCI.17-21-08621.1997>
- Cardin JA, Palmer LA, Contreras D. 2008. Cellular mechanisms underlying stimulus-dependent gain modulation in primary visual cortex neurons in vivo. *Neuron* **59**:150–160. DOI: <https://doi.org/10.1016/j.neuron.2008.05.002>

- Chance FS**, Nelson SB, Abbott LF. 1999. Complex cells as cortically amplified simple cells. *Nature Neuroscience* 2:277–282. DOI: <https://doi.org/10.1038/6381>
- Chance FS**, Abbott LF, Reyes AD. 2002. Gain modulation from background synaptic input. *Neuron* 35:773–782. DOI: [https://doi.org/10.1016/s0896-6273\(02\)00820-6](https://doi.org/10.1016/s0896-6273(02)00820-6)
- Chen C**, Bickford ME, Hirsch JA. 2016. Untangling the Web between Eye and Brain. *Cell* 165:20–21. DOI: <https://doi.org/10.1016/j.cell.2016.03.010>
- Clark A**. 2013. Whatever next? Predictive brains, situated agents, and the future of cognitive science. *The Behavioral and Brain Sciences* 36:181–204. DOI: <https://doi.org/10.1017/S0140525X12000477>
- Coen-Cagli R**, Kohn A, Schwartz O. 2015. Flexible gating of contextual influences in natural vision. *Nature Neuroscience* 18:1648–1655. DOI: <https://doi.org/10.1038/nn.4128>
- Crandall SR**, Cruikshank SJ, Connors BW. 2015. A corticothalamic switch: controlling the thalamus with dynamic synapses. *Neuron* 86:768–782. DOI: <https://doi.org/10.1016/j.neuron.2015.03.040>
- Crandall SR**, Patrick SL, Cruikshank SJ, Connors BW. 2017. Infrabarrels Are Layer 6 Circuit Modules in the Barrel Cortex that Link Long-Range Inputs and Outputs. *Cell Reports* 21:3065–3078. DOI: <https://doi.org/10.1016/j.celrep.2017.11.049>
- Cruz-Martín A**, El-Danaf RN, Osakada F, Sriram B, Dhande OS, Nguyen PL, Callaway EM, Ghosh A, Huberman AD. 2014. A dedicated circuit links direction-selective retinal ganglion cells to the primary visual cortex. *Nature* 507:358–361. DOI: <https://doi.org/10.1038/nature12989>
- Cudeiro J**, Sillito AM. 1996. Spatial frequency tuning of orientation-discontinuity-sensitive corticofugal feedback to the cat lateral geniculate nucleus. *The Journal of Physiology* 490 (Pt 2):481–492. DOI: <https://doi.org/10.1113/jphysiol.1996.sp021159>
- Dan Y**, Atick JJ, Reid RC. 1996. Efficient coding of natural scenes in the lateral geniculate nucleus: experimental test of a computational theory. *The Journal of Neuroscience* 16:3351–3362.
- de Labra C**, Rivadulla C, Grieve K, Mariño J, Espinosa N, Cudeiro J. 2007. Changes in visual responses in the feline dLGN: selective thalamic suppression induced by transcranial magnetic stimulation of V1. *Cerebral Cortex (New York, N.Y)* 17:1376–1385. DOI: <https://doi.org/10.1093/cercor/bhl048>
- Denman DJ**, Contreras D. 2015. Complex Effects on In Vivo Visual Responses by Specific Projections from Mouse Cortical Layer 6 to Dorsal Lateral Geniculate Nucleus. *The Journal of Neuroscience* 35:9265–9280. DOI: <https://doi.org/10.1523/JNEUROSCI.0027-15.2015>
- Denman DJ**, Contreras D. 2016. On Parallel Streams through the Mouse Dorsal Lateral Geniculate Nucleus. *Frontiers in Neural Circuits* 10:20. DOI: <https://doi.org/10.3389/fncir.2016.00020>
- DiCarlo JJ**, Zoccolan D, Rust NC. 2012. How does the brain solve visual object recognition? *Neuron* 73:415–434. DOI: <https://doi.org/10.1016/j.neuron.2012.01.010>
- Disney AA**, Aoki C, Hawken MJ. 2007. Gain modulation by nicotine in macaque V1. *Neuron* 56:701–713. DOI: <https://doi.org/10.1016/j.neuron.2007.09.034>
- Dossi RC**, Nuñez A, Steriade M. 1992. Electrophysiology of a slow (0.5–4 Hz) intrinsic oscillation of cat thalamocortical neurones in vivo. *The Journal of Physiology* 447:215–234. DOI: <https://doi.org/10.1113/jphysiol.1992.sp018999>
- Erisken S**, Vaiceliunaite A, Jurjut O, Fiorini M, Katzner S, Busse L. 2014. Effects of locomotion extend throughout the mouse early visual system. *Current Biology* 24:2899–2907. DOI: <https://doi.org/10.1016/j.cub.2014.10.045>
- Ferguson KA**, Cardin JA. 2020. Mechanisms underlying gain modulation in the cortex. *Nature Reviews. Neuroscience* 21:80–92. DOI: <https://doi.org/10.1038/s41583-019-0253-y>
- Frndolig JE**, Matney CJ, Lee K, Kim J, Chevée M, Kim S-J, Bickert AA, Brown SP. 2019. The Synaptic Organization of Layer 6 Circuits Reveals Inhibition as a Major Output of a Neocortical Sublamina. *Cell Reports* 28:3131–3143. DOI: <https://doi.org/10.1016/j.celrep.2019.08.048>, PMID: 31533036
- Funke K**, Pape HC, Eysel UT. 1993. Noradrenergic modulation of retinogeniculate transmission in the cat. *The Journal of Physiology* 463:169–191. DOI: <https://doi.org/10.1113/jphysiol.1993.sp019590>
- Gelman A**, Hill J. 2007. *Data Analysis Using Regression and Multilevel/Hierarchical Models*, Ser. Analytical Methods for Social Research. Cambridge: Cambridge University Press.
- Gilbert CD**, Li W. 2013. Top-down influences on visual processing. *Nature Reviews. Neuroscience* 14:350–363. DOI: <https://doi.org/10.1038/nrn3476>
- Goard M**, Dan Y. 2009. Basal forebrain activation enhances cortical coding of natural scenes. *Nature Neuroscience* 12:1444–1449. DOI: <https://doi.org/10.1038/nn.2402>
- Godwin DW**, Van Horn SC, Eriir A, Sesma M, Romano C, Sherman SM. 1996. Ultrastructural localization suggests that retinal and cortical inputs access different metabotropic glutamate receptors in the lateral geniculate nucleus. *The Journal of Neuroscience* 16:8181–8192. DOI: <https://doi.org/10.1523/JNEUROSCI.16-24-08181.1996>
- Gouwens NW**, Sorensen SA, Berg J, Lee C, Jarsky T, Ting J, Sunkin SM, Feng D, Anastassiou CA, Barkan E, Bickley K, Blesie N, Braun T, Brouner K, Budzillo A, Caldejon S, Casper T, Castelli D, Chong P, Crichton K, et al. 2019. Classification of electrophysiological and morphological neuron types in the mouse visual cortex. *Nature Neuroscience* 22:1182–1195. DOI: <https://doi.org/10.1038/s41593-019-0417-0>
- Grubb MS**, Thompson ID. 2003. Quantitative characterization of visual response properties in the mouse dorsal lateral geniculate nucleus. *Journal of Neurophysiology* 90:3594–3607. DOI: <https://doi.org/10.1152/jn.00699.2003>
- Grubb MS**, Thompson ID. 2005. Visual response properties of burst and tonic firing in the mouse dorsal lateral geniculate nucleus. *Journal of Neurophysiology* 93:3224–3247. DOI: <https://doi.org/10.1152/jn.00445.2004>

- Gulyás B, Lagae L, Eysel U, Orban GA. 1990. Corticofugal feedback influences the responses of geniculate neurons to moving stimuli. *Experimental Brain Research* **79**:441–446. DOI: <https://doi.org/10.1007/BF00608257>
- Guo W, Clause AR, Barth-Marion A, Polley DB. 2017. A Corticothalamic Circuit for Dynamic Switching between Feature Detection and Discrimination. *Neuron* **95**:180–194. DOI: <https://doi.org/10.1016/j.neuron.2017.05.019>
- Hasse JM, Briggs F. 2017. Corticogeniculate feedback sharpens the temporal precision and spatial resolution of visual signals in the ferret. *PNAS* **114**:E6222–E6230. DOI: <https://doi.org/10.1073/pnas.1704524114>
- Hasse JM, Bragg EM, Murphy AJ, Briggs F. 2019. Morphological heterogeneity among corticogeniculate neurons in ferrets: quantification and comparison with a previous report in macaque monkeys. *The Journal of Comparative Neurology* **527**:546–557. DOI: <https://doi.org/10.1002/cne.24451>
- Heeger DJ. 2017. Theory of cortical function. *PNAS* **114**:1773–1782. DOI: <https://doi.org/10.1073/pnas.1619788114>
- Heumann D, Leuba G, Rabinowicz T. 1977. Postnatal development of the mouse cerebral neocortex. II. Quantitative cytoarchitectonics of visual and auditory areas. *Journal Fur Hirnforschung* **18**:483–500.
- Hô N, Destexhe A. 2000. Synaptic background activity enhances the responsiveness of neocortical pyramidal neurons. *Journal of Neurophysiology* **84**:1488–1496. DOI: <https://doi.org/10.1152/jn.2000.84.3.1488>
- Hochstein S, Ahissar M. 2002. View from the top: hierarchies and reverse hierarchies in the visual system. *Neuron* **36**:791–804. DOI: [https://doi.org/10.1016/s0896-6273\(02\)01091-7](https://doi.org/10.1016/s0896-6273(02)01091-7)
- Holdefer RN, Jacobs BL. 1994. Phasic stimulation of the locus coeruleus: effects on activity in the lateral geniculate nucleus. *Experimental Brain Research* **100**:444–452. DOI: <https://doi.org/10.1007/BF02738404>
- Hubel DH, Wiesel TN. 1962. Receptive fields, binocular interaction and functional architecture in the cat's visual cortex. *The Journal of Physiology* **160**:106–154. DOI: <https://doi.org/10.1113/jphysiol.1962.sp006837>, PMID: [14449617](https://pubmed.ncbi.nlm.nih.gov/14449617/)
- Jahnsen H, Llinás R. 1984. Voltage-dependent burst-to-tonic switching of thalamic cell activity: an in vitro study. *Archives Italiennes de Biologie* **122**:73–82.
- Jones HE, Andolina IM, Ahmed B, Shipp SD, Clements JTC, Grieve KL, Cudeiro J, Salt TE, Sillito AM. 2012. Differential feedback modulation of center and surround mechanisms in parvocellular cells in the visual thalamus. *The Journal of Neuroscience* **32**:15946–15951. DOI: <https://doi.org/10.1523/JNEUROSCI.0831-12.2012>
- Kara P, Reinagel P, Reid RC. 2000. Low response variability in simultaneously recorded retinal, thalamic, and cortical neurons. *Neuron* **27**:635–646. DOI: [https://doi.org/10.1016/s0896-6273\(00\)00072-6](https://doi.org/10.1016/s0896-6273(00)00072-6)
- Keller AJ, Roth MM, Scanziani M. 2020. Feedback generates a second receptive field in neurons of the visual cortex. *Nature* **582**:545–549. DOI: <https://doi.org/10.1038/s41586-020-2319-4>
- Kim J, Matney CJ, Blankenship A, Hestrin S, Brown SP. 2014. Layer 6 corticothalamic neurons activate a cortical output layer, layer 5a. *The Journal of Neuroscience* **34**:9656–9664. DOI: <https://doi.org/10.1523/JNEUROSCI.1325-14.2014>
- King JL, Lowe MP, Stover KR, Wong AA, Crowder NA. 2016. Adaptive Processes in Thalamus and Cortex Revealed by Silencing of Primary Visual Cortex during Contrast Adaptation. *Current Biology* **26**:1295–1300. DOI: <https://doi.org/10.1016/j.cub.2016.03.018>
- Kuznetsova A, Brockhoff PB, Christensen RHB. 2017. lmerTest Package: Tests in Linear Mixed Effects Models. *Journal of Statistical Software* **82**:13. DOI: <https://doi.org/10.18637/jss.v082.i13>
- Lamme VAF, Roelfsema PR. 2000. The distinct modes of vision offered by feedforward and recurrent processing. *Trends in Neurosciences* **23**:571–579. DOI: [https://doi.org/10.1016/s0166-2236\(00\)01657-x](https://doi.org/10.1016/s0166-2236(00)01657-x)
- Larkum M. 2013. A cellular mechanism for cortical associations: an organizing principle for the cerebral cortex. *Trends in Neurosciences* **36**:141–151. DOI: <https://doi.org/10.1016/j.tins.2012.11.006>
- Lee TS, Mumford D. 2003. Hierarchical Bayesian inference in the visual cortex. *Journal of the Optical Society of America. A, Optics, Image Science, and Vision* **20**:1434–1448. DOI: <https://doi.org/10.1364/josaa.20.001434>
- Lee SH, Dan Y. 2012. Neuromodulation of brain states. *Neuron* **76**:209–222. DOI: <https://doi.org/10.1016/j.neuron.2012.09.012>, PMID: [23040816](https://pubmed.ncbi.nlm.nih.gov/23040816/)
- Lesica NA, Stanley GB. 2004. Encoding of natural scene movies by tonic and burst spikes in the lateral geniculate nucleus. *The Journal of Neuroscience* **24**:10731–10740. DOI: <https://doi.org/10.1523/JNEUROSCI.3059-04.2004>
- Lesica NA, Weng C, Jin J, Yeh CI, Alonso JM, Stanley GB. 2006. Dynamic encoding of natural luminance sequences by LGN bursts. *PLOS Biology* **4**:7. DOI: <https://doi.org/10.1371/journal.pbio.0040209>
- Lesica NA, Jin J, Weng C, Yeh CI, Butts DA, Stanley GB, Alonso JM. 2007. Adaptation to stimulus contrast and correlations during natural visual stimulation. *Neuron* **55**:479–491. DOI: <https://doi.org/10.1016/j.neuron.2007.07.013>
- Li Y, Ibrahim LA, Liu B, Zhang LI, Tao HW. 2013. Linear transformation of thalamocortical input by intracortical excitation. *Nature Neuroscience* **16**:1324–1330. DOI: <https://doi.org/10.1038/nn.3494>
- Liang L, Fratzl A, Goldey G, Ramesh RN, Sugden AU, Morgan JL, Chen C, Andermann ML. 2018. A Fine-Scale Functional Logic to Convergence from Retina to Thalamus. *Cell* **173**:1343–1355. DOI: <https://doi.org/10.1016/j.cell.2018.04.041>
- Liang L, Fratzl A, Reggiani JDS, El Mansour O, Chen C, Andermann ML. 2020. Retinal Inputs to the Thalamus Are Selectively Gated by Arousal. *Current Biology* **30**:3923–3934. DOI: <https://doi.org/10.1016/j.cub.2020.07.065>

- Liang Y, Fan JL, Sun W, Lu R, Chen M, Ji N. 2021. A Distinct Population of L6 Neurons in Mouse V1 Mediate Cross-Callosal Communication. *Cerebral Cortex (New York, N.Y)* **31**:4259–4273. DOI: <https://doi.org/10.1093/cercor/bhab084>
- Lien AD, Scanziani M. 2013. Tuned thalamic excitation is amplified by visual cortical circuits. *Nature Neuroscience* **16**:1315–1323. DOI: <https://doi.org/10.1038/nn.3488>
- Lien AD, Scanziani M. 2018. Cortical direction selectivity emerges at convergence of thalamic synapses. *Nature* **558**:80–86. DOI: <https://doi.org/10.1038/s41586-018-0148-5>
- Lu SM, Guido W, Sherman SM. 1992. Effects of membrane voltage on receptive field properties of lateral geniculate neurons in the cat: contributions of the low-threshold Ca²⁺ conductance. *Journal of Neurophysiology* **68**:2185–2198. DOI: <https://doi.org/10.1152/jn.1992.68.6.2185>
- Lu SM, Guido W, Sherman SM. 1993. The brain-stem parabrachial region controls mode of response to visual stimulation of neurons in the cat's lateral geniculate nucleus. *Visual Neuroscience* **10**:631–642. DOI: <https://doi.org/10.1017/s0952523800005332>
- Luke SG. 2017. Evaluating significance in linear mixed-effects models in R. *Behavior Research Methods* **49**:1494–1502. DOI: <https://doi.org/10.3758/s13428-016-0809-y>
- Mahn M, Gibor L, Patil P, Cohen-Kashi Malina K, Oring S, Printz Y, Levy R, Lampl I, Yizhar O. 2018. High-efficiency optogenetic silencing with soma-targeted anion-conducting channelrhodopsins. *Nature Communications* **9**:4125. DOI: <https://doi.org/10.1038/s41467-018-06511-8>
- Makino H, Komiyama T. 2015. Learning enhances the relative impact of top-down processing in the visual cortex. *Nature Neuroscience* **18**:1116–1122. DOI: <https://doi.org/10.1038/nn.4061>
- Mante V, Frazor RA, Bonin V, Geisler WS, Carandini M. 2005. Independence of luminance and contrast in natural scenes and in the early visual system. *Nature Neuroscience* **8**:1690–1697. DOI: <https://doi.org/10.1038/nn1556>
- Marshall JH, Kaye AP, Nauhaus I, Callaway EM. 2012. Anterior-posterior direction opponency in the superficial mouse lateral geniculate nucleus. *Neuron* **76**:713–720. DOI: <https://doi.org/10.1016/j.neuron.2012.09.021>
- McClurkin JW, Marrocco RT. 1984. Visual cortical input alters spatial tuning in monkey lateral geniculate nucleus cells. *The Journal of Physiology* **348**:135–152. DOI: <https://doi.org/10.1113/jphysiol.1984.sp015103>
- McCormick DA. 1992. Neurotransmitter actions in the thalamus and cerebral cortex and their role in neuromodulation of thalamocortical activity. *Progress in Neurobiology* **39**:337–388. DOI: [https://doi.org/10.1016/0301-0082\(92\)90012-4](https://doi.org/10.1016/0301-0082(92)90012-4)
- Mease RA, Krieger P, Groh A. 2014. Cortical control of adaptation and sensory relay mode in the thalamus. *PNAS* **111**:6798–6803. DOI: <https://doi.org/10.1073/pnas.1318665111>
- Mease RA, Kuner T, Fairhall AL, Groh A. 2017. Multiplexed Spike Coding and Adaptation in the Thalamus. *Cell Reports* **19**:1130–1140. DOI: <https://doi.org/10.1016/j.celrep.2017.04.050>
- Mitzdorf U. 1985. Current source-density method and application in cat cerebral cortex: investigation of evoked potentials and EEG phenomena. *Physiological Reviews* **65**:37–100. DOI: <https://doi.org/10.1152/physrev.1985.65.1.37>
- Molnár B, Sere P, Bordé S, Koós K, Zsigri N, Horváth P, Lőrincz ML. 2021. Cell Type-Specific Arousal-Dependent Modulation of Thalamic Activity in the Lateral Geniculate Nucleus. *Cerebral Cortex Communications* **2**:tgab020. DOI: <https://doi.org/10.1093/texcom/tgab020>
- Morgan JL, Berger DR, Wetzel AW, Lichtman JW. 2016. The Fuzzy Logic of Network Connectivity in Mouse Visual Thalamus. *Cell* **165**:192–206. DOI: <https://doi.org/10.1016/j.cell.2016.02.033>
- Murata Y, Colonnese MT. 2018. Thalamus Controls Development and Expression of Arousal States in Visual Cortex. *The Journal of Neuroscience* **38**:8772–8786. DOI: <https://doi.org/10.1523/JNEUROSCI.1519-18.2018>
- Murphy PC, Sillito AM. 1987. Corticofugal feedback influences the generation of length tuning in the visual pathway. *Nature* **329**:727–729. DOI: <https://doi.org/10.1038/329727a0>
- Nestvogel DB, McCormick DA. 2022. Visual thalamocortical mechanisms of waking state-dependent activity and alpha oscillations. *Neuron* **110**:120–138. DOI: <https://doi.org/10.1016/j.neuron.2021.10.005>
- Niell CM, Stryker MP. 2008. Highly selective receptive fields in mouse visual cortex. *The Journal of Neuroscience* **28**:7520–7536. DOI: <https://doi.org/10.1523/JNEUROSCI.0623-08.2008>
- Niell CM, Stryker MP. 2010. Modulation of visual responses by behavioral state in mouse visual cortex. *Neuron* **65**:472–479. DOI: <https://doi.org/10.1016/j.neuron.2010.01.033>
- Oberlaender M, de Kock CPJ, Bruno RM, Ramirez A, Meyer HS, Dercksen VJ, Helmstaedter M, Sakmann B. 2012. Cell type-specific three-dimensional structure of thalamocortical circuits in a column of rat vibrissal cortex. *Cerebral Cortex (New York, N.Y)* **22**:2375–2391. DOI: <https://doi.org/10.1093/cercor/bhr317>
- Olsen SR, Bortone DS, Adesnik H, Scanziani M. 2012. Gain control by layer six in cortical circuits of vision. *Nature* **483**:47–52. DOI: <https://doi.org/10.1038/nature10835>
- Pachitariu M, Steinmetz NA, Kadir SN, Carandini M, Harris KD. 2016. Fast and accurate spike sorting of high-channel count probes with KiloSort. Lee DD, Sugiyama M, Luxburg UV, Guyon I, Garnett R (Eds). *In Advances in Neural Information Processing Systems* **29**. Curran Associates, Inc. p. 4448–4456.
- Pauzin FP, Krieger P. 2018. A Corticothalamic Circuit for Refining Tactile Encoding. *Cell Reports* **23**:1314–1325. DOI: <https://doi.org/10.1016/j.celrep.2018.03.128>
- Piscopo DM, El-Danaf RN, Huberman AD, Niell CM. 2013. Diverse visual features encoded in mouse lateral geniculate nucleus. *The Journal of Neuroscience* **33**:4642–4656. DOI: <https://doi.org/10.1523/JNEUROSCI.5187-12.2013>
- Poltoratski S, Maier A, Newton AT, Tong F. 2019. Figure-Ground Modulation in the Human Lateral Geniculate Nucleus Is Distinguishable from Top-Down Attention. *Current Biology* **29**:2051–2057. DOI: <https://doi.org/10.1016/j.cub.2019.04.068>

- Poynton CA. 1998. Human Vision and Electronic Imaging III. San Jose: Charles Poynton.
- Przybyszewski AW, Gaska JP, Foote W, Pollen DA. 2000. Striate cortex increases contrast gain of macaque LGN neurons. *Visual Neuroscience* **17**:485–494. DOI: <https://doi.org/10.1017/s0952523800174012>
- R Core Team. 2017. R: A Language and Environment for Statistical Computing, R Foundation for Statistical Computing. <https://www.R-project.org/>
- Radnikow G, Feldmeyer D. 2018. Layer- and Cell Type-Specific Modulation of Excitatory Neuronal Activity in the Neocortex. *Frontiers in Neuroanatomy* **12**:1. DOI: <https://doi.org/10.3389/fnana.2018.00001>
- Rao RPN, Ballard DH. 1999. Predictive coding in the visual cortex: A functional interpretation of some extra-classical receptive-field effects. *Nature Neuroscience* **2**:79–87. DOI: <https://doi.org/10.1038/4580>
- Reimer J, Froudarakis E, Cadwell CR, Yatsenko D, Denfield GH, Tolias AS. 2014. Pupil fluctuations track fast switching of cortical states during quiet wakefulness. *Neuron* **84**:355–362. DOI: <https://doi.org/10.1016/j.neuron.2014.09.033>
- Reinhold K, Resulaj A, Scanziani M. 2021. Brain State-Dependent Modulation of Thalamic Visual Processing by Cortico-Thalamic Feedback. [bioRxiv]. DOI: <https://doi.org/10.1101/2021.10.04.463017>
- Remtulla S, Hallett PE. 1985. A schematic eye for the mouse, and comparisons with the rat. *Vision Research* **25**:21–31. DOI: [https://doi.org/10.1016/0042-6989\(85\)90076-8](https://doi.org/10.1016/0042-6989(85)90076-8)
- Riesenhuber M, Poggio T. 1999. Hierarchical models of object recognition in cortex. *Nature Neuroscience* **2**:1019–1025. DOI: <https://doi.org/10.1038/14819>
- Riesenhuber M, Poggio T. 2000. Models of object recognition. *Nature Neuroscience* **3 Suppl**:1199–1204. DOI: <https://doi.org/10.1038/81479>
- Roelfsema PR, de Lange FP. 2016. Early Visual Cortex as a Multiscale Cognitive Blackboard. *Annual Review of Vision Science* **2**:131–151. DOI: <https://doi.org/10.1146/annurev-vision-111815-114443>, PMID: 28532363
- Román Rosón M, Bauer Y, Kotkat AH, Berens P, Euler T, Busse L. 2019. Mouse dLGN Receives Functional Input from a Diverse Population of Retinal Ganglion Cells with Limited Convergence. *Neuron* **102**:462–476. DOI: <https://doi.org/10.1016/j.neuron.2019.01.040>
- Rueden CT, Schindelin J, Hiner MC, DeZonia BE, Walter AE, Arena ET, Eliceiri KW. 2017. ImageJ2: ImageJ for the next generation of scientific image data. *BMC Bioinformatics* **18**:1. DOI: <https://doi.org/10.1186/s12859-017-1934-z>
- Sakatani T, Isa T. 2007. Quantitative analysis of spontaneous saccade-like rapid eye movements in C57BL/6 mice. *Neuroscience Research* **58**:324–331. DOI: <https://doi.org/10.1016/j.neures.2007.04.003>
- Schindelin J, Arganda-Carreras I, Frise E, Kaynig V, Longair M, Pietzsch T, Preibisch S, Rueden C, Saalfeld S, Schmid B, Tinevez JY, White DJ, Hartenstein V, Eliceiri K, Tomancak P, Cardona A. 2012. Fiji: an open-source platform for biological-image analysis. *Nature Methods* **9**:676–682. DOI: <https://doi.org/10.1038/nmeth.2019>
- Scholl B, Tan AYY, Corey J, Priebe NJ. 2013. Emergence of orientation selectivity in the Mammalian visual pathway. *The Journal of Neuroscience* **33**:10616–10624. DOI: <https://doi.org/10.1523/JNEUROSCI.0404-13.2013>
- Schröder S, Steinmetz NA, Krumin M, Pachitariu M, Rizzi M, Lagnado L, Harris KD, Carandini M. 2020. Arousal Modulates Retinal Output. *Neuron* **107**:487–495. DOI: <https://doi.org/10.1016/j.neuron.2020.04.026>
- Sherman SM, Koch C. 1986. The control of retinogeniculate transmission in the mammalian lateral geniculate nucleus. *Experimental Brain Research* **63**:1–20. DOI: <https://doi.org/10.1007/BF00235642>
- Sherman SM, Guillery RW. 1998. On the actions that one nerve cell can have on another: distinguishing “drivers” from “modulators.” *PNAS* **95**:7121–7126. DOI: <https://doi.org/10.1073/pnas.95.12.7121>
- Sherman SM. 2001. Tonic and burst firing: dual modes of thalamocortical relay. *Trends in Neurosciences* **24**:122–126. DOI: [https://doi.org/10.1016/s0166-2236\(00\)01714-8](https://doi.org/10.1016/s0166-2236(00)01714-8)
- Sherman SM, Guillery RW. 2002. The role of the thalamus in the flow of information to the cortex. *Philosophical Transactions of the Royal Society of London. Series B, Biological Sciences* **357**:1695–1708. DOI: <https://doi.org/10.1098/rstb.2002.1161>
- Sherman SM. 2016. Thalamus plays a central role in ongoing cortical functioning. *Nature Neuroscience* **19**:533–541. DOI: <https://doi.org/10.1038/nn.4269>
- Shu Y, Hasenstaub A, Badoual M, Bal T, McCormick DA. 2003. Barrages of synaptic activity control the gain and sensitivity of cortical neurons. *The Journal of Neuroscience* **23**:10388–10401.
- Sillito AM, Kemp JA, Berardi N. 1983. The cholinergic influence on the function of the cat dorsal lateral geniculate nucleus (dLGN). *Brain Research* **280**:299–307. DOI: [https://doi.org/10.1016/0006-8993\(83\)90059-8](https://doi.org/10.1016/0006-8993(83)90059-8)
- Sillito AM, Cudeiro J, Murphy PC. 1993. Orientation sensitive elements in the corticofugal influence on centre-surround interactions in the dorsal lateral geniculate nucleus. *Experimental Brain Research* **93**:6–16. DOI: <https://doi.org/10.1007/BF00227775>
- Sillito AM, Jones HE. 2002. Corticothalamic interactions in the transfer of visual information. *PNAS* **357**:1739–1752. DOI: <https://doi.org/10.1098/rstb.2002.1170>
- Skottun BC, De Valois RL, Grosf DH, Movshon JA, Albrecht DG, Bonds AB. 1991. Classifying simple and complex cells on the basis of response modulation. *Vision Research* **31**:1079–1086. DOI: [https://doi.org/10.1016/0042-6989\(91\)90033-2](https://doi.org/10.1016/0042-6989(91)90033-2)
- Spacek MA, Blanche TJ, Swindale NV. 2009. Python for large-scale electrophysiology. *Frontiers in Neuroinformatics* **2**:2008. DOI: <https://doi.org/10.3389/neuro.11.009.2008>
- Squire RF, Noudoost B, Schafer RJ, Moore T. 2013. Prefrontal contributions to visual selective attention. *Annual Review of Neuroscience* **36**:451–466. DOI: <https://doi.org/10.1146/annurev-neuro-062111-150439>

- Stoelzel CR**, Bereshpolova Y, Alonso JM, Swadlow HA. 2017. Axonal Conduction Delays, Brain State, and Corticogeniculate Communication. *The Journal of Neuroscience* **37**:6342–6358. DOI: <https://doi.org/10.1523/JNEUROSCI.0444-17.2017>
- Sundberg SC**, Lindström SH, Sanchez GM, Granseth B. 2018. Cre-expressing neurons in visual cortex of Ntsr1-Cre GN220 mice are corticothalamic and are depolarized by acetylcholine. *The Journal of Comparative Neurology* **526**:120–132. DOI: <https://doi.org/10.1002/cne.24323>
- Swadlow HA**, Weyand TG. 1987. Corticogeniculate neurons, corticotectal neurons, and suspected interneurons in visual cortex of awake rabbits: receptive-field properties, axonal properties, and effects of EEG arousal. *Journal of Neurophysiology* **57**:977–1001. DOI: <https://doi.org/10.1152/jn.1987.57.4.977>
- Swadlow HA**. 1989. Efferent neurons and suspected interneurons in S-1 vibrissa cortex of the awake rabbit: receptive fields and axonal properties. *Journal of Neurophysiology* **62**:288–308. DOI: <https://doi.org/10.1152/jn.1989.62.1.288>
- Swadlow HA**, Gusev AG. 2001. The impact of “bursting” thalamic impulses at a neocortical synapse. *Nature Neuroscience* **4**:402–408. DOI: <https://doi.org/10.1038/86054>
- Swindale NV**, Spacek MA. 2014. Spike sorting for polytrodes: a divide and conquer approach. *Frontiers in Systems Neuroscience* **8**:6. DOI: <https://doi.org/10.3389/fnsys.2014.00006>
- Takahashi N**, Oertner TG, Hegemann P, Larkum ME. 2016. Active cortical dendrites modulate perception. *Science (New York, N.Y.)* **354**:1587–1590. DOI: <https://doi.org/10.1126/science.aah6066>
- Tasic B**, Menon V, Nguyen TN, Kim TK, Jarsky T, Yao Z, Levi B, Gray LT, Sorensen SA, Dolbeare T, Bertagnolli D, Goldy J, Shapovalova N, Parry S, Lee C, Smith K, Bernard A, Madisen L, Sunkin SM, Hawrylycz M, et al. 2016. Adult mouse cortical cell taxonomy revealed by single cell transcriptomics. *Nature Neuroscience* **19**:335–346. DOI: <https://doi.org/10.1038/nn.4216>
- Usrey WM**, Sherman SM. 2019. Corticofugal circuits: Communication lines from the cortex to the rest of the brain. *The Journal of Comparative Neurology* **527**:640–650. DOI: <https://doi.org/10.1002/cne.24423>
- van der Togt C**, Spekrijse H, Supér H. 2005. Neural responses in cat visual cortex reflect state changes in correlated activity. *The European Journal of Neuroscience* **22**:465–475. DOI: <https://doi.org/10.1111/j.1460-9568.2005.04237.x>
- Vélez-Fort M**, Rousseau CV, Niedworok CJ, Wickersham IR, Rancz EA, Brown APY, Strom M, Margrie TW. 2014. The stimulus selectivity and connectivity of layer six principal cells reveals cortical microcircuits underlying visual processing. *Neuron* **83**:1431–1443. DOI: <https://doi.org/10.1016/j.neuron.2014.08.001>
- Vinck M**, Batista-Brito R, Knoblich U, Cardin JA. 2015. Arousal and locomotion make distinct contributions to cortical activity patterns and visual encoding. *Neuron* **86**:740–754. DOI: <https://doi.org/10.1016/j.neuron.2015.03.028>
- Vinje WE**, Gallant JL. 2000. Sparse coding and decorrelation in primary visual cortex during natural vision. *Science (New York, N.Y.)* **287**:1273–1276. DOI: <https://doi.org/10.1126/science.287.5456.1273>
- Wang W**, Jones HE, Andolina IM, Salt TE, Sillito AM. 2006. Functional alignment of feedback effects from visual cortex to thalamus. *Nature Neuroscience* **9**:1330–1336. DOI: <https://doi.org/10.1038/nn1768>
- Wang X**, Wei Y, Vaingankar V, Wang Q, Koepsell K, Sommer FT, Hirsch JA. 2007. Feedforward excitation and inhibition evoke dual modes of firing in the cat’s visual thalamus during naturalistic viewing. *Neuron* **55**:465–478. DOI: <https://doi.org/10.1016/j.neuron.2007.06.039>
- Wang W**, Andolina IM, Lu Y, Jones HE, Sillito AM. 2018. Focal Gain Control of Thalamic Visual Receptive Fields by Layer 6 Corticothalamic Feedback. *Cerebral Cortex (New York, N.Y.)* **28**:267–280. DOI: <https://doi.org/10.1093/cercor/bhw376>
- Webb BS**, Tinsley CJ, Barraclough NE, Easton A, Parker A, Derrington AM. 2002. Feedback from V1 and inhibition from beyond the classical receptive field modulates the responses of neurons in the primate lateral geniculate nucleus. *Visual Neuroscience* **19**:583–592. DOI: <https://doi.org/10.1017/s0952523802195046>
- Whitmire CJ**, Waiblinger C, Schwarz C, Stanley GB. 2016. Information Coding through Adaptive Gating of Synchronized Thalamic Bursting. *Cell Reports* **14**:795–807. DOI: <https://doi.org/10.1016/j.celrep.2015.12.068>
- Wiegert JS**, Mahn M, Prigge M, Printz Y, Yizhar O. 2017. Silencing Neurons: Tools, Applications, and Experimental Constraints. *Neuron* **95**:504–529. DOI: <https://doi.org/10.1016/j.neuron.2017.06.050>
- Williamson RS**, Hancock KE, Shinn-Cunningham BG, Polley DB. 2015. Locomotion and Task Demands Differentially Modulate Thalamic Audiovisual Processing during Active Search. *Current Biology* **25**:1885–1891. DOI: <https://doi.org/10.1016/j.cub.2015.05.045>
- Wolfart J**, Debay D, Le Masson G, Destexhe A, Bal T. 2005. Synaptic background activity controls spike transfer from thalamus to cortex. *Nature Neuroscience* **8**:1760–1767. DOI: <https://doi.org/10.1038/nn1591>
- Wörgötter F**, Eyding D, Macklis JD, Funke K. 2002. The influence of the corticothalamic projection on responses in thalamus and cortex. *Philosophical Transactions of the Royal Society of London. Series B, Biological Sciences* **357**:1823–1834. DOI: <https://doi.org/10.1098/rstb.2002.1159>
- Yatsenko D**, Walker EY, Tolia AS. 2018. DataJoint: A Simpler Relational Data Model. [arXiv]. DOI: <https://doi.org/10.48550/arXiv.1807.11104>
- Zagha E**, McCormick DA. 2014. Neural control of brain state. *Current Opinion in Neurobiology* **29**:178–186. DOI: <https://doi.org/10.1016/j.conb.2014.09.010>, PMID: 25310628
- Zhao X**, Chen H, Liu X, Cang J. 2013. Orientation-selective responses in the mouse lateral geniculate nucleus. *The Journal of Neuroscience* **33**:12751–12763. DOI: <https://doi.org/10.1523/JNEUROSCI.0095-13.2013>
- Zhuang J**, Larsen RS, Takasaki KT, Ouellette ND, Daigle TL, Tasic BT, Waters J, Zeng H, Reid RC. 2019. The Spatial Structure of Feedforward Information in Mouse Primary Visual Cortex. [BBioRxiv]. DOI: <https://doi.org/10.1101/2019.12.24.888156>

3 On the temporal structure of modulation in the mouse dLGN

The following chapter is reproduced from an article originally published in *PLOS Biology*:

Davide Crombie, Martin A Spacek, Christian Leibold, Laura Busse (2024). Spiking activity in the visual thalamus is coupled to pupil dynamics across temporal scales. *PLOS Biology*, *Plos Biology*, 22(5), e3002614. DOI: <https://doi.org/10.1371/journal.pbio.3002614>.

Author contributions

The study was conceptualized by DC, CL and LB. MAS performed the experiments. The data was curated by DC and MAS. The methodology was developed by DC, CL, and LB. The formal analysis was performed by DC. DC and MAS contributed to developing the software infrastructure supporting the investigation. Data visualization was performed by DC. DC, CL, and LB wrote the original draft. DC, CL, and LB contributed to reviewing and editing the manuscript. CL and LB were responsible for project administration and supervision. Funding for the project was acquired by CD, CL, and LB.

Personal contributions

The code for all analyses and data visualizations was written by DC. DC also contributed substantially to developing the software infrastructure supporting the investigation. Furthermore, DC regularly made decisions regarding methodology, wrote the majority of the methods and results sections, collaborated with the co-authors in producing the introduction and discussions sections, as well as the editing and review process. The funding for the first year of the project was acquired by DC with the supervision of LB and CL through the “SmartStart2” fellowship program administered by the Bernstein Center for Computational Neuroscience.

Copyright

This article was published under the CC-BY 4.0 International licence.

RESEARCH ARTICLE

Spiking activity in the visual thalamus is coupled to pupil dynamics across temporal scales

Davide Crombie^{1,2}, Martin A. Spacek¹, Christian Leibold^{1,3†*}, Laura Busse^{1,4†*}

1 Division of Neuroscience, Faculty of Biology, LMU Munich, Munich, Germany, **2** Graduate School of Systemic Neurosciences, LMU Munich, Munich, Germany, **3** Fakultät für Biologie & Bernstein Center Freiburg, Albert-Ludwigs-Universität Freiburg, Freiburg im Breisgau, Germany, **4** Bernstein Center for Computational Neuroscience, Munich, Germany

† These authors share senior authorship to this work.

* christian.leibold@biologie.uni-freiburg.de (CL); busse@bio.lmu.de (LB)



Abstract

The processing of sensory information, even at early stages, is influenced by the internal state of the animal. Internal states, such as arousal, are often characterized by relating neural activity to a single “level” of arousal, defined by a behavioral indicator such as pupil size. In this study, we expand the understanding of arousal-related modulations in sensory systems by uncovering multiple timescales of pupil dynamics and their relationship to neural activity. Specifically, we observed a robust coupling between spiking activity in the mouse dorsolateral geniculate nucleus (dLGN) of the thalamus and pupil dynamics across timescales spanning a few seconds to several minutes. Throughout all these timescales, 2 distinct spiking modes—individual tonic spikes and tightly clustered bursts of spikes—preferred opposite phases of pupil dynamics. This multi-scale coupling reveals modulations distinct from those captured by pupil size per se, locomotion, and eye movements. Furthermore, coupling persisted even during viewing of a naturalistic movie, where it contributed to differences in the encoding of visual information. We conclude that dLGN spiking activity is under the simultaneous influence of multiple arousal-related processes associated with pupil dynamics occurring over a broad range of timescales.

OPEN ACCESS

Citation: Crombie D, Spacek MA, Leibold C, Busse L (2024) Spiking activity in the visual thalamus is coupled to pupil dynamics across temporal scales. *PLoS Biol* 22(5): e3002614. <https://doi.org/10.1371/journal.pbio.3002614>

Academic Editor: Jonathan Demb, Yale University, UNITED STATES

Received: July 14, 2023

Accepted: April 5, 2024

Published: May 14, 2024

Peer Review History: PLOS recognizes the benefits of transparency in the peer review process; therefore, we enable the publication of all of the content of peer review and author responses alongside final, published articles. The editorial history of this article is available here: <https://doi.org/10.1371/journal.pbio.3002614>

Copyright: © 2024 Crombie et al. This is an open access article distributed under the terms of the [Creative Commons Attribution License](https://creativecommons.org/licenses/by/4.0/), which permits unrestricted use, distribution, and reproduction in any medium, provided the original author and source are credited.

Data Availability Statement: The data and code required to generate the results and figures presented in this manuscript are available at <https://doi.org/10.12751/g-node.ls6w8h>.

Introduction

Information processing, even at the earliest sensory stages, can be modulated by several influences. One prominent influence is that of arousal-related behavioral states, which have been shown to change neural activity throughout the brain [1–4]. One classic indicator for arousal is pupil size, a metric that is relatively simple to measure and analyze and that has provided fundamental insights into neuromodulatory and cognitive influences on brain activity [2–8]. However, a multitude of factors converge to affect the pupil size signal, and how they are combined into this single indicator of arousal is not known. Likewise, how the various influences on the pupil signal relate to spontaneous and stimulus driven neural activity is not well understood.

Funding: This research was supported by the German Research Foundation (DFG) RTG2175 “Perception in context and its neural basis” (CL); DFG SFB 870 “Assembly and function of neural circuits”, TP 19 (118803580) (LB); DFG SFB 1233 “Robust Vision: Inference Principles and Neural Mechanisms”, TP 13 (276693517) (LB); ONE Munich Strategy Forum grant (LMU Munich, TU Munich and the Bavarian Ministry for Science and Art) (LB) and by the SmartStart program of the Bernstein Network for Computational Neuroscience funded by the Volkswagen Foundation (DC). None of the sponsors or funders had any role in the study design, data collection and analysis, decision to publish, or preparation of the manuscript.

Competing interests: The authors have declared that no competing interests exist.

Abbreviations: BF, basal forebrain; CPD, components of pupil dynamic; dLGN, dorsal lateral geniculate nucleus; EMD, empirical mode decomposition; LC, locus coeruleus; LCD, liquid crystal display; SVC, support-vector classifier; RVR, response variability ratio.

An ideal system to investigate arousal-related modulations of neural activity and sensory processing is the visual thalamus. The thalamic dorsal lateral geniculate nucleus (dLGN) is the primary relay of visual signals from the retina to the visual cortex, and dLGN neurons, like those in other thalamic nuclei, have long been known to display prominent patterns of activity associated with arousal [9–12]. In particular, 2 state-related firing modes have been described: burst firing, which is more prevalent during low-arousal states [9] and behavioral inactivity [12,13], and tonic firing, which is observed during alertness. Burst firing in the thalamus is characterized by a high frequency discharge of action potentials after sustained hyperpolarization, and it relies on the activation of low-threshold, transient (T-type) calcium channels (reviewed in [14]). In contrast, tonic firing occurs when the membrane potential is relatively depolarized, and T-type calcium channels are inactivated [14]. Since thalamorecipient circuits in primary sensory cortices are highly sensitive to the temporal coordination of inputs [15–17], the presence of bursts and tonic firing can have different effects on postsynaptic cortical neurons [18]. This has led to the hypothesis that thalamic nuclei use burst and tonic firing modes to gate or alter the flow of information to and between cortical areas according to the arousal state of the animal [14].

While previous studies have often relied on a single variable to define the state of the animal, several lines of evidence suggest that arousal-related modulations of neuronal activity cannot be adequately characterized by assigning mutually exclusive states to experimental epochs. For example, studies simultaneously measuring locomotion and pupil-linked arousal have revealed distinct effects of each in the visual cortex [6,8]. More generally, a substantial fraction of shared variability in visual cortex activity can be explained by high-dimensional sets of behaviors [19], suggesting that the state of sensory systems at any given moment results from a combination of multiple processes [3]. One potential factor that may distinguish these processes is the timescale over which they extend. For example, single arousal-related neuromodulators can have an impact across several timescales [20–23], and multiple neuromodulatory systems can influence neural activity over broadly different timescales [24].

To move beyond relating neural modulations to mutually exclusive states of arousal, we characterized modulations of spiking activity in the dLGN with respect to pupil size dynamics, taking into account that arousal-related processes occur across a wide range of temporal scales. We discovered that both tonic and burst spiking in the dLGN were coupled to fluctuations in pupil size over timescales ranging from seconds to minutes. Across these timescales, tonic spikes preferred opposite phases of the pupil signal compared to bursts. These multi-scale pupil dynamics captured modulations of dLGN activity beyond those explained by the pupil size per se and could occur in the absence of changes in locomotion state or saccadic eye movements. Furthermore, these modulations were also prevalent during presentation of naturalistic movies, despite the presence of rich stimulus-driven neural activity. Finally, we found that opposing phases of pupil dynamics across all timescales were associated with differences in the encoding of naturalistic movies by the dLGN, indicating that pupil-linked neural activity modulations across various timescales contribute to state-dependent differences in the flow of sensory information to the cortex. Our findings support the notion that arousal-related modulation, rather than being a singular process, likely involves an interplay of changes occurring over diverse timescales.

Results

To assess how dLGN spiking activity is influenced by internal state, we paired extracellular silicon probe recordings with video-based analysis of pupil size. During these recordings, mice were head-fixed, but free to run on an air-cushioned styrofoam ball while viewing a static gray

screen or a sparse noise stimulus (Fig 1A). We measured pupil size and locomotion speed as indicators of the internal and behavioral states of the animal. Throughout these recordings under largely isoluminant conditions, pupil size, a marker for internal states such as arousal, was in continuous fluctuation (see example in Fig 1B, black trace and S1A₁ Fig, gray and pink; $N = 15$ recording sessions in 10 mice). Similarly, active and quiescent behavioral states, as measured by locomotion (Fig 1B, green trace), were observed in all experiments. The proportion of time spent in locomotion varied across recordings, ranging from 0.11 to 0.47 (median = 0.27; S1B₁ Fig). Consistent with previous studies [8,12,25], bouts of locomotion were often accompanied by increases in pupil size (S1B₄ Fig). However, we also noticed that the fluctuations in pupil size were generally similar between active and quiescent behavioral states (S1B₅ Fig). In accordance with previous results [6,7], this suggests that diverse internal states may coexist within a behavioral state.

We observed that fluctuations in pupil size during both locomotion and quiescence were accompanied by changes in the spiking activity of dLGN neurons. For example, the neuron shown in Fig 1B generally increased its firing rate when the pupil was large. To characterize the relationship between pupil size and firing rates, we binned the spiking activity of individual dLGN neurons in 250 ms windows and examined mean spike counts across pupil sizes. We observed that the relationship between pupil size and dLGN firing rate varied between neurons, and was often non-monotonic (Fig 1C₁), reminiscent of previous observations in cortex [7]. Indeed, among the 89.7% of recorded dLGN neurons showing significant modulation across pupil sizes (140/156 neurons; one-way ANOVA, $p \leq 0.05$), the majority (78/140) had their peak firing rate outside the top decile of pupil size. Indeed, peak firing rates were observed across the entire range of pupil sizes (Fig 1C₁). Similarly, bursts of spikes (see Fig 2A) were also linked to pupil size in most dLGN neurons (Fig 1C₂; 93/145), but, unlike overall firing rates, burst rates tended to be highest at the smallest pupil sizes (72/93; only 21/93 had non-monotonic modulation profiles). To assess the degree to which the relationship between pupil size and spiking activity originated from changes in retinal illumination, we repeated these analyses for experiments conducted in darkness. We found that even in darkness, firing rates and bursting were modulated across pupil sizes in the majority of dLGN neurons (firing rate: 89/94 neurons; burst rate: 44/83 neurons), with many neurons showing high firing rates when the pupil was large (S1C₁ Fig) and bursting when the pupil was small (S1C₂ Fig), suggesting that under these stimulus conditions the overall relationship between pupil size and spiking activity originates from nonvisual factors. We therefore conclude that firing rates and bursting depend on pupil size in the majority of dLGN neurons.

Returning to Fig 1B, beyond the relationship to pupil size per se, we also found instances where firing rate increases were coupled to dilating phases of the pupil dynamics (Fig 1B, marked by 1). These dilation-related firing rate changes could occur while the pupil was relatively constricted (Fig 1B, marked by 2) or dilated (Fig 1B, marked by 3). Indeed, even in darkness, for a given pupil size the firing rate variability was often larger than the mean (median Fano factor = 1.4; $W = 4.4 \times 10^3$, $p = 6.4 \times 10^{-16}$, $N = 94$ neurons; S1C₃ Fig), suggesting the presence of additional modulatory processes not captured by pupil size. We thus sought to develop a framework that could capture this breadth of modulations in dLGN spiking activity by focusing on the multi-scale dynamics of pupil size.

To gain a better understanding of these modulations of dLGN firing rates, we explored the multi-scale dynamics of the pupil signal, aiming to extract information about changes in internal state beyond the size of the pupil per se. Indeed, previous studies dating to the beginning of pupillometry have suggested that pupil dynamics can be a relevant indicator of arousal [26–28]. The relationship between pupil dynamics and internal states has also been explored in mouse visual cortex [6], where associations between neuromodulatory signaling and pupil

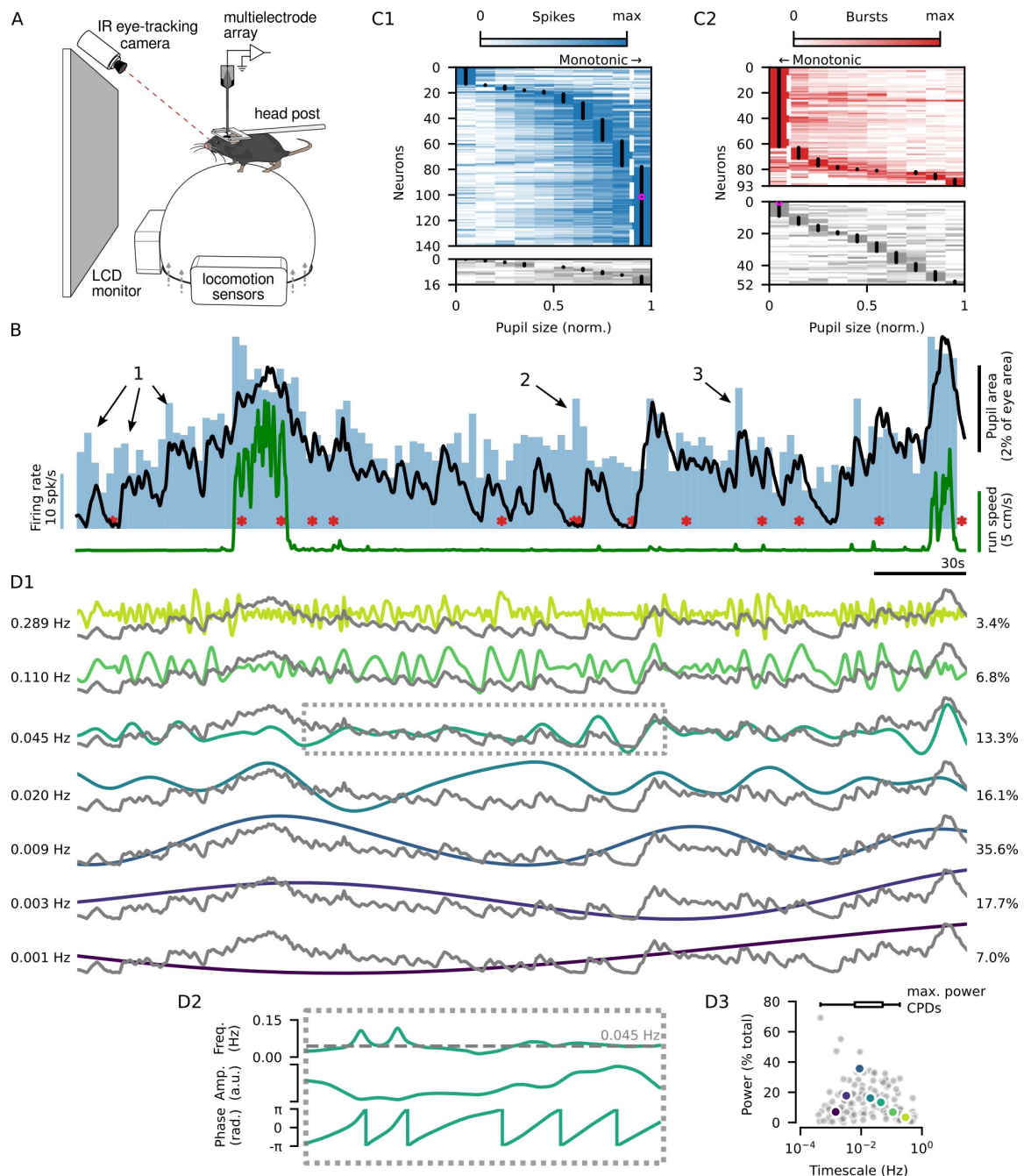


Fig 1. Extracellular recordings from the dLGN reveal diverse arousal-related modulations of firing rate. (A) Schematic of the experimental setup. (B) Pupil size (black) and locomotion speed (green) overlaid on the firing rate (blue, binned in 2.5 s windows) and spike bursts (red asterisks) from an example dLGN neuron. (C1) Spike counts (min-max normalized) across pupil sizes (min-max normalized) for 140/156 dLGN neurons with significant modulation (top, one-way ANOVA $p \leq 0.05$ across 10 pupil size bins) and 16/156 dLGN neurons without significant modulation (bottom). Neurons were sorted by the pupil size with the highest spike count (black dots). The example neuron from (B) is shown in magenta. The dashed white line indicates the 90th percentile of pupil size. (C2) Same as (C1) but for bursts of spikes. Neurons were sorted by the pupil size with the highest burst count. The dashed white line indicates the 10th percentile of pupil size. (D) The pupil size trace in (B) (gray traces) separated into CPDs (colored traces) occurring over different timescales. The components are described by their characteristic timescale (D1, left) and power (% total, D1, right), as illustrated for the trace indicated by the dashed box in (D2). (D2) Top: The characteristic timescale (gray dashed line) is computed as the amplitude-weighted mean of the component's instantaneous frequency. Middle: The component's power is defined as fraction of total power density, computed from the squared amplitudes of all CPDs derived from the

same pupil signal. Bottom: The phase of the CPD describes if the pupil is undergoing dilation ($-\pi$ to 0) or constriction (0 to π) at the timescale defined by the component. (D3) Gray dots: The characteristic timescale of each CPD plotted against its power for CPDs extracted from all recordings ($N = 14$). Colored dots: Components from the example recording in (B, D). The inset box plot (top) shows the range and IQR of the components with the maximum power from each recording. CPD, components of pupil dynamics; dLGN, dorsal lateral geniculate nucleus.

<https://doi.org/10.1371/journal.pbio.3002614.g001>

dynamics were reported [24]. Building on these studies (see also [7]), we observed that pupil size dynamics could be described over a variety of temporal scales: from minutes-long changes to cycles of dilation and constriction lasting 10s of seconds, to quicker changes on the order of seconds. We therefore employed a data-driven approach, called empirical mode decomposition (EMD, see [Materials and methods](#); [29]), to split the pupil signal without prior assumptions into components capturing its underlying dynamics (Fig 1D). Each component of pupil dynamics (henceforth, CPD) is described by its characteristic timescale (Fig 1D₁, left) and its relative power (Fig 1D₁, right). The characteristic timescale describes the average period of the pupil dilation-contraction cycles captured by the component (Fig 1D₂; see [Materials and methods](#)). The extracted CPDs spanned several orders of magnitude in their characteristic timescale, capturing dilation-contraction cycles lasting from several minutes ($10^{-3} = 0.001$ Hz) to just a second ($10^0 = 1$ Hz). Components with high power were found across this entire range, underscoring the multi-component nature of pupil size dynamics (Fig 1D₃). Additionally, the broad distribution of the CPD timescale with the highest power from each recording (Fig 1D₃, top) illustrates the diversity of pupil dynamics across recording sessions. Importantly, the set of CPDs extracted from a single pupil recording progress through dilation-contraction cycles largely independently from each other (S1D Fig; see [Materials and methods](#)), indicating that CPDs capture distinct aspects of pupil size dynamics.

Having captured pupil dynamics at multiple timescales, we went on to characterize their relationship to arousal-related dLGN activity. We separated the spiking activity from each dLGN neuron into tonic spiking and bursting (Fig 2A; bursts were defined as ≥ 2 spikes with ≤ 4 ms ISI preceded by ≥ 100 ms without spikes [30]). Consistent with previous findings in awake animals, we found that bursts were relatively rare, accounting for only 3% of spikes on average (median burst ratio for the 93% of neurons with bursting; S2A₂ Fig). Despite their small contribution to the total spike count (S2A₁ Fig), bursts provide an extracellular marker for the membrane potential status of thalamic neurons (indicating prolonged hyperpolarization) and play a role in determining rhythmic cortical states ([13]; see also S2B and S2C Fig). After separating burst and tonic spikes, we performed a phase coupling analysis for each neuron and simultaneously recorded CPD, collecting the phase of the CPD at the time of tonic spikes or bursts—considering all spikes in the burst as one single event (Fig 2B and 2C). The preferred phase of each spike type indicates whether they mainly occur during pupil dilation ($-\pi$ to 0) or constriction (0 to π) as captured by the CPD. Meanwhile, the coupling strength indicates the degree to which spikes and bursts adhere to the preferred phase and was computed with a bias-corrected metric that allows comparison between neurons with different rates of tonic spiking and bursting (see [Materials and methods](#); S2A Fig). The statistical significance of the coupling was assessed using a permutation test that accounts for short-timescale spiking patterns that typically inflate coupling strength metrics (see [Materials and methods](#); S2B Fig).

We found that both tonic spiking and bursts in dLGN neurons were coupled to the extracted components of pupil dynamics (CPDs) across a wide range of timescales (Fig 2C). Significant coupling of to at least 1 component of pupil dynamics was measured in 98.1% of dLGN neurons (153/156) for tonic spiking and 87.3% (110/126) for bursting. Examining the phase coupling for all neurons and simultaneously recorded CPDs (Fig 2C), we found that this

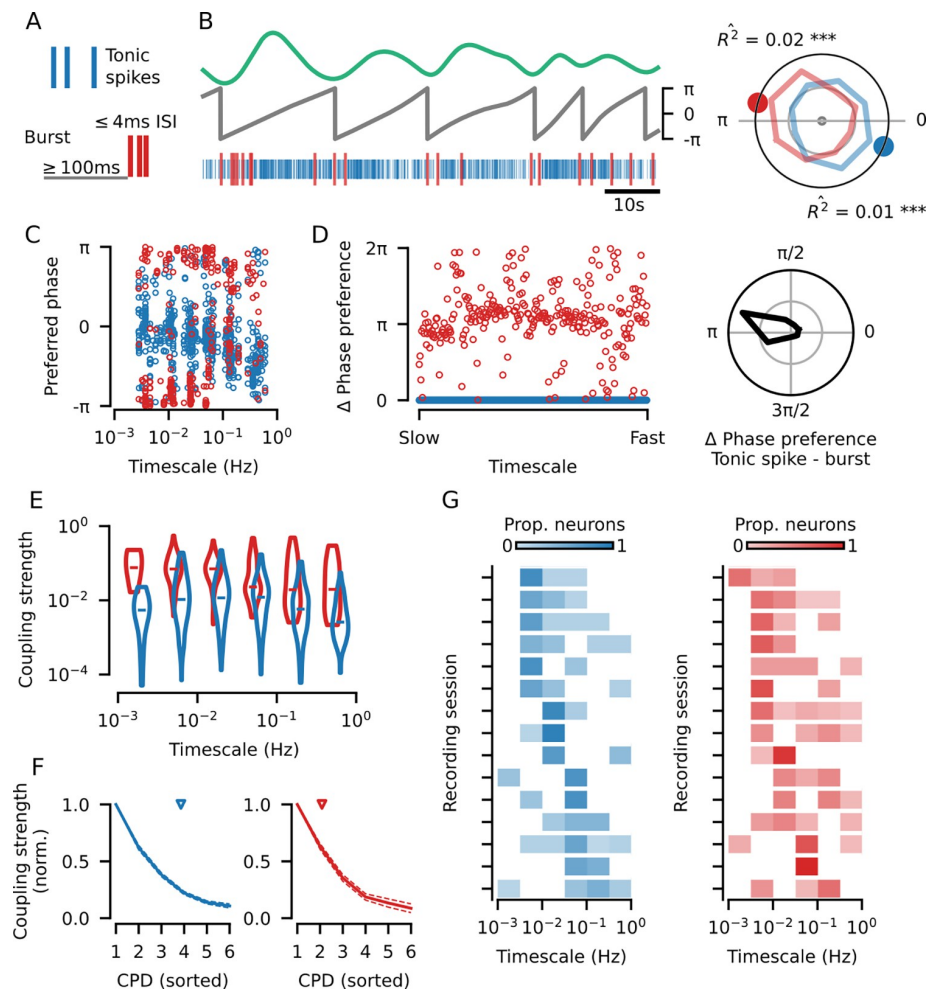


Fig 2. Tonic spikes and bursts in the dLGN are coupled to pupil dynamics across multiple timescales. (A) Bursts (red) were defined as ≥ 2 spikes occurring after > 100 ms of silence and with an inter-spoke interval less than 4 ms [30]; all remaining spikes were classified as tonic spikes (blue). For the phase coupling analysis below, all spikes in a burst were treated as a single burst event. (B) Top: example component of pupil dynamics (CPD). Middle: the corresponding phases of the example CPD. Bottom: simultaneously recorded tonic spiking (blue) and bursting (red) from an example neuron. Right: the phase distributions for bursts and tonic spikes from the example neuron-CPD pair (R^2 : coupling strength; colored dots: preferred phase). The statistical significance of coupling to a CPD was determined using a permutation test by shuffling 300 ms bins of spiking activity (see Materials and methods; asterisks: * for $p \leq 0.05$, ** for $p \leq 0.01$, *** for $p \leq 0.001$). (C) The preferred coupling phase of bursts and tonic spikes for all neuron-CPD pairs with significant coupling. Significant tonic spike coupling was observed in 98.1% of neurons (153/156) and burst coupling in 87.3% of neurons (110/126). (D) Left: Burst—tonic spike phase differences for each neuron-CPD pair in (C) with significant coupling for both types of spiking ($N = 284$ neuron-CPD pairs), sorted by CPD timescale. Right: distribution of burst—tonic spike phase differences (mean = 2.8, V-test for non-uniform distribution with a mean of π : $V = 140.7$, $p < 0.001$; grid lines indicate proportion of 0.25). (E) Coupling strength distributions for all significantly coupled neuron-CPD pairs, binned by CPD timescale (horizontal bars: median coupling strength; Kruskal–Wallis one-way ANOVA across timescale bins for tonic spike coupling strengths: $H = 66.4$, $p = 5.8 \times 10^{-13}$, $N = 681$ neuron-CPD pairs; burst coupling strengths: $H = 32.1$, $p = 5.8 \times 10^{-6}$, $N = 320$ neuron-CPD pairs; Wilcoxon rank-sum test for burst versus tonic spike coupling strengths: $W = 3.3 \times 10^3$, $p = 2.0 \times 10^{-33}$, $N = 284$ neuron-CPD pairs). (F) Coupling strength decay across the multiple CPDs to which single neurons were coupled. Coupling strengths were measured after removal of periods of phase coupling between CPDs (S3B Fig; see Materials and methods) and normalized to the highest coupling strength for each unit (mean \pm SEM; left: tonic spiking; right: bursting). Only neuron-CPD pairs with significant coupling after removal of CPD phase coupling were included (blue arrow: tonic spiking mean = 3.8 CPDs per neuron; red arrow: bursting mean = 2.1 CPDs per neuron). (G) Distribution of the preferred coupling timescale (CPD with the strongest coupling) of neurons recorded in each recording session for tonic spiking (left) and bursting (right). There is some variability in timescale preference between recording

sessions (one-way ANOVA for tonic spiking: $F = 3.2, p = 2.5 \times 10^{-4}$; bursting: $F = 2.6, p = 2.5 \times 10^{-3}$), sessions are sorted by the timescale to which most neurons had their strongest tuning. CPD, components of pupil dynamics; dLGN, dorsal lateral geniculate nucleus.

<https://doi.org/10.1371/journal.pbio.3002614.g002>

coupling was not limited to a single temporal scale, but rather occurred over time scales spanning seconds to several minutes (1 to 0.001 Hz). Across this wide range of time scales, tonic spikes, and bursts consistently preferred opposite phases of pupil dynamics (Fig 2D; mean tonic spike—burst preferred phase difference = 2.8; V-test for non-uniform distribution with a mean of π : $V = 140.0, p \leq 0.001, N = 284$ neuron-CPD pairs with significant coupling of both spike types). The coupling strengths for both tonic spiking and bursting differed across temporal scales (Fig 2E; Kruskal–Wallis one-way ANOVA for tonic spiking: $H = 68.6, p = 2.0 \times 10^{-13}, N = 681$ neuron-CPD pairs; bursting: $H = 34.7, p = 1.7 \times 10^{-6}, N = 320$ neuron-CPD pairs), although bursting consistently displayed stronger coupling than tonic spiking (Fig 2E; Wilcoxon rank-sum test: $W = 3.4 \times 10^3, p = 7.1 \times 10^{-34}, N = 284$ neuron-CPD pairs), possibly because bursts are more exclusive to a certain membrane potential state of dLGN neurons. The same analyses performed on data collected in darkness also revealed phase coupling across temporal scales, with significant coupling observed in almost all neurons (S3A₁ Fig; tonic spiking: 96.8%, 91/94 neurons; bursting: 64.8%, 35/54 neurons). In darkness, the opposing phase preference between bursting and tonic spiking was largely preserved (S3A₂ Fig; mean tonic spike—burst preferred phase difference = 2.5; $V = 25.8, p = 5.1 \times 10^{-5}, N = 88$ neuron-CPD pairs with significant coupling of both spike types), and coupling was also consistently stronger for bursting than tonic spiking (S3A₃ Fig; Wilcoxon rank-sum test: $W = 58.0, p = 2.7 \times 10^{-15}, N = 88$ neuron-CPD pairs), together suggesting that coupling to CPDs was likely driven by changes in internal state rather than the changes in retinal illumination caused by pupil size fluctuation.

Next, we asked whether the coupling we observed across multiple temporal scales resulted from different neurons being modulated at different time scales, or if modulation at multiple temporal scales was present within the spiking of single neurons. Many neurons showed significant coupling to more than 1 CPD for both tonic spiking (mean = 4.4 CPDs with significant coupling per neuron) and bursting (mean = 2.5 CPDs per neuron). To ensure that potential phase relationships between the CPDs themselves (S1D Fig) did not underlie the observed coupling to multiple temporal scales, we repeated the phase coupling analysis after removing periods of time in which the components themselves are coupled (S3B Fig; see Materials and methods). Neurons retained their coupling to more than 1 temporal scale (tonic spiking mean = 3.8 CPDs per neuron; bursting mean = 2.1 CPDs per neuron), and coupling strengths across timescales remained unchanged for both tonic spiking (S3B₃ Fig; median = 0.0089, $N = 563$ neuron-CPD pairs versus original median = 0.0081, $N = 682$ neuron-CPD pairs; Mann–Whitney U test: $U = 1.9 \times 10^5, p = 0.34$) and bursting (median = 0.0583, $N = 250$ neuron-CPD pairs versus original median = 0.0528, $N = 320$ neuron-CPD pairs; $U = 3.9 \times 10^4, p = 0.56$). Among these neurons with multi-scale coupling, the gradual decay in coupling strengths from the strongest to the weakest indicated that modulations at the non-preferred timescales were not negligible (Fig 2F). Considering again the full dataset (Fig 2C–2E), the specific timescale to which a neuron was most strongly coupled was stable for individual neurons across subsamples of the data (S3D Fig) but varied between neurons such that strong coupling was observed across the entire range of timescales measured (Fig 2G). Notably, part of this variability could be attributed to the mouse and/or recording session (one-way ANOVA for tonic spiking timescale preferences across recordings: $F = 3.2, p = 2.5 \times 10^{-4}$; bursting: $F = 2.6, p = 2.5 \times 10^{-3}$), specifically, to the frequency of switches between locomotion and quiescence

in a given session (Pearson's $R = 0.71$, $p = 4.3 \times 10^{-3}$, $N = 14$ recording sessions; S3C₁ Fig). However, in almost all recording sessions, we found the CPD associated with the strongest coupling (preferred timescale) of neurons from the same recording was distributed across more than 1 component (tonic spiking: 15/15 sessions; bursting: 14/15 sessions), indicating that the timescale of strongest modulation was not only influenced by factors common to the recording session, but also by neuron-specific factors. We thus conclude that the spiking activity of individual dLGN neurons can be coupled to pupil dynamics across multiple independent temporal scales, and that there is diversity in the timescale to which neurons are most strongly coupled.

Our phase coupling framework introduced above (Fig 2) not only captures modulations associated with aspects of pupil dynamics, but it is also capable of capturing modulations usually related to pupil size per se. For example, in Fig 1D, it is apparent that peaks and troughs of certain components coincide with large and small pupil sizes. To disentangle the influence of pupil size from CPD phase coupling, we used a subsampling approach to minimize differences in the distribution of pupil size between the phases of each CPD (Fig 3A; see Materials and methods). We then assessed phase coupling considering only the spikes that occurred in these subsampled periods, noting that, especially for slower CPDs, sometimes only a small proportion of the original data could be retained for analysis (median proportion retained (IQR) for timescales <0.1 Hz: 52% (39, 61); timescales >0.1 Hz: 82% (82, 88)). Despite this reduction in available data, we found that coupling to CPDs in most neurons was largely preserved for tonic spiking (significant coupling observed in 93.9% of neurons, 139/148; mean = 3.3 CPDs per neuron) and burst events, albeit in a smaller proportion (63.6% of neurons, 77/121; mean = 1.0 CPD per neuron). For neurons that retained phase coupling, the characteristic opposing phase preferences of bursts and tonic spikes within neurons was also preserved (Fig 3B; mean = -2.9 ; V-test for non-uniformity and a mean of π : $V = 20.4$, $p = 6.4 \times 10^{-4}$, $N = 80$ neuron-CPD pairs). Overall, coupling strengths decreased for both tonic spikes (Fig 3C; overall median = 0.0081, $N = 681$ neuron-CPD pairs versus size-matched median = 0.0046, $N = 489$ neuron-CPD pairs; Mann-Whitney U test: $U = 2.0 \times 10^5$, $p = 4.4 \times 10^{-7}$) and bursts (overall median = 0.0528, $N = 320$ neuron-CPD pairs versus size-matched median = 0.0250, $N = 115$; Mann-Whitney U test: $U = 2.2 \times 10^4$, $p = 1.0 \times 10^{-3}$). This coupling strength decrease, however, was only present for a middle-range of temporal scales, suggesting that pupil size per se may not contribute to slow (timescale <0.03 Hz) or fast (>0.1 Hz) coupling in dLGN neurons. We then examined how the preferred timescale of individual neurons was affected after controlling for the influence of pupil size per se, finding that many neurons shifted the timescale to which they were most strongly coupled (Fig 3D, faded slices; tonic spikes: 55.9%; bursts: 30.2%). For bursting, such shifting of timescales was particularly prominent among neurons whose activity was monotonically related to pupil size (S3E Fig; Chi-squared test: $\chi^2 = 9.5$, $p = 8.7 \times 10^{-3}$; see also Fig 1C). Strikingly, however, we also found a sizeable proportion of neurons whose strongest coupling increased after controlling for pupil size (Fig 3D, highlighted slices; tonic spikes: 25.5%; bursts: 15.1%), suggesting that for these neurons effects related to pupil size per se were masking other firing rate modulations related to pupil dynamics. We thus conclude that the majority of dLGN neurons undergo multi-scale modulations of bursting and tonic spiking beyond those associated with pupil size per se.

We next investigated whether coupling between dLGN spiking and pupil size dynamics could be attributed to modulations driven by transitions in behavioral states. Previous studies have shown that changes in behavior, such as the transition from quiescence to locomotion, are accompanied by firing rate changes in dLGN neurons [12,31,32]. Consistent with these findings, we observed a decrease in tonic spiking in a 5 s window surrounding the offset of a locomotion bout (S4A₁ Fig; see also [8]), and a sharp increase in tonic spiking, preceded by a

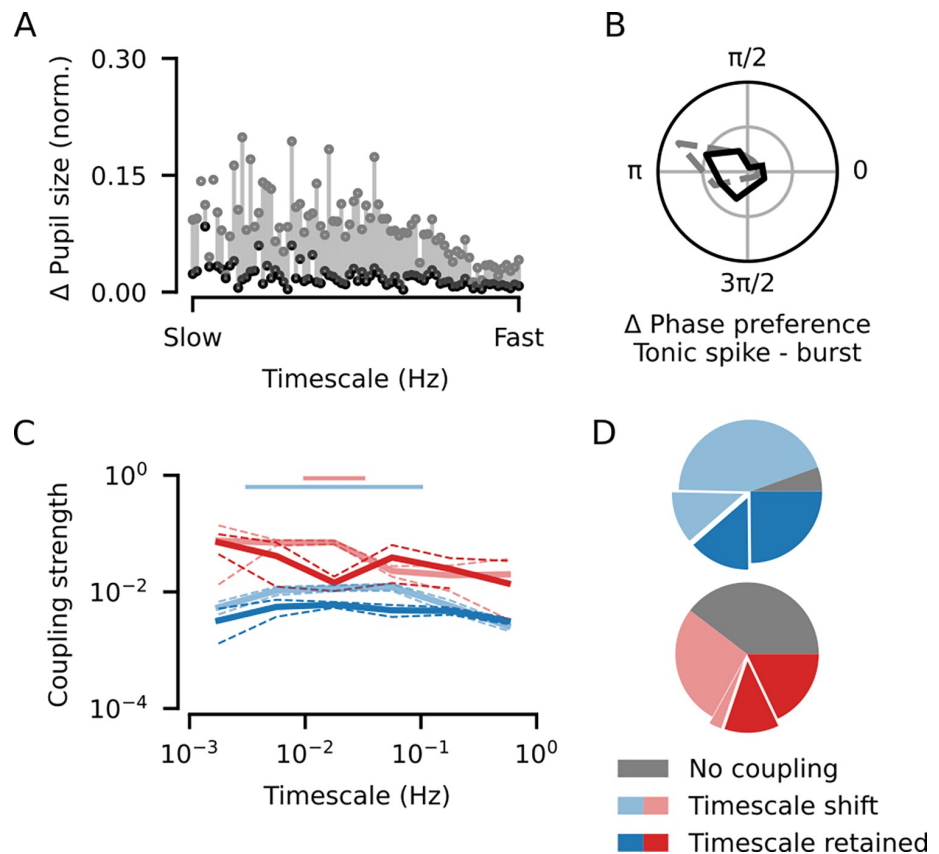


Fig 3. Coupling of dLGN spiking to pupil dynamics persists after controlling for pupil size. (A) Comparison of the difference in pupil size (min-max normalized) between the phase bins from each CPD sorted by CPD timescale before (gray) and after subsampling (black; see [Materials and methods](#)), illustrating the efficacy of the size matching procedure. (B) Distribution of burst—tonic spike phase differences measured after the size-matching procedure ($N = 80$ neuron-CPD pairs; mean = -2.94 , V-test for non-uniform distribution with a mean of π : $V = 20.4$, $p = 6.4 \times 10^{-4}$; gray: distribution from [Fig 2D](#); grid lines indicate proportion of 0.25). (C) Coupling strengths (solid lines: median; dashed lines: bootstrapped SE of the median) measured before (faded lines; [Fig 2E](#)) and after (bold lines) the size-matching procedure for tonic spikes (blue; overall median = 0.0081, $N = 681$ neuron-CPD pairs vs. size-matched median = 0.0046, $N = 489$ neuron-CPD pairs; Mann-Whitney U test: $U = 1.96 \times 10^5$, $p = 4.37 \times 10^{-7}$) and bursts (red; overall median = 0.0528, $N = 320$ neuron-CPD pairs vs. size-matched median = 0.0250, $N = 115$; Mann-Whitney U test: $U = 2.22 \times 10^4$, $p = 1.04 \times 10^{-3}$). (D) Proportion of neurons with significant phase coupling from [Fig 2](#) that kept the same preferred coupling timescale (bold slices; 38.6% for tonic spiking, 30.2% for bursting), shifted their preferred coupling timescale (faded slices; 55.9% for tonic spiking, 30.2% for bursting), or lost their coupling (gray slices; 5.5% for tonic spiking, 39.6% for bursting). The highlighted slices show the proportion of neurons that had an increase in coupling strength after controlling for pupil size (25.5% for tonic spiking, 15.1% for bursting). CPD, components of pupil dynamics; dLGN, dorsal lateral geniculate nucleus.

<https://doi.org/10.1371/journal.pbio.3002614.g003>

slight decrease in bursting, in a 4 s window surrounding the onset of a locomotion bout ([S4A₂](#) Fig). Periods of locomotion were also associated with an increased pupil size ([S1B₄](#) Fig). Unsurprisingly then, 55.3% of CPDs (52/94) had a small positive correlation with locomotion speed ([S4B](#) Fig; permutation test: $p \leq 0.05$, see [Materials and methods](#)). Given these findings, we asked if the CPD-linked spiking modulations we observed might be driven by these locomotion-correlated components. As a first step, we compared phase coupling across components, and observed that significant coupling for tonic spikes was equally likely regardless of whether the component was correlated to locomotion or not (neuron-CPD pairs with significant coupling: correlated = 73.5% (305/415) versus uncorrelated = 75.9% (341/449); Chi-

squared test: $\chi^2 = 0.56$, $p = 0.45$). For bursting, locomotion-correlated components were even less likely to have significant coupling (correlated = 38.2% (128/335) versus uncorrelated = 50.3% (186/370); Chi-squared test: $\chi^2 = 9.9$, $p = 1.7 \times 10^{-3}$). Thus, while locomotion can drive changes in spiking activity, and locomotion speed is partially reflected in certain CPDs, these relationships do not appear to be the sole cause of coupling to pupil dynamics.

To explicitly remove the influence of behavioral state changes on the coupling between pupil dynamics and spiking activity, we computed the phase coupling taking into account only the spiking activity that occurred within a given behavioral state. We also excluded spiking activity in the transitional windows between behavioral states (S4A Fig; quiescence to locomotion: -2 to 2 s; locomotion to quiescence: -1 to 4 s). We first focused on periods of quiescence (Fig 4A₁), which constituted on average 72% of the recordings (median proportion of time outside of locomotion bouts; S1B₁ Fig). During these quiescent periods, where variance in locomotion speed was low (S1B₃ Fig), we found that the coupling between spiking activity and pupil dynamics was largely the same as when measured across the entire recording (Fig 4A₂; significant tonic spike coupling in 97.3% (143/147); burst coupling in 77.1% (84/109) of neurons). Neurons retained the anti-phase relationship between tonic spiking and bursting (Fig 4A₃; mean tonic spike—burst phase difference = 2.9, $N = 221$ neuron-CPD pairs; V-test for non-uniform distribution with a mean of π : $V = 111.1$, $p < 0.001$), with coupling to multiple timescales of pupil dynamics (tonic spiking mean = 4.2 CPDs per neuron; bursting mean = 2.3 CPDs per neuron), and similar coupling strengths across all timescales compared to the coupling measured across the whole recording for tonic spiking (Fig 4A₄; quiescence median = 0.0100, $N = 591$ neuron-CPD pairs versus overall median = 0.0081, $N = 681$ neuron-CPD pairs; Mann-Whitney U test: $U = 1.9 \times 10^5$, $p = 2.6 \times 10^{-2}$) and bursting (quiescence median = 0.0564, $N = 256$ versus overall median = 0.0528, $N = 320$ neuron-CPD pairs; Mann-Whitney U test: $U = 3.9 \times 10^4$, $p = 0.28$).

Having shown that phase coupling across timescales persisted when measured only during periods of quiescence, we next repeated the same analyses focusing on periods with locomotion bouts (Fig 4B₁) and found similar coupling characteristics as for the other states (Fig 4B₂; significant tonic spike coupling in 85.3% (122/143), burst coupling in 77.9% (60/77) of neurons). Tonic spikes and bursts showed preferences for opposing phases (Fig 4B₃; mean tonic spike—burst phase difference = 3.1, $N = 87$ neuron-CPD pairs; V-test for non-uniform distribution with a mean of π : $V = 56.7$, $p < 0.001$). There was a notable increase in coupling strengths for both tonic spikes (Fig 4B₄; locomotion median = 0.0254, $N = 359$ neuron-CPD pairs; Mann-Whitney U test: $U = 7.2 \times 10^4$, $p = 2.6 \times 10^{-28}$) and bursts (locomotion median = 0.0927, $N = 133$ neuron-CPD pairs; Mann-Whitney U test: $U = 1.3 \times 10^4$, $p = 6.2 \times 10^{-10}$). Given the higher locomotion speed variability during locomotion bouts (S1B₃ Fig), we hypothesized that particularly strong dLGN modulation in this state might be linked to these changes in overt behavior. We therefore identified CPDs that were correlated to locomotion speed only within bouts of locomotion (64.9% of CPDs, 61/94; S4C Fig). Consistent with this hypothesis, we found that the locomotion-correlated components were more likely to drive significant phase coupling for both tonic spikes (neuron-CPD pairs with significant coupling: correlated = 77.2% (477/618), uncorrelated = 68.7% (169/246); Chi-squared test: $\chi^2 = 6.3$, $p = 0.01$) and bursts (correlated = 49.6% (256/516), uncorrelated = 30.7% (58/189); Chi-squared test: $\chi^2 = 19.3$, $p = 1.1 \times 10^{-5}$). Tonic spike coupling strengths were also higher for locomotion-correlated components (correlated median = 0.0099, $N = 477$ versus uncorrelated median = 0.0054, $N = 169$; Mann-Whitney U test: $U = 4.6 \times 10^4$, $p = 7.1 \times 10^{-3}$). Thus, while transitions between quiescence and locomotion bouts do not drive dLGN-pupil phase coupling, movement-related modulations may underlie a particularly strong coupling between dLGN spiking and pupil dynamics within periods of locomotion.

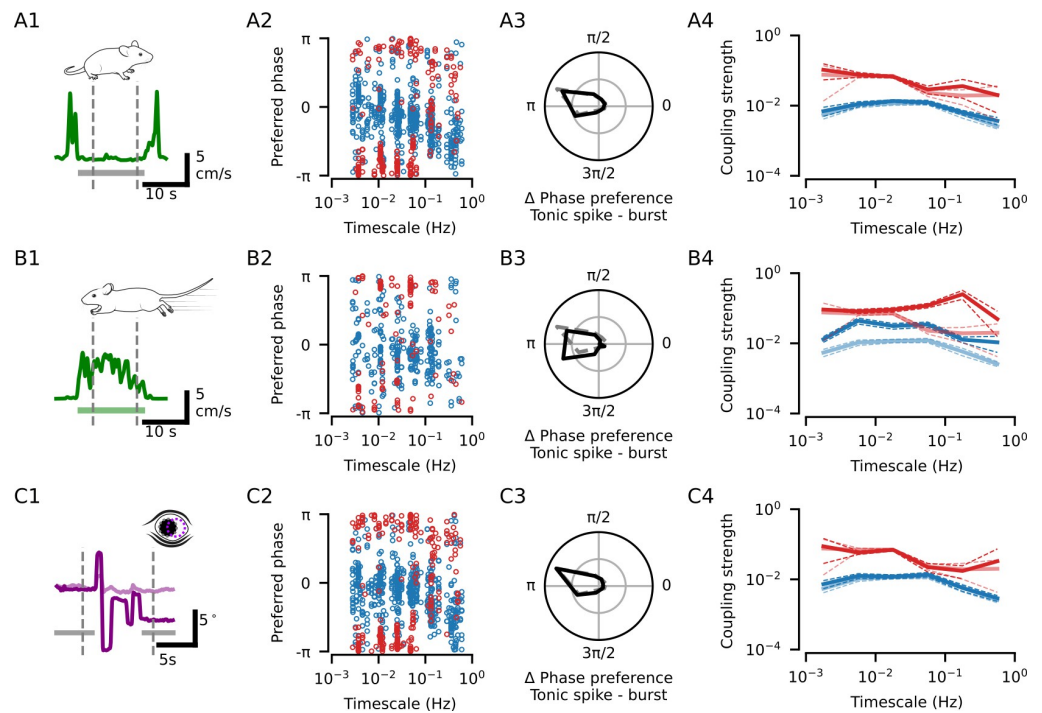


Fig 4. The coupling between dLGN spiking and pupil dynamics is not driven by overt behaviors. (A) Locomotion speed for an example period of quiescence (gray bar: period of quiescence). Dashed lines: period during which spikes were taken for the subsequent phase coupling analysis; note that the 4 s after the offset of the first locomotion bout and 2 s prior to the next locomotion bout were not included in this time window. (A2) Preferred coupling phase of tonic spikes (blue) and bursts (red) for all neuron-CPD pairs with significant coupling during quiescence. Significant tonic spike coupling was observed in 97.3% of neurons (143/147; mean = 4.2 CPDs per neuron) and burst coupling in 77.1% of neurons (84/109; mean = 2.3 CPDs per neuron). (A3) Distribution of the preferred phase differences between tonic spiking and bursting for neuron-CPD pairs with significant coupling of both spike types (mean = 2.9, $N = 221$ neuron-CPD pairs; V-test for non-uniform distribution with a mean of π : $V = 111.1$, $p < 0.001$; grid lines indicate proportion of 0.25). (A4) Coupling strengths (median \pm bootstrapped SE) measured during quiescence (bold lines) or across the whole recording (faded lines) for tonic spikes (blue; quiescence median = 0.0100, $N = 591$ neuron-CPD pairs vs. overall median = 0.0081, $N = 681$ neuron-CPD pairs; Mann-Whitney U test: $U = 1.9 \times 10^5$, $p = 2.6 \times 10^{-2}$) and bursts (red; quiescence median = 0.0564, $N = 256$ vs. overall median = 0.0528, $N = 320$ neuron-CPD pairs; Mann-Whitney U test: $U = 3.9 \times 10^4$, $p = 0.28$). (B1) Locomotion speed for an example bout (green bar: period of locomotion). Dashed lines: period during which spikes were taken for the subsequent phase coupling analysis; note that the first and final 1 s of the bout were not included in this time window. (B2–5) Same as (A2–5) but for phase coupling measured during locomotion bouts. Significant tonic spike coupling was observed in 85.3% of neurons (122/143; mean = 2.5 CPDs per neuron; median coupling strength during locomotion = 0.0254, $N = 359$ neuron-CPD pairs; Mann-Whitney U test: $U = 7.2 \times 10^4$, $p = 2.6 \times 10^{-28}$) and burst coupling in 77.9% of neurons (60/77; mean = 1.7 CPDs per neuron; median coupling strength during locomotion = 0.0927, $N = 133$ neuron-CPD pairs; Mann-Whitney U test: $U = 1.3 \times 10^4$, $p = 6.2 \times 10^{-10}$). Tonic spiking and bursting in neuron-CPD pairs with significant coupling of both spike types tended to occur at opposing phases (mean tonic spike—burst phase difference = 3.1, $N = 87$ neuron-CPD pairs; V-test for non-uniform distribution with a mean of π : $V = 56.7$, $p < 0.001$). (C1) Eye position for an example recording period with saccadic eye movements (dark purple: azimuth; light purple: elevation; gray bars: the time windows without saccades). Dashed lines: period during which spikes were taken for the subsequent phase coupling analyses, note that the -2 to 2 s of activity surrounding each saccade was excluded. (C2–5) Same as (A2–5) but for phase coupling measured during periods with no saccadic eye movements. Significant tonic spike coupling was observed in 97.4% of neurons (151/155); mean = 4.1 CPDs per neuron; median coupling strength without saccades = 0.0090, $N = 634$ neuron-CPD pairs; Mann-Whitney U test: $U = 2.1 \times 10^5$, $p = 0.11$) and burst coupling in 81.7% of neurons (94/115; mean = 2.5 CPDs per neuron; median coupling strength without saccades = 0.0545, $N = 284$ neuron-CPD pairs; Mann-Whitney U test: $U = 4.5 \times 10^4$, $p = 0.99$). Tonic spiking and bursting in neuron-CPD pairs with significant coupling of both spike types tended to occur at opposing phases (mean tonic spike—burst phase difference = 2.9, $N = 203$ neuron-CPD pairs; V-test for non-uniform distribution with a mean of π : $V = 131.5$, $p < 0.001$). CPD, components of pupil dynamics; dLGN, dorsal lateral geniculate nucleus.

<https://doi.org/10.1371/journal.pbio.3002614.g004>

Apart from locomotion, other behaviors, such as eye movements, may also be associated with arousal [33] and can induce changes in spiking activity. Indeed, upon visual inspection of eye position data, we noticed that saccades tended to occur during the dilation phase of large, slow pupil fluctuations, but also appeared to be related to smaller, faster fluctuations (S5A Fig), resembling the relationship between tonic spiking and pupil dynamics. To explore this further, we performed the same phase coupling analysis for saccades as we did for spiking and found that saccades had an almost identical phase coupling profile to that of tonic spikes: saccades predominantly occurred during the dilating phases of multiple temporal scales of pupil dynamics (S5B Fig; significant coupling of saccades to at least 1 CPD in 15/15 recording sessions; mean = 3.7 CPDs per session). To further investigate this relationship, we next asked if saccades could drive changes in spiking activity. Consistent with previous findings in primates (reviewed in [34]), we observed that bursting and tonic spiking in dLGN neurons was modulated in a short timescale window surrounding saccades. In a 4-s window surrounding saccades, tonic spiking increased, and bursting decreased, with the exception of a brief increase at the time of the saccade (S5C₁ Fig; $N = 118/121$ neurons had significant peri-saccadic modulation). With regards to tonic spiking, neurons displayed diverse peri-saccadic activity patterns, among which we identified at least 2 distinct response types (S5C₂ Fig). Despite this diversity in profiles, the overall effect of this modulation was a consistent increase in tonic spiking in 89.0% of saccade-responsive neurons (S5C₃ Fig; modulation strength median = 0.20; Wilcoxon rank-sum test: $W = 5.4 \times 10^2$, $p = 1.6 \times 10^{-15}$). In contrast, bursting activity tended to decrease (modulation strength median = -0.06; Wilcoxon rank-sum test: $W = 1.4 \times 10^3$, $p = 6.2 \times 10^{-3}$). We conclude that saccades occur during dilating phases of pupil dynamics and have a marked impact on dLGN spiking activity.

We therefore hypothesized that the changes in spiking activity during the peri-saccadic period might contribute to the observed coupling between tonic spiking and pupil dynamics. We reasoned that, if the peri-saccadic modulation was driving the coupling between tonic spikes and pupil dynamics, then coupling strengths and saccadic modulation strengths should be correlated. Indeed, we found that saccadic modulation strengths could correlate with coupling strengths, but only for fast timescales of pupil dynamics, and only for tonic spiking (S5D Fig). To eliminate the effect of saccade-driven changes in spiking activity, similar to our approach for locomotion, we excluded spiking activity in a window from -2 s to 2 s surrounding saccades (Fig 4C₁) and repeated the phase coupling analysis. We found that the main characteristics of the coupling between spiking activity and pupil dynamics were preserved across temporal scales, even without peri-saccadic activity. Significant coupling for tonic spiking was observed in 97.4% of neurons (151/155; mean = 4.1 CPDs per neuron) and 81.7% of neurons for bursting (94/115; mean = 2.5 CPDs per neuron; Fig 4C₂). Tonic spiking and bursting retained their anti-phase relationship within neurons (mean tonic spike = burst phase difference = 2.9; V-test for non-uniform distribution with a mean of π : $V = 144.0$, $p = 0.0$; Fig 4C₃), and coupling strengths were similar (median tonic spike coupling strength without saccades = 0.0090, $N = 634$ neuron-CPD pairs; Mann-Whitney U test: $U = 2.1 \times 10^5$, $p = 0.11$; median burst coupling strength without saccades = 0.0545, $N = 284$ neuron-CPD pairs; Mann-Whitney U test: $U = 4.5 \times 10^4$, $p = 0.99$; Fig 4C₄). We therefore conclude that, although behaviors like locomotion and eye movements are reflected in some components of pupil size dynamics, and can induce changes in spiking, the coupling between spiking activity and pupil dynamics is not dominated by modulations related to these overt behaviors.

So far, we reported a multi-scale coupling of dLGN activity to pupil dynamics in the absence of a patterned visual stimulus, but how stable is this coupling in the presence of a rich visual stimulus? At least 2 factors could potentially disrupt this coupling. Firstly, naturalistic stimuli have been shown to elicit repeated patterns of both tonic and burst firing in the dLGN

[32,35], which may dominate internally driven activity fluctuations. Secondly, luminance changes or other salient features of the stimulus could induce pupil size changes that might interfere with those driven by internal state fluctuations. To investigate dLGN spike coupling to pupil dynamics during stimulus viewing, we presented 5-s long naturalistic movie clips to mice while recording pupil size and dLGN activity (Fig 5; data from [32]). We observed that many neurons in the dLGN responded to the movies with repeated patterns of activity, as exemplified by the neuron shown in Fig 5A₁. However, the average response to the stimulus (Fig 5A₁, bottom) often appeared weaker than the trial-to-trial variability in the time-averaged mean firing rates (Fig 5A₁, right). We quantified this difference using the “response variability ratio” (RVR; see Materials and methods) and discovered that 100% of neurons had an RVR below 1 ($N = 64$ neurons; Fig 5A₂). In fact, for 90.6% of neurons, the variability was more than twice as strong as the signal ($\text{RVR} < 0.5$; Fig 5A₂), indicating that dLGN neurons showed considerable variability in their firing rates that could not be accounted for by the visual stimulus. Similarly, when we repeated the same analysis for pupil size, we found that the movies did not systematically drive pupil size changes (Fig 5B₁), resulting in an overwhelming dominance of trial-to-trial variance in pupil size (Fig 5B₂). Thus, internally driven pupil dynamics remain largely uninterrupted by the naturalistic movie we presented. The analyses above suggest that factors unrelated to the stimulus, such as coupling to arousal-related variables, may be prevalent despite the spiking responses evoked by the movie stimulus.

To investigate the coupling of spiking activity to pupil dynamics during naturalistic stimulus viewing, we decomposed the pupil size signal as before and characterized the phase coupling of bursts and tonic spikes ($N = 9$ recording sessions in 6 mice). We found significant tonic spike coupling in 98.4% of neurons (62/63; mean = 4.3 CPDs per neuron) and burst coupling in 62.7% of neurons (32/51; mean = 1.3 CPDs per neuron; Fig 5C₁), with opposite phase preferences at slower CPDs (timescales < 0.1 Hz; Fig 5C₂). Although stimulus presentation appeared to disrupt the preferred phase relationship between bursts and tonic spikes for faster CPDs (timescales > 0.1 Hz; Fig 5C₂), the opposing-phase relationship was still present overall (mean tonic spike—burst phase difference = 2.85, $N = 56$ neuron-CPD pairs with significant coupling to both spike types; V-test for non-uniform distribution with a mean of π : $V = 16.0$, $p = 1.6 \times 10^{-3}$; Fig 5C₃). The disruption at faster timescales is likely due to the presence of stimulus-driven bursts [35,36], and also demonstrates that the opposing phase relationship is not guaranteed based on intrinsic biophysical properties of dLGN neurons, such as the burst generation mechanism. Coupling strengths tended to be lower for tonic spikes during movies (median = 0.0050, $N = 273$ neuron-CPD pairs) compared to gray screen conditions (median = 0.0081, $N = 681$ neuron-CPD pairs; Mann–Whitney U test: $U = 1.1 \times 10^5$, $p = 1.1 \times 10^{-3}$; Fig 5C₄). In contrast, coupling strengths remained similar for bursts (movie median = 0.0332, $N = 68$ versus gray screen median = 0.0528, $N = 320$ neuron-CPD pairs; Mann–Whitney U test: $U = 1.2 \times 10^4$, $p = 0.16$; Fig 5C₄).

To examine the implications of these findings for the encoding of arousal-related variables by dLGN spiking activity, we leveraged the repeating patterns of activity induced by the stimulus and next asked if pupil dynamics could be decoded from patterns of spiking activity. We first split each 5 s trial into 1 s segments, and, for each CPD, used the mean phase during each segment to assign one of 2 phase labels. We then used spiking activity from each individual neuron with significant phase coupling to decode the phase label. We found that the phase labels could be decoded above chance level for every timescale of pupil dynamics, both when using tonic spikes (S6A Fig) or bursts (S6B Fig). Together, these results show that dLGN neurons also represent multi-scale aspects of pupil dynamics during encoding of a naturalistic visual stimulus.

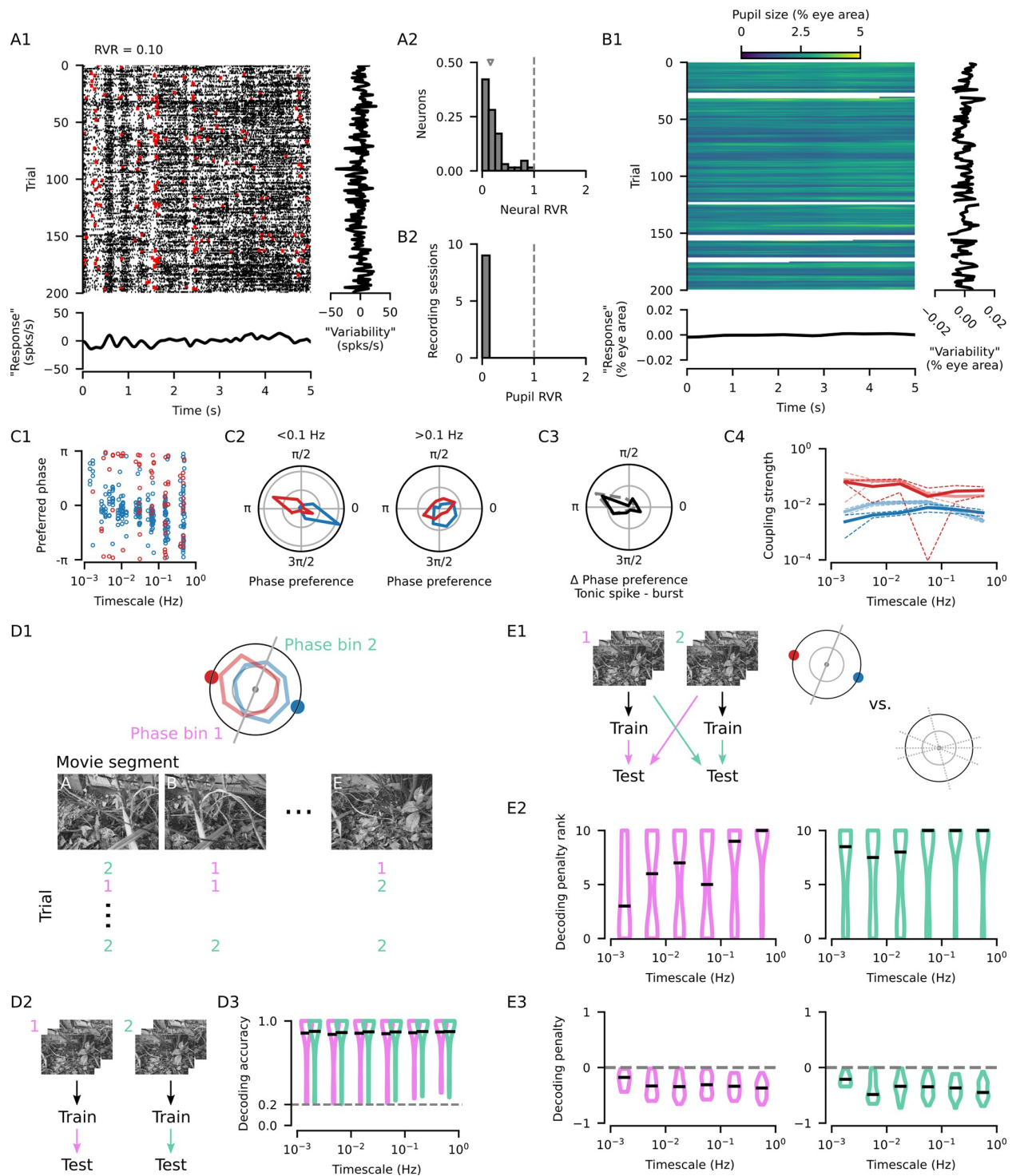


Fig 5. Coupling of dLGN activity to pupil dynamics is related to differences in visual stimulus encoding. (A1) Raster plot showing the responses of an example neuron to a movie (black: tonic spikes; red: burst spikes). Bottom: The mean response of the example neuron, centered on the mean across time. Right: The mean firing rate on each trial, centered on the mean across trials. Note that the “Response” and “Variability” axes have the same scale. (A2) The “response variability ratio” (RVR) compares the variance in the mean stimulus response to the mean variance for matching time points across trials (median = 0.16, $N = 64$ neurons; see [Materials and methods](#)). An RVR less than 1 indicates that the trial-to-trial changes in stimulus responses are larger

than the change induced by the stimulus. **(B1)** Trial-by-trial pupil size responses for the same experiment as in (A1). **(B2)** Distribution of pupil RVRs for all recording sessions with naturalistic movie stimulus presentation ($N = 9$ recording sessions in 6 mice). An RVR of near zero indicates that stimulus induced fluctuations in pupil size were negligible compared to across-trial fluctuations. **(C1)** Preferred coupling phase of tonic spikes (blue) and bursts (red) for all neuron-CPD pairs with significant coupling during stimulus presentation. Significant tonic spike coupling was observed in 98.4% of neurons (62/63; mean = 4.3 CPDs per neuron) and burst coupling in 62.7% of neurons (32/51; mean = 1.3 CPDs per neuron). **(C2)** Preferred phase distribution for tonic spikes and bursts for slower timescales (left: timescale < 0.1 Hz; $N = 183$ neuron-CPD pairs with tonic spike coupling; $N = 37$ neuron-CPD pairs with burst coupling; grid lines indicate proportion of 0.25) and faster timescales (right: timescale > 0.1 Hz; $N = 90$ neuron-CPD pairs with tonic spike coupling; $N = 31$ neuron-CPD pairs with burst coupling). **(C3)** Distribution of the preferred phase differences between tonic spiking and bursting for neuron-CPD pairs with significant coupling of both spike types (mean = 2.85, $N = 56$ neuron-CPD pairs, V-test for non-uniform distribution with a mean of π : $V = 16.0$, $p = 1.6 \times 10^{-3}$). **(C4)** Coupling strengths (median \pm bootstrapped SE) measured during stimulus presentation (bold lines) or without patterned visual stimulation (faded lines, Fig 2E) for tonic spikes (movie median = 0.0050, $N = 273$ neuron-CPD pairs vs. gray median = 0.0081, $N = 681$ neuron-CPD pairs; Mann-Whitney U test: $U = 1.1 \times 10^5$, $p = 1.1 \times 10^{-3}$) and bursts (movie median = 0.0332, $N = 68$ vs. gray median = 0.0528, $N = 320$ neuron-CPD pairs; Mann-Whitney U test: $U = 1.2 \times 10^4$, $p = 0.16$). **(D1)** Schematic representation of how the data was partitioned in (D) and (E). Each trial of naturalistic stimulus presentation was split into five 1-s segments and a decoder was trained to identify the stimulus segment using spiking activity. Two decoders were trained for each neuron-CPD pair, one for each of 2 CPD phase groupings. Turquoise: Decoders trained on segments during which the CPD was in the phase bin where tonic spiking preferentially occurred. Pink: Decoders trained on segments during which the CPD was in the opposing phase bin. **(D2)** Schematic of the movie segment decoding, initially performed by training and testing within data partitions. **(D3)** Decoding accuracy distributions for the 2 phase-groupings for each CPD timescale (black lines: median decoding accuracy; gray line: chance-level performance). **(E1)** Schematic of the movie segment decoding, now performed by training a decoder on one of the data partitions and testing it on data from the other. The decoding performance across CPD phases was compared to the scores from (D3) to yield a “decoding penalty.” This penalty was compared to the penalty obtained by repeating the same procedure on 10 random partitions of the data segments. A decoding penalty was considered significant if it was greater than the penalties obtained from all 10 random partitions. **(E2)** Distribution of the ranks of decoding penalties obtained from partitions based on CPD phases among those obtained from 10 random partitions (black lines: median rank). High ranks indicate that the penalty for training and testing across data partitions based on CPD phases were greater than those obtained by random partitions. **(E3)** Distributions of decoding penalties, only for neuron-CPD pairs with significant penalties (black lines: median decoding penalty). The penalty for training and testing across CPD phases can be as high as 50% across most timescales, suggesting that all timescales of modulation contribute to substantial differences in how stimuli are encoded. CPD, components of pupil dynamics; dLGN, dorsal lateral geniculate nucleus; RVR, response variability ratio.

<https://doi.org/10.1371/journal.pbio.3002614.g005>

Given the different stimulus-response functions of bursts and tonic spikes [35–37], and changes in feature selectivity that can occur with arousal [38–40], we next asked whether the movie stimulus is differently represented by spiking activity during different phases of pupil dynamics. To this end, we used spiking activity to decode which of the five 1-s stimulus segments was presented. For each neuron-CPD pair, we sorted the stimulus segments into 2 groups according to the phase of the component at the time when the segment was on screen (Fig 5D₁). These 2 phase groupings were designed such that one phase bin was centered on the preferred phase of tonic spiking, while the other phase bin was centered 180° opposite. Critically, we used all spikes to decode the identity of the stimulus segment, regardless of whether they were tonic spikes or part of a burst, to simulate the perspective of a downstream neuron in the cortex that would be blind to this classification.

We observed that decoders trained and tested on data from the same phase group (Fig 5D₂) achieved nearly perfect performance (Fig 5D₃; phase bin 1 decoding accuracy median = 99.6%, phase bin 2 decoding accuracy median = 99.6%, $N = 399$ neuron-CPD pairs), indicating that spiking activity during either phase was informative about the stimulus segment. However, when we tested the decoder trained using spiking activity from one phase group with activity occurring during the opposite phase grouping (Fig 5E₁), we found a marked decrease in decoding performance (Fig 5E₃; median penalty for train 1 \rightarrow test 2 decoding = -33.6%, train 2 \rightarrow test 1 = -34.5%). Critically, this decoding penalty was only considered significant if it was greater than the penalties obtained by performing the same cross-group decoding analysis on random partitions of the data (Fig 5E₂). The overall negative decoding penalty implies that encoding of the stimulus into firing rates differs between the phases of pupil dynamics. Overall, high within-state decoding accuracy and prominent decoding penalties across states suggest that the trial-to-trial variability in Fig 5A is not random but may stem from arousal-related changes in the stimulus-response properties of dLGN neurons. Importantly, these results were not limited to a specific temporal scale of pupil dynamics but were observed across

the entire range of timescales examined, indicating that multiple temporal scales of modulation affect stimulus encoding.

Discussion

Our results establish that activity in dLGN, the primary visual thalamic nucleus, is coupled to distinct CPDs that occur over multiple timescales, ranging from several seconds to several minutes. Throughout these timescales, bursts and tonic spikes exhibited robust phase preferences, occurring during opposite phases of pupil dynamics across all timescales. Individual neurons were coupled to multiple timescales and were diverse in the timescale that drove the strongest modulation. The coupling between dLGN spiking and pupil dynamics extended beyond effects related to differences in pupil size per se and could not be attributed to transitions between quiescence and locomotion, or to saccadic eye movements. Furthermore, the coupling persisted even during viewing of a rich naturalistic movie, where we observed differences in how visual stimuli were encoded across phases of pupil dynamics. Together, our findings support the notion that arousal-related modulation of visual thalamus in the waking state results from a combination of changes in dLGN spiking activity linked to diverse temporal scales.

Our data-driven decomposition of the pupil signal moves beyond a binary classification of behavioral state and reveals CPDs which together predict dLGN activity modulations across multiple timescales. It is important to note that the components we recovered here do not necessarily map directly onto the time-courses of independent internal processes or behavioral sequences. Yet, our results support the idea that modulations of both the pupil signal and dLGN neural activity result from a combination of multiple intrinsic and/or extrinsic influences, possibly separated by the temporal scale over which they occur. Multi-scale influences have been described in other contexts, including the presence of diverse activity timescales within and between neurons [41–43], the action of several behavioral state-related neuromodulators with distinct timescales [24,44] or the largely non-overlapping activation dynamics of different ensembles of neurons within the same neuromodulatory system [45]. Furthermore, quantification of behavior in freely moving animals has revealed a multi-scale organization, where long-lasting “idle” states can be punctuated by rapid “active” behaviors (and vice-versa; [46]), mirroring the modulations we observed here, where slow and fast modulations were superimposed in dLGN activity. Finally, in the context of task performance, cognitive processes orchestrated by arousal-related neuromodulators can change on fast and slow timescales [21], such as quick reorienting to surprising stimuli or the choice of specific behavioral strategies over longer timescales. In humans, variations in stimulus detection ability have been linked to the phase of slow components (0.01 to 0.1 Hz) of EEG signals [47]. Thus, the multi-scale modulation we observed in the dLGN could reflect sensory processes adapting to the various timescales of behavioral organization of the organism.

While providing a quantitative account of dLGN modulations linked to multi-scale pupil dynamics, locomotion, and saccades, a limitation of our study is that it has not addressed these modulations on a mechanistic level. However, the relationship to pupil size strongly implicates the neuromodulators norepinephrine (NE) [20,24,48] and acetylcholine (ACh) [11,24] in the present findings. NE is provided to the thalamus by the locus coeruleus (LC) [49,50], while ACh in the rodent thalamus comes from several brainstem nuclei (PPN/LDT and PBG) [51–53] and the basal forebrain (BF) [51,54]. Consistent with a potential role for the LC-NE system in the present findings, stimulation of the LC in vivo has been shown to suppress bursting in the dLGN [55] and primary somatosensory thalamus (VPM) [56], while causing pupil dilation [48]. Additionally, NE levels in the mouse thalamus during NREM sleep have been found to

fluctuate with a frequency of 0.02 Hz and are linked to correlates of sensory arousability [57]. Given the prevalence of high power of CPDs around 0.02 Hz we observed, it also seems likely that the LC-NE system drives some of the coupling between dLGN spiking and pupil dynamics at such timescales during wakefulness. In addition, stimulation of the cholinergic PPT/LDT increases firing rates in the VPM [58], and switches dLGN neurons from burst to tonic mode [59], supporting the role of cholinergic nuclei in the modulations observed here. Although the activity of the PPN/LDT and PBG have not been directly linked to pupil size fluctuations, they are involved in coordinating locomotor patterns and eye movements [60,61], meaning they could specifically drive the subset of modulations we observed linked to these behaviors. It is important to note that neuromodulatory influences in the thalamocortical system extend beyond direct effects on thalamic neurons, and also involve the thalamic reticular nucleus [51,54,62–64], corticothalamic L6 neurons [65,66], and retinal boutons [40,67,68], all of which could contribute to additional arousal-related influences on thalamic neurons. Furthermore, although our analyses in darkness control for changes in retinal illumination linked to pupil size per se, there are known effects of pupil size on feed-forward signaling. Changes in retinal irradiation linked to pupil size can shift color selectivity in the visual system [39], and there is evidence for interactions between luminance and behavioral modulation [69] that warrants further exploration. Future studies directly tracking and manipulating the activity of these modulatory systems in the thalamus promise to yield further insight into the relationship between internal states and feed-forward sensory signals across diverse time scales.

The modulations in burst and tonic spiking we observed indicate that, throughout periods of wakefulness, and even during stimulus viewing, the dLGN is in constant alternation between 2 distinct information processing modes. One prominent view is that tonic spikes encode information about a stimulus linearly, while stimulus-driven bursts provide an all-or-none “wake-up call” to the cortex [14], by providing augmented retinogeniculate [37] and geniculocortical [18] communication, and improved stimulus detectability [70] (for related work in the somatosensory system, see e.g., [71,72]). Burst spikes, in comparison with tonic spikes, also have different feature selectivity: they track low frequency stimulus content [9,73,74] with an earlier response phase [32,36,75], integrate input over longer timescales with biphasic response kernels [35,36,76–78], and prefer smaller stimuli [79] with a stronger suppressive surround [36]. Such differences likely contribute to the decoding penalty we observed when training and testing decoders on spiking activity from opposing phases of the modulations we observed. However, it is also possible that neuromodulatory mechanisms change the stimulus response properties of dLGN neurons, without eliciting a switch in firing mode from tonic spiking to bursting. It remains to be seen whether spatiotemporal receptive fields change across phases of pupil dynamics, and whether these changes can be attributed to membrane hyperpolarization and bursting.

Our results focused on the commonalities of multi-scale modulation across the recorded population of dLGN neurons. However, we also observed a substantial diversity across neurons in the strength of coupling within a timescale, the timescale with strongest coupling, and the degree to which stimulus decoding was influenced. The mouse dLGN consists of various cell types [80] and functional subtypes [81,82], some of which are known to be differentially affected by arousal-linked variables [38,68]. Moving forward, considering the specific functional role of a given neuron, along with its temporal structure of modulation, will lead to a better understanding of dynamic stimulus processing in the visual system.

In this study, revealing the multi-scale nature of arousal-related activity modulations in dLGN was possible by applying a decomposition approach to the pupil signal. This approach builds on previous studies using raw pupil size as a marker for internal arousal processes in sensory circuits [7,40,66,83–87] or the pupil's dynamics within a restricted frequency range

[6,24,43]. Importantly, however, our analysis of pupil components and phases in relation to spiking activity is not intended to undermine the usefulness of pupil size itself, which remains an accessible signal that offers a relevant index into internal state. Indeed, our analyses show that modulations indexed by pupil size may be viewed as a specific case of phase coupling to pupil dynamics: coupling to high amplitude peaks or troughs of a component. We therefore view these approaches as complimentary and considering both allows for a more nuanced and comprehensive account of the modulations of sensory processing.

While our study has expanded the use of the pupil signal to reveal arousal-related modulations to multiple temporal scales, recent work has emphasized that a larger array of behaviors may also help to better explain activity in sensory systems [19,88]. Individual behaviors, such as locomotion onset [8,12], eye movements [89], head movements [69], or particular postures in freely moving conditions [90], modulate activity in the rodent early visual system. In the present study, locomotion and eye movements were shown to relate to a subset of pupil-linked modulations. However, given that a larger set of behavioral components has been linked to activity modulation in the visual cortex, this subset may expand as more behaviors are measured. These behavior-related modulations often occur in time-windows of seconds or less, which may be explained by the need to account for their immediate influence on sensory inputs [34,91]. Our present work shows that sensory neurons are modulated not only at these faster timescales, but also at longer timescales. In the future, a more complete characterization of the organization of spontaneous behaviors across temporal scales [46] promises to advance our understanding of multi-scale modulations of sensory processing by behavioral states.

Materials and methods

Ethics statement

All procedures complied with the European Communities Council Directive 2010/63/EU and the German Law for Protection of Animals, and were approved by local authorities (Regierung von Oberbayern, license #: ROB-55.2-2532.Vet_02-17-40; Regierungspräsidium Tübingen, license #: CIN 4/12), following appropriate ethics review.

Surgical procedure

Experiments were carried out in 6 adult transgenic PV-Cre mice (median age at first recording session: 23.4 weeks; B6;129P2-Pvalb^{tm1(cre)Arbr}/J; Jackson Laboratory), 4 adult Ntsr1-Cre mice (median age: 24.7 weeks; B6.FVB(Cg)-Tg(Ntsr1-cre)GN220Gsat/Mmcd; MMRRC), and 1 wild-type BL6 mouse (age: 33.9 weeks), of either sex. Transgenic mice were used, as these mice were also included in another study [32] which required selective viral expression of ChR2 in area V1. For the present study, data mostly came from experiments where no optogenetic manipulation was present, with the exception of the data in Figs 5 and S6. Here, only trials without optogenetic stimulation were considered for the analyses.

The majority of experiments were performed under Licence ROB-55.2-2532.Vet_02-17-40. Thirty minutes prior to surgical procedures, mice were injected with an analgesic (Metamizole, 200 mg/kg, sc, MSD Animal Health, Brussels, Belgium). To induce anesthesia, animals were placed in an induction chamber and exposed to isoflurane (5% in oxygen, CP-Pharma, Burgdorf, Germany). After induction of anesthesia, mice were fixated in a stereotaxic frame (Drill & Microinjection Robot, Neurostar, Tuebingen, Germany). At the beginning of the surgical procedure, an additional analgesic was administered (Buprenorphine, 0.1 mg/kg, sc, Bayer, Leverkusen, Germany) and the isoflurane level was lowered (0.5% to 2% in oxygen), such that a stable level of anesthesia could be achieved as judged by the absence of a pedal reflex. Throughout the procedure, the eyes were covered with an eye ointment (Bepanthen, Bayer,

Leverkusen, Germany) and a closed loop temperature control system (ATC 1000, WPI Germany, Berlin, Germany) ensured that the animal's body temperature was maintained at 37°C. The animal's head was shaved and thoroughly disinfected using iodine solution (Braun, Melsungen, Germany). Before performing a scalp incision along the midline, a local analgesic was delivered (Lidocaine hydrochloride, sc, bela-pharm, Vechta, Germany). The skin covering the skull was partially removed and cleaned from tissue residues with a drop of H₂O₂ (3%, AppliChem, Darmstadt, Germany). Using 4 reference points (bregma, lambda, and 2 points 2 mm to the left and to the right of the midline respectively), the animal's head was positioned into a skull-flat configuration. The exposed skull was covered with OptiBond FL primer and adhesive (Kerr dental, Rastatt, Germany) omitting 3 locations: V1 (AP: -2.8 mm, ML: -2.5 mm), dLGN (AP: -2.3 mm, ML: -2 mm), and a position roughly 1.5 mm anterior and 1 mm to the right of bregma, designated for a miniature reference screw (00-96 X 1/16 stainless steel screws, Bilaney) soldered to a custom-made connector pin. Unrelated to the purpose of this study, 2 µl of the adeno-associated viral vector rAAV9/1.EF1a.DIO.hChr2(H134R)-eYFP.WPRE.hGH (Addgene, #20298-AAV9) was dyed with 0.3 µl fast green (Sigma-Aldrich, St. Louis, United States of America), and after performing a small craniotomy over V1, a total of approximately 0.5 µl of this mixture was injected across the entire depth of cortex (0.05 µl injected every 100 µm, starting at 1,000 µm and ending at 100 µm below the brain surface), using a glass pipette mounted on a Hamilton syringe (SYR 10 µl 1701 RN no NDL, Hamilton, Bonaduz, Switzerland). A custom-made lightweight stainless steel head bar was positioned over the posterior part of the skull such that the round opening contained in the bar was centered on V1/dLGN and attached with dental cement (Ivoclar Vivadent, Ellwangen, Germany) to the primer/adhesive. The opening was later filled with the silicone elastomer sealant Kwik-Cast (WPI Germany, Berlin, Germany). At the end of the procedure, an antibiotic ointment (Imax, Merz Pharmaceuticals, Frankfurt, Germany) was applied to the edges of the wound and a long-term analgesic (Meloxicam, 2 mg/kg, sc, Böhringer Ingelheim, Ingelheim, Germany) was administered and continued to be administered for 3 consecutive days. For at least 5 days post-surgery, the animal's health status was assessed via a score sheet.

One mouse was treated in accordance with Licence CIN 4/12, in which general surgical procedures were identical to the foregoing with the following exceptions. After induction of anesthesia, mice were additionally injected with atropine (atropine sulfate, 0.3 mg/kg, s.c.; Braun). The head post consisted of a small S-shaped piece of aluminum, which was cemented to the skull between lambda and bregma and to the right of the midline. Posterior to the head post, overlying the cerebellum, 2 miniature screws serving as ground and reference were implanted. At the end of the procedure, antibiotics (Baytril, 5 mg/kg, s.c.; Bayer) and a long-term analgesic (Carprofen, 5 mg/kg, s.c.; Rimadyl, Zoetis) were administered and were given for 3 days after surgery.

After at least 1 week of recovery, animals were gradually habituated to the experimental setup by first handling them and then simulating the experimental procedure. To allow for virus expression, neural recordings started no sooner than 3 weeks after injection. On the day prior to the first day of recording, mice were fully anesthetized using the same procedures as described for the initial surgery, and a craniotomy (ca. 1.5 mm²) was performed over dLGN and V1 and re-sealed with Kwik-Cast (WPI Germany, Berlin, Germany). As long as the animals did not show signs of discomfort, the long-term analgesic Metacam was administered only once at the end of surgery, to avoid any confounding effect on experimental results. Recordings were performed daily and continued for as long as the quality of the electrophysiological signals remained high.

Electrophysiological recordings

Mice were head-fixed on a styrofoam ball and allowed to run freely. Extracellular signals were recorded at 30 kHz (Blackrock Microsystems). For each recording session, the silicon plug sealing the craniotomy was removed. To record from dLGN, a 32-channel linear silicon probe (Neuronexus A1x32Edge-5mm-20-177-A32, Ann Arbor, USA) was lowered to a depth of approximately 2,700–3,700 μm below the brain surface. We judged recording sites to be located in dLGN based on the characteristic progression of RFs from upper to lower visual field along the electrode shank [81] and the presence of responses strongly modulated at the temporal frequency of the drifting gratings (F1 response). For post hoc histological reconstruction of the recording site, the electrode was stained with DiI (Invitrogen, Carlsbad, USA) for one of the final recording sessions.

For the purposes of a different study [32], during recordings involving naturalistic movie stimulation (Figs 5 and S6), V1 was optogenetically stimulated using 470 nm light on half of the trials, which were randomly interleaved with control trials. Here, only electrophysiological data from trials without optogenetic stimulation were considered.

Histology

After the final recording session under Licence ROB-55.2-2532.Vet_02-17-40, mice were first administered an analgesic (Metamizole, 200 mg/kg, sc, MSD Animal Health, Brussels, Belgium) and following a 30 min latency period were transcardially perfused under deep anesthesia using a cocktail of Medetomidin (Domitor, 0.5 mg/kg, Vetoquinol, Ismaning, Germany), Midazolam (Climasol, 5 mg/kg, Ratiopharm, Ulm, Germany), and Fentanyl (Fentadon, 0.05 mg/kg, Dechra Veterinary Products Deutschland, Aulendorf, Germany). Perfusion was first done with Ringer's lactate solution followed by 4% paraformaldehyde (PFA) in 0.2 M sodium phosphate buffer (PBS).

To verify recording site and virus expression, we performed histological analyses. Brains were removed, postfixed in PFA for 24 h, and then rinsed with and stored in PBS at 4°C. Slices (40 μm) were cut using a vibrotome (Leica VT1200 S, Leica, Wetzlar, Germany), mounted on glass slides with Vectashield DAPI (Vector Laboratories, Burlingame, USA), and coverslipped. A fluorescent microscope (BX61, Olympus, Tokyo, Japan) was used to inspect slices for the presence of yellow fluorescent protein (eYFP) and DiI. Recorded images were processed using FIJI [92,93].

For experiments under Licence CIN 4/12, general histological procedures were identical to those described above, except that mice were injected with sodium pentobarbital (Narcoren, = 200 mg/kg intraperitoneally; Böhringer Ingelheim) before perfusion. Coronal brain slices (50 μm) were obtained by using a vibratome (Microm HM 650V, Thermo Fisher Scientific) and inspected with a Zeiss Imager.Z1m fluorescent microscope (Zeiss).

Visual stimulation

Visual stimulation was presented using custom written software (EXPO, <https://sites.google.com/a/nyu.edu/expo/home>) on a liquid crystal display (LCD) monitor (Samsung SyncMaster 2233RZ, 47×29 cm, 1680×1050 resolution at 60 Hz, mean luminance 50 cd/m^2) positioned at a distance of 25 cm from the animal's right eye. The data presented in all figures, with the exception of Figs 5 and S6, was recorded while animals were viewing either a static gray screen ($N = 5$ experiments) or a sparse noise stimulus ($N = 10$ experiments). The sparse noise stimulus consisted of a non-overlapping white and black square, simultaneously flashed for 200 ms on a square grid spanning 60 deg, while individual squares spanned 5 deg. Data was collected in darkness (S1 and S2 Figs) by switching off the display monitor and blocking smaller light

sources produced by the recording equipment. The data presented in Figs 5 and S6 were recorded while the animals were repeatedly presented with 5 s naturalistic movie clips (as described in [32]).

Behavioral tracking

During electrophysiological recording, head-fixed mice were allowed to run on an air cushioned Styrofoam ball. Ball movements were recorded by 2 optical computer mice which interfaced with a microcontroller (Arduino Duemilanove) and sampled ball movements at 90 Hz. Locomotor activity was quantified by computing the Euclidean norm of 2 perpendicular components of ball velocity (pitch and roll), and herein referred to as locomotion speed. Locomotion bouts were defined as periods of time where the ball speed exceeded 1 cm/s for at least 2 s, with a break of no more than 2 s, and during which the locomotion speed exceeded the threshold for at least half of the bout duration. Quiescence was defined as any period of time outside of a locomotion bout.

To track pupil size, the stimulus-viewing eye was illuminated with an infrared LED light (850 nm), and the eye was filmed with a camera (Guppy AVT camera; frame rate 50 Hz, Allied Vision, Exton, USA) equipped with a zoom lens (Navitar Zoom 6000). Pupil size was extracted from the videos using a custom, semi-automated algorithm. Each video frame was equalized using an adaptive bi-histogram equalization procedure, and then smoothed using median and bilateral filters. The center of the pupil was initially estimated by taking the darkest point in a convolution of the filtered image with a black square. Next, the peaks of the image gradient along lines extending radially from the center point were used to define the pupil contour. Lastly, an ellipse was fit to the contour, and the area of the ellipse was taken as pupil size, and the center of the ellipse was taken as the pupil position. Frames in which the eye was obscured, occurring during eye closure or grooming, were detected by applying a threshold to the mean pixel-wise difference between each frame and a reference frame compiled by taking the median of several manually selected frames during which the eye was open. Data points with eye closure, as well as the 4 points immediately adjacent, were excluded. Because the pupil size and eyelid closure are correlated, many periods when the pupil was at its smallest could not be analyzed, including some periods of very low arousal and sleep-related states. Adjustable parameters in the above algorithm were set manually for each experiment. After ellipse fitting, data points at which the fitted pupil position, size, eccentricity, or rate of change, were outside of a plausible range were removed from consideration. Unreliable segments, occurring due to eye-closure, grooming, or unstable ellipse fitting, were automatically removed according to a priori criteria. Cubic splines were used to interpolate over gaps of <5 s, and the remaining segments of continuous data were smoothed with a Gaussian kernel ($\sigma = 250$ ms). From each recording session, we only included data from the single longest continuous segment of reliable pupil data (median = 1,159 s, min = 596 s, max = 2,507 s). Pupil size is reported as a percentage of the total area of the exposed eye visible in the recording, as we found this to be a more stable normalization metric across recordings than the mean or maximum pupil size.

Pupil size signal decomposition

The pupil size signal was decomposed into intrinsic mode functions (herein referred to as CPDs) by EMD (<https://emd.readthedocs.io>). In contrast to the original broad-band pupil size signal, the CPDs are locally narrow-band and thus amenable to Hilbert spectral analysis [29]. In contrast to the Fourier or wavelet transforms, EMD extracts these components without predefined filters and can capture nonstationarities present in biological signals with individual frequency- and amplitude-modulated components [29]. To minimize edge effects during

subsequent spectral analysis, each CPD was extrapolated from the beginning and end by mirroring the 3 closest peaks/troughs across the signal edge and interpolating between the mirrored extrema with third-order Bernstein polynomials restricted by the gradient at the signal edge. CPDs with fewer than 3 extrema were extended using the first derivative at the signal edges. The Hilbert transform was applied to the extended CPDs to obtain the complex-valued analytic signal of each CPD, from which the instantaneous phase and amplitude at each time point were computed as the angle and length of the signal vector, respectively. Instantaneous frequency was given by the time derivative of the unwrapped phase. Only time points corresponding to the un-extrapolated signal were used in further analysis. Pupil size power spectral density was compiled by binning the instantaneous frequency and collecting power (squared amplitude) for each frequency bin across CPDs and time (referred to as the “marginal spectrum” in [29]). This generally corresponded well with the PSD obtained via Fourier transform (median Pearson’s $R = 0.71$, $N = 15$ recordings). Each CPD was assigned a “characteristic time-scale” by taking the mean frequency across all time points weighted by the amplitudes. The relative power of each CPD was assigned by taking the power (squared amplitude density of each CPD and expressing it as a fraction of the sum of the power densities from all CPDs extracted from the recording segment). At this point, some of the lower frequency CPDs were eliminated from further consideration if they did not complete at least 4 cycles within the recording segment to ensure sufficient sampling of each phase.

The relationship between pairs of CPDs from the same recording segment was assessed using a permutation test designed to find periods of phase coupling between CPDs. The CPDs resulting from EMD, although broadly different in frequency content, are not guaranteed to have independent phase progressions. Therefore, the same aspect of pupil dynamics can end up being captured by multiple CPDs. To address this problem, we reasoned that, if this mixing occurred, it would be reflected in transient periods of phase alignment between 2 CPDs. This alignment would appear as peaks in the joint phase distribution of 2 CPDs, causing the distribution to deviate from uniformity. However, because the phase distribution of each CPD itself is not uniform, for each pair of simultaneously recorded CPDs we simulated the expected joint distribution in the absence of phase coupling by shuffling the cycle order of each CPD independently 1,000 times. The real and simulated joint distributions were then compared to a uniform distribution using the Kullback–Leibler divergence (Δ KLD, [S1D Fig](#)). The CPDs were considered significantly coupled if the Δ KLD of the true joint distribution exceeded the 95th percentile of the Δ KLDs computed from the simulated distributions (p -value ≤ 0.05 ; [S1D1 Fig](#), magenta outlines; [S1D2 Fig](#), right). The specific combination of phases driving the coupling was determined by asking which points in the joint phase space exceeded the 95th percentile of the simulated distributions at the same point ([S1D1 Fig](#), white outlines). These phase combinations were only considered significant if the Δ KLD also indicated overall coupling between the 2 CPDs. For the analysis in [Figs 2F](#) and [S3B](#), the periods of time during which coupled CPDs passed through these phase combinations were excluded.

Spike sorting

For recordings under protocol ROB-55.2-2532.Vet_02-17-40, the spiking activity of isolated single units was initially extracted from extracellular recordings using the Kilosort spike-sorting toolbox [94]. The resulting spike clusters were subject to manual curation in Spyke [95], where spikes within a cluster were temporally aligned and plotted in a 3D space (multichannel PCA, ICA, and/or spike time). In this space, clusters could be merged to account for drift in spike shape over the recording session (for example, if the first 2 wave shape PCs changed smoothly as a function of spike time), or further split using a gradient ascent-based clustering

algorithm [96]. Clusters containing only spikes with no consistent and clearly discernible voltage deflection were eliminated from further consideration. Finally, cluster auto-correlograms were examined to ensure that a clear refractory period was present; while the presence of a refractory period was not an indicator of a well-isolated unit, the absence of a refractory period was taken as an indicator that the cluster might need to be further split or contained a high amount of noise. Remaining clusters were compared using empirical distance metrics to ensure that they were well separated.

For the few sessions recorded under protocol CIN 4/12, single neurons in our linear array recordings were isolated by grouping neighboring channels into 5 equally sized “virtual octodes” (8 channels per group with 2-channel overlap for 32 channel probes). Using an automatic spike detection threshold [97] multiplied by a factor of 1.5, spikes were extracted from the high-pass-filtered continuous signal for each group separately. The first 3 principal components of each channel were used for semi-automatic isolation of single neurons with KlustaKwik [98], and the resulting clusters were manually refined with Klusters [99]. Only clusters whose auto-correlogram displayed a clear refractory period and whose mean voltage trace showed a characteristic spike waveshape were further considered. To avoid duplication of neurons extracted from linear probe recordings, we computed cross-correlograms (1-ms bins) between pairs of neurons from neighboring groups. Pairs for which the cross-correlogram’s zero bin was 3 times larger than the mean of nonzero bins were considered to be in conflict and only one was kept.

Bursts of action potentials are associated with a slow, hyperpolarization de-inactivated Ca^{2+} conductance present in thalamic neurons, which cannot be directly measured in extracellular recordings. However, studies combining intra- and extracellular recordings have established reliable empirical criteria for identification of these thalamic bursts [30], according to which ≥ 2 spikes with a prior period without spiking of 100 ms and an ISI of < 4 ms are part of a burst (Fig 2A). Spikes satisfying these criteria were categorized as burst spikes, whereas all other spikes were considered tonic spikes. Downstream analyses were performed separately on tonic spikes and burst events, for which all spikes in a burst were treated as a single event. Among our recorded dLGN units, the vast majority (89.5%) displayed bursting events, which and accounted for 3% of dLGN spikes (burst ratio: the proportion of all spikes in the recording that were part of a burst; S2A₂ Fig).

Short timescale serial dependence of burst events and tonic spiking was assessed by computing the auto-correlogram for each activity type in a -1 s to 1 s window. Taking the average auto-correlation over all neurons, it was determined by visual inspection that both event types had a primary peak lasting approximately 300 ms. In addition, we also note that the mean burst auto-correlation had a secondary peak, indicating rhythmicity in the ~ 5 Hz range [13].

Modulation of spiking by pupil size

To assess the modulation of spiking activity by arousal states, we began by collecting, for each neuron, spike counts in 250 ms bins. We then sorted these spike counts into 10 bins according to the min-max normalized pupil size. A neuron was considered to be significantly modulated by pupil size if a one-way ANOVA across the pupil size bins was significant, regardless of which pupil size bin had the highest firing rate.

Phase coupling

To assess the modulation of spiking activity by arousal states, we developed a phase coupling analysis to relate events such as bursts and tonic spikes to the CPDs. We required that at least 8 bursts or tonic spikes occurred over the course of the recording segment for a neuron to be considered in this analysis. Considering tonic spikes and burst events from each neuron

separately, the Hilbert phase of each ongoing CPD was collected at times when bursts (the time of the first spike of the burst) and tonic spikes occurred. Although coupling might be directly assessed by compiling phase histograms and computing the circular mean of these phases, we adopted various bias-corrections resulting in a more stringent assessment of phase coupling.

Firstly, CPDs are not guaranteed to have a linear phase progression, which is beneficial in that they can capture naturalistic asymmetric wave shapes but presents a difficulty when assessing phase coupling as the underlying distribution of phases could itself be biased. These biases could lead one to falsely infer phase coupling simply because more recording time may be spent in a certain phase, and therefore more spikes attributed to this phase. We therefore converted phases to circular ranks, yielding a uniform underlying distribution to which bursts and tonic spikes could be related [100]. The angle of the circular mean rank was then converted back to a phase using the original distribution, and this value was reported as the “preferred phase.” Next, as the circular mean resultant vector length is a biased statistic (its value is inflated for small number of observations), we opted for an unbiased measure of phase coupling strength to allow comparison of coupling strength across units with different firing rates, between tonic spikes and bursts, and between conditions where spikes were subsampled from the recording period. Rather than using mean resultant vector length (R), we used its squared value, which can be easily bias-corrected [101]. We thus quantified coupling strength as follows:

$$\hat{R}^2 = \frac{n}{n-1} \left(R^2 - \frac{1}{n} \right),$$

where R is the mean resultant vector length computed using the circular phase ranks, and n is the number of tonic spikes or bursts. Finally, we sought to assess the statistical significance of phase coupling with a measure that was insensitive to the short-term serial dependence of spike trains, which effectively reduces the degrees of freedom of the sample. We adopted the null hypothesis that, if there were no relationship between spiking activity and CPD phase, then the coupling strength of a neuron-CPD pair would be the same as that measured from a spike train with the same short-term structure, but with no relationship to the CPD. We tested coupling strengths against this null hypothesis by splitting burst and tonic spike trains into segments of 300 ms, which were shuffled in order to destroy the relationship between CPD phase and spiking activity, and then phase coupling to the CPD was assessed as described above. This procedure was repeated 1,000 times for each neuron-CPD pair to compile a null-distribution of coupling strengths. The true coupling strength was then compared to this distribution and assigned an exact p -value (precise to 3 decimal places) based on how many elements of the null set had a higher coupling strength value.

In general, we computed phase coupling using all recorded spikes. However, to account for the influence of spiking activity surrounding behaviors such as locomotion and eye movements (Figs 4, S4, and S5), we excluded spiking activity that occurred during these behaviors from consideration. To measure coupling during periods of quiescence, spikes that occurred during locomotion bouts were excluded, as well as spikes occurring 2 s before bout onset, and 4 s after bout offset. For coupling during locomotion, spikes occurring during quiescence were excluded, as well as spikes occurring during the first and last 2 s of the bout, meaning that bouts shorter than 4 s in length were not considered. To eliminate the influence of peri-saccadic activity, we excluded spiking activity occurring in a time window from 1 s before to 2 s after the saccade. Finally, because 2 simultaneously recorded CPDs could themselves have phase coupling (S1D Fig), we assessed the coupling of single neurons to multiple CPDs after

removing periods of time where significant coupling between a given CPD and any other CPD in the set was observed according to the statistical procedure detailed above (Figs 2F and S3B). In the case of the phase coupling comparison across data partitions (S3D Fig), for each neuron and CPD, the spiking from adjacent CPD cycles was placed into one of the 2 partitions. Coupling was assessed for each partition separately, then the difference in preferred phase across partitions was compared for each neuron-CPD pair. For coupling strength ranking across CPDs, the partition with data from odd CPD cycles was arbitrarily assigned to 1 group, and even cycles to the other group. Coupling strength was then ranked within groups and the top CPD was compared across groups for each neuron.

Pupil size distribution matching

We observed that pupil size could co-vary with CPD phase (Fig 3A), thus presenting a confound for genuine phase coupling. To control for effects of pupil size per se from the measurement of CPD phase coupling, we adopted a histogram matching procedure [102,103] to minimize the differences in the distribution of pupil sizes across the phase bins of each CPD. For each CPD, the recording was split into segments based on 4 phase bins. For each visit to a phase bin, the mean pupil size during the visit was collected and compiled into a histogram (10 bins). From these histograms (1 for each phase bin), we assembled a “minimum common distribution” of pupil sizes by selecting the phase bin with the smallest number of entries for each pupil size. For each of these entries in the selected phase bin, we collected the entry from the other 3 phase bins with the closest pupil size, thus obtaining an equal number of samples from each phase bin, with pupil sizes matched as closely as possible. To assess the efficacy of this procedure, we computed the pair-wise difference in mean pupil size (this time collecting the full time-course of pupil size from each bin visit, rather than the mean) between each pair of phase bins, and took the maximum difference. We compared this difference before and after the subsampling procedure (Fig 3A). The phase coupling analysis in Fig 3 results from taking only spikes that occurred during the time periods subsampled with the matching procedure.

Correlation analyses

Locomotion speed is known to be reflected in the pupil size signal (S1B4 Fig, [8]). To assess the potential contributions of locomotion speed to the phase coupling we observed, we performed correlation analyses relating each CPD to the animal's locomotion speed. Because serial dependence in signals can inflate correlation values and violates the independence assumption required to directly calculate a p -value, we adopted a permutation-based approach to assess the statistical significance of CPD-speed cross-correlations [104]. Each CPD was correlated with 1,000 locomotion speed traces collected from other experiments and compared the peak value cross-correlation to the distribution of nonsense correlations in order to obtain a p -value. To further reduce the detection of spurious correlations, we limited our search for the peak to lags in the range of $[-T, T]$, where T is the mean period of the CPD. For example, for a CPD with a mean period of 5 s, the search window would be restricted to lags of $[-10$ s, 10 s], and maximum value of the absolute cross-correlation in this window would be compared to the distribution of nonsense correlations. The cross-correlation was considered significant only if the maximum value within the prescribed range had a p -value ≤ 0.05 .

Spiking responses

To compute spiking responses to behavioral events (locomotion onsets, locomotion offsets, saccades) and experimental events (stimulus onsets), we first estimated the instantaneous firing rate surrounding each event via kernel density estimation ([105], implemented in the

statistics.instantaneous_rate function from <https://elephant.readthedocs.io>). Instantaneous rates were estimated using a Gaussian kernel with 100 ms bandwidth and sampled with a resolution of 50 ms. Responses were considered significant if at any point the mean response was outside the [2.5, 97.5] percentile range of responses computed using a shuffled version of the spike train (300 ms bins, 1,000 shuffles). In the case of saccade responses (S5C Fig), K-means clustering (sklearn.cluster.KMeans, with $k = 3$) was performed after taking the top principal components (explaining 80% of the variance) of the mean responses of each neuron in a window of [-1 s, 1 s] surrounding the saccade. To quantify the trial-to-trial variability in stimulus responses (Fig 5A2 and 5B2), we constructed a “response variance ratio” (RVR) comparing the variance across time of the mean stimulus response to the mean across-trial variance for each time point.

$$SNR = \frac{Var_t(E_k(X))}{E_t(Var_k(X))},$$

where $X = [x_1, \dots, x_k]^T \in R^{K \times L}$ is the response matrix compiled from K trials of duration L , and $E_d()$ and $Var_d()$ denote taking the mean or variance across the indicated dimension of the matrix.

Decoding analyses

For each neuron-CPD combination, we trained support-vector classifiers (SVCs; sklearn.svm.SVC) to decode CPD phase and visual stimulus identity from spiking activity during naturalistic stimulus viewing (Figs 5 and S6). Spike times (tonic spike times, burst times, or all spikes) from each trial were converted into instantaneous rates (see above), and each 5 s trial was split into 1 s segments. To decode the CPD phase (S6 Fig), we assigned a label to each 1 s segment of activity by taking the circular mean phase of the CPD during the segment and placing this mean phase into one of 2 phase bins. We then trained an SVC (with a radial basis function kernel) to decode the phase label using only burst rates or only tonic spike rates occurring during the 1 s segment and assessed the decoding performance with 5-fold cross-validation. To decode the visual stimulus (Fig 5D), we assigned each 1 s segment with a label (e.g., 1 for the first second of the stimulus, 5 for the last second of the stimulus), and then split the segments into 2 groups according to the mean CPD phase during the segment. We used the instantaneous rates (estimates using all spikes together regardless of their categorization as tonic or burst) from one group to train an SVC (with a linear kernel) to perform “one-versus-rest” decoding of the stimulus labels and tested the decoder using the same data as well as the data from the other group. We took the difference in decoding scores between the 2 groups as the “decoding penalty.” We compared the decoding penalty obtained when splitting the segments by CPD phase to the decoding penalties obtained from 10 random splits of the data as a control. The decoding penalty for the neuron-CPD pair was considered significant if it was greater than all 10 random splits. In both of the above decoding schemes, we determined the 2 CPD phase bins based on the preferred coupling of each neuron: one bin was centered around the preferred phase of tonic spiking of the neuron (preferred phase $\pm \pi/2$), and the other bin was centered around the opposing phase (preferred phase $-\pi \pm \pi/2$).

Supporting information

S1 Fig. Characterizations of pupil and running behavior, relationship of spikes to pupil size during darkness, and independence of CPDs. (A1) Pupil size distributions for all recording sessions. Pupil size is expressed as a fraction of the total exposed eye area (see [Materials and methods](#)). Data from the gray screen and sparse noise sessions are grouped together for

the analyses in Figs 1, 2, 4, S2, S3B, S3C and S4. **(A2)** Pupil size power spectral density (mean \pm SEM, min-max normalized) for gray screen recordings ($N = 5$) and recordings in darkness ($N = 5$). **(B1)** Distribution of proportion of time spent in a locomotion bout (green, see [Materials and methods](#)) versus sitting (gray) for $N = 14$ sessions where locomotion speed was recorded (Horizontal bars: median proportion). **(B2)** Distribution of locomotion bout and inter-bout-interval lengths. **(B3)** Distribution of locomotion speed variance during locomotion bouts versus sitting. Whereas locomotion bouts were characterized by larger behavioral variability, the inter-bout-intervals had very low variability in locomotion speed. **(B4)** Pupil size (mean \pm SEM, normalized to the pre-bout pupil area) surrounding locomotion bout onsets (left) and offsets (right). **(B5)** Pupil size power spectral density (mean \pm SEM) for periods of locomotion (green) and quiescence (gray). **(C1)** Spike counts (min-max normalized) across pupil sizes (min-max normalized) for the dLGN neurons with significant modulation by pupil size (top, one-way ANOVA across 10 pupil size bins, $p \leq 0.05$) and without significant modulation (bottom) during recordings performed in darkness. Neurons are sorted by the location of the maximum firing rate (black dots). The majority of significantly modulated neurons (61.8%) had “non-monotonic” modulation profiles, with their maximum firing rates outside of the 90th percentile of pupil size (dashed white line). **(C2)** Same as (C1) but for bursts of spikes. Neurons are sorted by the location of the maximum burst rate (black dots). The majority of significantly modulate neurons had “monotonic” modulation profiles, with their maximum burst rates in the 10th percentile of pupil size. **(C3)** For each dLGN neuron in the light ([Fig 1C1](#)) and dark ([S1C1 Fig](#)), the spike count Fano factor (spike count variance/mean) in each pupil size bin was computed, and the mean across pupil size was taken. The Fano factor is >1 in both the light (median Fano factor = 1.95, Wilcoxon rank-sum test for mean Fano factor >1 : $W = 1.2 \times 10^4$, $p = 5.2 \times 10^{-26}$, $N = 156$ neurons) and dark (median Fano factor = 1.38, mean Fano factor >1 : $W = 4.4 \times 10^3$, $p = 6.4 \times 10^{-16}$, $N = 94$ neurons). **(D1)** Joint phase distributions for the CPDs from the recording in [Fig 1B](#), illustrating the results of our statistical test for phase coupling between CPDs (see [Materials and methods](#)). Magenta outlines: CPD pairs where the distribution as a whole showed that the CPDs were coupled ($p \leq 0.05$). White outlines: regions in the joint phase space where coupling might have occurred. **(D2)** Phase coupling z-scores quantifying the amount of coupling occurring between 2 simultaneously recorded CPDs from gray screen and sparse noise recordings. Top: CPD pairs without significant coupling (77.0%, 354/460 CPD pairs). Bottom: CPD pairs with significant phase coupling (23.0%, 106/460 CPD pairs). The majority of CPD pairs did not have coupling, suggesting that they represent independent aspects of pupil dynamics. Those that had coupling tended to be similar in temporal scale (i.e., were close to the diagonal). (TIFF)

S2 Fig. Firing rate distributions, auto- and cross-correlograms of tonic spiking and bursting. **(A1)** Distribution of firing rates (black) for all neurons recorded in spontaneous or sparse noise sessions (mean = 4.49 spk/s, $N = 156$). Blue: The firing rate distribution considering only tonic spikes (mean = 4.11 spk/s), showing that overall firing rates were primarily determined by tonic spiking. Neurons with a firing rate <0.01 spk/s were excluded from all analyses. **(A2)** Distribution of burst ratios (number of spikes assigned to a burst/total number of spikes, median = 3.0%). Bursts were detected in 92.9% of neurons (145/156). **(B1)** Mean auto-correlogram of tonic spiking (mean \pm SEM). The dashed line at 300 ms indicates the bin-width used to generate shuffled spike trains used to test phase coupling significance (see [Materials and methods](#)). **(B2)** Mean auto-correlogram of bursting (mean \pm SEM). Note that the peaks are spaced apart by approximately 200 ms, indicating that approximately 5 Hz rhythmic bursting was present (see also Nestvogel and colleagues). **(C)** Mean burst cross-correlogram

(mean \pm SEM) for all simultaneously recorded pairs of neurons ($N = 1,185$ pairs). The peaks at zero and approximately 200 ms indicate that neurons tend to burst synchronously and rhythmically.
(TIFF)

S3 Fig. Coupling of spikes to CPDs in darkness and detailed characterization of CPD preferences. (A) Phase coupling analysis relating dLGN spiking to CPDs for recordings performed in darkness. (A1) Preferred coupling phase of tonic spikes (blue) and bursts (red) for all neuron-CPD pairs with significant coupling. Significant tonic spike coupling was observed in 96.8% of neurons (91/94; mean = 3.4 CPDs per neuron) and burst coupling in 64.8% of neurons (35/54; mean = 1.9 CPDs per neuron). (A2) Distribution of the preferred phase differences between tonic spiking and bursting for neuron-CPD pairs with significant coupling of both spike types (mean = 2.5; $N = 88$ neuron-CPD pairs; V-test for non-uniformity and a mean of π : $V = 25.8$, $p = 5.1 \times 10^{-5}$; grid lines indicate proportion of 0.25). While the mean phase difference is similar to Fig 2D (dashed gray line), we also note that in darkness a small proportion of neurons appear to have a spiking pattern where tonic spikes immediately follow bursts without a phase delay (Δ phase preference $\sim 2\pi$). (A3) Coupling strengths (solid lines: median, dashed lines: bootstrapped SE of the median) measured in darkness (bold lines) or in an illuminated environment (faded lines; Fig 2E) for tonic spiking (dark median = 0.0058, $N = 321$ neuron-CPD pairs vs. illuminated median = 0.0081, $N = 682$ neuron-CPD pairs; Mann-Whitney U test: $U = 1.2 \times 10^5$, $p = 2.9 \times 10^{-3}$) and bursting (dark median = 0.0386, $N = 100$ neuron-CPD pairs vs. illuminated median = 0.0528, $N = 320$ neuron-CPD pairs; Mann-Whitney U test: $U = 1.8 \times 10^4$, $p = 0.05$). (B) Phase coupling analysis performed on the same recordings as in Fig 2, but excluding spikes that occurred during periods of phase coupling between CPDs (S1D Fig; see Materials and methods). (B1) Preferred coupling phase of tonic spikes (blue) and bursts (red) for all neuron-CPD pairs with significant coupling. Significant tonic spike coupling was observed in 98.6% of neurons (146/148; mean = 3.8 CPDs per neuron) and burst coupling in 74.2% of neurons (89/120; mean = 2.1 CPDs per neuron). (B2) Distribution of the preferred phase differences between tonic spiking and bursting for neuron-CPD pairs with significant coupling of both spike types (mean = 2.7; $N = 203$ neuron-CPD pairs; V-test for non-uniformity and a mean of π : $V = 109.1$, $p < 0.001$; grid lines indicate proportion of 0.25). (B3) Coupling strengths (median \pm bootstrapped SE) measured after removal of periods of phase coupling between CPDs (bold lines) or over the whole recording (faded lines; Fig 2E) for tonic spiking (no coupling median = 0.0089, $N = 563$ neuron-CPD pairs vs. overall median = 0.0081, $N = 682$ neuron-CPD pairs; Mann-Whitney U test: $U = 1.9 \times 10^5$, $p = 0.34$) and bursting (no coupling median = 0.0583, $N = 250$ neuron-CPD pairs vs. overall median = 0.0528, $N = 320$ neuron-CPD pairs; Mann-Whitney U test: $U = 3.9 \times 10^4$, $p = 0.56$). (C1) For each recording session, the mean preferred timescale across neurons plotted against the frequency of behavioral state switches (1/mean duration of locomotion and quiescence periods). The correlation (Pearson's $R = 0.71$, $p = 4.3 \times 10^{-3}$, $N = 14$ recording sessions) indicates that part of variability in timescale preferences between recordings (Fig 3G) is related to differences in behavior. (C2) Proximity of the CPDs with the strongest and second strongest coupling for tonic spikes (blue) and bursts (red), a value of 1 indicates that the CPD with the second strongest coupling is adjacent in characteristic timescale to the strongest. These results suggest that although neurons may be modulated at multiple timescales, the range of temporal scales with strong modulation is limited. (D) Preferred timescale and phase tend to be stable across data sub-samples (blue: tonic spikes, red: bursts). The phase coupling of individual neurons was compared across each of 2 interleaved partitions of the data (see Materials and methods). The change in the CPD to which a neuron is most strongly coupled is shown in (D1) for

all neurons, 0 indicates that the strongest CPD remained unchanged, 1 indicates that the strongest CPD shifted to a CPD adjacent in characteristic timescale. The overwhelming majority of neurons either retain the same preferred CPD or switch to the next closest timescale. The change in preferred phase for each neuron-CPD pair is shown in (D2) for pairs in which the coupling was significant in both subsamples (colored distribution) and in which coupling did not reach significance in one or both of the subsamples (gray distributions). For both tonic spikes and bursts, the change in phase preference was 90° for $>90\%$ of neurons. (E) Proportion of neurons that shift (faded sections) or maintain (bold sections) their preferred coupling timescales after controlling for pupil size (Fig 3), split by the profile of modulation by pupil size (Monotonic: neurons with peak rate in the top decile for tonic spiking, or bottom decile for bursting vs. Other: all other neurons with significant modulation across pupil sizes vs. None: neurons with no modulation across pupil sizes; see Fig 1C). For tonic spikes (top), there was no significant difference between groups (mono = 37/63 vs. other = 43/65 vs. none = 6/11; Chi-squared test: $X^2 = 1.0$, $p = 0.60$). Meanwhile, neurons with monotonic burst modulation by pupil size (in contrast to tonic spiking, this class constituted the majority of neurons for bursting) were significantly more likely to switch preferred timescales (bottom; mono = 34/46 vs. other = 7/13 vs. none = 5/16; Chi-squared test: $X^2 = 9.5$, $p = 8.7 \times 10^{-3}$). (TIFF)

S4 Fig. Spiking activity and pupil dynamics are correlated with locomotion speed. (A1) Firing rate responses to the offset of locomotion bouts (mean \pm SEM, relative to the baseline from -5 to -3 s and min-max normalized for each neuron) for tonic spiking (blue; $N = 111/121$ neurons with significant tonic spiking modulation) and bursting (red; $N = 98/121$ neurons with significant bursting modulation). Vertical lines denote the period surrounding the offset of locomotion bouts during which the mean firing rate deviates from baseline (-1 s to 4 s), and therefore spiking activity during this transition period was excluded for the analysis in Fig 4A, in addition to all activity during locomotion bouts. (A2) Same as (A1) but for the onset of a locomotion bout ($N = 108/121$ neurons with significant tonic spiking modulation; $N = 96/121$ neurons with significant bursting modulation). Vertical lines denote the transition period (-2 s to 2 s) surrounding the onset of a bout from which spiking activity was excluded for the analysis in Fig 4B, in addition to all activity during quiescence. (A3) Median burst ratio (number of burst spikes/total number of spikes, error bars: bootstrapped SE of the median) across quiescence (gray, excluding 2 s prior to and following locomotion bouts) and locomotion (green, split for the first 2 s of bouts, the middle portion of bouts, and the final 2 s of bouts) showing burst spikes are less prevalent, but not absent, during locomotion (Friedman chi-squared test: $Q = 22.0$, $p = 6.7 \times 10^{-5}$). (B) Left: Mean cross-correlation between CPDs and locomotion speed, grouped by the timescale of the CPD (black dots: location of the peak correlation for each CPD with a significant correlation; gray dots: location of the peak correlation for each component without a significant correlation). Correlation significance was determined by comparing the maximum value of the cross-correlation to a null-distribution obtained by correlating the CPD with locomotion speed traces taken from different recording sessions (see Materials and methods). To eliminate nonsense correlations, we only considered the cross-correlation significant if the peak was found at lags shorter than the mean period of each CPD. Right: Proportion of CPDs in each timescale bin with a significant correlation to locomotion speed (significant correlation in 55.3% of CPDs, $52/94$). (C) Same as (B), but only considering the CPD and locomotion speed within locomotion bouts (significant correlation in 64.9% of CPDs, $61/94$). (TIFF)

S5 Fig. Saccades are linked to pupil dynamics and trigger changes in dLGN activity. (A) Example eye position (top) and pupil size (bottom) traces. Detected saccades are marked by the dashed lines. (B) This coupling of saccades to pupil dynamics was verified using the same phase coupling analysis as in Fig 2, relating saccades to each of the CPD. Shown here are the preferred phases at which saccades occur, for CPDs across various timescales (significant saccade coupling to at least 1 CPD was observed in 15/15 recording sessions). Across all time-scales, saccades tend to occur during pupil dilations, similar to tonic spikes (Fig 2C). (C1) Firing rate responses to saccades (mean \pm SEM, relative to the baseline from -5 to -3 s and min-max normalized for each neuron) for tonic spiking (blue; $N = 118/121$ neurons with significant tonic spiking modulation) and bursting (red; $N = 88/121$ neurons with significant bursting modulation). Vertical lines denote the period surrounding saccades during which the mean firing rate deviates from baseline (-2 s to 2 s); therefore, spiking activity during this transition period was excluded for the analysis in Fig 4C. (C2) Neurons in the dLGN have diverse saccade-triggered tonic spiking responses. Clustering the normalized peri-saccadic responses (see Materials and methods) revealed at least 2 distinct response types, in addition to a minimally responsive/mixed cluster (left). The first responsive cluster (middle) had a transient increase in firing tightly locked to saccade onsets. The second responsive cluster (right) was characterized by gradually increased firing rates prior to saccade onset, with a brief suppression immediately following saccade onset, before returning to a sustained facilitation. (C3) Despite the diversity in responses, the peri-saccadic period (-2 to 2 s) was characterized by an overall increase in tonic spiking rates. The modulation was quantified by taking the area under the normalized saccadic response curve in a window spanning -2 to 2 s for tonic spiking (median = 0.2 ; Wilcoxon rank-sum test: $W = 5.4 \times 10^2$, $p = 1.6 \times 10^{-15}$, $N = 118$) and bursting (median = -0.06 ; Wilcoxon rank-sum test: $W = 1.4 \times 10^3$, $p = 6.2 \times 10^{-3}$, $N = 88$). (D) Pearson correlation between CPD coupling strengths and saccadic modulation strengths for each time-scale (p -value denoted by asterisks, * for $p \leq 0.05$, ** for $p \leq 0.01$, *** for $p \leq 0.001$). The correlation was not significant for the majority of timescales, suggesting that the coupling between tonic spiking and pupil dynamics was independent from the rapid peri-saccadic changes in firing rate observed in (C).

(TIFF)

S6 Fig. CPD phase can be decoded from spiking activity during stimulus viewing. (A) Distributions of CPD phase decoding accuracy using tonic spiking ($N = 273$ neuron-CPD pairs; dashed line: chance-level performance). For each neuron with significant tonic spike-CPD coupling, a support-vector classifier was trained to select between 2 phase bins, one of which was centered around the preferred phase of tonic spike coupling, the other was centered 180° opposite. Decoding accuracy was cross-validated using 5 training-test splits. The distribution of decoding accuracy was significantly greater than chance for all timescales (Wilcoxon rank-sum test for each timescale, p -value denoted by asterisks, * for $p \leq 0.05$, ** for $p \leq 0.01$, *** for $p \leq 0.001$). (B) Same as (A), but for CPD phase decoding using bursting. For each neuron with significant burst-CPD coupling, a support-vector classifier was trained using bursting activity, and the phase bins were centered around the preferred phase of bursting.

(TIFF)

Acknowledgments

We would like to thank M. Sotgia for lab management and support with animal handling and histology, Y. Bauer, G. Born, and A. H. Kotkat for their contributions to the data collections

and spike sorting, S. Schörnich for IT support, and B. Grothe for providing excellent research infrastructure.

Author Contributions

Conceptualization: Davide Crombie, Christian Leibold, Laura Busse.

Data curation: Davide Crombie, Martin A. Spacek.

Formal analysis: Davide Crombie.

Funding acquisition: Davide Crombie, Christian Leibold, Laura Busse.

Investigation: Martin A. Spacek.

Methodology: Davide Crombie, Christian Leibold, Laura Busse.

Project administration: Christian Leibold, Laura Busse.

Software: Davide Crombie, Martin A. Spacek.

Supervision: Christian Leibold, Laura Busse.

Visualization: Davide Crombie.

Writing – original draft: Davide Crombie, Christian Leibold, Laura Busse.

Writing – review & editing: Davide Crombie, Christian Leibold, Laura Busse.

References

- Harris KD, Thiele A. Cortical state and attention. *Nat Rev Neurosci*. 2011; 12(9):509–523. <https://doi.org/10.1038/nrn3084> PMID: 21829219
- McGinley MJ, Vinck M, Reimer J, Batista-Brito R, Zaghera E, Cadwell CR, et al. Waking state: rapid variations modulate neural and behavioral responses. *Neuron*. 2015; 87(6):1143–1161. <https://doi.org/10.1016/j.neuron.2015.09.012> PMID: 26402600
- McCormick DA, Nestvogel DB, He BJ. Neuromodulation of brain state and behavior. *Annu Rev Neurosci*. 2020; 43:391–415. <https://doi.org/10.1146/annurev-neuro-100219-105424> PMID: 32250724
- Poulet JF, Crochet S. The cortical states of wakefulness. *Front Syst Neurosci*. 2019; 12:64. <https://doi.org/10.3389/fnsys.2018.00064> PMID: 30670952
- Hess EH, Polt JM. Pupil size as related to interest value of visual stimuli. *Science*. 1960; 132(3423):349–350. <https://doi.org/10.1126/science.132.3423.349> PMID: 14401489
- Reimer J, Froudarakis E, Cadwell CR, Yatsenko D, Denfield GH, Tolias AS. Pupil fluctuations track fast switching of cortical states during quiet wakefulness. *Neuron*. 2014; 84(2):355–362. <https://doi.org/10.1016/j.neuron.2014.09.033> PMID: 25374359
- McGinley MJ, David SV, McCormick DA. Cortical membrane potential signature of optimal states for sensory signal detection. *Neuron*. 2015; 87(1):179–192. <https://doi.org/10.1016/j.neuron.2015.05.038> PMID: 26074005
- Vinck M, Batista-Brito R, Knoblich U, Cardin JA. Arousal and locomotion make distinct contributions to cortical activity patterns and visual encoding. *Neuron*. 2015; 86(3):740–754. <https://doi.org/10.1016/j.neuron.2015.03.028> PMID: 25892300
- Bezdudnaya T, Cano M, Bereshpolova Y, Stoelzel CR, Alonso JM, Swadlow HA. Thalamic burst mode and inattention in the awake LGNd. *Neuron*. 2006; 49(3):421–432. <https://doi.org/10.1016/j.neuron.2006.01.010> PMID: 16446145
- Steriade M, McCormick DA, Sejnowski TJ. Thalamocortical oscillations in the sleeping and aroused brain. *Science*. 1993; 262(5134):679–685. <https://doi.org/10.1126/science.8235588> PMID: 8235588
- McCormick DA. Neurotransmitter actions in the thalamus and cerebral cortex and their role in neuromodulation of thalamocortical activity. *Prog Neurobiol*. 1992; 39(4):337–388. [https://doi.org/10.1016/0301-0082\(92\)90012-4](https://doi.org/10.1016/0301-0082(92)90012-4) PMID: 1354387
- Erisken S, Vaiceliunaite A, Jurjut O, Fiorini M, Katzner S, Busse L. Effects of Locomotion Extend throughout the Mouse Early Visual System. *Curr Biol*. 2014; 24(24):2899–2907. <https://doi.org/10.1016/j.cub.2014.10.045> PMID: 25484299

13. Nestvogel DB, McCormick DA. Visual Thalamocortical Mechanisms of Waking State Dependent Activity and Alpha Oscillations. *Neuron*. 2022; 1(5):120–138.e4. <https://doi.org/10.1016/j.neuron.2021.10.005> PMID: 34687663
14. Sherman SM. Tonic and burst firing: dual modes of thalamocortical relay. *Trends Neurosci*. 2001; 24(2):122–126. [https://doi.org/10.1016/s0166-2236\(00\)01714-8](https://doi.org/10.1016/s0166-2236(00)01714-8) PMID: 11164943
15. Alonso JM, Usrey WM, Reid RC. Precisely Correlated Firing in Cells of the Lateral Geniculate Nucleus. *Nature*. 1996; 383(6603):815–819. <https://doi.org/10.1038/383815a0> PMID: 8893005
16. Kremkow J, Perrinet LU, Masson GS, Aertsen A. Functional Consequences of Correlated Excitatory and Inhibitory Conductances in Cortical Networks. *J Comput Neurosci*. 2010; 28(3):579–594. <https://doi.org/10.1007/s10827-010-0240-9> PMID: 20490645
17. Bruno RM. Synchrony in Sensation. *Curr Opin Neurobiol*. 2011; 21(5):701–708. <https://doi.org/10.1016/j.conb.2011.06.003> PMID: 21723114
18. Swadlow HA, Gusev AG. The impact of 'bursting' thalamic impulses at a neocortical synapse. *Nat Neurosci*. 2001; 4(4):402–408. <https://doi.org/10.1038/86054> PMID: 11276231
19. Stringer C, Pachitariu M, Steinmetz N, Reddy CB, Carandini M, Harris KD. Spontaneous behaviors drive multidimensional, brainwide activity. *Science*. 2019; 364(6437):255–255. <https://doi.org/10.1126/science.aav7893> PMID: 31000656
20. Aston-Jones G, Cohen JD. An integrative theory of locus coeruleus-norepinephrine function: adaptive gain and optimal performance. *Annu Rev Neurosci*. 2005; 28:403–450. <https://doi.org/10.1146/annurev.neuro.28.061604.135709> PMID: 16022602
21. Totah NK, Logothetis NK, Eschenko O. Noradrenergic ensemble-based modulation of cognition over multiple timescales. *Brain Res*. 2019; 1709:50–66. <https://doi.org/10.1016/j.brainres.2018.12.031> PMID: 30586547
22. Cohen JY, Amoroso MW, Uchida N. Serotonergic neurons signal reward and punishment on multiple timescales. *Elife*. 2015; 4:e06346. <https://doi.org/10.7554/eLife.06346> PMID: 25714923
23. Parikh V, Kozak R, Martinez V, Sarter M. Prefrontal acetylcholine release controls cue detection on multiple timescales. *Neuron*. 2007; 56(1):141–154. <https://doi.org/10.1016/j.neuron.2007.08.025> PMID: 17920021
24. Reimer J, McGinley MJ, Liu Y, Rodenkirch C, Wang Q, McCormick DA, et al. Pupil fluctuations track rapid changes in adrenergic and cholinergic activity in cortex. *Nat Commun*. 2016; 7(1):1–7. <https://doi.org/10.1038/ncomms13289> PMID: 27824036
25. Williamson RS, Hancock KE, Shinn-Cunningham BG, Polley DB. Locomotion and task demands differentially modulate thalamic audiovisual processing during active search. *Curr Biol*. 2015; 25(14):1885–1891. <https://doi.org/10.1016/j.cub.2015.05.045> PMID: 26119749
26. Hess EH, Polt JM. Pupil size in relation to mental activity during simple problem-solving. *Science*. 1964; 143(3611):1190–1192. <https://doi.org/10.1126/science.143.3611.1190> PMID: 17833905
27. Schriver BJ, Bagdasarov S, Wang Q. Pupil-linked arousal modulates behavior in rats performing a whisker deflection direction discrimination task. *J Neurophysiol*. 2018; 120(4):1655–1670. <https://doi.org/10.1152/jn.00290.2018> PMID: 29995602
28. de Gee JW, Tsetsos K, Schwabe L, Urai AE, McCormick D, McGinley MJ, et al. Pupil-linked phasic arousal predicts a reduction of choice bias across species and decision domains. *Elife*. 2020; 9:e54014. <https://doi.org/10.7554/eLife.54014> PMID: 32543372
29. Huang NE, Shen Z, Long SR, Wu MC, Shih HH, Zheng Q, et al. The empirical mode decomposition and the Hilbert spectrum for nonlinear and non-stationary time series analysis. *Proc Math Phys Eng Sci*. 1971; 1998(454):903–995.
30. Lu SM, Guido W, Sherman SM. Effects of membrane voltage on receptive field properties of lateral geniculate neurons in the cat: contributions of the low-threshold Ca²⁺ conductance. *J Neurophysiol*. 1992; 68(6):2185–2198. <https://doi.org/10.1152/jn.1992.68.6.2185> PMID: 1337104
31. Niell CM, Stryker MP. Modulation of visual responses by behavioral state in mouse visual cortex. *Neuron*. 2010; 65(4):472–479. <https://doi.org/10.1016/j.neuron.2010.01.033> PMID: 20188652
32. Spacek MA, Crombie D, Bauer Y, Born G, Liu X, Katzner S, et al. Robust effects of corticothalamic feedback and behavioral state on movie responses in mouse dLGN. *Elife*. 2022; 11:e70469. <https://doi.org/10.7554/eLife.70469> PMID: 35315775
33. Burlingham CS, Mirbagheri S, Heeger DJ. A unified model of the task-evoked pupil response. *Science Adv*. 2022; 8(16):eabi9979. <https://doi.org/10.1126/sciadv.abi9979> PMID: 35442730
34. Wurtz RH. Neuronal mechanisms of visual stability. *Vis Res*. 2008; 48(20):2070–2089. <https://doi.org/10.1016/j.visres.2008.03.021> PMID: 18513781

35. Lesica NA, Stanley GB. Encoding of natural scene movies by tonic and burst spikes in the lateral geniculate nucleus. *J Neurosci*. 2004; 24(47):10731–10740. <https://doi.org/10.1523/JNEUROSCI.3059-04.2004> PMID: 15564591
36. Alitto HJ, Weyand TG, Usrey WM. Distinct properties of stimulus-evoked bursts in the lateral geniculate nucleus. *J Neurosci*. 2005; 25(2):514–523. <https://doi.org/10.1523/JNEUROSCI.3369-04.2005> PMID: 15647497
37. Alitto H, Rathbun DL, Vandeleeest JJ, Alexander PC, Usrey WM. The augmentation of retinogeniculate communication during thalamic burst mode. *J Neurosci*. 2019; 39(29):5697–5710. <https://doi.org/10.1523/JNEUROSCI.2320-18.2019> PMID: 31109958
38. Aydın Ç, Couto J, Giugliano M, Farrow K, Bonin V. Locomotion modulates specific functional cell types in the mouse visual thalamus. *Nat Commun*. 2018; 9(1):1–12.
39. Franke K, Willeke KF, Ponder K, Galdamez M, Zhou N, Muhammad T, et al. State-dependent pupil dilation rapidly shifts visual feature selectivity. *Nature*. 2022; 610(7930):128–134. <https://doi.org/10.1038/s41586-022-05270-3> PMID: 36171291
40. Liang L, Fratzl A, Reggiani JDS, El Mansour O, Chen C, Andermann ML. Retinal Inputs to the Thalamus Are Selectively Gated by Arousal. *Curr Biol*. 2020; 30(20):3923–3934. <https://doi.org/10.1016/j.cub.2020.07.065> PMID: 32795442
41. Zeraati R, Shi YL, Steinmetz NA, Gieselmann MA, Thiele A, Moore T, et al. Intrinsic timescales in the visual cortex change with selective attention and reflect spatial connectivity. *Nat Commun*. 2023; 14(1):1858. <https://doi.org/10.1038/s41467-023-37613-7> PMID: 37012299
42. Cavanagh SE, Hunt LT, Kennerley SW. A diversity of intrinsic timescales underlie neural computations. *Front Neural Circuits*. 2020; 14:615626. <https://doi.org/10.3389/fncir.2020.615626> PMID: 33408616
43. Okun M, Steinmetz NA, Lak A, Dervinis M, Harris KD. Distinct structure of cortical population activity on fast and infraslow timescales. *Cereb Cortex*. 2019; 29(5):2196–2210. <https://doi.org/10.1093/cercor/bhz023> PMID: 30796825
44. Collins L, Francis J, Emanuel B, McCormick DA. Cholinergic and noradrenergic axonal activity contains a behavioral-state signal that is coordinated across the dorsal cortex. *Elife*. 2023; 12:e81826. <https://doi.org/10.7554/eLife.81826> PMID: 37102362
45. Noei S, Zouridis IS, Logothetis NK, Panzeri S, Totah NK. Distinct ensembles in the noradrenergic locus coeruleus are associated with diverse cortical states. *Proc Natl Acad Sci U S A*. 2022; 119(18):e2116507119. <https://doi.org/10.1073/pnas.2116507119> PMID: 35486692
46. Marshall JD, Aldarondo DE, Dunn TW, Wang WL, Berman GJ, Ölveczky BP. Continuous whole-body 3D kinematic recordings across the rodent behavioral repertoire. *Neuron*. 2021; 109(3):420–437. <https://doi.org/10.1016/j.neuron.2020.11.016> PMID: 33340448
47. Monto S, Palva S, Voipio J, Palva JM. Very Slow EEG Fluctuations Predict the Dynamics of Stimulus Detection and Oscillation Amplitudes in Humans. *J Neurosci*. 2008; 28(33):8268–8272. <https://doi.org/10.1523/JNEUROSCI.1910-08.2008> PMID: 18701689
48. Joshi S, Li Y, Kalwani RM, Gold JI. Relationships between pupil diameter and neuronal activity in the locus coeruleus, colliculi, and cingulate cortex. *Neuron*. 2016; 89(1):221–234. <https://doi.org/10.1016/j.neuron.2015.11.028> PMID: 26711118
49. Lindvall O, Björklund A, Nobin A, Stenevi U. The adrenergic innervation of the rat thalamus as revealed by the glyoxylic acid fluorescence method. *J Comp Neurol*. 1974; 154(3):317–347. <https://doi.org/10.1002/cne.901540307> PMID: 4826099
50. Mackay-Sim A, Sefton AJ, Martin PR. Subcortical projections to lateral geniculate and thalamic reticular nuclei in the hooded rat. *J Comp Neurol*. 1983; 213(1):24–35. <https://doi.org/10.1002/cne.902130103> PMID: 6826786
51. Hallanger AE, Levey AI, Lee HJ, Rye DB, Wainer BH. The origins of cholinergic and other subcortical afferents to the thalamus in the rat. *J Comp Neurol*. 1987; 262(1):105–124. <https://doi.org/10.1002/cne.902620109> PMID: 2442206
52. Sokhadze G, Seabrook TA, Guido W. The absence of retinal input disrupts the development of cholinergic brainstem projections in the mouse dorsal lateral geniculate nucleus. *Neural Dev*. 2018; 13(1):1–15.
53. Huerta-Ocampo I, Hacıoglu-Bay H, Dautan D, Mena-Segovia J. Distribution of Midbrain Cholinergic Axons in the Thalamus. *eNeuro*. 2019; 7(1):ENEURO.0454–19.2019. <https://doi.org/10.1523/eneuro.0454-19.2019> PMID: 31882534
54. Sokhadze G, Campbell PW, Guido W. Postnatal development of cholinergic input to the thalamic reticular nucleus of the mouse. *Eur J Neurosci*. 2019; 49(8):978–989. <https://doi.org/10.1111/ejn.13942> PMID: 29761601

55. Holdefer RN, Jacobs BL. Phasic Stimulation of the Locus Coeruleus: Effects on Activity in the Lateral Geniculate Nucleus. *Exp Brain Res*. 1994; 100(3):444–452. <https://doi.org/10.1007/BF02738404> PMID: 7813682
56. Rodenkirch C, Liu Y, Schriver BJ, Wang Q. Locus coeruleus activation enhances thalamic feature selectivity via norepinephrine regulation of intrathalamic circuit dynamics. *Nat Neurosci*. 2019; 22(1):120–133. <https://doi.org/10.1038/s41593-018-0283-1> PMID: 30559472
57. Osorio-Forero A, Cardis R, Vantomme G, Guillaume-Gentil A, Katsioudi G, Devenoges C, et al. Noradrenergic circuit control of non-REM sleep substates. *Curr Biol*. 2021; 31(22):5009–5023.e7. <https://doi.org/10.1016/j.cub.2021.09.041> PMID: 34648731
58. Castro-Alamancos MA, Oldford E. Cortical sensory suppression during arousal is due to the activity-dependent depression of thalamocortical synapses. *J Physiol*. 2002; 541(1):319–331.
59. Lu SM, Guido W, Sherman SM. The brain-stem parabrachial region controls mode of response to visual stimulation of neurons in the cat's lateral geniculate nucleus. *Vis Neurosci*. 1993; 10(4):631–642. <https://doi.org/10.1017/s0952523800005332> PMID: 8338800
60. Leiras R, Cregg JM, Kiehn O. Brainstem circuits for locomotion. *Ann Rev Neurosci*. 2022; 45:63–85. <https://doi.org/10.1146/annurev-neuro-082321-025137> PMID: 34985919
61. Ma R, Cui H, Lee SH, Anastasio TJ, Malpeli JG. Predictive encoding of moving target trajectory by neurons in the parabrachial nucleus. *J Neurophysiol*. 2013; 109(8):2029–2043. <https://doi.org/10.1152/jn.01032.2012> PMID: 23365185
62. Asanuma C. Noradrenergic innervation of the thalamic reticular nucleus: a light and electron microscopic immunohistochemical study in rats. *J Comp Neurol*. 1992; 319(2):299–311. <https://doi.org/10.1002/cne.903190209> PMID: 1381728
63. Bickford M, Günlük A, Van Horn S, Sherman S. GABAergic projection from the basal forebrain to the visual sector of the thalamic reticular nucleus in the cat. *J Comp Neurol*. 1994; 348(4):481–510. <https://doi.org/10.1002/cne.903480402> PMID: 7836559
64. Woolf NJ, Butcher LL. Cholinergic systems in the rat brain: III. Projections from the pontomesencephalic tegmentum to the thalamus, tectum, basal ganglia, and basal forebrain. *Brain Res Bull*. 1986; 16(5):603–637. [https://doi.org/10.1016/0361-9230\(86\)90134-6](https://doi.org/10.1016/0361-9230(86)90134-6) PMID: 3742247
65. Sundberg SC, Lindström SH, Sanchez GM, Granseth B. Cre-expressing neurons in visual cortex of Ntsr1-Cre GN220 mice are corticothalamic and are depolarized by acetylcholine. *J Comp Neurol*. 2018; 526(1):120–132. <https://doi.org/10.1002/cne.24323> PMID: 28884467
66. Augustinaite S, Kuhn B. Complementary Ca²⁺ Activity of Sensory Activated and Suppressed Layer 6 Corticothalamic Neurons Reflects Behavioral State. *Curr Biol*. 2020; 30(20):3945–3960. <https://doi.org/10.1016/j.cub.2020.07.069> PMID: 32822605
67. Chen C, Regehr WG. Presynaptic modulation of the retinogeniculate synapse. *J Neurosci*. 2003; 23(8):3130–3135. <https://doi.org/10.1523/JNEUROSCI.23-08-03130.2003> PMID: 12716920
68. Reggiani JDS, Jiang Q, Barbini M, Lutas A, Liang L, Fernando J, et al. Brainstem serotonergic neurons selectively gate retinal information flow to thalamus. *Neuron*. 2023; 111(5):711–726.e11. <https://doi.org/10.1016/j.neuron.2022.12.006> PMID: 36584680
69. Bouvier G, Senzai Y, Scanziani M. Head movements control the activity of primary visual cortex in a luminance-dependent manner. *Neuron*. 2020; 108(3):500–511. <https://doi.org/10.1016/j.neuron.2020.07.004> PMID: 32783882
70. Guido W, Weyand T. Burst responses in thalamic relay cells of the awake behaving cat. *J Neurophysiol*. 1995; 74(4):1782–1786. <https://doi.org/10.1152/jn.1995.74.4.1782> PMID: 8989413
71. Borden PY, Wright NC, Morrisette AE, Jaeger D, Haider B, Stanley GB. Thalamic bursting and the role of timing and synchrony in thalamocortical signaling in the awake mouse. *Neuron*. 2022; 110(17):2836–2853.e8. <https://doi.org/10.1016/j.neuron.2022.06.008> PMID: 35803270
72. Whitmire CJ, Waiblinger C, Schwarz C, Stanley GB. Information Coding through Adaptive Gating of Synchronized Thalamic Bursting. *Cell Rep*. 2016; 14(4):795–807. <https://doi.org/10.1016/j.celrep.2015.12.068> PMID: 26776512
73. Mukherjee P, Kaplan E. Dynamics of neurons in the cat lateral geniculate nucleus: in vivo electrophysiology and computational modeling. *J Neurophysiol*. 1995; 74(3):1222–1243. <https://doi.org/10.1152/jn.1995.74.3.1222> PMID: 7500146
74. Reinagel P, Godwin D, Sherman SM, Koch C. Encoding of visual information by LGN bursts. *J Neurophysiol*. 1999; 81(5):2558–2569. <https://doi.org/10.1152/jn.1999.81.5.2558> PMID: 10322089
75. Grubb MS, Thompson ID. Visual response properties of burst and tonic firing in the mouse dorsal lateral geniculate nucleus. *J Neurophysiol*. 2005; 93(6):3224–3247. <https://doi.org/10.1152/jn.00445.2004> PMID: 15601741

76. Lesica NA, Weng C, Jin J, Yeh CI, Alonso JM, Stanley GB. Dynamic encoding of natural luminance sequences by LGN bursts. *PLoS Biol.* 2006; 4(7):e209. <https://doi.org/10.1371/journal.pbio.0040209> PMID: 16756389
77. Mease RA, Kuner T, Fairhall AL, Groh A. Multiplexed spike coding and adaptation in the thalamus. *Cell Rep.* 2017; 19(6):1130–1140. <https://doi.org/10.1016/j.celrep.2017.04.050> PMID: 28494863
78. Zeldenrust F, Chameau P, Wadman WJ. Spike and burst coding in thalamocortical relay cells. *PLoS Comput Biol.* 2018; 14(2):1–36. <https://doi.org/10.1371/journal.pcbi.1005960> PMID: 29432418
79. Rivadulla C, Martinez L, Grieve KL, Cudeiro J. Receptive field structure of burst and tonic firing in feline lateral geniculate nucleus. *J Physiol.* 2003; 553(2):601–610. <https://doi.org/10.1113/jphysiol.2003.048561> PMID: 12972624
80. Kerschensteiner D, Guido W. Organization of the dorsal lateral geniculate nucleus in the mouse. *Vis Neurosci.* 2017;34. <https://doi.org/10.1017/S0952523817000062> PMID: 28965501
81. Piscopo DM, El-Danaf RN, Huberman AD, Niell CM. Diverse visual features encoded in mouse lateral geniculate nucleus. *J Neurosci.* 2013; 33(11):4642–4656. <https://doi.org/10.1523/JNEUROSCI.5187-12.2013> PMID: 23486939
82. Rosón MR, Bauer Y, Kotkat AH, Berens P, Euler T, Busse L. Mouse dLGN receives functional input from a diverse population of retinal ganglion cells with limited convergence. *Neuron.* 2019; 102(2):462–476. <https://doi.org/10.1016/j.neuron.2019.01.040> PMID: 30799020
83. Molnár B, Sere P, Bordé S, Koós K, Zsigri N, Horváth P, et al. Cell-Type Specific Arousal-Dependent Modulation of Thalamic Activity in the Lateral Geniculate Nucleus. *Cereb Cortex Commun.* 2021. <https://doi.org/10.1093/texcom/tgab020> PMID: 34296165
84. Neske GT, Nestvogel D, Steffan PJ, McCormick DA. Distinct waking states for strong evoked responses in primary visual cortex and optimal visual detection performance. *J Neurosci.* 2019; 39(50):10044–10059. <https://doi.org/10.1523/JNEUROSCI.1226-18.2019> PMID: 31672787
85. Petty GH, Kinnischtzke AK, Hong YK, Bruno RM. Effects of arousal and movement on secondary somatosensory and visual thalamus. *eLife.* 2021; 10. <https://doi.org/10.7554/eLife.67611> PMID: 34842139
86. Schröder S, Steinmetz NA, Krumin M, Pachitariu M, Rizzi M, Lagnado L, et al. Arousal Modulates Retinal Output. *Neuron.* 2020; 107(3):487–495.e9. <https://doi.org/10.1016/j.neuron.2020.04.026> PMID: 32445624
87. Schwartz ZP, Buran BN, David SV. Pupil-associated states modulate excitability but not stimulus selectivity in primary auditory cortex. *J Neurophysiol.* 2020; 123(1):191–208. <https://doi.org/10.1152/jn.00595.2019> PMID: 31721652
88. Parker PRL, Brown MA, Smear MC, Niell CM. Movement-Related Signals in Sensory Areas: Roles in Natural Behavior. *Trends Neurosci.* 2020. <https://doi.org/10.1016/j.tins.2020.05.005> PMID: 32580899
89. Parker PRL, Martins DM, Leonard ESP, Casey NM, Sharp SL, Abe ETT, et al. A dynamic sequence of visual processing initiated by gaze shifts. *Nat Neurosci.* 2023; 26(12):2192–2202. <https://doi.org/10.1038/s41593-023-01481-7> PMID: 37996524
90. Orłowska-Feuer P, Ebrahimi AS, Zippo AG, Petersen RS, Lucas RJ, Storch R. Look-up and look-down neurons in the mouse visual thalamus during freely moving exploration. *Curr Biol.* 2022; 32(18):3987–3999. <https://doi.org/10.1016/j.cub.2022.07.049> PMID: 35973431
91. Saleem AB, Busse L. Interactions between rodent visual and spatial systems during navigation. *Nat Rev Neurosci.* 2023. <https://doi.org/10.1038/s41583-023-00716-7> PMID: 37380885
92. Rueden CT, Schindelin J, Hiner MC, DeZonia BE, Walter AE, Arena ET, et al. ImageJ2: ImageJ for the next Generation of Scientific Image Data. *BMC Bioinf.* 2017; 18(1). <https://doi.org/10.1186/s12859-017-1934-z> PMID: 29187165
93. Schindelin J, Arganda-Carreras I, Frise E, Kaynig V, Longair M, Pietzsch T, et al. Fiji: An Open-Source Platform for Biological-Image Analysis. *Nat Methods.* 2012; 9(7):676–682. <https://doi.org/10.1038/nmeth.2019> PMID: 22743772
94. Pachitariu M, Steinmetz NA, Kadir SN, Carandini M, Harris KD. Fast and Accurate Spike Sorting of High-Channel Count Probes with KiloSort. In: Lee DD, Sugiyama M, Luxburg UV, Guyon I, Garnett R, editors. *Advances in Neural Information Processing Systems 29*. Curran Associates, Inc.; 2016. p. 4448–4456.
95. Spacek MA, Blanche TJ, Swindale NV. Python for large-scale electrophysiology. *Front Neuroinform.* 2009; 2:9. <https://doi.org/10.3389/neuro.11.009.2008> PMID: 19198646
96. Swindale NV, Spacek MA. Spike sorting for polytrodes: a divide and conquer approach. *Front Syst Neurosci.* 2014; 8:6. <https://doi.org/10.3389/fnsys.2014.00006> PMID: 24574979

97. Quiroga RQ, Nadasdy Z, Ben-Shaul Y. Unsupervised spike detection and sorting with wavelets and super-paramagnetic clustering. *Neural Comput.* 2004; 16(8):1661–1687. <https://doi.org/10.1162/089976604774201631> PMID: 15228749
98. Henze DA, Borhegyi Z, Csicsvari J, Mamiya A, Harris KD, Buzsaki G. Intracellular Features Predicted by Extracellular Recordings in the Hippocampus In Vivo. *J Neurophysiol.* 2000; 84(1):390–400. <https://doi.org/10.1152/jn.2000.84.1.390> PMID: 10899213
99. Hazan L, Zugaro M, Buzsaki G. Klusters, NeuroScope, NDManager: A free software suite for neurophysiological data processing and visualization. *J Neurosci Methods.* 2006; 155(2):207–216. <https://doi.org/10.1016/j.jneumeth.2006.01.017> PMID: 16580733
100. Siapas AG, Lubenov EV, Wilson MA. Prefrontal phase locking to hippocampal theta oscillations. *Neuron.* 2005; 46(1):141–151. <https://doi.org/10.1016/j.neuron.2005.02.028> PMID: 15820700
101. Biased Kutil R. and unbiased estimation of the circular mean resultant length and its variance. *Statistics.* 2012; 46(4):549–561.
102. Churchland MM, Byron MY, Cunningham JP, Sugrue LP, Cohen MR, Corrado GS, et al. Stimulus onset quenches neural variability: a widespread cortical phenomenon. *Nat Neurosci.* 2010; 13(3):369–378. <https://doi.org/10.1038/nn.2501> PMID: 20173745
103. Stuart EA. Matching methods for causal inference: A review and a look forward. *Stat Sci.* 2010; 25(1):1. <https://doi.org/10.1214/09-STS313> PMID: 20871802
104. Harris KD. Nonsense correlations in neuroscience. *bioRxiv.* 2020. <https://doi.org/10.1101/2020.11.29.402719>
105. Shimazaki H, Shinomoto S. Kernel bandwidth optimization in spike rate estimation. *J Comput Neurosci.* 2010; 29:171–182. <https://doi.org/10.1007/s10827-009-0180-4> PMID: 19655238

4 A unified model of dLGN stimulus-responses and modulation

The following chapter is reproduced from an article originally published in *bioRxiv*:

Lisa Schmors, Ann H Kotkat, Yannik Bauer, Ziwei Huang, Davide Crombie, Lukas Meyerolbersleben, Sacha Sokoloski, Philipp Berens, Laura Busse (2024). The combination of stimulus-driven and modulatory inputs in visual thalamus depend on visual responsiveness and stimulus type. *bioRxiv*, 2023.10.18.562960. DOI: <https://doi.org/10.1101/2023.10.18.562960>.

Author contributions

The study was conceptualized by SS, PB, and LB. YB, AK, and LM performed the experiments. LS, AK, YB, LM, and DC all contributed to the data curation. The methodology was developed by LS, YB, AK, ZH, DC, SS, PB, and LB. The formal analysis was performed by LS, AK, and YB. LS, AK, YB, ZH, and DC all contributed to developing the software infrastructure supporting the investigation. Data visualization was performed by LS, AK, and YB. LB, LS, AK, and YB wrote the original draft, and all authors contributed to reviewing and editing the manuscript. Supervision was provided by SS, PB and LB. PB and LB were responsible for project administration, funding acquisition, and provided the resources necessary to carry out the study.

Personal contributions

DC wrote the software used to perform video-based eye tracking and curated the eye tracking data, which was then used as input to the spline-GLM model. DC also contributed substantially to the software infrastructure used to support the investigation. DC further participated in early discussions on how behavioural variables might be included in the model, and contributed to reviewing and editing the manuscript.

Copyright

This article was published with all rights reserved. Permission was obtained from the supervising author, LB, to reproduce the article here.

The combination of stimulus-driven and modulatory inputs in visual thalamus depend on visual responsiveness and stimulus type

Lisa Schmors^{1,*}, Ann H. Kotkat^{3,4,*}, Yannik Bauer^{3,4,*}, Ziwei Huang^{1,2}, Davide Crombie^{3,4}, Lukas S. Meyerolbersleben^{3,4}, Sacha Sokoloski¹, Philipp Berens^{1,2,+}, and Laura Busse^{3,5,+}

¹Hertie Institute for AI in Brain Health, University of Tübingen, 72076 Tübingen, Germany

²Tübingen AI Center, University of Tübingen, 72076 Tübingen, Germany

³Division of Neuroscience, Faculty of Biology, LMU Munich, 82152 Munich, Germany

⁴Graduate School of Systemic Neurosciences (GSN), LMU Munich, 82152 Munich, Germany

⁵Bernstein Center for Computational Neuroscience, 82152 Munich, Germany

*These authors contributed equally to this work

+Correspondence: busse@bio.lmu.de (L.B.), philipp.berens@uni-tuebingen.de (P.B.)

ABSTRACT

In the dorsolateral geniculate nucleus (dLGN) of the thalamus, stimulus-driven signals are combined with modulatory inputs such as corticothalamic (CT) feedback and behavioural state. How these shape dLGN activity remains an open question. We recorded extracellular responses in dLGN of awake mice to a movie stimulus, while photosuppressing CT feedback, and tracking locomotion and pupil size. To assess the relative impact of stimulus and modulatory inputs, we fit single neuron responses with generalized linear models. While including CT feedback and behavioural state as predictors significantly improved the model's overall performance, the improvement was especially pronounced for a subpopulation of neurons poorly responsive to the movie stimulus. In addition, the observed impact of CT feedback was faster and more prevalent in the absence of a patterned visual stimulus. Finally, for neurons that were sensitive to CT feedback, visual stimuli could be more easily discriminated based on spiking activity when CT feedback was suppressed. Together, these results show that effects of modulatory inputs in dLGN depend on visual responsiveness and stimulus type.

Introduction

Visual information is processed through a hierarchy of brain areas, which are connected by feedforward and feedback projections. Early in this hierarchy is the dorsolateral geniculate nucleus (dLGN) of the thalamus, a central node for visual information *en route* from the retina to the primary visual cortex (V1) (1, 2). The dLGN has long been recognized as one of the first visual stages that combines stimulus-driven inputs with additional modulatory inputs (3), such as signals arising from L6 cortico-thalamic (CT) feedback (4, 5, 6, 7, 8), and signals from the brainstem carrying information related to behavioural state (9, 10, 11, 12) and arousal (10, 13, 14, 3). Since these factors have often been investigated in separate studies, their combined effects on dLGN responses remain poorly understood. Overall, we lack a quantitative understanding of the relative strengths of these modulatory effects on dLGN responses during wakefulness and how they might interact and depend on stimulus-driven input.

On the one hand, it has been firmly established that, even during wakefulness, dLGN responses are modulated according to the animal's internal (15, 9) and overt behavioural state (16, 15, 17). For instance, in the mouse, locomotion- (11, 18) or pupil-indexed arousal (10, 9, 14, 19, 13) are associated with overall enhancements of firing rates in dLGN, which seem to preferentially affect specific neuronal populations depending on their spatio-temporal feature selectivity (18, 19). Similar to related findings in the somatosensory system (20), the increase in dLGN firing rates seems to be a necessary condition for the sustained depolarisation of primary visual cortex during active behaviours (9).

On the other hand, little consensus has been achieved for dLGN modulations by CT feedback, where a plethora of previous studies have together highlighted its diverse and potentially stimulus-dependent effects. For instance, given that CT feedback can sharpen spatial dLGN RFs and increase contextual effects (21, 22, 23, 6, 24, 7), CT feedback might enhance or suppress overall firing rates, depending on the size, feature-selectivity and retinotopic position of dLGN neurons (6, 7, 22). The combination of enhancing and suppressing effects of CT feedback are likely mediated by a differential engagement of both direct excitatory

and indirect inhibitory pathways, whose balance will depend on the stimulus selectivity, connectivity and intrinsic properties of corticothalamic neurons in L6 V1, neurons in the thalamic reticular nucleus (TRN) and dLGN (8, 25).

Generalized linear models (GLMs) provide an established framework for statistical analysis of neural responses, that can help to disentangle the combined impact of multiple stimulus-driven and modulatory influences and investigate their properties (26, 27, 28). While GLMs are relatively simple phenomenological models, they offer the advantage of being interpretable: for instance, GLM kernels learned for the visual stimulus approximate the integration by the spatio-temporal receptive field (RF), and kernels learned for any additional inputs represent spike-induced gain adjustments (29, 27). First applied in the retina (30, 27), GLMs have since then been used in numerous studies to separate influences of the visual stimulus and other variables, like spike history, interneuronal interaction effects, task-engagement, learning, reward prediction, task-related motor action, locomotion, and arousal (31, 32, 33, 34, 35, 36, 37). One recent extension of classical GLMs is to estimate RFs by choosing a set of cubic spline basis functions in order to encode smoothness, decrease the number of parameters, and thus be more data efficient (38).

Here, we investigated how feedforward, stimulus-driven signals, feedback signals, and behavioural state jointly influence dLGN activity in awake, head-fixed mice viewing a rich movie stimulus. We simultaneously recorded extracellular dLGN activity, mouse run speed and pupil size, while photosuppressing CT feedback. We then fitted a spline-GLM model containing kernels for the spatio-temporal RF, CT feedback and behaviour to predict responses of dLGN neurons. The learned kernels were biologically plausible, including diverse spatio-temporal RFs, as well as kernels for behaviour and CT feedback. We found that our model could successfully capture response components derived from the movie input, yielding RF kernels which were generally aligned with response features obtained from simple luminance steps. Including modulatory inputs overall improved the prediction of dLGN responses; the improvements, however, were most prominent for a subpopulation of neurons that were poorly predicted by the movie stimulus. Focusing on effects of CT feedback, we found that these effects depended on stimulus type in both the model and the data, being stronger, more prevalent and faster during the absence of a patterned visual stimulus. Finally, we used the spline-GLM for *in silico* experiments isolating the impact of CT feedback suppression, and demonstrate that stimulus discrimination for CT feedback-modulated neurons was enhanced. We conclude that effects of modulatory inputs in dLGN depend on visual responsiveness and stimulus type.

Results

dLGN responses to movies are modulated by behavioural variables and CT feedback suppression

To investigate how CT feedback, locomotion and arousal modulate thalamic responses, we recorded *in vivo* extracellular dLGN activity in response to a rich movie stimulus in four head-fixed mice together with running speed and pupil size, while randomly photo-suppressing CT feedback (Figure 1a). For photo-suppression of CT feedback, we conditionally expressed the soma-targeting, chloride-conducting channelrhodopsin stGtACR2-RFP (39) in L6 CT pyramidal cells, by injecting a small volume of Cre-dependent AAV into V1 of Ntsr1-Cre mice (40). The localisation of stGtACR2 to L6 CT somata and the accurate placement of electrodes were confirmed through post-mortem histological analyses (Figure 1b). During electrophysiological recordings, the mouse viewed a rich movie stimulus that consisted of a sequence of black-and-white clips from various feature films ('movies', Figure 1c, top). Here, photo-suppression occurred with 50% probability in each 1 second time bin. We also measured the mouse's run speed and pupil size to infer the animal's changing behavioural state.

To develop initial insights into the modulations of dLGN responses by CT feedback and the other potentially modulating inputs, we aligned movie responses to onsets of photo-suppression, running, and pupil dilation. We found that certain neurons responded to the onset of CT feedback suppression with a substantial reduction in firing rate (Figure 1d,e, OFF-ON transitions in blue), while others showed milder effects or no modulation at all (Figure 1f, left). Despite the relatively small effect size, the overall reduction of dLGN firing rates during CT feedback suppression was genuine, as none of the recorded neurons in a control mouse without opsin expression showed systematic modulations at light onset (Figure S1a, b). Furthermore, neural responses aligned to time points in which the light was not switched on (i.e., OFF-OFF transitions in grey, Figure 1d, e) did not show any systematic modulation (Figure S1c). Finally, neurons with stronger CT feedback effects were closer to each other (Figure S2), as predicted by the topography of the corticothalamic system (41, 7, 42, 43). Consistent with previous findings (11, 18, 10, 44), we also found that during our movie stimulus, firing rates could gradually increase around transitions from sitting to running (Figure S3a), and during pupil dilation (Figure S3b).

These modulations of dLGN responses were also observed across the population of recorded neurons. Specifically, dLGN firing rates during the time of CT feedback suppression compared to periods without CT feedback suppression were reduced (*control vs. CT FB supp.* mean: 12.6 vs. 11.5 Hz, $p = 1.24 \times 10^{-2}$, paired Wilcoxon signed-rank test; Figure 1f, left), while time windows with running and dilated pupil were associated with an overall increase in average firing rates (*sit vs. run* mean: 11.0 vs. 12.8 Hz, $p = 8.31 \times 10^{-16}$, Figure 1f, middle; *small vs. large pupil* mean: 11.0 vs. 13.0 Hz, $p = 4.98 \times 10^{-7}$, paired Wilcoxon signed-rank test; Figure 1f, right). Although these modulations affected the recorded dLGN population on average, we also noticed considerable neuron-to-neuron variability. Indeed, for all three modulatory inputs, we found neurons that

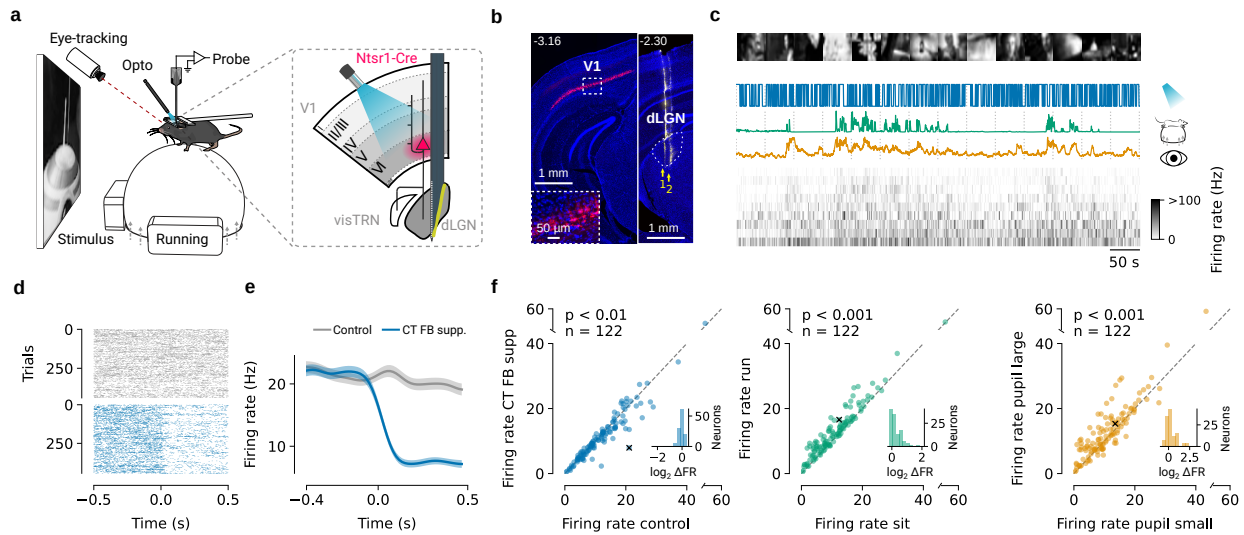


Figure 1 | CT feedback and behaviour modulates dLGN responses to movies (a) Schematic of the recording setup and photo-suppression of V1 L6 CT pyramidal neurons in *Ntsr1-Cre* mice with Cre-dependent AAV-stGtACR2-RFP. (b) Histology. *Left*: Coronal section near the V1 injection site, with stGtACR2-RFP expression (red) in *Ntsr1+* somata. Blue: DAPI; scale bar: 1 mm. *Inset*: Magnification of area marked by dotted rectangle. Scale bar: 50 μ m. *Right*: Coronal section of dLGN recording sites, with electrode tracks for two consecutive recording sessions (arrows 1 and 2) marked with DiI (yellow). Scale bar: 1 mm. *Dotted line*: dLGN contour. *Numbers on top*: position relative to Bregma in mm. (c) Snippet of an example dLGN recording. *Top to bottom*: example frames of the movie stimulus, photo-suppression pulse train (blue), running speed (green), pupil area (yellow), and time-varying firing rate (sorted by first principal component) of simultaneously recorded dLGN neurons. (d) Raster plot of responses of an example dLGN neuron, time locked to the onset of CT feedback photo-suppression (blue, OFF-ON transition) and to control periods without photosuppression (grey, OFF-OFF transition). Note that the example neuron illustrates the observed effect of CT feedback photo-suppression, but the size of the effect is not representative of that observed in the population of recorded dLGN neurons. (e) Corresponding PSTHs (solid line: average across trials, shaded area: standard error of the mean). (f) Effects of CT feedback photo-suppression (*left*), locomotion (*middle*), and pupil size (*right*) on dLGN mean firing rates. Example neuron from (d, e) marked with \times . *p* values denote results of a Wilcoxon signed-rank test, $n = 122$ neurons. *Insets*: Histogram of firing rate fold-change relative to control (Δ FR \log_2 -ratio).

exhibited substantial variations in firing rates across the different conditions (Figure 1f, insets).

So far, it seems that our movie stimulus elicited various responses in dLGN, which were modulated by multiple additional inputs, this simple analysis on the mean firing rates does not take into account potential correlations between the different inputs. Consistent with previous studies that have shown that pupil size and running index partially overlapping behavioural states (45, 46, 9), we found a positive correlation between pupil diameter and running speed ($r = 0.18 \pm 0.17$, mean \pm SD; $p < 0.001$ for 7/10 experiments, permutation test; Figure S3c). Moreover, we found pupil size to also be influenced by stimulus brightness, where lower average intensity of movie frames was associated with larger pupil diameters ($r = -0.41 \pm 0.15$, mean \pm SD; $p < 0.001$ for 10/10 experiments, permutation test; Figure S3c). Pupil diameter, in turn, is known, to influence responses in the early visual system (47, 48).

A spline-based GLM captures dLGN spatio-temporal RFs and their modulation by CT feedback and behaviour

To disentangle how the various potential influences shape the responses of dLGN neurons, we used a generalized linear model (GLM) (27) that predicted the neuron's firing rate based on a combination of stimulus-driven and modulatory inputs (running speed, pupil size, and CT feedback suppression) (Figure 2). The model consisted of one linear kernel for each input, followed by a softplus function that accounted for response nonlinearities (Figure 2a). The shape of the stimulus kernel captured the neuron's spatio-temporal RF, while the shapes of the modulatory kernels captured modulations of the neuron's firing. We employed a GLM with a spline basis (38) in order to efficiently generate smooth kernels, rather than operating directly on the pixels of the visual stimulus or the discrete time bins of the additional inputs (Figure S6a-d). The GLM allowed us to effectively capture the temporal correlations between the inputs (see also above, Figure S3c), and the spatio-temporal correlations in pixel intensities in naturalistic stimuli (49, 50) (Figure S4a).

We trained and evaluated the spline-GLM on the recorded data set as follows: Given the known diversity of mouse dLGN

feature selectivity (51, 52), we performed a separate hyperparameter search for each neuron. Hyperparameters included the number of spline bases for the stimulus and modulatory inputs and the weight for L1 regularisation (see Methods). All GLM fits in this study were cross-validated. The models analysed here were configured with the selected optimal hyperparameters and the reported performance is based on the held-out test set.

After model fitting, we assessed the predictive power of the learned kernel shapes using a session-based permutation test (Figure 2b). To keep the temporal statistics of the time series data intact, we provided the model with input data recorded on a different day (for the model inputs ‘stimulus’, ‘running’, ‘pupil size’) or with synthetic inputs generated with the same statistics as the original (for the ‘CT feedback suppression’ input). Subsequently, we compared for each input the actual model performance (Pearson’s r) against a distribution of model performances with that specific input permuted. Inputs were considered significant if the actual performance differed from the permuted performance with $p \leq 0.05$.

We observed a rich diversity of learned GLM kernels for the dLGN neurons’ spatio-temporal RFs, the effects of CT feedback, and the behavioural variables. To begin with, we considered three example neurons (Figure 2c). Of these, the first had a negative spatial and a transient temporal stimulus response kernel, which contributed significantly to the model’s performance ($p = 3.51 \times 10^{-2}$, permutation test; Figure 2c₁, top, same neuron as in Figure 1d,e). In addition, it had a significant negative kernel for CT feedback suppression ($p = 2.67 \times 10^{-4}$, permutation test; Figure 2c₂, c₃, top). In contrast, the running and pupil size kernels had minimal impact on this neuron’s model predictions ($p > 0.05$, permutation test). The second example neuron exhibited a positive spatial RF with an antagonistic surround ($p = 2.31 \times 10^{-3}$, permutation test; Figure 2c₁, middle). While both behavioural kernels seemed to contribute (Figure 2c₂, middle), only the kernel for pupil size reached significance in the permutation test ($p = 1.13 \times 10^{-2}$). This neuron was also not influenced by CT feedback suppression ($p > 0.05$; Figure 2c₃, middle). Finally, example neuron 3 was primarily visually driven, with a positive RF centre and a more sustained temporal response kernel ($p = 2.31 \times 10^{-3}$, permutation test; Figure 2c₁, bottom). It also had a significant negative kernel for CT feedback suppression ($p = 2.67 \times 10^{-4}$, permutation test; Figure 2c₃, bottom). The other two modulatory kernels had only negligible influences (permutation test, $p > 0.05$; Figure 2c₃, bottom).

The diversity observed in the three example neurons was also evident in the model fits across the population of recorded dLGN neurons, where we obtained a variety of spatio-temporal RFs, and combinations of modulatory influences. Assessing the learned spatio-temporal kernels, we found that $\sim 70\%$ of the recorded dLGN neurons were visually responsive to our movie stimulus (85/122 neurons; permutation test visual stimulus, $p \leq 0.05$; Figure S6e). For many of these neurons (representative examples in Figure 2d), the spline-GLM recovered spatial RF properties that were consistent with previous descriptions of mouse dLGN RFs obtained using artificial stimuli (51, 54, 55) and in many cases resembled those obtained from conventional sparse noise experiments (Figure S4b,c). These properties included various RF locations, RFs with either positive (66%, 56/85 neurons) or negative polarity kernels (34%, 29/85 neurons), a broad range of RF surround strengths (Figure S4d,f), and various RF centre sizes (Figure S4e). Furthermore, the GLM captured the well-known diversity of temporal response properties of dLGN neurons (56, 51), with some neurons showing more sustained, and others showing more transient temporal kernels (Figure 2e). Importantly, both the spatial and temporal GLM kernels matched well with the expected polarity and the dynamics obtained from clustering responses into sustained-OFF, Sustained-ON, and Transient groups during full-field luminance steps (Figure S5). This correspondence further underscores our model’s capacity to capture meaningful spatio-temporal RF properties and essential visual response characteristics of the recorded dLGN neurons.

We next assessed the learned kernels for the modulatory inputs. According to the permutation test, approximately 10% (12/122 neurons) of the recorded dLGN neurons were affected by CT feedback suppression, 11% (13/122 neurons) by running, and 19% (23/122 neurons) by pupil size (Figure 2f–h, Figure S6f–h). The overall direction of modulation for the significant kernels aligned with the modulation indices obtained directly from the data (Figure 1f): for the significantly modulated neurons, CT feedback suppression kernels were predominantly negative (Figure 2f), while running speed (Figure 2g) and pupil size (Figure 2h) kernels were predominantly positive. These results indicate that both CT feedback and behavioural state variables during natural movie viewing contribute to an overall increase of dLGN responses. Beyond the general sign of modulation, the learned model kernels also offered insights into the temporal dynamics of the modulatory influences: consistent with the well-known slow impact of pupil indexed arousal on responses in the visual system (46, 45), we found that kernels for pupil size had a more sustained profile compared to kernels for running modulations (time to half max kernel running vs. pupil size: 106.3 ms vs. 146.3 ms, Wilcoxon signed-rank test: $p = 7.51 \times 10^{-3}$, Figure S6p). This ability to learn differential kernels and a close correspondence between data-driven modulation indices and the impact of the modulatory inputs for model performance (Figure S7d–g) demonstrates that our GLM model was successful in extracting the impact of the various modulatory inputs.

Despite the spline-GLM’s overall success in predicting dLGN responses and learning biologically plausible kernels, it faced challenges in capturing fast modulations and response peaks, as typical also for traditional GLMs (26, 57). We also observed increased variance at the left side of some kernels particularly evident for running modulated neurons (Figure 2e–h and Figure S6i–l). This could potentially stem from typical boundary artefacts associated with splines (Figure S6a–d). Nevertheless, despite these challenges, incorporating running information proved beneficial, as confirmed by the permutation

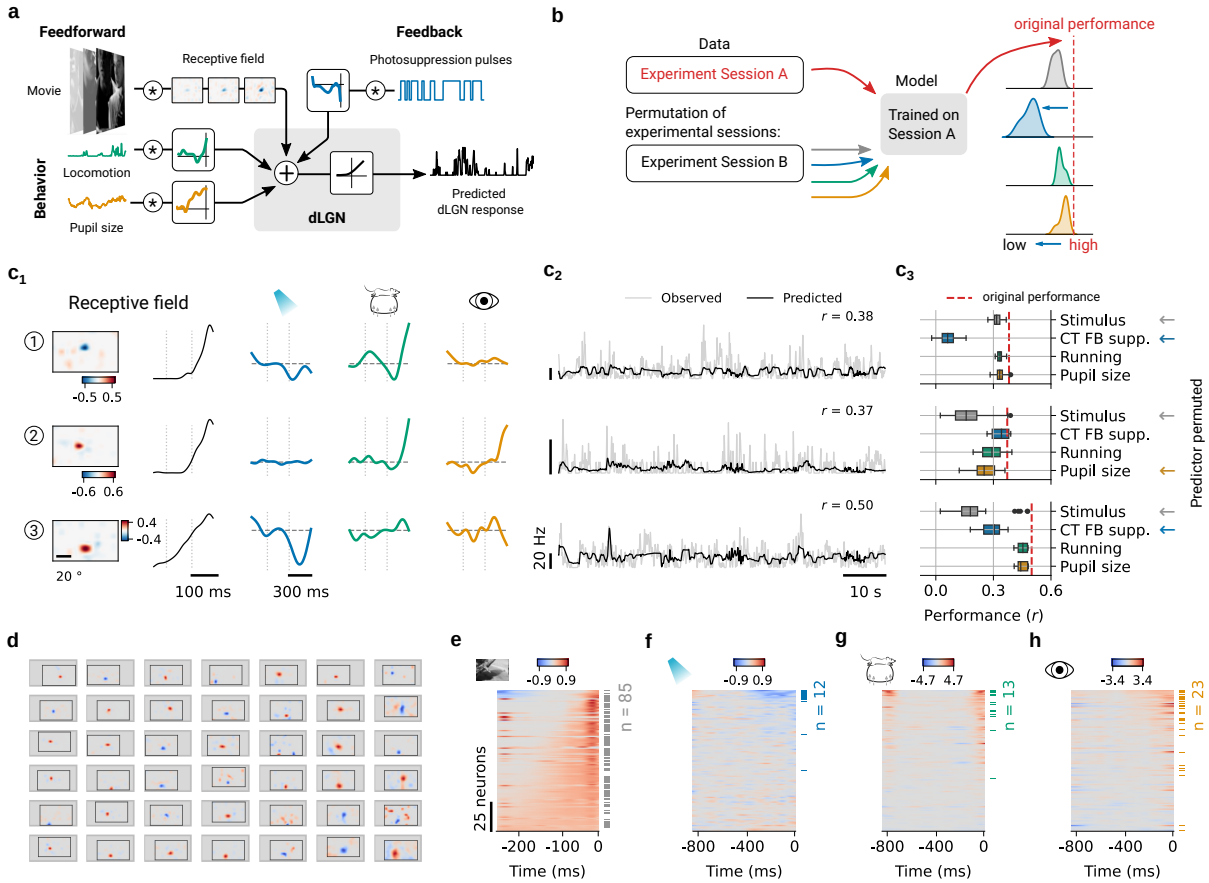


Figure 2 | Spline-based GLM captured the RF, the influence of CT feedback and the impact of behaviour on responses of dLGN neurons. (a) Schematics of the spline-GLM model architecture. Firing rate in dLGN was predicted as a combination of kernel outputs summed at the linear stage and then passed through a softplus nonlinearity. Each modelled neuron had a kernel for the stimulus and kernels for the three modulatory inputs: run speed (green), pupil size (orange), and CT feedback suppression (blue). (b) Schematics of the permutation test (53) to evaluate the significance of the learned kernels. Model performance was evaluated by comparing the actual correlation (Pearson r) between predicted and observed firing rates to correlations when one of the inputs was taken from an unrelated experimental session (for movie, running, and pupil size) or randomly generated with the same statistics (for CT feedback suppression). (c) Three dLGN example neurons, their learned kernels, firing rate predictions, and outcomes of the permutation test (neuron 1 is the same example neuron as in Figure 1d-e). (c₁) Spatial and temporal RF components separated by singular value decomposition (SVD, see Methods), along with kernels for the modulatory inputs. (c₂) Observed (gray) versus predicted (black) firing rates during 80 s of movie presentation. (c₃) Actual model performance (Pearson's r , red dashed line) and performance for permuted stimulus (gray), CT feedback suppression (blue), running (green), and pupil size (orange) inputs. Kernels that contribute significantly to the model's performance are marked with ←. (d) Spatial RFs of example neurons with significant stimulus kernels. Gray: outline of common visual space (azimuth: -35–110 deg; elevation: -35–50 deg); Solid lines: monitor border. (e) Temporal RFs (SVD component) of the stimulus kernel in the recorded dLGN population, sorted by their area under the curve. (f–h) Modulatory kernels in the recorded dLGN population, sorted by their area under the curve, for CT feedback suppression (f), running (g), and pupil size (h). Horizontal bars, side: Neurons with significant kernels based on the permutation test. Panels (e–h) show data from all $n = 122$ neurons.

test (Figure S6g). Reassuringly, these running modulated neurons showed reduced response reliability in repeated stimulus trials (Figure S6m,n) as their activity was substantially influenced by locomotion state. In line with a previous study (58), these neurons also had overall low firing rates (Figure S6o).

Is the contribution of modulatory inputs to dLGN neurons' activity consistent and strong enough to improve the prediction of dLGN responses? While dLGN has long been known to exhibit state-dependent changes in firing (15, 11, 59, 18) and to receive extensive feedback from cortex (60, 61), the impact of these influences, in particular during viewing of naturalistic stimuli, is not well understood. Thus, to quantitatively assess the contributions of CT feedback suppression and behavioural variables, we compared the performance between our model including all inputs and reduced variants of the model with only a subset of inputs (Figure 3a,b). Starting with the 'Stimulus only' model that only considered the stimulus as input, we found that incorporating one or more modulatory inputs increased the correlation between observed and predicted dLGN responses (ANOVA: $p = 0.022$; Figure 3a). In particular, adding pupil size or a combination of two or more predictors showed a significantly better performance than the 'Stimulus only' model ('Stimulus only' vs. 'Stimulus + Pupil size': 0.186 vs. 0.235, Wilcoxon signed-rank test: Bonferroni corrected $p = 3.39 \times 10^{-6}$; 'Stimulus only' vs. 'Full model': 0.186 vs. 0.249, Wilcoxon signed-rank test: Bonferroni corrected $p = 2.08 \times 10^{-7}$; Figure 3a). Note that even in the full model we still observed neurons with suboptimal predictions, maybe due to low response reliability (Figure S6m,n) and sparse firing (Figure S6o).

Indeed, when we compared the prediction performance of the 'Stimulus-only' model with the 'Full model' (Figure 3b), we noticed that the inclusion of the modulatory inputs did not merely shift the distribution to higher performances. Instead, a closer examination allowed us to identify a subgroup of neurons whose responses could be predicted only poorly by the visual stimulus, but which showed substantial improvements in their response prediction with the inclusion of modulatory factors (Figure 3c,d; we call them the 'Modulation-sensitive' group; Figure S7a-f). In contrast, another subgroup showed no improvement when we added the modulatory inputs (Figure 3c,d; 'Stimulus-explained' group). To test the extent to which this reflected a ceiling effect in explainable variance, we fitted models that had only the modulatory factor as inputs but not the stimulus ('CT FB supp.' + 'Running' + 'Pupil size'; 'Modulation only' models; Figure 3f). For these models, neurons substantially affected by modulatory inputs still performed well (Figure 3f, 'Modulation-sensitive', dark dots), whereas those well-explained by the visual stimulus exhibited lower performance, although not zero (Figure 3f, 'Stimulus-explained', light grey dots). This indicates that even in the 'Stimulus-explained' group, modulatory inputs might have some, albeit generally weak effect that was obscured in the full model; alternatively, some modulatory factors might contain stimulus information, in particular pupil size, which is known to be related not only to arousal, but also to stimulus brightness (Figure S3c). Taken together, our analysis of model performance suggests that dLGN neurons are explained by the visual stimulus, behaviour and CT feedback, albeit with considerable heterogeneity.

CT feedback is enhanced in the absence of a patterned visual stimulus

Our model showed only a relatively small subset of dLGN neurons with significant effects of CT feedback. Could the reason for this be that the responses elicited by the rich naturalistic movie stimulus might have dominated dLGN activity relative to the effects of CT feedback? We thus predicted that CT feedback effects might be stronger without patterned stimulus input (Figure 4a).

To test this prediction, we expanded our analyses to the period of blank screen stimulation flanking the movie presentation, and compared the effects of CT feedback suppression in the recorded data and in models fit separately to responses during movies vs. blank periods (Figure 4b). Consistent with our prediction, we indeed observed that CT feedback suppression reduced the firing rates of individual example neurons more strongly during blanks ($MI_{CT\ FB\ supp.}$: -0.65, Figure 4c₁) compared to movies ($MI_{CT\ FB\ supp.}$: -0.45, Figure 4c₂). This observation held true across the recorded dLGN population (mean $MI_{CT\ FB\ supp.}$: -0.09 vs. -0.03; $p = 2.5 \times 10^{-6}$, Wilcoxon signed-rank test; Figure 4d). Furthermore, during blank periods, more dLGN neurons were affected by the suppression of CT feedback (45% vs. 18% with $|MI_{CT\ FB\ supp.}| \geq 0.1$; Figure 4j). The stronger effect of CT feedback suppression could not be explained by the difference in overall firing rate between the two stimulus conditions (Figure S8a-b), nor was it related to the different number of optogenetic pulses (Figure S8c).

Is the stronger modulation by CT feedback suppression during blank periods vs. movies also captured by our spline-GLM model? We indeed found that the model learned a more negative CT feedback suppression kernel for the blank condition compared to the movie, both in the example neuron (peak amplitude -1.8 vs. -0.94; Figure 4f) as well as in the population of neurons with a significant CT feedback suppression kernel (-0.86 vs. -0.46, $p = 0.044$, Mann-Whitney-U test, Figure 4g; all neurons: -0.4 vs. -0.2, $p = 5 \times 10^{-8}$, Wilcoxon signed-rank test). To avoid potential confounds of firing rates on kernel amplitudes (Figure S8d,e) and enable a more direct comparison to the recorded data, we used the model predictions in the two stimulus conditions and calculated model-derived $MI_{CT\ FB\ supp.}$, analogously to those based on the recorded data. Consistent with our data-driven observations, we found that CT feedback suppression reduced modelled responses more strongly during the blank periods (modelled $MI_{CT\ FB\ supp.}$: -0.057) compared to movies (-0.017; $p = 0.002$, Wilcoxon signed-rank test, Figure 4h).

Inspecting the learned model kernels (Figure 4f,g) suggested that, besides amplitude, the dynamics of the CT feedback

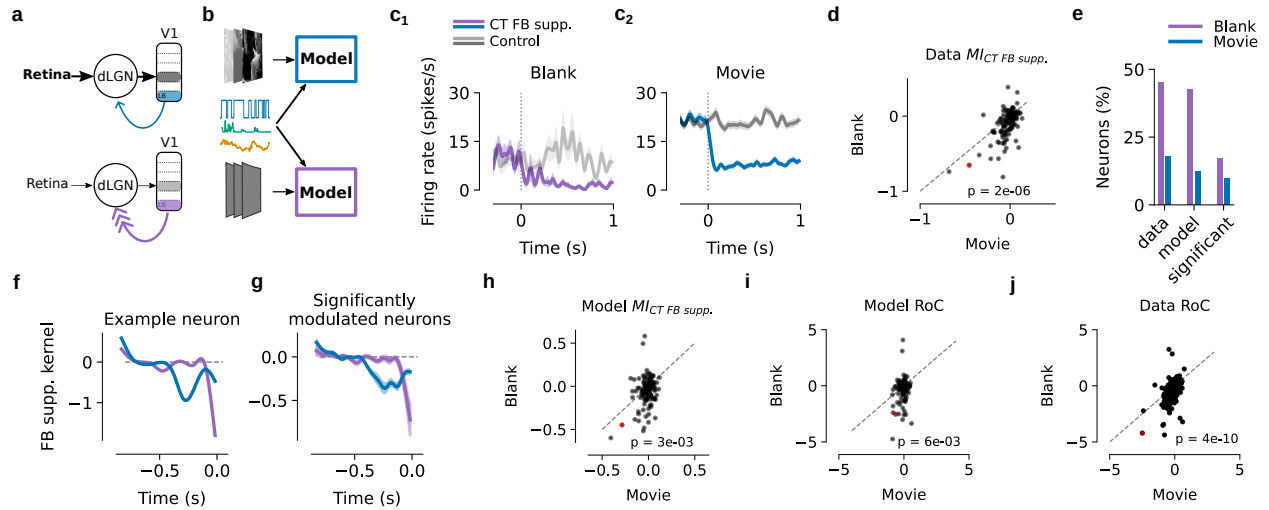


Figure 4 | The effect of CT feedback is dependent on the presence or absence of the visual stimulus. (a) Schematics of the hypothesis that the absence of a patterned visual stimulus elicits weaker stimulus-driven input to dLGN, which is in turn accompanied by stronger CT feedback. Note that the schematics should not imply stronger L6 CT pyramidal neuron firing, but that the net effect of CT feedback on dLGN firing is stronger in the absence of a patterned visual stimulus. (b) Schematics of fitting the spline-GLM model separately during movies (*top*) vs. blank periods (*bottom*). (c) Effects of CT feedback suppression. (c₁) Mean PSTHs time locked to onset of photosuppression for one example dLGN neuron (same example neuron as in [Figure 1d-e](#)) during blank periods (gray screen) flanking the movie presentation. The shaded area represents the SEM. (c₂) Same as (c₁), during movie presentation. *Purple, blue*: PSTH during CT feedback suppression (OFF-ON transition), *light grey, dark grey*: PSTH during control condition (OFF-OFF transition). (d) Comparison of $MI_{CT\ FB\ supp.}$ during blanks vs. movies for the recorded dLGN population (number of neurons $n = 122$). (e) Percentage of recorded dLGN neurons modulated by CT feedback during the two stimulus conditions. Three modulation metrics were separately considered to count the modulated neurons. A neuron was considered modulated (1) based on data: $|MI_{CT\ FB\ supp.}|$ from (d) ≥ 0.1 , (2) based on model predictions: $|MI_{CT\ FB\ supp.}|$ from (h) ≥ 0.1 , or (3) based on model performance: permutation test $p \leq 0.05$. Notably, all three modulation metrics consistently revealed a higher proportion of neurons displaying CT feedback modulation during the blank condition compared to the movie condition. (f) CT feedback suppression kernel for the example dLGN neuron in (c₁). The model was either trained on the data from movie presentation (*dark blue*) or blank periods (*light blue*). (g) Same for all significantly CT feedback modulated neurons ($n_{movie} = 12$, $n_{blank} = 21$). Solid lines represent the mean of the kernels and transparent surrounds represent the standard error of the mean (SEM). (h) Comparison of $MI_{CT\ FB\ supp.}$ for blanks vs. movies calculated from simulated data using the fitted model for the dLGN population to the two stimuli. (i) Comparison of the Rate of Change (RoC) of model-predicted neurons' responses to CT feedback suppression during movie presentation vs. blank periods. (j) Same as (i), for the recorded data. Panels (h-j) show data from all 122 neurons.

suppression effects might also differ between visual stimulus conditions. Specifically, the spline-GLM learned a kernel characterised by a faster and briefer time course for blank periods compared to movie stimulation. This observation could be quantified by calculating the rate of change (RoC) of the neurons' predicted and actual responses after photosuppression (see Methods). Indeed, we found that the effect of CT feedback suppression was faster during blank periods (model-based RoC: $p = 0.004$, Wilcoxon signed-rank test, [Figure 4i](#); data-based: $p = 9 \times 10^{-12}$, Wilcoxon signed-rank test, [Figure 4j](#)). In conclusion, the fitted spline-GLM models revealed that the observed impact of CT feedback suppression was weaker and slower during the presence of a rich patterned visual stimulus in comparison to blank periods, suggesting that the observed effect of CT feedback depends on the visual stimulus characteristics.

CT feedback affects stimulus decoding

Finally, we sought to better understand if and how the suppression of CT feedback affected how dLGN encoded visual information ([Figure 5](#)). Specifically, we tested the degree to which suppression of CT feedback might affect the decoding of movie information based on the responses of single dLGN neurons, compared to the control condition where feedback was intact.

To address our question, we used the trained model ('Full model') to describe how individual dLGN neurons encode stimulus information ([Figure 5a](#)). In this way, we were able to isolate the effects of CT feedback suppression *in silico*, by keeping stimulus, running and pupil inputs intact, and only changing CT feedback suppression (setting the CT feedback suppression either OFF (0) or ON (1)). We then performed a decoding experiment, using simulated model responses to

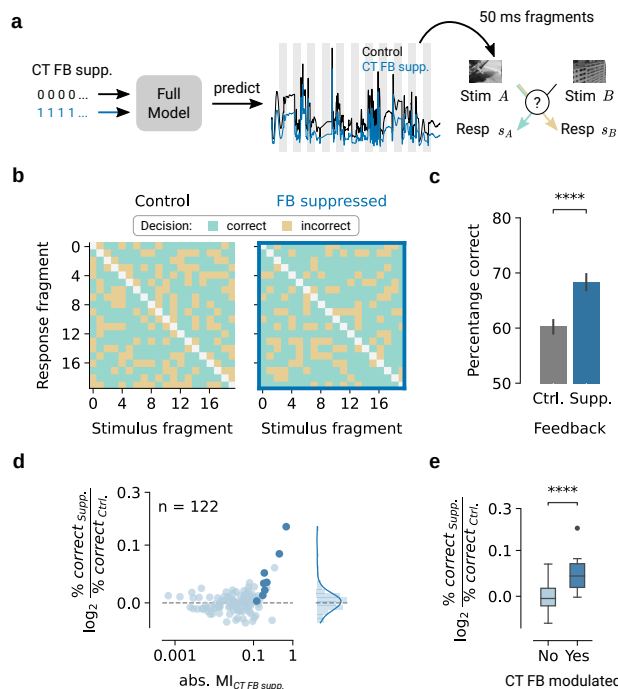


Figure 5 | Two-alternative-forced-choice decoder shows better stimulus discrimination for CT feedback modulated neurons when feedback is suppressed. (a) Schematics of the decoder: the trained model was used to simulate responses with CT feedback being either on (blue) or off (black; 70 s example trace). Random 50 ms stimulus fragments (A and B) were chosen, each with corresponding simulated responses. The decoder's task was to determine which stimulus was more likely based on the observed responses. (b) Decision matrix for one example neuron with 20 random stimulus fragments and their simulated responses. Green: correct pairing of stimulus and response; yellow: incorrect pairing. Left: control condition; right: CT feedback suppressed condition. (c) Percentage of correct decisions in the control and the CT feedback suppressed condition, same example modelled neuron as in (b). Error bars indicate 95% confidence intervals. (d) Decoder performance across all neurons ($n = 122$) as a function of the amount of modulation by photosuppression observed in the experiment. Dark blue: neurons with a significant CT feedback kernel. (e) Relative decoder performance during CT feedback suppression and control conditions, split according to whether neurons were significantly modulated by CT feedback suppression (dark blue) or not modulated (light blue).

discriminate between video clips in a two-alternative forced choice (2AFC) setting (30). We randomly selected 50 ms fragments of stimulus-response-pairs from the test set that had not been used for model fitting. To discriminate between two movie clips, we used the maximum-likelihood decoding rule from Pillow et al. (2005) (30). The decision of the 2AFC decoder was directly derived from the model likelihood for the correct and incorrect pairing (see Methods and (30)). We considered the 2AFC decoder to make a correct decision if the likelihood for the correct pairing was higher compared to the incorrect one. We found that the decoder made more correct decisions in the FB suppressed condition compared to the control condition (Figure 5b, 20 representative stimulus-response pairs for one example neuron; Figure 5c, across all 100 stimulus pairs 68.34 % vs. 60.27 %, $p = 1.20 \times 10^{-12}$, Wilcoxon rank sum test).

To quantify the discrimination performance for each neuron, we computed the log ratio of the percent of correct choices in the FB suppressed condition and the control condition (Figure 5d), with positive log ratios indicating better decoding performance in the CT feedback suppressed state. The observed log-ratios near zero for the majority of neurons suggest that there was no difference in stimulus information between control conditions and CT feedback suppression (average 1.003 ± 0.021 , mean \pm SD; Figure 5d). However, we found significantly higher log-ratios in neurons modulated by CT feedback compared to non-modulated neurons ($p = 5.84 \times 10^{-14}$, skew test against null; Figure 5d, right and Figure 5e). Consequently, our model predicts that with intact CT feedback, short duration activity of individual dLGN neurons can be less informative about the visual stimulus.

Discussion

Here, we quantitatively characterised how dLGN responses during viewing of a naturalistic movie are influenced by the combination of visual stimulus-related inputs, CT feedback and behavioural state. We modelled the responses of individual dLGN neurons using a data-efficient GLM, which predicted the spatio-temporal RFs and response modulations by CT FB suppression, the animal's run speed, and pupil size. We found that overall model performance improved when including the modulatory predictors, in particular for a subpopulation of dLGN neurons whose responses were poorly explained by the visual stimulus. Guided by the model, we found that the effect of CT FB suppression depended on stimulus type, being relatively stronger, more prevalent, and faster in the absence of a patterned visual stimulus. Finally, using Bayesian decoding, we found that the responses of a subset of CT-feedback-sensitive dLGN neurons contained more visual information when CT feedback was suppressed. Together, our results show that the activity of dLGN neurons is governed by a combination of stimulus-driven and modulatory inputs and is mediated by their visual responsiveness and the stimulus type.

Using a spline-GLM for modelling thalamic responses

Our work extends previous approaches that modelled thalamic processing of naturalistic visual stimuli (e.g., (62, 37, 36)). In particular, our framework allowed us to test model variants with different combination of predictors, which revealed a subpopulation of dLGN neurons whose responses were poorly predicted by the movie stimulus and more strongly affected by the modulatory inputs. These might correspond to a previously reported set of neurons in mouse dLGN, amounting to 30–40%, with poor or unclear visual feature selectivity (63, 56). Given that this subpopulation also contained an over-representation of low-firing neurons, their relatively stronger modulation (see also (58)) might be indicative of a tight inhibitory / excitatory coupling in the recorded network (64). Such tight coupling in the thalamo-cortico-thalamic network might be mechanistically achieved through joint modulations of dLGN relay cells, and inhibitory neurons in dLGN and the thalamic reticular nucleus by CT feedback and neuromodulation (1, 4, 7, 9).

The general success of our model is indicated by the close neuron-by-neuron correspondence between RF properties and response types derived from the model and more traditional analyses and stimuli, and by the prominent relationship between learned model kernels and data-driven modulation indices for CT feedback suppression, run speed and pupil size. Yet, while our data-driven modulation indices generally matched well with the magnitudes of modulatory influences previously observed in mouse dLGN (11, 18, 10, 7, 14), we were surprised to find only a relatively small fraction of dLGN neurons with significant kernels for CT feedback suppression, running and pupil size. Reasons for the small fraction might be at least threefold: (1) the conservative method for assessing significance in the model derived from session-based permutation tests (53), (2) the continuous nature of inputs to the model rather than a split into extreme conditions for some of the modulation indices (e.g., locomotion slower than 0.25 cm/s was considered as sitting but only faster than 1 cm/s was considered as running (11, 18)), (3) the direct suppression of L6 CT feedback through the light-gated chloride channel stGtACR2 (39), which might have yielded comparatively weaker effects (see also (10, 65)) than alternative approaches recruiting powerful intracortical inhibition through photostimulation of inhibitory V1 neurons (7, 6, 66, 10, 65, 9).

In the future, our spline-GLM could be extended by thalamic mechanisms, such as the fast adaptation of integration time according to luminance and contrast (67, 62), accounting for the constant changes in spatial and temporal integration elicited by dynamic natural stimuli (68). Further, by combining the model inputs, one could test for interactions, for instance to clarify the dependence of CT feedback effects and behavioural state-related modulations as proposed by some studies (65). Incorporating adaptive amplitudes of input and post-spike kernels (69) could differentiate tonic and burst spiking behaviours, characteristic of thalamic neurons (70) and known to be affected by both stimulus-related (71) and modulatory inputs (72, 15, 11, 10). Finally, alternative modelling approaches based on deep neural networks (DNNs) (73, 74, 75) promise to better capture non-linear dynamics and provide faster computations, potentially enhancing our capabilities to emulate neuronal responses and complex neural interactions, yet likely at the expense of interpretability and uncontrolled biases (76, 77). Some recent efforts have been made to increase the interpretability and biological plausibility of such models (78, 79), at times, by crafting an integrative model combining the advantageous non-linearity of DNNs with linear models like ours (80, 81).

Spatio-temporal RFs and modulatory inputs of mouse dLGN neurons

Through a combination of analysing receptive fields obtained from the model using a naturalistic movie stimulus, a noise stimulus, and more traditional RF mapping techniques, we identified both expected and unexpected types of dLGN spatio-temporal RFs. Indeed, consistent with previous studies quantifying RFs in mouse dLGN to simple stimuli (51, 56, 55, 54), our model learned circular spatial RFs for the majority of neurons, which often consisted of a single domain resembling the well known ON and OFF fields. Reminiscent of a study showing that retinal ganglion cells can reverse the polarity of their RFs in response to different natural images (82), we found that some dLGN neurons had an opposite RF polarity when characterised with simple luminance steps or the movie stimulus. Finally, some of the RFs obtained with our modelling approach had a complex spatial structure, and might thus correspond to a subset of dLGN neurons that had been previously noted to lack clearly localised RFs (56, 54). Future studies, for instance based on the “maximally exciting image” approach initially applied to mouse V1 (83), are needed to verify to which degree these complex RF structures indeed reflect complex feature selectivity of dLGN neurons or might be potential consequences of the modelling approach.

Despite its frequent portrayal as a relay station, the dLGN of the thalamus has long been recognised as one of the earliest stages in the visual system that integrates visual representations with additional information (3, 15, 12, 4, 84). Corroborating this, we found that the performance of our model generally improved with the inclusion of modulatory inputs, albeit with considerable neuron-by-neuron diversity. Previous studies have already reported differential effects of behavioural state and arousal, and could relate them to the neurons’ feature selectivity (85, 18, 19). In dLGN, the firing of neurons with nonlinear responses to high spatial frequencies and with transient ON responses seem preferentially enhanced by locomotion (18). In addition, retinal boutons preferring low spatial frequencies and luminance decrements seem preferentially suppressed by arousal (19). The neuron-by-neuron diversity in the impact of the modulatory inputs might thus serve to enhance particular visual inputs during active states.

CT feedback effects on single dLGN neuron stimulus encoding and decoding

Our observation of faster and relatively stronger CT feedback effects during blank periods compared to movie viewing contributes to the growing appreciation that CT feedback effects on dLGN firing rates seem to be stimulus-dependent, and potentially overridden by strong visual stimulation (see also (86, 10)). Indeed, the effect of CT feedback seems to be most potent in the absence of patterned stimulus input, both in mice (this study and (41, 10) for related findings with gratings) and ferrets (86), which might point to a common mechanism across species. We propose that a greater influence of CT feedback suppression during spontaneous activity than movie viewing could arise from a differential engagement of direct excitatory and inhibitory feedback pathways during these visual stimulus types. Supplying thalamic relay neurons with different ratios of excitatory and inhibitory conductances, mimicking the impact of modulatory inputs, can shift their input/output function, such that the same somatic input can generate markedly different spiking responses (87, 88). Future studies will need to use more subtle manipulations of stimulus type, including contrast and spatial structure, together with pathway-specific CT feedback suppression, to test the hypothesis that CT feedback might be most effective under challenging sensory conditions. In addition, future studies will profit from simultaneous recordings of V1 and dLGN to further disentangle the origin and potential interaction of CT feedback and other modulatory influences.

We also observed that suppressing CT feedback enhanced the decoding of visual information in individual, feedback-sensitive neurons. This was surprising given prior research associating cortico-cortical feedback with attention and enhancements of stimulus encoding (e.g., (89, 90, 91, 92, 93)). What could be potential reasons why our model predicted improved decoding during CT feedback suppression? Past research has proposed that one role of CT feedback could be to linearise the input-output relationship of thalamic neurons through the injection of synaptic noise (87, 88). This linearisation would enhance the excitability of thalamic neurons to weaker inputs, but would additionally push them into more unreliable firing regimes. This could be one potential explanation why our decoder operating on single stimulus segments performed worse with CT feedback intact. A shift towards more unreliable firing regimes by CT feedback would also be in line with results of a previous study (10), showing that CT feedback during repeated movie segments increased the trial-by-trial variability of dLGN neurons' responses. Such increased variability in individual dLGN neurons could be offset and even exploited by the strong convergence in the thalamocortical system (94, 95). Specifically, synaptic noise mediated by CT feedback might allow to extract from the pooled afferent signal stimulus-related information with better resolution and with enhanced sensitivity to weaker inputs (87, 88). Thus, in the future, a more realistic decoder would consider local populations of thalamocortical neurons, to test the hypothesis that, through CT feedback mediated synaptic noise, cortex regulates the trade-off between heightened sensitivity towards ambiguous inputs and reliable representation of clear inputs.

In conclusion, our results add to the growing body of evidence that dLGN activity is influenced not only by visual inputs but also by modulatory influences from CT feedback and behavioural state. Our work presents an important step towards a quantitative understanding of how dLGN responses to complex, naturalistic stimuli are shaped by the simultaneous influences of stimulus-related feedforward inputs, CT feedback and behaviour.

References

1. W Guido, Development, form, and function of the mouse visual thalamus. *J. Neurophysiol.* **120**, 211–225 (2018).
2. WM Usrey, HJ Alitto, Visual Functions of the Thalamus. *Annu. Rev. Vis. Sci.* **1**, 351–371 (2015).
3. TG Weyand, The multifunctional lateral geniculate nucleus. *Rev. Neurosci.* **27**, 135–157 (2016).
4. AM Sillito, J Cudeiro, HE Jones, Always returning: feedback and sensory processing in visual cortex and thalamus. *Trends Neurosci.* **29**, 307–316 (2006).
5. F Briggs, WM Usrey, Corticogeniculate feedback and parallel processing in the primate visual system. *J. Physiol.* **589**, 33–40 (2011).
6. SR Olsen, DS Bortone, H Adesnik, M Scanziani, Gain control by layer six in cortical circuits of vision. *Nature* **483**, 47–52 (2012).
7. G Born, et al., Corticothalamic feedback sculpts visual spatial integration in mouse thalamus. *Nat. Neurosci.* **24**, 1711–1720 (2021).
8. GMG Shepherd, N Yamawaki, Untangling the cortico-thalamo-cortical loop: cellular pieces of a knotty circuit puzzle. *Nat. Rev. Neurosci.* **22**, 389–406 (2021).
9. DB Nestvogel, DA McCormick, Visual thalamocortical mechanisms of waking state-dependent activity and alpha oscillations. *Neuron* **110**, 120–138.e4 (2022).
10. MA Spacek, et al., Robust effects of corticothalamic feedback and behavioral state on movie responses in mouse dLGN. *Elife* **11**, e70469 (2022).
11. S Erisken, et al., Effects of locomotion extend throughout the mouse early visual system. *Curr. Biol.* **24**, 2899–2907 (2014).
12. DA McCormick, Neurotransmitter actions in the thalamus and cerebral cortex and their role in neuromodulation of thalamocortical activity. *Prog. Neurobiol.* **39**, 337–388 (1992).
13. D Crombie, MA Spacek, C Leibold, L Busse, Spiking activity in the visual thalamus is coupled to pupil dynamics across temporal scales. *PLoS Biol.* **22**, e3002614 (2024).
14. B Molnár, et al., Cell Type-Specific Arousal-Dependent Modulation of Thalamic Activity in the Lateral Geniculate Nucleus. *Cereb. Cortex Commun.* **2**, tgab020 (2021).
15. T Bezdudnaya, et al., Thalamic burst mode and inattention in the awake LGNd. *Neuron* **49**, 421–432 (2006).
16. HA Swadlow, TG Weyand, Corticogeniculate neurons, corticotectal neurons, and suspected interneurons in visual cortex of awake rabbits: receptive-field properties, axonal properties, and effects of EEG arousal. *J. Neurophysiol.* **57**, 977–1001 (1987).
17. M Cano, T Bezdudnaya, HA Swadlow, JM Alonso, Brain state and contrast sensitivity in the awake visual thalamus. *Nat. Neurosci.* **9**, 1240–1242 (2006).
18. Ç Aydın, J Couto, M Giugliano, K Farrow, V Bonin, Locomotion modulates specific functional cell types in the mouse visual thalamus. *Nat. Commun.* **9**, 4882 (2018).
19. L Liang, et al., Retinal inputs to the thalamus are selectively gated by arousal. *Curr. Biol.* **30**, 3923–3934.e9 (2020).
20. JFA Poulet, LMJ Fernandez, S Crochet, CCH Petersen, Thalamic control of cortical states. *Nat. Neurosci.* **15**, 370–372 (2012).
21. JW McClurkin, RT Marrocco, Visual cortical input alters spatial tuning in monkey lateral geniculate nucleus cells. *The J. Physiol.* **348**, 135–152 (1984).
22. PC Murphy, AM Sillito, Corticofugal feedback influences the generation of length tuning in the visual pathway. *Nature* **329**, 727–729 (1987).
23. HE Jones, et al., Differential feedback modulation of center and surround mechanisms in parvocellular cells in the visual thalamus. *The J. Neurosci.* **32**, 15946–15951 (2012).
24. JM Hasse, F Briggs, Corticogeniculate feedback sharpens the temporal precision and spatial resolution of visual signals in the ferret. *Proc. Natl. Acad. Sci. United States Am.* **114**, E6222–E6230 (2017).
25. SR Crandall, SJ Cruikshank, BW Connors, A corticothalamic switch: controlling the thalamus with dynamic synapses. *Neuron* **86**, 768–782 (2015).

26. L Paninski, Maximum likelihood estimation of cascade point-process neural encoding models. *Network: Comput. Neural Syst.* **15**, 243–262 (2004).
27. JW Pillow, et al., Spatio-temporal correlations and visual signalling in a complete neuronal population. *Nature* **454**, 995–999 (2008).
28. DA Butts, Data-driven approaches to understanding visual neuron activity. *Annu. Rev. Vis. Sci.* **5**, 451–477 (2019).
29. L Paninski, J Pillow, J Lewi, *Statistical models for neural encoding, decoding, and optimal stimulus design*. (Elsevier), p. 493–507 (2007).
30. JW Pillow, L Paninski, VJ Uzzell, EP Simoncelli, EJ Chichilnisky, Prediction and decoding of retinal ganglion cell responses with a probabilistic spiking model. *J. Neurosci.* **25**, 11003–11013 (2005).
31. NA Steinmetz, P Zatzka-Haas, M Carandini, KD Harris, Distributed coding of choice, action and engagement across the mouse brain. *Nature* **576**, 266–273 (2019).
32. CA Runyan, E Piasini, S Panzeri, CD Harvey, Distinct timescales of population coding across cortex. *Nature* **548**, 92–96 (2017).
33. IM Park, MLR Meister, AC Huk, JW Pillow, Encoding and decoding in parietal cortex during sensorimotor decision-making. *Nat. Neurosci.* **17**, 1395–1403 (2014).
34. S Musall, MT Kaufman, AL Juavinett, S Gluf, AK Churchland, Single-trial neural dynamics are dominated by richly varied movements. *Nat. Neurosci.* **22**, 1677–1686 (2019).
35. PM Goltstein, S Reinert, T Bonhoeffer, M Hübener, Mouse visual cortex areas represent perceptual and semantic features of learned visual categories. *Nat. Neurosci.* **24**, 1441–1451 (2021).
36. B Babadi, A Casti, Y Xiao, E Kaplan, L Paninski, A generalized linear model of the impact of direct and indirect inputs to the lateral geniculate nucleus. *J. Vis.* **10**, 22–22 (2010).
37. DA Butts, C Weng, J Jin, JM Alonso, L Paninski, Temporal precision in the visual pathway through the interplay of excitation and stimulus-driven suppression. *J. Neurosci.* **31**, 11313–11327 (2011).
38. Z Huang, Y Ran, J Oesterle, T Euler, P Berens, Estimating smooth and sparse neural receptive fields with a flexible spline basis. *Neurons, Behav. Data analysis, Theory* **8**, 1–14 (2021).
39. M Mahn, et al., High-efficiency optogenetic silencing with soma-targeted anion-conducting channelrhodopsins. *Nat. Commun.* **9**, 4125 (2018).
40. S Gong, et al., Targeting Cre Recombinase to Specific Neuron Populations with Bacterial Artificial Chromosome Constructs. *J. Neurosci.* **27**, 9817–9823 (2007).
41. MA Kirchgessner, AD Franklin, EM Callaway, Distinct “driving” versus “modulatory” influences of different visual corticothalamic pathways. *Curr. Biol.* **31**, 5121–5137 (2021).
42. T Tsumoto, O Creutzfeldt, C Legendy, Functional organization of the corticofugal system from visual cortex to lateral geniculate nucleus in the cat: With an appendix on geniculo-cortical mono-synaptic connections. *Exp. Brain Res.* **32** (1978).
43. JM Ichida, VA Casagrande, Organization of the feedback pathway from striate cortex (V1) to the lateral geniculate nucleus (LGN) in the owl monkey (*aotus trivirgatus*). *J. Comp. Neurol.* **454**, 272–283 (2002).
44. L Liang, et al., A fine-scale functional logic to convergence from retina to thalamus. *Cell* **173**, 1343–1355.e24 (2018).
45. J Reimer, et al., Pupil Fluctuations Track Fast Switching of Cortical States during Quiet Wakefulness. *Neuron* **84**, 355–362 (2014).
46. M Vinck, R Batista-Brito, U Knoblich, JA Cardin, Arousal and Locomotion Make Distinct Contributions to Cortical Activity Patterns and Visual Encoding. *Neuron* **86**, 740–754 (2015).
47. K Franke, et al., State-dependent pupil dilation rapidly shifts visual feature selectivity. *Nature* **610**, 128–134 (2022).
48. T Boissonnet, M Tripodi, H Asari, Awake responses suggest inefficient dense coding in the mouse retina. *eLife* **12** (2023).
49. G Felsen, Y Dan, A natural approach to studying vision. *Nat. Neurosci.* **8**, 1643–1646 (2005).
50. PR Parker, ET Abe, ES Leonard, DM Martins, CM Niell, Joint coding of visual input and eye/head position in v1 of freely moving mice. *Neuron* **110**, 3897–3906.e5 (2022).

51. DM Piscopo, RN El-Danaf, AD Huberman, CM Niell, Diverse Visual Features Encoded in Mouse Lateral Geniculate Nucleus. *J. Neurosci.* **33**, 4642–4656 (2013).
52. M Román Rosón, et al., Mouse dLGN Receives Functional Input from a Diverse Population of Retinal Ganglion Cells with Limited Convergence. *Neuron* **102**, 462–476 (2019).
53. KD Harris, A shift test for independence in generic time series. *arXiv* pp. 1–6 (2020).
54. S Durand, et al., A comparison of visual response properties in the lateral geniculate nucleus and primary visual cortex of awake and anesthetized mice. *J. Neurosci.* **36**, 12144–12156 (2016).
55. J Tang, SCA Jimenez, S Chakraborty, SR Schultz, Visual receptive field properties of neurons in the mouse lateral geniculate nucleus. *PLOS ONE* **11**, e0146017 (2016).
56. MS Grubb, ID Thompson, Quantitative characterization of visual response properties in the mouse dorsal lateral geniculate nucleus. *J. Neurophysiol.* **90**, 3594–3607 (2003).
57. BA Olshausen, DJ Field, How close are we to understanding V1? *Neural computation* **17**, 1665–1699 (2005).
58. B Dearnley, M Jones, M Dervinis, M Okun, Brain state transitions primarily impact the spontaneous rate of slow-firing neurons. *Cell Reports* **42**, 113185 (2023).
59. CM Niell, MP Stryker, Modulation of visual responses by behavioral state in mouse visual cortex. *Neuron* **65**, 472–479 (2010).
60. AM Sillito, HE Jones, Corticothalamic interactions in the transfer of visual information. *Philos. Transactions Royal Soc. London. Ser. B: Biol. Sci.* **357**, 1739–1752 (2002).
61. F Briggs, WM Usrey, Corticogeniculate feedback and visual processing in the primate. *J. Physiol.* **589**, 33–40 (2010).
62. NA Lesica, et al., Adaptation to stimulus contrast and correlations during natural visual stimulation. *Neuron* **55**, 479–491 (2007).
63. JH Siegle, et al., Survey of spiking in the mouse visual system reveals functional hierarchy. *Nature* **592**, 86–92 (2021).
64. A Sanzeni, et al., Mechanisms underlying reshuffling of visual responses by optogenetic stimulation in mice and monkeys. *Neuron* **111**, 4102–4115.e9 (2023).
65. K Reinhold, A Resulaj, M Scanziani, Brain state-dependent modulation of thalamic visual processing by cortico-thalamic feedback. *The J. Neurosci.* **43**, 1540–1554 (2023).
66. J Kim, CJ Matney, A Blankenship, S Hestrin, SP Brown, Layer 6 corticothalamic neurons activate a cortical output layer, layer 5a. *J Neurosci* **34**, 9656–9664 (2014).
67. V Mante, V Bonin, M Carandini, Functional Mechanisms Shaping Lateral Geniculate Responses to Artificial and Natural Stimuli. *Neuron* **58**, 625–638 (2008).
68. R Coen-Cagli, A Kohn, O Schwartz, Flexible gating of contextual influences in natural vision. *Nat. Neurosci.* **18**, 1648–1655 (2015).
69. AI Weber, JW Pillow, Capturing the dynamical repertoire of single neurons with generalized linear models. *Neural Comput.* **29**, 3260–3289 (2017).
70. SM Sherman, Tonic and burst firing: Dual modes of thalamocortical relay. *Trends Neurosci.* **24**, 122–126 (2001).
71. NA Lesica, et al., Dynamic encoding of natural luminance sequences by lgn bursts. *PLoS Biol.* **4**, e209 (2006).
72. CM Niell, MP Stryker, Modulation of Visual Responses by Behavioral State in Mouse Visual Cortex. *Neuron* **65**, 472–479 (2010).
73. E Mounier, B Abdullah, H Mahdi, S Eldawlatly, A deep convolutional visual encoding model of neuronal responses in the lgn. *Brain Informatics* **8** (2021).
74. DL Yamins, JJ DiCarlo, Using goal-driven deep learning models to understand sensory cortex. *Nat. neuroscience* **19**, 356–365 (2016).
75. J Lindsey, SA Ocko, S Ganguli, S Deny, A unified theory of early visual representations from retina to cortex through anatomically constrained deep cnns. *arXiv preprint arXiv:1901.00945* (2019).
76. F Doshi-Velez, B Kim, Towards a rigorous science of interpretable machine learning. *arXiv preprint arXiv:1702.08608* (2017).

77. R Geirhos, et al., Imagenet-trained cnns are biased towards texture; increasing shape bias improves accuracy and robustness. *arXiv preprint arXiv:1811.12231* (2022).
78. N Maheswaranathan, et al., Interpreting the retinal neural code for natural scenes: From computations to neurons. *Neuron* **111**, 2742–2755 (2023).
79. BR Cowley, PL Stan, JW Pillow, MA Smith, Compact deep neural network models of visual cortex. *bioRxiv* (2023).
80. KK Lurz, et al., Generalization in data-driven models of primary visual cortex. *bioRxiv* pp. 2020–10 (2020).
81. D Klindt, AS Ecker, T Euler, M Bethge, Neural system identification for large populations separating “what” and “where”. *Adv. neural information processing systems* **30** (2017).
82. MA Goldin, et al., Context-dependent selectivity to natural images in the retina. *Nat. Commun.* **13**, 5556 (2022).
83. EY Walker, et al., Inception loops discover what excites neurons most using deep predictive models. *Nat. Neurosci.* **22**, 2060–2065 (2019).
84. SM Sherman, RW Guillery, The role of the thalamus in the flow of information to the cortex. *Philos. transactions Royal Soc. Lond.* **357**, 1695–708 (2002).
85. PJ Mineault, E Tring, JT Trachtenberg, DL Ringach, Enhanced Spatial Resolution During Locomotion and Heightened Attention in Mouse Primary Visual Cortex. *J. Neurosci.* **36**, 6382–6392 (2016).
86. S Zhu, J Hasse, F Briggs, Optogenetic suppression of corticogeniculate feedback in anesthetized ferrets is overridden by visual stimulation. *bioRxiv* (2021).
87. S Béhuret, C Deleuze, T Bal, Corticothalamic synaptic noise as a mechanism for selective attention in thalamic neurons. *Front. Neural Circuits* **9**, 80 (2015).
88. J Wolfart, D Debay, G Le Masson, A Destexhe, T Bal, Synaptic background activity controls spike transfer from thalamus to cortex. *Nat. Neurosci.* **8**, 1760–1767 (2005).
89. JL Herrero, MA Gieselmann, M Sanayei, A Thiele, Attention-induced variance and noise correlation reduction in macaque v1 is mediated by nmda receptors. *Neuron* **78**, 729–739 (2013).
90. A Thiele, Optimizing brain processing. *Nat. neuroscience* **12**, 1359–1360 (2009).
91. PR Roelfsema, FP de Lange, Early visual cortex as a multiscale cognitive blackboard. *Annu. review vision science* **2**, 131–151 (2016).
92. VA Lamme, PR Roelfsema, The distinct modes of vision offered by feedforward and recurrent processing. *Trends Neurosci.* **23**, 571–579 (2000).
93. S Zhang, et al., Long-range and local circuits for top-down modulation of visual cortex processing. *Science* **345**, 660–665 (2014).
94. WM Usrey, JB Reppas, RC Reid, Paired-spike interactions and synaptic efficacy of retinal inputs to the thalamus. *Nature* **395**, 384–387 (1998).
95. JM Alonso, WM Usrey, RC Reid, Precisely correlated firing in cells of the lateral geniculate nucleus. *Nature* **383**, 815–819 (1996).
96. J Wietek, et al., Anion-conducting channelrhodopsins with tuned spectra and modified kinetics engineered for optogenetic manipulation of behavior. *Sci. Reports* **7**, 1–18 (2017).
97. EG Govorunova, OA Sineshchekov, R Janz, X Liu, JL Spudich, Natural light-gated anion channels: A family of microbial rhodopsins for advanced optogenetics. *Science* **349**, 647–650 (2015).
98. L Madisen, et al., A robust and high-throughput Cre reporting and characterization system for the whole mouse brain. *Nat. Neurosci.* **13**, 133–140 (2010).
99. Z Josh Huang, H Zeng, ZJ Huang, H Zeng, Genetic Approaches to Neural Circuits in the Mouse. *Annu. review neuroscience* **36**, 183–215 (2013).
100. DS Bortone, SR Olsen, M Scanziani, Translaminar inhibitory cells recruited by layer 6 corticothalamic neurons suppress visual cortex. *Neuron* **82**, 474–485 (2014).
101. JE Frandolig, et al., The Synaptic Organization of Layer 6 Circuits Reveals Inhibition as a Major Output of a Neocortical Sublamina. *Cell Reports* **28**, 3131–3143 (2019).
102. M Mahn, M Prigge, S Ron, R Levy, O Yizhar, Biophysical constraints of optogenetic inhibition at presynaptic terminals. *Nat. Neurosci.* **19**, 554–556 (2016).

103. JS Wiegert, TG Oertner, How (not) to silence long-range projections with light. *Nat. Neurosci.* **19**, 527–528 (2016).
104. JS Wiegert, M Mahn, M Prigge, Y Printz, O Yizhar, Silencing Neurons: Tools, Applications, and Experimental Constraints. *Neuron* **95**, 504–529 (2017).
105. CA Poynton, Rehabilitation of gamma in *Human Vision and Electronic Imaging III*, eds. BE Rogowitz, TN Pappas. (International Society for Optical Engineering, San Jose, CA), Vol. 3299, pp. 232–249 (1998).
106. CT Rueden, et al., ImageJ2: ImageJ for the next generation of scientific image data. *BMC Bioinf.* **18** (2017).
107. J Schindelin, et al., Fiji: An open-source platform for biological-image analysis. *Nat. Methods* **9**, 676–682 (2012).
108. M Pachitariu, N Steinmetz, S Kadir, M Carandini, KD Harris, Kilosort: realtime spike-sorting for extracellular electrophysiology with hundreds of channels. *bioRxiv* p. 061481 (2016).
109. MA Spacek, TJ Blanche, NV Swindale, Python for large-scale electrophysiology. *Front. Neuroinform.* **2**, 9 (2009).
110. NV Swindale, MA Spacek, Spike sorting for polytrodes: a divide and conquer approach. *Front. Syst. Neurosci.* **8** (2014).
111. D Yatsenko, EY Walker, AS Tolias, DataJoint: A simpler relational data model (2018).
112. WE Vinje, JL Gallant, Sparse coding and decorrelation in primary visual cortex during natural vision. *Science* **287**, 1273–1276 (2000).

Acknowledgements

This research was supported by the Deutsche Forschungsgesellschaft (DFG) Sonderforschungsbereich (SFB) 1233, *Robust Vision: Inference Principles and Neural Mechanisms*, Teilprojekt (TP) 13, project number: 276693517 (L.B., P.B.), by SPP2041 (BU 1808/6-1 and BU 1808/6-2; L.B.), the RTG 2175 “Perception in context and its neural basis” (L.B.) and the Hertie Foundation (P.B.). Lisa Schmor was supported by the International Max Planck Research School for Intelligent Systems (IMPRS-IS). We thank E. Froudarakis (A. Tolias Lab, Baylor College of Medicine, Houston, TX) for providing of the movie stimulus files, S. Renner for helping with the database implementation, and A. Ecker and T. Euler for discussion of the stimulus design. Thanks also go to M. Sotgia for lab management and support with animal handling and histology, S. Schörnich for IT support, and B. Grothe for providing excellent research infrastructure.

Author contributions

Conceptualization, L.B., P.B., S.S.; Methodology, L.S., Y.B., A.K., Z.H., D.C. P.B., S.S., L.B.; Software, L.S., A.K., Y.B., Z.H., D.C.; Formal Analysis, L.S., A.K., Y.B.; Investigation, Y.B., A.K., L.M.; Resources, L.B., P.B.; Data Curation, L.S., A.K., Y.B., L.M., D.C.; Writing – Original Draft, L.B., L.S., A.K., Y.B.; Writing – Review & Editing, all authors; Visualization, L.S., A.K., Y.B.; Supervision, L.B., P.B., S.S.; Project Administration, L.B., P.B.; Funding Acquisition, L.B., P.B.

Declaration of Interests

The authors declare no competing interests.

Data and code availability

Data and code will be made available upon submission.

Methods

All procedures complied with the European Communities Council Directive 2010/63/EU and the German Law for Protection of Animals, and were approved by local authorities, following appropriate ethics review.

Surgical procedures

Experiments were carried out under under Licence ROB-55.2-2532.Vet_02-17-40 in 4 adult Ntsr1-Cre mice (median age: 15.5 ± 6.45 weeks; B6.FVB(Cg)-Tg(Ntsr1-cre)GN220Gsat/Mmcd; MMRRRC) of either sex. Stereotactic surgeries were performed to implant a head-post for head-fixation, implant a ground/reference screw for electrophysiology, inject a virus for optogenetic feedback manipulation, and drill a craniotomy for acute electrode insertions.

Stereotactic surgery preparation and initiation

Thirty minutes prior to the surgical procedure, mice were injected with an analgesic (Metamizole, 200 mg/kg, sc, MSD Animal Health, Brussels, Belgium). To induce anesthesia, animals were placed in an induction chamber and exposed to isoflurane (5% in oxygen, CP-Pharma, Burgdorf, Germany). After induction of anesthesia, mice were fixated in a stereotaxic frame (Drill & Microinjection Robot, Neurostar, Tuebingen, Germany) and the isoflurane level was lowered (0.5 %–2 % in oxygen), such that a stable level of anesthesia could be achieved as judged by the absence of an interstitial reflex. Throughout the procedure, the eyes were covered with an eye ointment (Bepanthen, Bayer, Leverkusen, Germany) and a closed loop temperature control system (ATC 1000, WPI Germany, Berlin, Germany) ensured that the animal's body temperature was maintained at 37° C. At the beginning of the surgical procedure, an additional analgesic was administered (Buprenorphine, 0.1 mg/kg, sc, Bayer, Leverkusen, Germany) and the animal's head was shaved and thoroughly disinfected using iodine solution (Braun, Melsungen, Germany). Before performing a scalp incision along the midline, a local analgesic was delivered (Lidocaine hydrochloride, sc, bela-pharm, Vechta, Germany). The skin covering the skull was partially removed and cleaned from tissue residues with a drop of H₂O₂ (3 %, AppliChem, Darmstadt, Germany). Using four reference points (bregma, lambda, and two points 2 mm to the left and to the right of the midline respectively), the animal's head was positioned into a skull-flat configuration for the further steps.

Virus injection

In order to suppress V1 L6 CT FB selectively and reversibly, we conditionally expressed the chloride-conducting channelrhodopsin stGtACR2 (39, 96, 97) in L6a CT pyramidal cells (84, 60, 61) by injecting AAV-stGtACR2-RFP into the left hemisphere V1 of Ntsr1-Cre mice (40, 98, 99) (Figure 1a). Ntsr1+ neurons are known to correspond with > 90% specificity to L6 CT pyramidal cells (6, 100, 101). Furthermore, the opsin stGtACR2 restricts expression to somata and the axon-initial segment which prevents possible accidental axonal depolarization due to a differential Cl⁻ ion reversal potential across different neuronal compartments (102, 103, 104). It also offers improved photocurrents and higher sensitivity, which are of particular relevance to manipulating deeply located L6 CT neurons, while avoiding light artifacts and tissue damage arising from excessive light intensities (104).

Before surgery, the Cre-dependent, stGtACR2-expressing *adeno-associated virus* (AAV) vector (pAAV_hSyn1-SIO-stGtACR2-FusionRed, Addgene, #105677) stock solution was diluted to 5 × 10¹¹ gc/ml titers, and aliquotted to 4 μL.

During surgery, aliquots were front-loaded into a glass pipette mounted on a Hamilton syringe (SYR 10 μL 1701 RN no ND, Hamilton, Bonaduz, Switzerland), controlled by the Injection Robot of the Neurostar Stereotax. After performing a small craniotomy for injection (100 μm diameter), we injected 300 nl of virus solution into V1 (2 × 50 nl shots injected at a rate of 50 nl / 30 s at a respective depth of 900 μm, 800 μm and 700 μm below the brain surface.

Head-post and ground and reference screw implantation

For implant fixation, the exposed skull was covered with OptiBond FL primer and adhesive (Kerr Dental, Rastatt, Germany) omitting three locations: V1 (AP: -3.28 mm, ML: -2.4 mm), dLGN (AP: -2.3 mm, ML: -2 mm), and a position roughly 1.5 mm anterior and 1 mm to the right of bregma, designated for a miniature ground and reference screw.

A custom-made lightweight stainless steel head bar was positioned over the posterior part of the skull such that the round opening in the bar was centered on V1/dLGN. The head bar was attached with dental cement (Ivoclar Vivadent, Ellwangen, Germany) to the primer/adhesive. The opening was later filled with the silicone elastomer sealant Kwik-Cast (WPI Germany, Berlin, Germany). Then the miniature screw (00-96 X 1/16 stainless steel screws, Bilaney), which served both as ground and reference that was soldered to a custom-made connector pin, was implanted.

Post-surgical treatment and animal setup habituation

At the end of the procedure, an iodine-based ointment (Braunodivon, 10%, B. Braun, Melsungen, Germany) was applied to the edges of the wound and a long-term analgesic (Meloxicam, 2 mg/kg, sc, Böhringer Ingelheim, Ingelheim, Germany) was administered and for 3 consecutive days. For at least 5 days post-surgery, the animal's health status was assessed via a score sheet.

After at least 1 week of recovery, animals were gradually habituated to the experimental setup by first handling them and then simulating the experimental procedure. To allow for virus expression, neural recordings started after an incubation time of 2-4 weeks after injection.

Craniotomy

On the day prior to the first day of recording, mice were fully anesthetized using the same procedures as described for the initial surgery, and a craniotomy (ca. 2 × 1 mm on the AP × BL axes) was performed over dLGN (ca. 2.5 mm posterior from bregma and 2.3 mm lateral from midline) and V1 and re-sealed with Kwik-Cast (WPI Germany, Berlin, Germany). As long as the animals did not show signs of discomfort, the long-term analgesic Metacam was administered only once at the end of surgery, to avoid any confounding effect on experimental results. Recordings were performed daily and continued for as long as the

quality of the electrophysiological signals remained high.

Extracellular multi-electrode array (MEA) recordings

After 2-4 weeks of incubation time, we performed *in vivo* extracellular multi-electrode array (MEA) recordings of dLGN neurons in awake, head-fixed mice (Figure 1a). Extracellular signals were recorded at 30 kHz (Blackrock microsystems, Blackrock Microsystems Europe GmbH, Hanover, Germany). For each recording session, the silicon plug sealing the craniotomy was removed. For dLGN recordings, a 32 channel linear silicon probe (Neuronexus A1x32Edge-5mm-20-177-A32) was lowered to a depth of $\sim 2500\text{--}3500\ \mu\text{m}$ below the brain surface. We judged recording sites to be located in dLGN based on the characteristic progression of RFs from upper to lower visual field along the electrode shank (51), the presence of responses strongly modulated at the temporal frequency of the drifting gratings (F1 response), and the preference of responses to high temporal frequencies (56, 51). For *post hoc* histological reconstruction of the recording site, the electrode was stained with DiI (Invitrogen, Carlsbad, USA) for some (typically the last) recording sessions.

Locomotion

During the experiment, mice were free to run on an air-floating Styrofoam ball and the run speed was recorded via locomotion sensors (Figure 1a). Two optical computer mice interfaced with a microcontroller (Arduino Duemilanove) sampled ball movements at 90 Hz.

To compute animal run speed, we used the Euclidean norm of three perpendicular components of ball velocity (roll, pitch and yaw) and smoothed traces with a Gaussian kernel ($\sigma = 0.2\ \text{s}$). To quantify the effect of running vs. sitting on various response properties, the run modulation index (MI_{Run}) was defined based on the mean firing rates during running vs. sitting periods as

$$MI_{Run} = \frac{\text{running} - \text{sitting}}{\text{running} + \text{sitting}}, \quad (1)$$

where running periods were defined as those for which speed exceeded 1 cm/s, and sit periods as those for which speed fell below 0.25 cm/s.

To test for a significant difference in mean FRs between the run vs. sit conditions matched for each neuron, we used the Wilcoxon signed-rank test.

Eye tracking

To record eye position and pupil size, the animal's eye that was viewing the stimulus was illuminated with infrared LED light and monitored using a zoom lens (Navitar Zoom 6000) coupled with a camera (Guppy AVT camera; frame rate 50 Hz, Allied Vision, Exton, USA).

Pupil position was extracted from the eye-tracking videos using a custom, semi-automated algorithm. Briefly, each video frame was equalized using an adaptive bi-histogram equalization procedure, and then smoothed using median and bilateral kernels. The center of the pupil was detected by taking the darkest point in a convolution of the kernelled image with a black square. Next, the peaks of the image gradient along lines extending radially from the center point were used to define the pupil contour. Lastly, an ellipse was fit to the contour, and the center and area of this ellipse was taken as the position and size of the pupil, respectively. A similar procedure was used to extract the position of the corneal reflection (CR) of the LED illumination. Eye-closure, grooming, or implausible ellipse fitting was automatically detected and the adjacent data points 0.15 s before and after were excluded. Linear interpolation and a subsequent Gaussian smoothing ($\sigma = 0.06\ \text{s}$) was applied to fill the removed segments. Adjustable algorithm parameters, such as the threshold of the mean pixel-wise difference between each frame and a reference frame to detect blinks, were set manually for each experiment.

To quantify the effect of large vs. small pupil sizes on various response properties, the eye modulation index (MI_{Pupil}) was defined based on the mean firing rates during periods of large vs. small pupils as

$$MI_{Pupil} = \frac{\text{pupil large} - \text{pupil small}}{\text{pupil large} + \text{pupil small}}, \quad (2)$$

where periods of large pupils were defined as those for which pupil size was above the 50th percentile of the median normalized pupil trace, and periods of small pupils as those for which pupil size fell below the 25th percentile.

Optogenetic feedback suppression

To photosuppress V1 Ntsr1+ L6 CT pyramidal cells, an optic fiber (480 μm core diameter, MFP_480/500/1000-0.63_m_SMA, Doric Lenses, Quebec, Canada) was coupled to a light-emitting diode (blue LED, center wavelength 465 nm, LEDC2_465/635_SMA, Doric Lenses, Quebec, Canada) and positioned with a micromanipulator less than 1 mm above the exposed surface of V1. A

black metal foil surrounding the tip of the head bar holder prevented the photostimulation light from reaching the animal's eyes. To ensure that the photostimulation was effective, the first recording session for each mouse was carried out in V1. Only if the exposure to light reliably induced suppression of V1 activity was the animal used for subsequent dLGN recordings. LED light intensity was adjusted on a daily basis to evoke reliable effects and account for variations in exact virus titer, volume, incubation time, virus expression levels, and fiber position (0.85-9.5 mW at the fiber tip). Since the tip of the fiber never directly touched the surface of the brain, and since the clarity of the surface of the brain varied (generally decreasing every day following the craniotomy), the light intensity delivered even to superficial layers of V1 was inevitably lower. For the movie stimulus, optogenetic pulses of 1 s duration were sent randomly each second with a 50 % chance.

To quantify the effect of CT feedback suppression on various response properties, we defined the optogenetic modulation index ($MI_{CT\ FB\ supp.}$) based on the mean FRs during CT feedback suppression ('opto') versus the control condition as

$$MI_{CT\ FB\ supp.} = \frac{\text{opto} - \text{control}}{\text{opto} + \text{control}} \quad (3)$$

Joint modulation by additional inputs

In order to quantify the joint effect of all the modulatory inputs, we calculated MI_{Joint} as

$$MI_{Joint} = 1 - (1 - MI_{CT\ FB\ supp.})(1 - MI_{Run})(1 - MI_{Pupil}) \quad (4)$$

Visual stimulation

During the experiment, the mice were passively viewing visual stimuli on an LCD monitor screen in their right visual field. The visual stimuli were presented on a gamma-calibrated liquid crystal display (LCD) monitor (Samsung SyncMaster 2233RZ, 47×29 cm, 1680×1050 resolution at 60 Hz, mean luminance 50 cd/m²) positioned at a distance of 25 cm from the animal's right eye (spanning ~ 108×66° visual angle by small angle approximation) using custom written software (EXPO, <https://sites.google.com/a/nyu.edu/expo/home>). The display was gamma-corrected for the presentation of artificial stimuli, but not for movies (see below).

Movie stimulus

For movie stimulus generation, we adopted a set of randomly picked clips from various movies. Briefly, source movie clips were converted to grey scale, temporally downsampled to 30 frames per s, spatially resampled and cropped to 424×264 pixels, to be presented on our 47×29 cm monitor screen at 25 cm distance at 106×66° (4 pixels/°) visual angle (by small angle approximation, which preserves the desired pixel resolution at the screen center better than the arctangent). Movie frames were not histogram-equalized and presented at 60 Hz (repeating each frame twice) without monitor gamma correction, since cameras are already gamma corrected for consumer displays (105). To generate the movie sequence, we used a random set of 296 unique movie clips (5 s each) and split 188/296 clips into 8 parts of 36 unique clips (5 s×36 = 180 s per part). They were interleaved with set of 8 clips (5 s×8 = 40 s) which was repeated 9 times. The repeated clips served to give an estimate of response reliability to the same clips. The movie sequence was flanked by a period of blank grey screen presentation (1 min) at the beginning and at the end, to record spontaneous activity. This resulted in a total stimulus duration of ~ 32 mins. To rule out sequence effects, we randomized the clip order for different stimulus presentations. To investigate the effects of L6 CT FB suppression, we simultaneously presented a random optogenetic pulse train of 1 s pulses, occurring each second with a probability of 50 %, throughout the entire stimulus duration, including blank grey screen periods.

Sparse noise stimulus

To measure RFs in a more standard manner, we also presented an (artificial) sparse noise stimulus. The stimulus consisted of a rapid sequence of non-overlapping white and black squares appearing in succession within a 12x12 square grid presented on a grey background of mean luminance (50 cd/m²). The square grid spanned 60° per side, while individual squares spanned 5° per side. Each square flashed 20 times for 200 ms at random order. The stimulus triggered average (STA) for the sparse noise stimulus was computed using the onset of each square and then computing the normalised mean spike rate triggered by each position.

Histology

To verify virus expression and recording sites, we performed post-mortem histological analyses. After the final recording session, mice were first administered an analgesic (Metamizole, 200 mg/kg, sc, MSD Animal Health, Brussels, Belgium) and following a 30 min latency period were transcardially perfused under deep anesthesia using a cocktail of Medetomidin (Domitor, 0.5 mg/kg, Vetoquinol, Ismaning, Germany), Midazolam (Climasol, 5 mg/kg, Ratiopharm, Ulm, Germany) and Fentanyl (Fentadon, 0.05 mg/kg, Dechra Veterinary Products Deutschland, Aulendorf, Germany) (ip). Perfusion was first done with Ringer's lactate solution followed by 4% paraformaldehyde (PFA) in 0.2 M sodium phosphate buffer (PBS). Brains

were removed, postfixed in PFA for 24 h, and then rinsed with and stored in PBS at 4° C. Slices (50 μ m) were cut using a vibrotome (Leica VT1200 S, Leica, Wetzlar, Germany), stained with DAPI-solution (DAPI, Thermo Fisher Scientific, Waltham, Massachusetts, USA), mounted on glass slides with Vectashield mounting medium (Vectashield H-1000, Vector Laboratories, Burlingame, USA), and coverslipped. A scanning fluorescent microscope (BX61, Olympus, Tokyo, Japan) was used to inspect slices for the presence of red fluorescent protein (RFP/FusionRed) marking stGtACR2-channels, and DiI, marking electrode tracks. Recorded images were processed off-line using FIJI (106, 107).

Control experiments with Ntsr-negative mouse

Additionally, same experimental procedures were followed for control (Ntsr-negative) mouse, in order to assess the efficiency of optogenetic manipulations of CT feedback. Prior to experimentation, the genotype of the mice was confirmed via polymerase chain reaction (PCR) analysis.

Spike sorting and unit extraction

Spike sorting was performed to obtain single unit activity from extracellular recordings. Electrophysiological signal recordings were kernalled using a 4th-order Butterworth high-pass non-causal kernel with a low frequency cutoff of 300 Hz. We then used the open source, MATLAB-based (The Mathworks, Natick, Massachusetts, USA), automated spike sorting toolbox Kilosort and Kilosort2 (108). Resulting clusters were manually refined using Spyke (109), a Python application that allows for the selection of channels and time ranges around clustered spikes for realignment, as well as representation in 3D space using dimension reduction (multichannel PCA, ICA, and/or spike time). In 3D, clusters were then further split via a gradient-ascent based clustering algorithm (GAC) (110). Exhaustive pairwise comparisons of similar clusters allowed the merger of potentially over-clustered units. For subsequent analyses, we inspected autocorrelograms and mean voltage traces, and only considered units that displayed a clear refractory period and a distinct spike waveshape.

Data analysis

Data analysis was performed using custom-written code that applies general tools such as Numpy, sklearn, matplotlib, seaborn, pandas and carried out in a MySQL-based database using the DataJoint (111). We also used a customized version of RFest (<https://github.com/berenslab/RFest>) to allow for multiple model inputs.

Firing rate calculations

To obtain units firing rates in spikes per second (Hz), each unit's spike density function (SDF) was calculated by binning spikes into a firing rate histogram (bin width = 20 ms) and convolving this with a Gaussian of width $2\sigma = 10$ ms. Mean firing rates (FRs) over a given condition were calculated as the mean of the time-varying firing rates for the defined periods.

Identification of putative neuronal types

In order to identify putative excitatory and inhibitory neurons in V1, we analysed the extracellular spike waveform. For each neuron, the mean waveform of the maximally responsive electrode channel was obtained, and the time between trough and peak (trough-to-peak time) and the full-width at half-height of the peak (peak width) were calculated. Using the waveforms of all V1 neurons, a k-means algorithm was used to cluster the data into 2 populations.

Response reliability

To compute how reliable a neurons responded to the visual stimulus we used the set of 8 clips that where repeated 9 times throughout the experiment. We computed reliability by correlating each repetition with the mean of all other repetitions and averaging that over all splits.

Optogenetic significance

To compute the reliability of the optogenetic manipulation of L6 CT neurons, we developed a trial-based permutation test. In response to drifting gratings, we calculated the average firing rate during each trial and separated the trial with optogenetic CT feedback suppression ($trials_{CT\ FB\ supp.}$; n=90 – –130) from those without ($trials_{control}$; n=90 – –130). We calculated the observed statistics $effect_{CT\ FB\ supp.}$ as the difference in the means between the $trials_{CT\ FB\ supp.}$ and the $trials_{control}$. We assessed significance by permuting trial labels 1000 times and considered the effect significant if it fell outside of the distribution of permuted $effect_{CT\ FB\ supp.}$ s. Finally, we compared the percentage of neurons that passes the significance test between the included recording and a recording from a control mouse (Ntsr-negative).

Exclusion criteria

Neurons with mean evoked firing rates < 0.1 Hz were excluded from all further analysis. Further analysis-specific selection criteria are stated in the appropriate subsections.

Predictor correlations

To test for the correlations between the predictors *stimulus*, *opto*, *run*, and *eye*, we temporally aligned these traces, including only time points for which we had data points in all traces (e.g. removing periods of eye blinks). We then explored their cross-correlations in order to detect potential delays in their effects on each other. Such is the case, for instance in the pupil light reflex, where increases in stimulus intensity are followed by a delayed decrease in pupil size. We then used the delay time to shift the traces appropriately before computing their correlation value (Pearson's r ; **Figure S3c**).

In order to test for statistical significance of the obtained correlation values, we first needed to account for the fact that our time-series inherently contain autocorrelations which would lead to an overestimation of correlations between them (except for the random opto pulses) (53). We therefore used a permutation test in which we randomly permuted the stimulus traces for $k = 1000$ iterations, and then computed the p-value of the observed correlation value as its percentile within the null distribution of p-values for the permuted traces (53).

Spline-based generalized linear model

To estimate the spatio-temporal RFs (STRFs), we used the RFest Python toolbox for spline-based spatio-temporal RF estimation (38). Here, the spline-based GLM reduces the number of parameters compared to traditional approaches, which need to estimate every pixel in the RF independently, while spline-based GLM only estimate the weight of the bases. RFest is also less data demanding and reduces the computation time significantly (38). The number of parameters are given by the number of basis functions, also referred to the degrees of freedom. By using natural cubic splines as the basis (e.g., **Figure S6a-d**), the estimates are automatically smooth, which is a desirable property for single STRFs. To impose sparsity on the weights (also a desirable property of SRFs) we added L1 regularization, which pushed the weights for less relevant bases to zero. To compute the spline-based STRFs, w_{SPL} , the coefficients, b_{SPL} , were obtained as

$$b_{SPL} = (S^T X^T X S)^{-1} S^T X^T y \quad (5)$$

with X as the stimulus design matrix, y as the neural response vector, and S as the spline matrix. The spatio-temporal RF was computed as

$$w_{SPL} = S b_{SPL} = S (S^T X^T X S)^{-1} S^T X^T y \quad (6)$$

To generate the natural cubic spline matrices (S) the package Patsy (0.5.1) is integrated into RFest.

To approximate w_{SPL} we used a generalized linear model (GLM) that predicts the instantaneous firing rate for one neuron using the movie as a predictor. We extended this "Stimulus only" model by integrating also running speed and pupil size as behavioral predictors of neuronal firing rate. To estimate the effect of cortico-thalamic (CT) feedback, an additional bimodal input was used comprising the optogenetic light stimulation that could be either on ($o_t = 1$) or off ($o_t = 0$). All inputs were parameterized with a set of spline basis and multiplied with an extra weight vector (also referred to as kernel):

$$f(s, o, r, e) = g(w_s^T s[t : t - \Delta t] + w_o^T o[t : t - \Delta t] + w_r^T r[t : t - \Delta t] + w_e^T e[t : t - \Delta t]) \quad (7)$$

with s , o , r , and e denoting the additional model inputs of stimulus, optogenetics, running and eye, respectively, and $[t : t - \Delta t]$ defining the temporal integration window (250 ms for stimulus and 800 ms for the predictors for modulatory inputs).

We estimated the kernels by gradient descent with respect to the cost function with L1 regularization. As standard procedure for time series data, we used 150 out of the 188 unique movie clips (80 %) for cross-validation to select optimal hyperparameters and reserved the remaining 38 clips (20 %) as a held-out test set. To select optimal hyperparameters, we used five-fold cross-validation grid search on the training data (120 training clips and 30 validation clips in each fold). Hyperparameters included the number of spline basis (between 10 and 19) in temporal dimension (for stimulus, pupil size, locomotion, and feedback input) and spatial dimension (only stimulus), as well as the strength of the L1 regularization (with weights varying from 5 to 15). The STRFs were initialized randomly and optimized using gradient descent for 2000 iterations. We stopped the fitting early when the training cost changed less than 10^{-5} for 10 iterations. Finally, we selected the hyperparameters based on the mean performance on the validation set across folds. After optimal hyperparameter selection, models were retrained on the full training data (150 movie clips) and the final performance of the model was reported as the correlation coefficient between predicted and observed neural responses on the held out test data (38 movie clips).

We further fitted spline GLMs with responses to a sparse noise stimulus. We conducted a separate hyperparameter search for this stimulus, using a similar procedure as for the movie stimulus, involving cross-validation. For each neuron, we determined a unique set of optimal hyperparameters and kernels for the sparse noise stimulus and the movie stimulus.

Session based permutation test

Following Harris (2020) (53), we performed a permutation test to evaluate if data from a different experimental session would lead to the same or worse model performance, which indicated the significance of the input-output correlations captured by the

model. To achieve this, we provided the model with input data from the validation set of an unrelated session (for the model inputs ‘stimulus’, ‘running’, ‘pupil size’) or with synthetic inputs generated with the same statistics as the original (for the ‘CT feedback suppression’ input), one at a time. We repeated the process using all different data from all recording sessions. Subsequently, we compared for each input the actual model performance (Pearson’s r) on the validation set across its folds ($n=5$) against a distribution of model performances with that specific input permuted from the different recording sessions across their folds ($n=5$ folds \times 9 recording sessions). Inputs were considered significant if the actual performance differed from the permuted performance with $p \leq 0.05$ using the non-paired Mann-Whitney-U test.

Spatio-temporal RF component extraction

To separate spatial and temporal components of the 3D STRFs, we performed singular value decomposition (SVD) on the norm of the stimulus weight vector w . The temporal RF is extracted as the first left-singular vector of U , i.e. temporal dimension with the highest variance, and the spatial RF as the first right-singular vector of V , reshaped into the height- and width-dimensions of the input vector w . The extremes of the reshaped spatial RF vector are then used to quantify RF position and RF area. The extracted temporal RF components were normalized and multiplied with the RF center value before computing the slope (-150 ms to peak).

Spatial RF contour estimation

Model spatial RFs were estimated by extracting the 2D spatial RF component from the model weights (see subsection ‘Spatio-temporal RF component extraction’), and then drawing a contour line around the largest absolute peak (assumed to be the center of the spatial RF). The contour threshold gets gradually lowered until any further decrease would result in a second contour around the second largest extremum (background irregularities considered as noise). To avoid overly large RFs in very clean spatial components (without any major second extremum), the contour threshold had to be 2 standard deviations above or below the mean. To improve estimate accuracy, the spatial RF component was upsampled 16-fold via cubic spline interpolation.

Spatial RF area

The spatial RF areas were estimated by using the spatial RF component and contour (see subsection ‘Spatial RF contour estimation’) and calculating the number of pixels of the spatial RF contour mask in relation to the total number of pixels in the image frame, which was then scaled by the stimulus extent to obtain the value in squared degrees of visual angle. To improve estimate accuracy, the spatial RF component was upsampled 16-fold via cubic spline interpolation.

Spatial RF center-surround

stRFs were collapsed across the azimuth axis, and accordingly defined as a function of elevation and time. Then, we identified the time point with peak activity. Subsequently, centre regions were defined according to the spatial width of the peak activity, and surround regions were defined as a ring encircling the centre and extending up to trice the diameter or 9° . We then summed pixel intensities within the centre region and the surround regions separately and calculated surround-to-centre ratio as:

$$\text{surround-to-center} = \frac{2 * \sum \text{centre}}{\sum \text{surround}_1 + \sum \text{surround}_2} \quad (8)$$

Functional cell types clustering

To categorize neurons into functional subtypes, we employed dimensionality reduction (PCA) on their PSTH responses to a full-field light intensity step stimulus. Subsequently, we conducted clustering using a Gaussian mixture model on the principal components, resulting in the identification of four primary groups (Sustained ON, Sustained OFF, Transient, and Mixed). Nevertheless, we observed substantial response diversity even within these main groups. To address this, we further subdivided neurons within each group through empirical selection of cluster numbers, aiming to optimize silhouette scores and reduce the standard error of the PSTH mean response within the subclasses. This two-step clustering approach allowed capturing finer distinctions of response patterns (Figure S5a, b).

Rate of change (RoC) to CT feedback suppression

To quantify the temporal dynamics of the effect of suppressing CT feedback with optogenetic pulses, we calculated rate of change (RoC) in the neurons’ responses based on both data and model prediction. For each case, we first identified the time point t_{min} where the slope of neurons response flipped its sign (e.g. after light onset, firing rates decreased, negative slope, and then it either stays constant or fluctuates around its new value and the slope becomes zero or flips its sign to positive). Then, we calculated the normalised change in responses $MI_{CT\ FB\ supp.}$; (see subsection ‘Optogenetic feedback suppression’). Finally, RoC was defined as:

$$RoC = \frac{MI_{CT\ FB\ supp.}}{t_{min}} \quad (9)$$

Decoding analysis

We used a two-alternative forced choice (2AFC) decoder (30) to analyze if stimulus discriminability is easier with or without feedback. Given two spike trains $\{s_A, s_B\}$ in response to two movie clips $\{A, B\}$ we computed the model log-likelihood for the correct $((s_A, A), (s_B, B))$ and the incorrect pairing $((s_A, B), (s_B, A))$. We used the ‘Full model’ to predict spike trains in the two feedback conditions, (1) with the feedback component intact and (2) with the feedback component suppressed. In both conditions, we used 100 randomly selected 50 ms movie clips from the test set and their corresponding responses. Using all possible pairs, we computed the model log-likelihood for the correct and the incorrect pairing in both feedback conditions. The log probability for the correct pairing of response s_A and stimulus A is defined as follows:

$$\log p(s_A|A) = \sum_t s_{A,t} \log \lambda_t(A_t) - \lambda(A_t) \quad (10)$$

where λ is the instantaneous firing rate at time t predicted by the model. Analogously, we computed $\log p(s_B|B)$, $\log p(s_A|B)$, and $\log p(s_B|A)$. A correct choice was made if $\log p(s_A|A) > \log p(s_A|B)$ or $\log p(s_B|B) > \log p(s_B|A)$, respectively. We used the percentage correct over all possible pairs to quantify decoding performance. Finally, we computed the ratio of percentage correct for the feedback suppressed condition and the control condition. A ratio above one indicates better decoding performance in the feedback suppressed condition and a ratio below one in the control condition.

Supplementary Materials

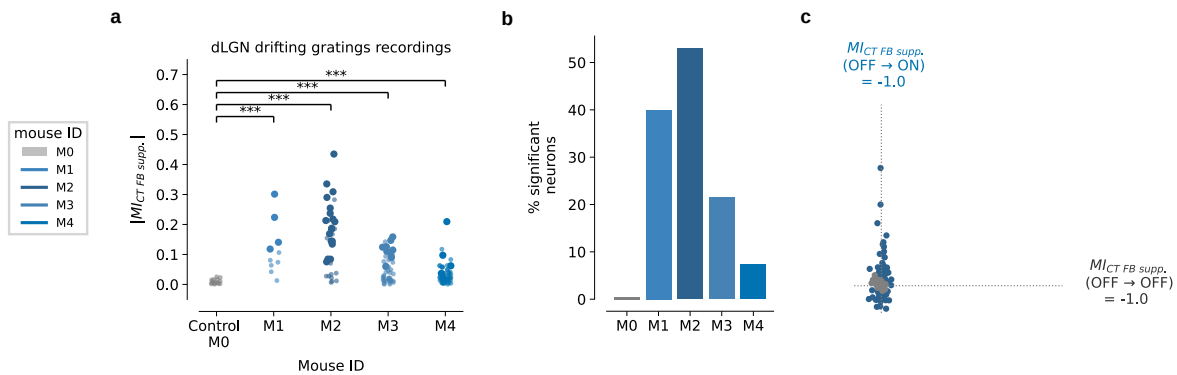


Figure S1 | Efficiency of optogenetic manipulation of CT feedback (a) Optogenetic modulation index (OMI) values for dLGN neurons ($n = 122$), separately by mouse. The four included mice showed significantly higher modulation indices than the control mouse M0 ($p < 0.01$, Mann-Whitney-U test). *Opaque dots*: Neurons that are significantly modulated by CT feedback suppression ($p < 0.05$, trial-based permutation test). *Transparent dots*: Neurons that did not pass the significance test ($p > 0.05$). (b) Percentage of neurons that were significantly modulated by CT feedback suppression per mouse ($p < 0.05$, trial-based permutation test). (c) Scatter of OMI values for the four included mice (blue) and the control mouse (Gray) for the OFF-ON transitions (i.e., triggered to the onset of CT feedback suppressing light pulses) vs. OFF-OFF transitions (i.e., triggered to times without onset of CT feedback suppressing light pulses).

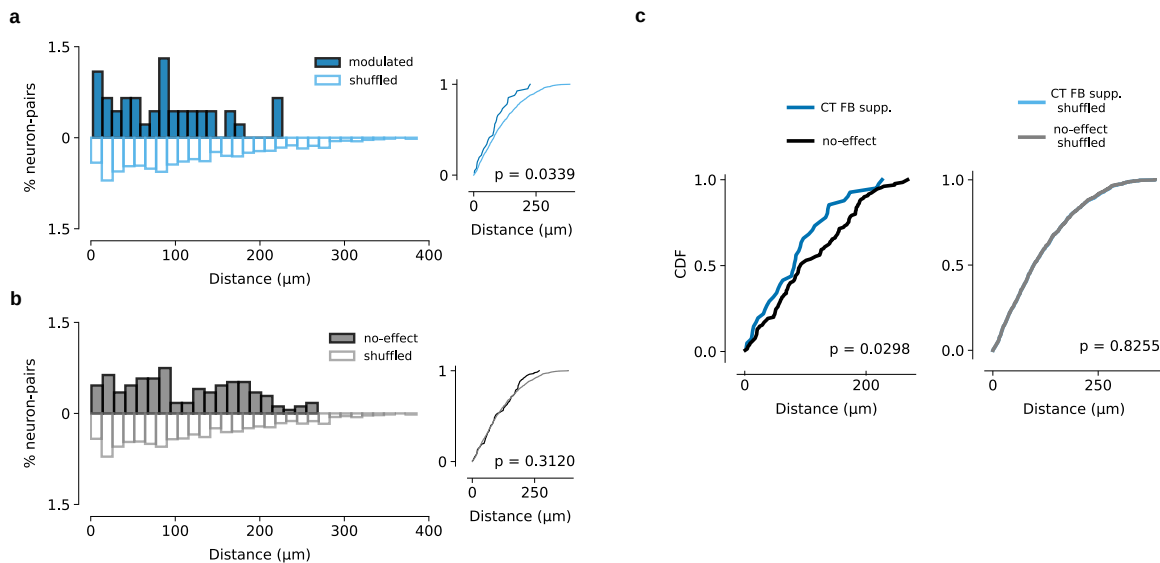


Figure S2 | CT feedback modulated neurons are closer to each other in the mouse dLGN. We identified all simultaneously recorded neuron pairs ($n = 171$), of which at least one neuron was positively or negatively modulated by CT feedback suppression ($|MI_{CT\ FB\ supp.}| \geq 0.1$), and calculated the distance in micrometer between each pair on the electrode. (a) *Left, solid bars*: Percentage of neuron pairs ($n = 41$) at each distance from each other on the electrode, when both neurons were modulated by CT feedback suppression. *Left, hollow bars*: Percentage of the same neuron-pairs with shuffled distances. *Right*: cumulative distributions of true and shuffled data ($p = 0.0339$, Kolmogorov-Smirnov test). (b) Same as (a), when only one neuron was modulated by CT feedback suppression ($n = 130$). $p = 0.312$, Kolmogorov-Smirnov test. (c) *Left*: Cumulative distributions of distances between neuron pairs ($p = 0.0298$, Kolmogorov-Smirnov test). *Right*: cumulative distributions of shuffled data ($p = 0.8255$, Kolmogorov-Smirnov test), re-plotted from (a) and (b).

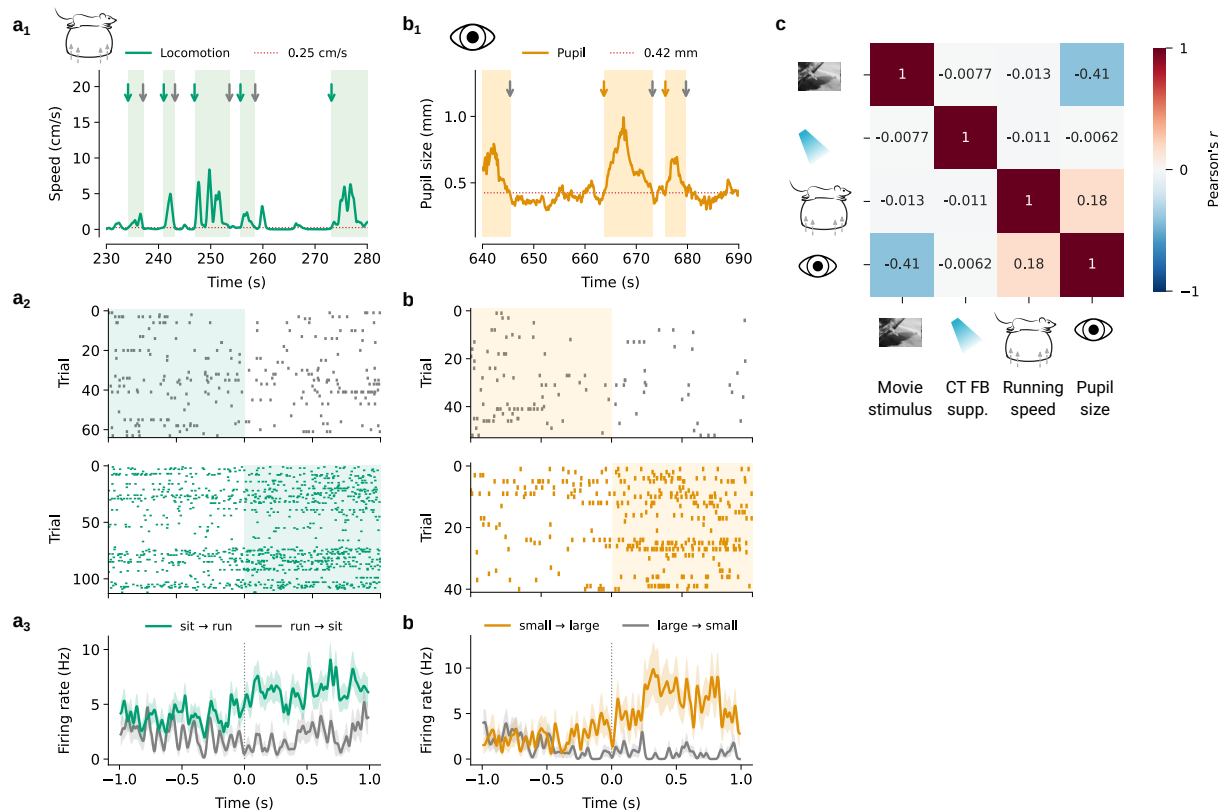


Figure S3 | CT feedback and behaviour modulates dLGN responses to movie clips (a) Modulation of firing rate by running speed for one dLGN example neuron: (a₁) We considered periods as “running” if the animal’s speed was > 1 cm/s, and “sitting” if the speed was < 0.25 cm/s (red). Transitions between periods are marked by green and grey arrows, respectively. (a₂) Spike raster plot triggered on transitions from running to sitting (top), and sitting to running (bottom). (a₃) Corresponding PSTHs. Green: transitions from sitting to running; grey: transitions from running to sitting. Only periods with durations > 2 s were considered. (b) Modulation of firing rate by pupil size for one dLGN example neuron: (b₁) We considered periods as “large pupil size” when pupil size exceeded the median pupil size during the experiment (red), and “small pupil size” if it was smaller than the 25th percentile. Transitions between periods are marked by orange and grey arrows, respectively. (b₂) Same as in a₂ but for transitions from large to small pupil (top) and from small to large pupil (bottom). (b₃) Same as in a₃ but for pupil size transitions. (c) Correlation matrix of average stimulus intensity, optogenetic light pulses, running speed and pupil size traces. Values denote average correlation values across experiments ($n = 10$).

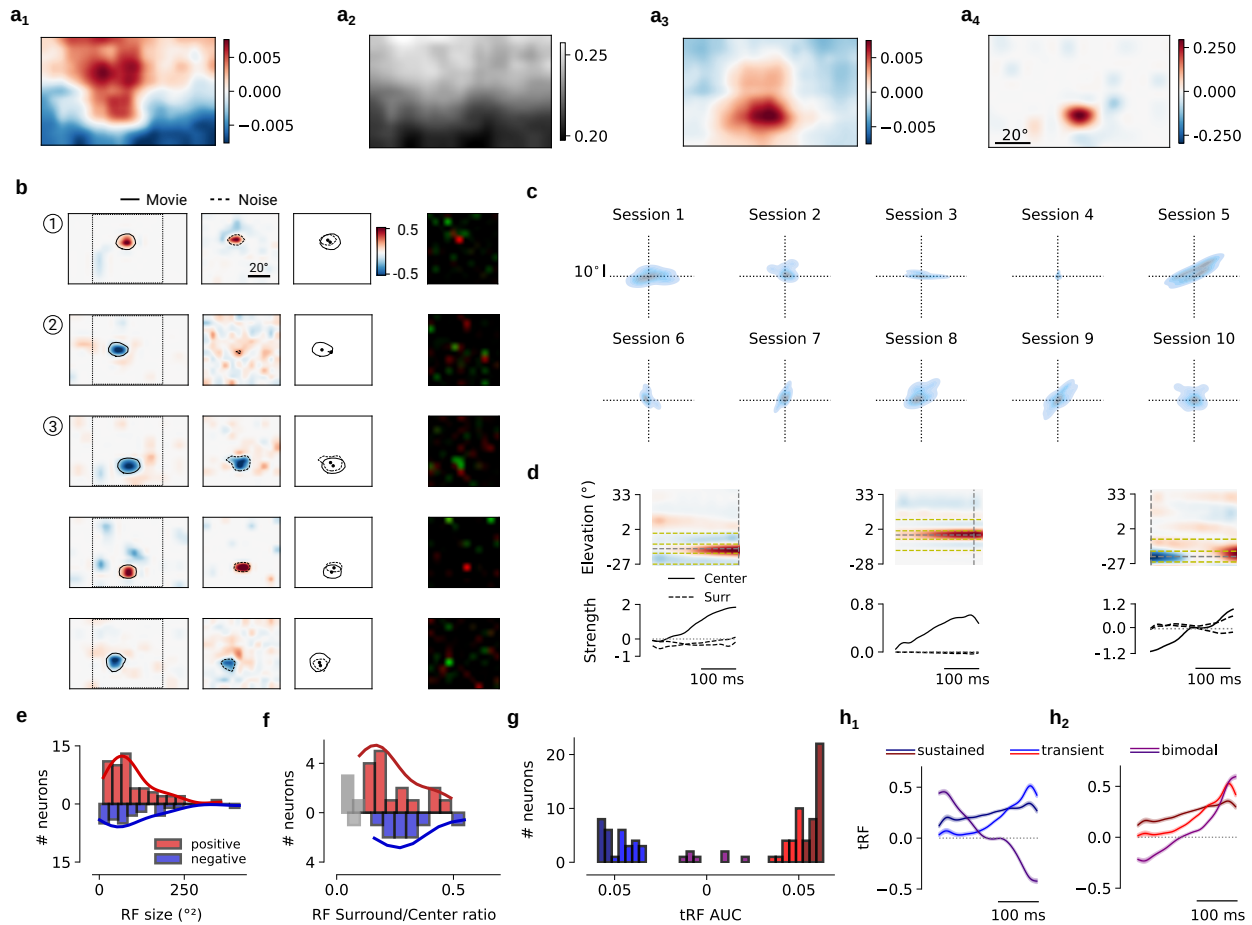


Figure S4 | Spatial RF estimation by the spline-GLM model. (a) Comparison of spatial RF (sRF) estimates during the movie stimulus for one example dLGN neuron. (a1) Simple spike triggered average (STA). (a2) Pixel intensity averaged across all movie frames, showing a gradient from top to bottom typical for naturalistic scenes. (a3) STA corrected for average intensity gradient. This yields a RF with similar centre and polarity compared to the one learned by the spline-GLM (a4), but with larger and more diffuse area. (a4) Learned sRF by the spline-GLM model. (b) To validate the sRF on a neuron-by-neuron basis, we compared the spline-GLM sRF learned from movies (*first column*) with spline-GLM sRF learned from sparse noise experiments (*second column*; overlay of the two sRF centres and contours in the *third column*; see Methods) and with the stimulus-triggered average response map for the sparse noise experiments computed independently from the model (*last column*). The first three example neurons are the same as in **Figure 2c**. (c) Centre shift between movie and sparse noise sRFs for all 10 experimental sessions (neurons with significant stimulus kernels, $n = 85$). Position around the origin indicates close to zero shift. (d) Spatio-temporal RF (stRF) for three example neurons. *Top*: stRFs collapsed across the azimuth axis, and plotted as a function of elevation and time. *Vertical dashed line*: time point with peak activity. *Horizontal dashed lines*: centre regions defined according to the spatial width of the peak activity, and surround regions defined as a ring encircling the centre and extending up to trice the diameter or 9° . *Bottom*: stRF centre (*solid*) and surround (*dashed*) activity. *Left*: antagonistic surround neuron (surround-to-centre ratio = 0.32). *Middle*: non-antagonistic surround neuron (surround-to-centre ratio = 0.02). *right*: bi-phasic response neuron. (e) Area of sRF centres, separately for neurons with positive (*red*) and negative (*blue*) RF centre and significant stimulus kernels. Of these, $\sim 61\%$ (52/85) had a positive centre, $\sim 29\%$ (25/82) had a negative centre, and $\sim 9\%$ (8/85) had a bimodal response where the detected RF changed its polarity across time. Median RF radius: 5 deg; median centre area: 81 deg² for positive RF centers and 77 deg² for negative RF centers. (f) Surround-to-centre ratios for the population of dLGN neurons with significant stimulus kernels, and antagonistic activity in the surround region ($\sim 41\%$ (35/85) neurons). We defined a threshold at 0.1 surround-to-centre ratio (*gray*). Of the remaining neurons with pronounced antagonistic surround, 16 neurons had positive RF centre with a negative surround (*red*), 9 neurons had negative RF centre with a positive surround (*blue*), and 4 neurons showed a biphasic response together with an antagonistic surround. (g) Quantification of tRF properties: histogram of area under the tRF, separately for neurons with positive (*red*) and negative (*blue*) RF centre. Neurons with small tRF AUC values ≤ 0.035 represent the bimodal neurons ($n = 8$, *purple*). Neurons with the largest tRF AUC values ≥ 0.052 were defined as neurons with sustained responses, while the remaining neurons were defined as neurons with transient responses. (h) Mean tRF split into sustained, transient, and biphasic.

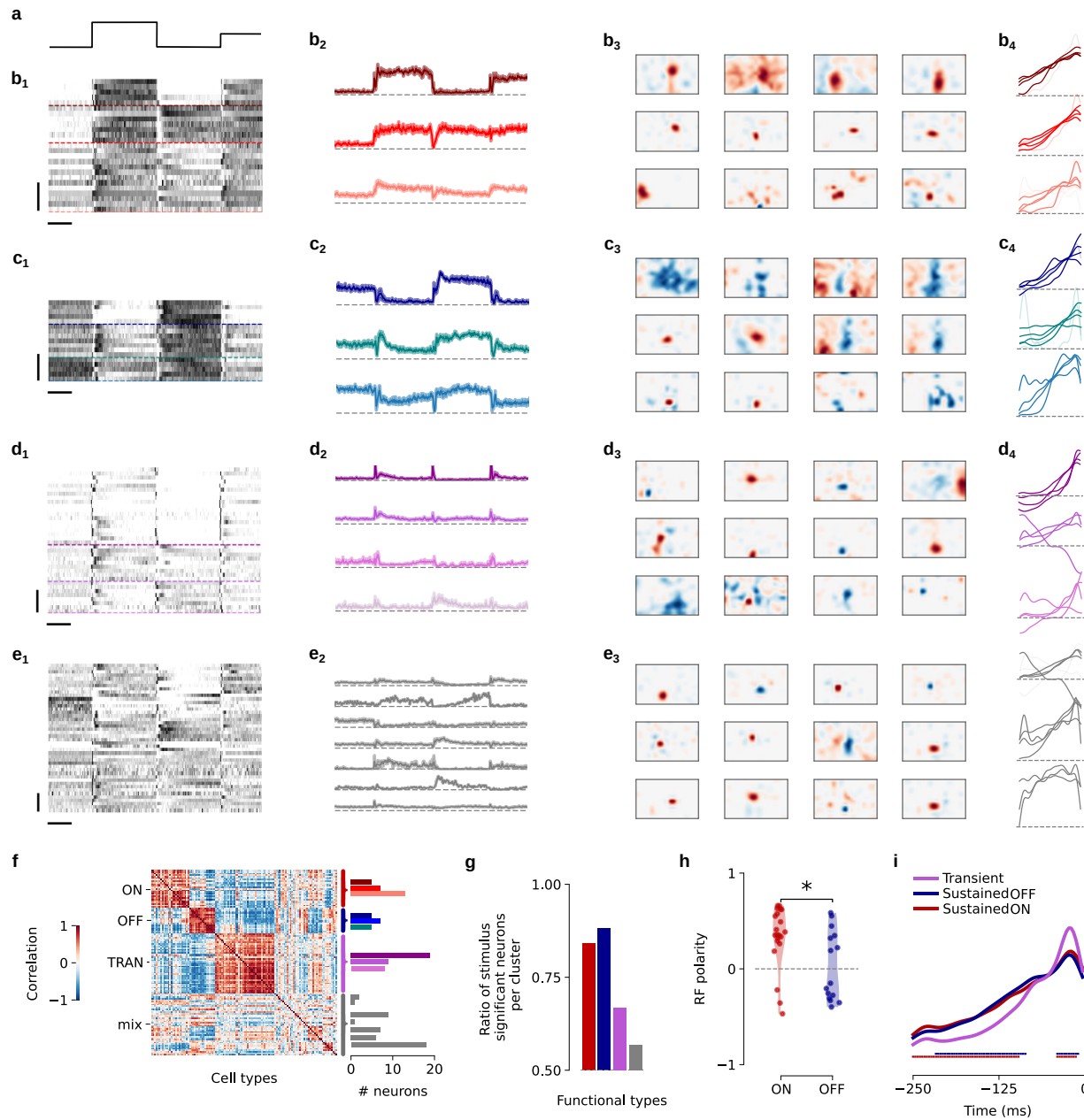


Figure S5 | Spline-based GLM captures spatio-temporal RFs of different functional cell types in dLGN. (a) Top, left: Light intensity steps of the full field stimulus used for functional cell type classification. (b) Responses of all neurons assigned to the Sustained ON group (b_1 , $n = 25$), along with their average sub-cluster responses (b_2). Spatial (b_3) and temporal RF kernels (b_4) of example neurons with significant movie stimulus kernel learned by the spline-GLM independently of the clustering. (c) Same as (b), for the Sustained OFF group ($n = 17$). (d) Same as (b), for the Transient group ($n = 36$). (e) Same as (b), for the remaining neurons (mixed cluster, $n = 44$). (f) Left: Correlation matrix of PCA features used for clustering. Neurons are sorted by groups. Right: Neuron counts per group. (g) Fraction of neurons with significant stimulus kernel in the spline-GLM model per functional type based on clustering. (h) Spatial RF polarity (sign of the spline-GLM fitted RF centre) for the ON and the OFF group based on clustering ($p = 0.018$, Mann-Whitney-U test). (i) Average temporal RF of movie kernels learned from spline-GLM for the OFF, ON, and Transient groups. Horizontal bars: Significant differences between OFF and Transient groups (blue) and between ON and Transient groups (red).

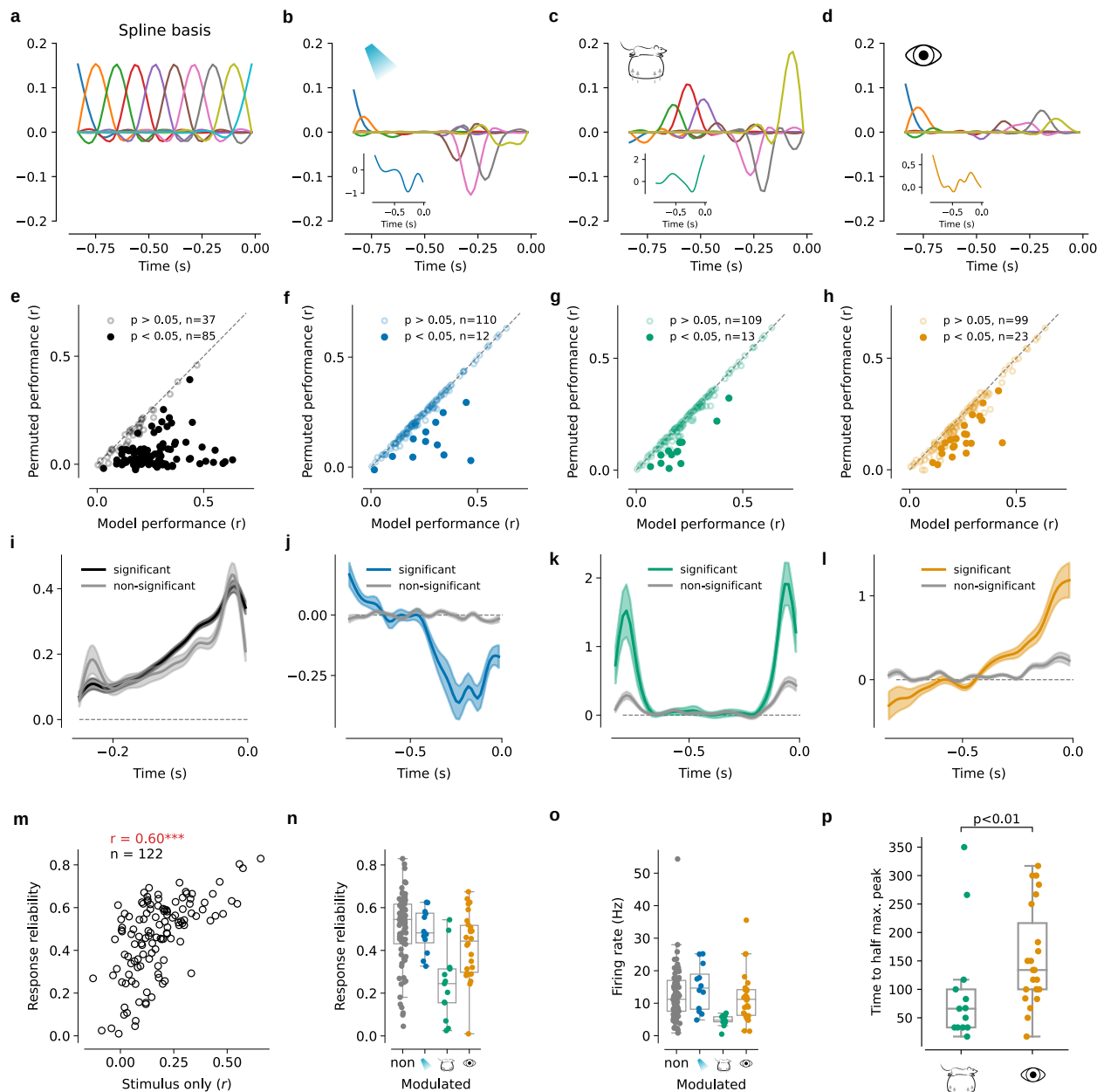


Figure S6 | Spline-GLM model kernels for modulatory inputs. (a) Illustration of the natural cubic spline basis functions ($n=10$). (b) Weighted bases of the natural cubic splines after fitting the CT feedback kernel to the data for one example neuron. CT feedback kernel is shown in the inset. (c) Same as (b), for run speed kernel. (d) Same as (b), for pupil size kernel. (e) Model performance for permuted visual stimulus input (mean over all permutations) vs. actual performance. *Filled circles*: significant neurons. (f) Same as (a), for CT feedback suppression. (g) Same as (a), for running. (h) Same as (a), for pupil size. (i) Average temporal RF kernels, separately for neurons with significant (*black*, $n = 85$) versus non-significant (*grey*, $n = 37$) spatio-temporal kernels. *Shaded areas*: SEM. (j) Same as (e), for neurons with significant (*blue*, $n = 12$) versus non-significant (*grey*, $n = 110$) CT feedback kernels. (k) Same as (e), for neurons with significant (*green*, $n = 13$) versus non-significant (*grey*, $n = 109$) run kernels. (l) Same as (e), for neurons with significant (*orange*, $n = 23$) versus non-significant (*grey*, $n = 99$) pupil kernels. (m) Model performance versus response reliability across all neurons. Response reliability was computed as the mean correlation of dLGN responses to each 40 s repeated movie clip with all other 8 repeats. (n) Response reliability of dLGN neurons split into neurons with significant kernels to CT feedback suppression, running, pupil size, or non-modulated. (o) Same as (j) but for firing rate of dLGN neurons. (p) Kernel time to half maximum peak for run and pupil size kernels.

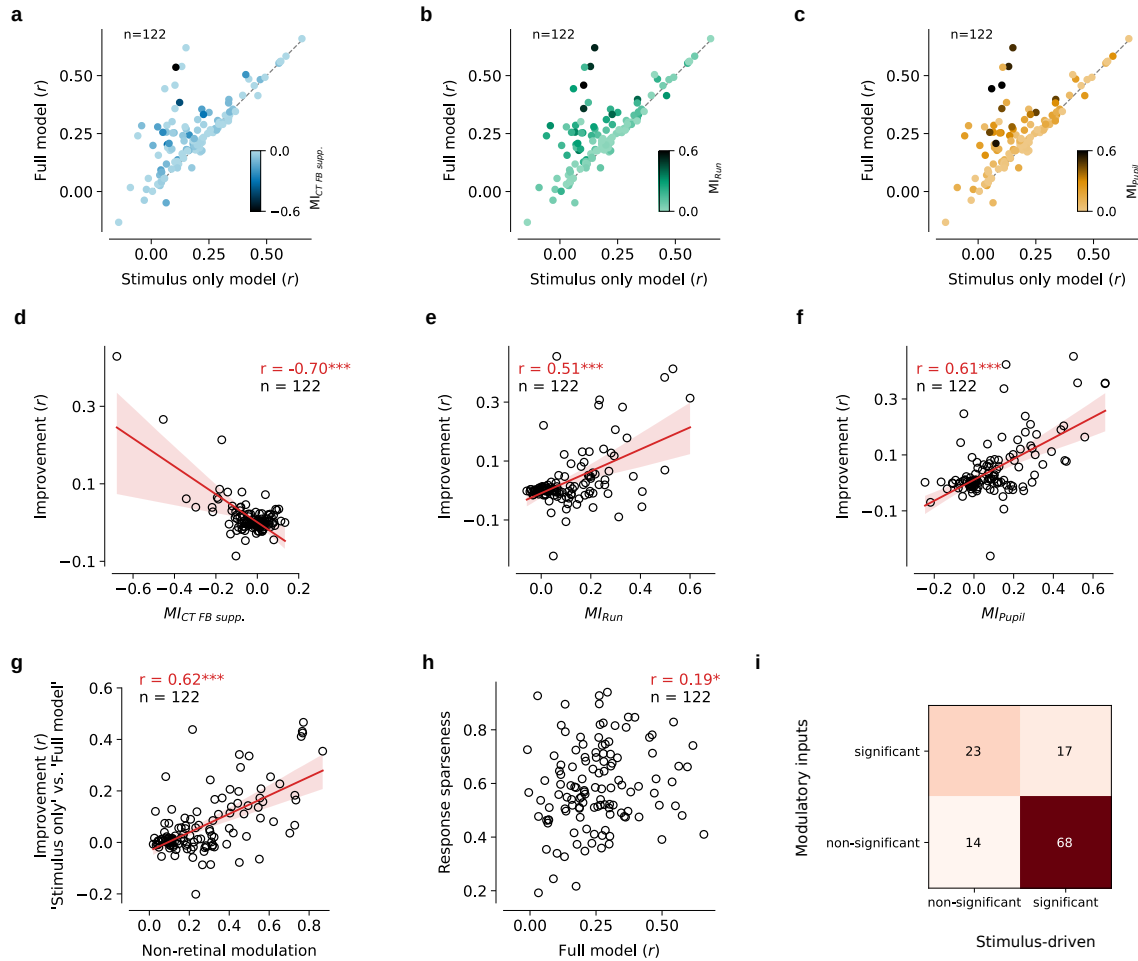


Figure S7 | Model performance depends on various factors. (a) Comparison of model performances on the test set for all neurons in the 'Stimulus only' model and the 'Full model'. Darker colours indicate stronger modulation by CT feedback quantified by $MI_{CT\ FB\ supp.}$ (see Methods). (b) Same as in (a) but for by running quantified by the modulation index MI_{Run} . (c) Same as in (a) but for pupil size quantified by the modulation index MI_{Pupil} . (d) Correlation of modulation by CT feedback suppression ($MI_{CT\ FB\ supp.}$) and model performance improvement. To measure improvement two models were compared: the 'Stimulus only' model and a model with Stimulus and CT feedback suppression as inputs. (e) Same as in h but for modulation by running (MI_{Run}). The 'Stimulus only' model was compared with a model that integrated stimulus and running as inputs. (f) Same as in h but for modulation by pupil size (MI_{Pupil}). The 'Stimulus only' model was compared with a model that integrated stimulus and pupil size as inputs. (g) Modulation by additional factors (MI_{Joint}) versus improvement of model performance when comparing the 'Stimulus only' model and the 'Full model'. $***p \leq 0.001$ (h) Model performance versus response sparseness. Sparseness was computed according to (112). $*p \leq 0.05$ (i) The matrix illustrates the neuron counts categorised into 68 neurons significant only to feedforward stimulus-related predictor, 23 neurons significant only to one or more of the predictors for modulatory inputs (CT feedback, run speed, and pupil dilation), 17 significant to all predictors, and 14 not exhibiting significance for any of the predictors.

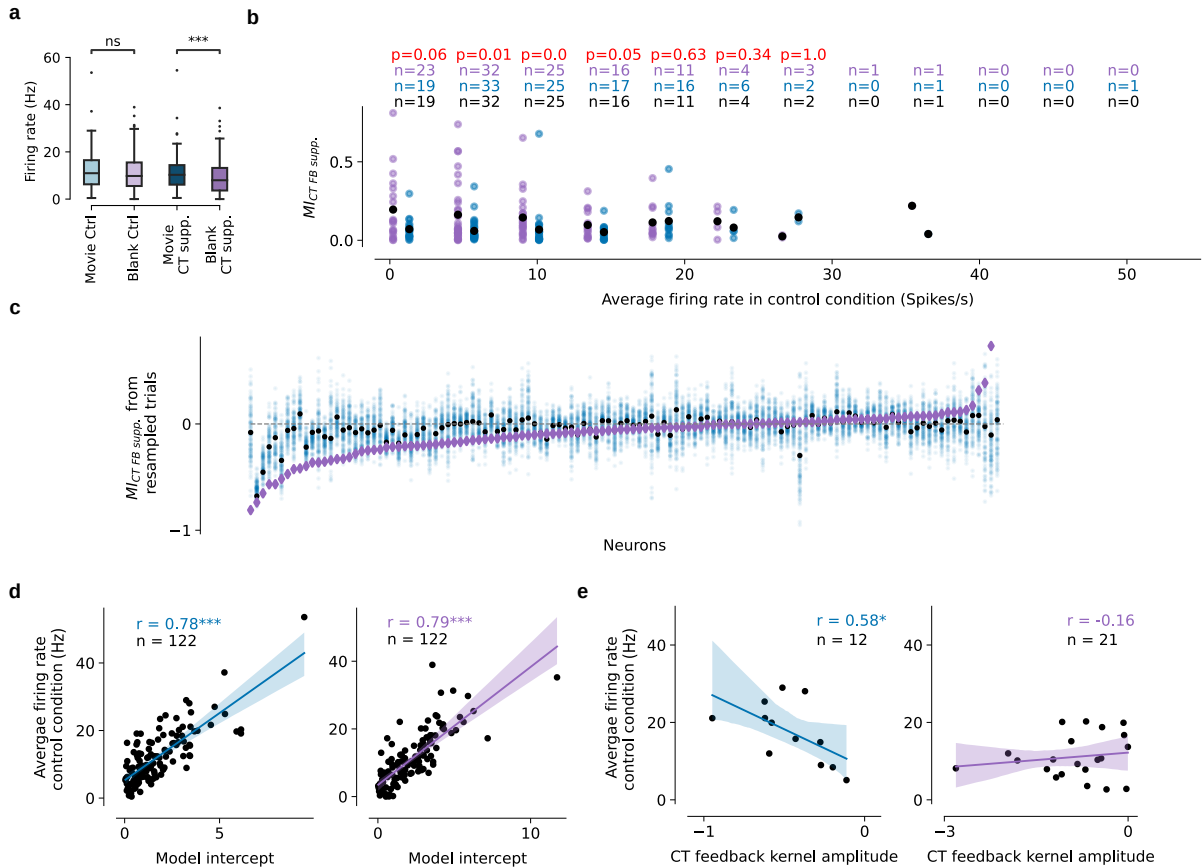


Figure S8 | Influences of visual stimulus on effects of CT FB suppression in dLGN. (a) Firing rate comparison between conditions. Bonferroni corrected p -values of paired Wilcoxon signed-rank test: $***p \leq 1.0 \times 10^{-3}$; ‘ns’ non-significant. (b) Analysis controlling potential influences of overall firing rate differences between conditions. $M_{CT\ FB\ supp.}$ for movies (blue) or blank periods (purple) as a function of binned average firing rate during the control condition. We counted the neurons that fell within each firing rate bin for the two stimulus conditions (top, coloured numbers). To ensure equal number of neurons per firing rate bin between the conditions, we randomly sampled the minimum number of neurons for that bin for one of the stimulus conditions (black numbers). Black dots represent the mean $M_{CT\ FB\ supp.}$ value per bin per condition after potential re-sampling. Even after approximating overall firing rates, $M_{CT\ FB\ supp.}$ remained significantly higher for low firing rate bins, where most neurons were sampled (red numbers, Mann-Whitney-U test). (c) Scatters of $M_{CT\ FB\ supp.}$ values recalculated based on re-sampled trials. Given that movie and blank conditions had different number of trials, and in order to rule out that the number of trials might affect the $M_{CT\ FB\ supp.}$ values and accordingly the reported results, we performed 100 repeats of a re-sampling procedure. During each repeat, we randomly sampled 24 trials for each neuron during movie condition and re-calculated the $M_{CT\ FB\ supp.}$ values (light blue dots). We found that the original movie $M_{CT\ FB\ supp.}$ values (black dots) well represented the median of the re-calculated values. We also found that our observation that the original Blank $M_{CT\ FB\ supp.}$ (purple) being stronger than movie $M_{CT\ FB\ supp.}$ held true after re-sampling. (d) Scatter plot of average firing rate during the control condition vs. intercept fitted by the model for the movie (left) and blank periods (right). Panels (a–d) show data from all 122 neurons. (e) Scatter plot of average firing rate vs. maximum amplitude of the fitted CT feedback kernels for significantly modulated neurons for the movie (left) and blank (right) conditions.

5 A transthalamic pathway for visual control of fear behaviour

The following chapter is reproduced from an article originally published in *Neuron*:

Davide Crombie, Laura Busse (2021). Should I stay or should I go? A thalamic circuit for modulating behavioral responses to visual threat. *Neuron*, 109(23), 3717-3719. DOI: <https://doi.org/10.1016/j.neuron.2021.11.005>.

Author contributions

The original draft writing, editing, and reviewing was performed equally by DC and LB. The invitation to produce the work was acquired by LB.

Personal contributions

DC contributed equally to writing the original draft and reviewing and edition, and produced the figure presented in the article.

Copyright

This article was published under the CC-BY 4.0 International licence.

Should I stay or should I go? A thalamic circuit for modulating behavioral responses to visual threat

Daive Crombie^{1,2} and Laura Busse^{1,3,*}

¹Division of Neurobiology, Faculty of Biology, LMU Munich, Martinsried 82152, Germany

²Graduate School of Systemic Neurosciences (GSN), LMU Munich, Martinsried 82152, Germany

³Bernstein Centre for Computational Neuroscience Munich, Martinsried 82152, Germany

*Correspondence: busse@bio.lmu.de

<https://doi.org/10.1016/j.neuron.2021.11.005>

In this issue of *Neuron* and in *Cell Reports*, [Fratzl et al. \(2021\)](#) and [Salay and Huberman \(2021\)](#) identify the ventral lateral geniculate nucleus (vLGN) of the thalamus as a key regulator for adjusting defensive behaviors according to the level of perceived visual threat.

For many animals, vision is an essential sense for detecting threats, such as approaching predators, and for initiating behavioral responses that can decide between life and death. For instance, across the animal kingdom, reductions in luminance caused by rapidly moving or expanding shadows ([Figure 1A](#)) can signal the approach of a potential threat and trigger defensive behaviors ([Branco and Redgrave, 2020](#); [Peek and Card, 2016](#)). In rodents, these behaviors typically encompass freezing to minimize detection, flight to escape an attack by a predator, or tail rattling to display aggression ([De Franceschi et al., 2016](#); [Yilmaz and Meister, 2013](#); [Salay and Huberman, 2021](#)).

A central hub linking vision and defensive behaviors is the optic tectum (OT), known as the superior colliculus (SC) in mammals. The SC is a retino-recipient, multilayered structure located in the dorsal midbrain, with highly conserved circuitry and functions. It is known for integrating visual input with information from other sensory modalities and orchestrating sensory-motor transformations ([Basso et al., 2021](#)). In particular, the SC is thought to be involved in computing saliency, selecting relevant information, and initiating short-latency orienting responses, which are necessary components for directing behavior toward specific points in space. These functional properties likely also support the SC in coordinating visually evoked defensive behaviors ([Branco and Redgrave, 2020](#)). Indeed, neurons in SC can be strongly

and selectively driven by visual threats, such as dark expanding stimuli from overhead space (looming disks) mimicking aerial predators ([Yilmaz and Meister, 2013](#); [Lee et al., 2020](#)).

Defensive behaviors, while sometimes being portrayed as deterministic and stereotyped, can be remarkably flexible, depending on the ethological context, physiological state of the animal, or the animal's past experience. For instance, looming disks initially elicit defensive responses with high reliability; repeated exposure in the lab without negative consequences, however, can lead to habituation, with reduced duration of freezing or lower probability of escape ([Yilmaz and Meister, 2013](#)). Until now, how neural circuits and cell types integrate sensory evidence with contextual and experience-related information to flexibly adjust visually defensive behaviors has been poorly understood.

In this issue of *Neuron* and in *Cell Reports*, two studies address this gap in knowledge by identifying the ventral lateral geniculate nucleus (vLGN) of the thalamus as a critical node in the circuit conferring flexibility to visually triggered defensive behaviors ([Fratzl et al., 2021](#); [Salay and Huberman, 2021](#)) ([Figure 1](#)).

The vLGN is a subdivision of the LGN, a retinorecipient thalamic structure, whose dorsal part (dLGN) is well studied because of its role in image-forming vision in mammals. The vLGN, which is comparable in size to the dLGN in rodents, does not contribute to cortical image-forming vision but instead sends out long-range

inhibitory projections to several nuclei with roles in sensorimotor behavior, eye movements, and vestibular and circadian function ([Monavarfeshani et al., 2017](#)). [Fratzl et al. \(2021\)](#) describe how activity of the inhibitory GABAergic projection of the vLGN to the medial SC (vLGN_{GABA} → mSC) tracks perceived visual threat and thereby exerts visual context-dependent control over escape responses. [Salay and Huberman \(2021\)](#) reveal distinct neuronal populations that project from the vLGN either to the SC or to the nucleus reuniens (Re) and have opposing functions, potentially to balance defensive actions and exploration depending on perceived risk in uncertain environments.

Using a wide array of state-of-the-art circuit investigation approaches—including viral circuit tracing, *in vivo* recordings of neural activity with fiber photometry and dense microelectrode arrays, and circuit manipulations with optogenetics and chemogenetics—as well as extensive quantification of behavior, both groups reveal that activity of vLGN_{GABA} neurons regulates defensive behaviors to imminent visual threats ([Figures 1B and 1C](#)). In both studies, when the experimenters suppressed the activity of vLGN_{GABA} neurons, mice had reduced control over the execution of their defensive behavioral programs: upon encounter with a threatening visual stimulus, they almost invariably fled to shelter ([Fratzl et al., 2021](#)) or displayed increased duration and probability of freezing ([Salay and Huberman, 2021](#))—a behavioral signature of anxiety-like states.



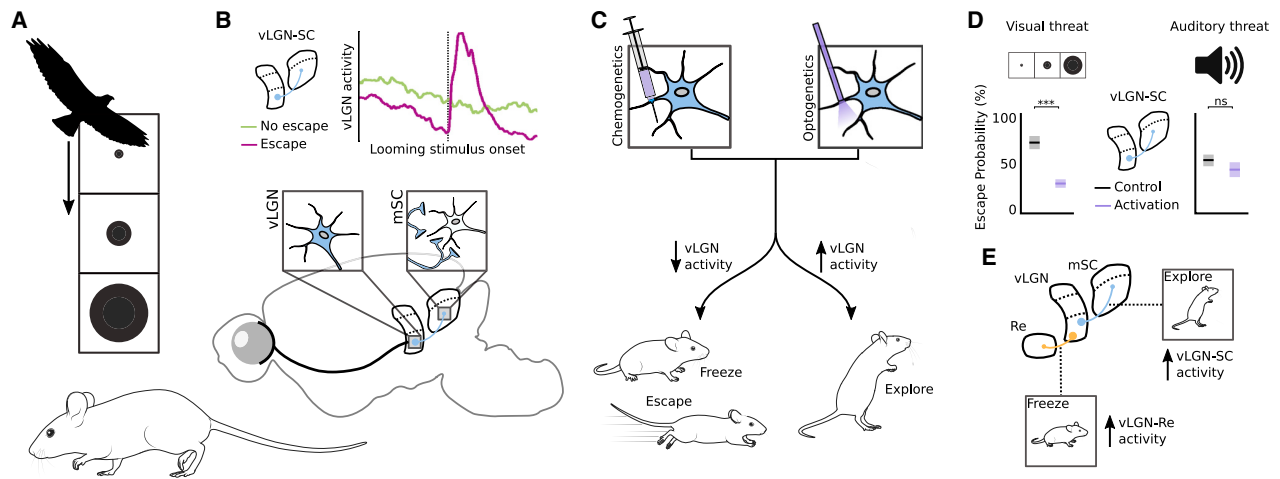


Figure 1. Key results of Fratzl et al. and Salay and Huberman

(A) Both studies used, among several other behavioral paradigms, looming disk stimuli mimicking aerial predators to study how circuits involving the ventral lateral geniculate nucleus (vLGN) modulate defensive responses to perceived visual threats in mice.
 (B) Fiber photometry recordings performed by Fratzl et al. (2021) show that activity in GABAergic projections from vLGN to medial superior colliculus (mSC) around lobe onset was particularly low during trials in which mice subsequently initiate an escape response. This pattern is consistent with the notion that the vLGN_{GABA} → mSC projection signals the level of perceived threat.
 (C) Using chemogenetic and optogenetic circuit manipulation techniques, the authors of both studies discovered that bidirectional control of GABAergic neurons in vLGN can shift the behavior of mice between defensive responses and exploration.
 (D) Fratzl et al. (2021) also revealed that the modulation of defensive behaviors by vLGN is specific to visual threats; activating vLGN axons in the mSC specifically suppresses escape from visual, but not auditory, threats.
 (E) Salay and Huberman (2021) focused on the diversity of neuronal cell types in vLGN. The authors propose a push-pull role of vLGN, demonstrating that activity in the vLGN population projecting to the SC promotes exploratory behaviors, while activity in the vLGN population projecting to the nucleus reuniens (Re) increases freezing and anxiety-like behaviors. The mice, along with the bird and neuron silhouettes in this figure, were sourced from <https://scidraw.io/>.

Conversely, when the authors activated the vLGN_{GABA} neurons, these defensive responses were mostly blocked, and mice favored exploration of their environment.

While both studies uncover a so-far unknown role for the vLGN_{GABA} → SC projection in regulating defensive behaviors, each study also offers unique insights into the circuits and function of vLGN. In particular, Fratzl et al. (2021) measured activity of vLGN_{GABA} → mSC axons during escapes to shelter triggered from a “threat zone,” where the mice had previously experienced a looming stimulus. The authors found that activity of vLGN axons over mSC was particularly low just before escapes, while it remained higher in non-escape trials (Figure 1B, top), occurring, for example, when the animal was habituated. This pattern of results suggests that the vLGN_{GABA} → mSC projection plays a prominent role in signaling the perceived level of threat. In addition, Fratzl et al. (2021) demonstrate that vLGN’s regulatory function is related to visual, but not auditory, threats (Figure 1D). When the authors presented loud, high-frequency sounds from the

threat zone, mice often escaped to shelter, similar to when facing a looming visual stimulus. However, while optogenetic activation of vLGN_{GABA} → SC axons decreased the probability of escape from visual threats, the same manipulation did not alter the probability of sound-evoked escapes. Consistent with a role for the vLGN in modulating defensive responses for visual threats specifically, the authors further discovered that the vLGN_{GABA} → SC axons preferentially target visually responsive neurons in the mSC. Indeed, neuropixel recordings in mSC revealed that photoactivation of the vLGN_{GABA} → SC projection specifically reduced the activity of those SC neurons that responded to visual, but not auditory, stimuli.

The study by Salay and Huberman (2021) elegantly complements and substantially extends these findings by focusing on the diversity of vLGN neuron types and projections and by providing evidence for their functional specificity. For instance, it was already known that, besides the projection to the SC, the vLGN also sends GABAergic projections to the

periaqueductal gray area (PAG) and the Re of the ventral midline thalamus, which both take part in the extensive network mediating behavioral responses to visual threats (Branco and Redgrave, 2020). After establishing that the vLGN’s projections to Re and SC arise from two distinct populations of GABAergic neurons, Salay and Huberman (2021) used chemogenetic manipulations to demonstrate their opposing effects (Figure 1E): while activating vLGN_{GABA} → SC neurons decreased freezing and promoted rapid habituation, increasing the activity of the vLGN_{GABA} → Re projection yielded dramatically prolonged freezing responses. Salay and Huberman (2021) additionally explored the impact of vLGN_{GABA} activity changes over longer timescales and found that the vLGN also plays a role in modulating autonomic arousal. By expressing a stabilized step function version of channelrhodopsin in vLGN_{GABA} neurons, which allows persistent increases of neuronal firing with a single pulse of blue light, Salay and Huberman (2021) found a long-lasting decrease of heart rate with delayed onset

over the course of tens of minutes. These results suggest that vLGN_{GABA} neurons not only exert rapid modulations of visually triggered threat responses but also promote delayed changes in autonomic arousal.

Both studies decisively demonstrate how neuronal circuits involving the vLGN can adjust visually evoked defensive behaviors, and in doing so they also raise several exciting new questions. For example, what exact role does the retinal input to the vLGN play in modulating behavioral responses according to the visual conditions? While it is known that the vLGN and SC are targeted by broadly different classes of retinal ganglion cells (Monavarfeshani et al., 2017), further insights into the specific retinal input and the vLGN's own visual representations (see, e.g., Ciftcioglu et al., 2020) will provide a deeper understanding of how the vLGN influences activity in downstream sensorimotor structures. Given that the vLGN is also innervated by numerous non-retinal afferents (Monavarfeshani et al., 2017), another crucial next step will be to gain insights into how the vLGN integrates these input streams to signal safety or danger based on past experience. Finally, a comparison to other

inhibitory long-range projections in the brain will likely generate novel insights into canonical purposes of signaling with this circuit motif.

In summary, the two studies by Fratzl et al. (2021) and Salay and Huberman (2021) provide a major leap forward in our understanding of the neural circuits that contribute to regulating innate defensive behaviors depending on visual context and experience. Such a mechanistic understanding of how fear-related behaviors and anxiety-like states are adjusted promises to be invaluable in the long term for the understanding and treatment of anxiety disorders.

ACKNOWLEDGMENTS

Work in the Busse laboratory is supported by the German Research Foundation (DFG; SFB870 TP19 project number 118803580; SFB1233 TP10 and TP13 project number 276693517; BU 1808/6-2). D.C. is supported by the DFG Research Training Group "Perception in Context and its neural basis" (RTG-DFG 2175, awarded to C. Leibold).

REFERENCES

Basso, M.A., Bickford, M.E., and Cang, J. (2021). Unraveling circuits of visual perception and cognition through the superior colliculus. *Neuron* 109, 918–937.

Branco, T., and Redgrave, P. (2020). The Neural Basis of Escape Behavior in Vertebrates. *Annu. Rev. Neurosci.* 43, 417–439.

Ciftcioglu, U.M., Suresh, V., Ding, K.R., Sommer, F.T., and Hirsch, J.A. (2020). Visual Information Processing in the Ventral Division of the Mouse Lateral Geniculate Nucleus of the Thalamus. *J. Neurosci.* 40, 5019–5032.

De Franceschi, G., Vivattanasarn, T., Saleem, A.B., and Solomon, S.G. (2016). Vision Guides Selection of Freeze or Flight Defense Strategies in Mice. *Curr. Biol.* 26, 2150–2154.

Fratzl, A., Koltchev, A.M., Vissers, N., Tan, Y.L., Marques-Smith, A., Stempel, A.V., Branco, T., and Hofer, S.B. (2021). Flexible inhibitory control of visually evoked defensive behavior by the ventral lateral geniculate nucleus. *Neuron* 109, 3810–3822.

Lee, K.H., Tran, A., Turan, Z., and Meister, M. (2020). The sifting of visual information in the superior colliculus. *eLife* 9, e50678.

Monavarfeshani, A., Sabbagh, U., and Fox, M.A. (2017). Not a one-trick pony: Diverse connectivity and functions of the rodent lateral geniculate complex. *Vis. Neurosci.* 34, E012.

Peek, M.Y., and Card, G.M. (2016). Comparative approaches to escape. *Curr. Opin. Neurobiol.* 41, 167–173.

Salay, L.D., and Huberman, A.D. (2021). Divergent outputs of the ventral lateral geniculate nucleus mediate visually evoked defensive behaviors. *Cell Rep.* 37, 109792.

Yilmaz, M., and Meister, M. (2013). Rapid innate defensive responses of mice to looming visual stimuli. *Curr. Biol.* 23, 2011–2015.

6 Discussion

6.1 Summary

In the above chapters, four manuscripts exploring the influence of various contextual factors on thalamic visual processing were presented. The first three manuscripts focused on the dorsal lateral geniculate nucleus (dLGN). Each taking a different perspective on measuring contextual modulation, these manuscripts uniquely contribute to our knowledge of how feedback signals, active behaviours, and arousal influence visual stimulus processing. In the final manuscript – a mini-review commenting on two recent publications from other research groups – the scope was broadened to ask the converse question: how do visual signals influence stereotyped behaviours? Ultimately, both of these lines of investigation support the notion that vision and action are intimately linked. Even at the earliest stages of processing, visual signals are formed by, and inform, ongoing behaviours and behavioural states.

In the first manuscript (Spacek et al., 2022, Chapter 2), the experimentally-manipulated presence of corticothalamic feedback (CT-FB) and the spontaneous occurrence of locomotion were used to partition neural activity recorded from the dLGN of awake mice in response to naturalistic movies. This was the first investigation to probe the effects of CT-FB in the dLGN using naturalistic stimuli and awake animals, which was important as both of these contextual factors are thought to be critical for the operation of the visual thalamocortical circuit. Furthermore, CT-FB was *suppressed*, rather than activated, in order to preserve its endogenous effects when intact. With the naturalistic visual stimulation, it was found that CT-FB consistently provided multiplicative gain to the stimulus responses of dLGN neurons, while decreasing the propensity for stimulus-triggered bursting. Meanwhile, during stimulation with artificial drifting gratings, there was no consistent effect on overall firing rate across neurons. These results are interpreted to indicate that the strength of CT-FB is determined by the spatiotemporal features of the visual stimulus. Interestingly, the overall effects of locomotion on dLGN responses to naturalistic stimuli was, at a population level, qualitatively similar to that of CT-FB. However, the effect of locomotion persisted in trials where CT-FB was suppressed, and the effects of CT-FB and locomotion were independent on a single-neuron level. Altogether, this pattern of results suggests that CT-FB and locomotion have similar effects on the dLGN as a whole, but that the measured effects of locomotion in the dLGN are not primarily conferred via CT-FB.

In the second manuscript (Crombie et al., 2024, Chapter 3), rather than locomotion, modulation of dLGN activity with behavioural states was captured using pupil size dynamics. Importantly, this manuscript moved beyond describing behavioural state in terms of a dichotomy, and used the multi-scale dynamics of pupil size as an index for modulations. In almost all dLGN neurons, both bursting and tonic spiking were linked to pupil size dynamics across a broad range of temporal scales. There was diversity both between neurons from the same recording, with neurons being most strongly modulated at different timescales, and within the activity of single neurons, with single neurons coupling to multiple components of pupil dynamics. This pattern of coupling supports the hypothesis that a single quantity, such as pupil size alone, is insufficient to provide a complete picture of arousal-related dLGN activity modulations, and may be only one aspect of a larger set of

modulations. Furthermore, although behaviours such as locomotion and eye movements were found to induce changes in dLGN activity, and were themselves linked to pupil size dynamics, neither fully accounted for the pupil-linked coupling, suggesting that, although internal states and active behaviours are linked, sensory systems are modulated by internal states beyond the direct effects of overt behaviours. Finally, this work showed that states defined by pupil dynamics across all temporal scales measured were linked to differences in sensory encoding in the dLGN. Together, these results challenge the notion that modulations in sensory processing are best described by mutually exclusive states, and support the interpretation that a multitude of behaviour- and state-related factors simultaneously exert their influence on sensory neurons.

The last research article (Schmors et al., 2023, Chapter 4) explored the use of a unified spline-GLM modelling framework to capture the effects of visual stimulation, CT-FB, and behavioural state on dLGN activity. The spatiotemporal receptive fields (RFs) recovered by the model matched well with empirically-determined stimulus responses in the dLGN, but the model also uncovered a large diversity in the amount of neural activity that could be explained by the stimulus alone. Specifically, for those neurons where the model performed poorly using the RF alone, allowing for additive contributions of CT-FB, locomotion, and pupil size greatly improved how well the model captured spiking activity, with the polarity of the kernels for these variables matching what was expected from the literature. With regards to CT-FB, it was found that the magnitude and temporal profile of its effects was strongly dependent on the stimulus context, with a stronger, but more temporally-restricted influence in the absence of a naturalistic stimulus. Counter-intuitively, the model predicted that stimulus decoding from the activity of single neurons would be less accurate with CT-FB left intact. These results nicely complement those obtained in Spacek et al. (2022, Chapter 2), where the strongest effect of CT-FB was measured in periods where visual stimulation was absent, and the presence of CT-FB was associated with higher response variability which could underlie worse stimulus decoding performance. Altogether, the model demonstrated good correspondence with results measured directly from the data, thus advancing a conceptual framework for understanding visual processing in context, and further showed how this class of model can generate predictions about dynamic dLGN circuit functions.

In the final enclosed manuscript (Crombie and Busse, 2021, Chapter 5), two recent studies were reviewed, both converging on a novel role for the thalamic ventral lateral geniculate nucleus (vLGN) in the modulation of behavioural responses to visual threat. While the responses themselves are thought to be orchestrated in the superior colliculus (SC), these recent publications suggest that the vLGN provides a contextual signal to the SC – namely, a safety signal that reduces the probability of performing defensive actions when confronted with a potentially threatening stimulus. Interestingly, this modulation was limited to responses to *visual* threats, raising many questions about the contributions of the retinorecipient vLGN to visual processing overall, and its role in the coordination of other behaviours related to visual processing.

6.2 Modulatory mechanisms

Visual signals

Arousal and active behaviours such as locomotion are often associated with relative pupil dilation (Erisken et al., 2014; Vinck et al., 2015), and, while this provides a useful external marker for internal state, it also provides a confound when working in the visual system. Indeed, the canonical purpose of pupil size changes is to control the amount of light reaching the visual system, which could influence downstream activity and be mistakenly attributed to internal factors. To what degree are the observed modulations caused by increased light influx onto the retina versus internal signals? Spacek et al. (2022, Chapter 2) and Crombie et al. (2024, Chapter 3) observed higher firing rates and less bursting (indicating relative membrane depolarization) in the dLGN during arousal, and, likewise, Schmors et al. (2023, Chapter 4) found that pupil size and locomotion had a positive impact on dLGN firing rates. A skeptical account could argue that when the pupil is larger during arousal, more light hits the retina, providing more feed-forward excitatory drive to ON cells of the dLGN. Although not *all* dLGN cells have ON responses, ON responses dominate output of the awake mouse retina (only 20% of RGCs are OFF responding; Boissonnet et al., 2023), the majority of mouse dLGN neurons with spatially restricted RFs are ON responding (67%; Grubb and Thompson, 2003), and up to 40% of mouse dLGN neurons increase their firing rate in response to full-field light increments (Brown et al., 2010).

However, several arguments against a purely visual cause of state-related modulations arise. The presence of similar modulations in the somatosensory system (Reimer et al., 2014; Petty et al., 2021) suggests that such modulations are non-visual in origin. However, suppressive effects of arousal have been observed in the auditory system (Zhou et al., 2014; McGinley et al., 2015a; Williamson et al., 2015; Shimaoka et al., 2018), suggesting that arousal-related modulations are not uniformly excitatory, and thus the excitation observed in the visual system could still be of retinal origin. While Spacek et al. (2022, Chapter 2) did not control for increased feed-forward retinal drive due to dilated pupils during locomotion, an earlier publication did. By fully dilating the pupils with atropine prior to measuring modulations, Erisken et al. (2014) revealed that dLGN modulation related to locomotion are almost identical in the absence of the accompanying pupil size changes. Furthermore, Crombie et al. (2024, Chapter 3) measured modulations related to pupil size dynamics that were not accounted for by pupil size *per se*, and, critically, revealed that these pupil-linked dLGN modulations had the same general characteristics even with sources of illumination removed from the recording chamber. Together, these results support the interpretation that a significant component of arousal-related modulation in the visual system is derived from internal, non-visual sources. But is it productive to try to exclude the effects of feed-forward drive from measurements of modulation in the visual system?

A more complete perspective emphasizes the interactions between visual and non-visual components of behavioural states, and even a functional role for the link between pupil size changes and behavioural states. The visual system has exquisite sensitivity down to the single photon level (Rieke and Baylor, 1998; Tinsley et al., 2016), and therefore the effect of light cannot be completely ruled out with typical experimental setups. More importantly, light is ubiquitously present for most mammals, and is indeed a prerequisite for visual

perception. Additionally, it has been hypothesized that pupil size changes may occur *purposefully* to change the way light impinges on the retina in order to optimize certain visual-perceptual functions based on cognitive demands (Ebitz and Moore, 2019; Mathôt, 2020). While it remains to be seen how such mechanisms are relevant in afoveate mice, these considerations underscore a fundamental role for pupil-linked changes to feed-forward visual signals in arousal. Thus, in studies concerned with visual stimulus encoding, such as those enclosed in the above chapters, it is more productive to discuss the possible interactions between visual stimuli and behavioural states.

For example, it has recently been shown that pupil-indexed arousal is linked to a shift in the spectral sensitivity of mouse V1, with increased relative sensitivity to the UV channel of naturalistic dichromatic stimuli (Franke et al., 2022). This relative shift in spectral sensitivity most likely depends on increased feed-forward drive from the retina, and could be recapitulated by artificial pupil dilation or changes in ambient illumination at fixed pupil sizes (Franke et al., 2022). Thus, the pupil size changes that co-occur with arousal and locomotion may be adaptive, priming the visual system towards detection of aerial objects which are best detected in the UV channel (Franke et al., 2022). Interactions between changes in feed-forward drive and behavioural modulations have also been observed in relation to locomotion (Pakan et al., 2016), head movements (Bouvier et al., 2020), and eye movements (Parker et al., 2023). Therefore, while pupil-linked changes in retinal illumination are likely not the driving factor in broad modulations such as arousal-linked changes in firing rate, there is a definite role for changes in luminance and feed-forward signalling in the state-related modulation of the visual system.

Neuromodulatory signals

Although the interactions between visual factors like illumination and behavioural state are just starting to be investigated, it has long been clear that neuromodulators play a large role in the determination of state-related brain activity. Acetylcholine (ACh) and norepinephrine (NE) have historically been linked to the transition from sleep to wakefulness in thalamocortical state (Moruzzi and Magoun, 1949; Steriade and McCarley, 1990), and more recently to locomotion (Polack et al., 2013; Fu et al., 2014; Lee et al., 2014; Nelson and Mooney, 2016; Reimer et al., 2016) and pupil size increases during wakefulness (Rajkowski et al., 1994; Aston-Jones and Cohen, 2005; Joshi et al., 2016; Reimer et al., 2016; Larsen and Waters, 2018). Application of ACh to dLGN neurons *in vitro* results in both rapid depolarization via nicotinic ion channels, and prolonged depolarization via muscarinic receptor-mediated block of potassium leak currents, capable of switching neurons from burst to tonic mode (McCormick, 1992). Similarly, NE acts via α_1 adrenergic receptors to blocks potassium leak currents resulting in a slow depolarization, and also enhances the hyperpolarization-activated cation current, both of which contribute to a reduction in bursting (McCormick, 1992). Both NE and ACh are therefore potential mechanism underlying the locomotion-related increase of firing rates and reduction of bursting (Spacek et al., 2022, Chapter 2), and switches from burst to tonic firing during pupil dilation (Crombie et al., 2024, Chapter 3) in dLGN neurons.

However, the effects of these neuromodulators on dLGN neurons *in vivo* might be complicated due to

simultaneous alterations in the activity of other circuit components such as V1-L6 or the TRN. As an illustrative example: NE has also been shown to depolarize TRN neurons (McCormick, 1992), which could lead to an increased tonic inhibition on dLGN neurons, counteracting the direct effects of NE on these neurons. Fortunately, activation of the LC-NE *in vivo* does indeed result in increased spontaneous firing rates and decreased bursting in the dLGN (Holdefer and Jacobs, 1994). Similarly, activation of either the BF or PPN causes depolarization and a burst-to-tonic switch in dLGN neurons (Hu et al., 1989; Lu et al., 1993; Goard and Dan, 2009). These *in vivo* observations further underscore a role for the BF-ACh, PPN-ACh, and LC-NE systems in the findings of Spacek et al. (2022, Chapter 2), Crombie et al. (2024, Chapter 3), and Schmors et al. (2023, Chapter 4), but precise mechanisms at play during locomotion and pupil size changes remains unclear. While the cortex and TRN are innervated by cholinergic fibers from the BF, the dLGN only directly receives ACh from the PPN (Huerta-Ocampo et al., 2020; Sokhadze et al., 2022), which, unlike the BF, has not been linked to the pupil size signal. Furthermore, *in vivo*, dLGN neurons are likely subject to combinations of these modulatory chemicals, which can have non-linear interactions (Yang et al., 2015). These considerations underscore the need for further investigation to achieve a mechanistic understanding of modulation in the geniculocortical circuit.

Although the pupil size is a useful external signal because of its broad correlation to neuromodulatory activity, making specific inferences about the mechanisms underlying pupil-linked modulation is difficult due to the wide variety of factors can contribute to changes in pupil size (Joshi and Gold, 2020; Larsen and Waters, 2018). Due to prominent reports of the correlation between pupil size and LC-NE activity (Rajkowski et al., 1994; Aston-Jones and Cohen, 2005), it is commonly assumed that pupil size provides a direct readout of LC-NE activity, but this is likely an oversimplification. While pupil size is correlated to both LC-NE and BF-ACh activity (Reimer et al., 2016; Collins et al., 2023), pupil linked LC-NE activity precedes pupil linked BF-ACh activity (Reimer et al., 2016), and BF neurons are directly activated by LC-NE axons (Jones, 2004), thus BF-pupil links could simply be a byproduct of LC-pupil coupling. However, LC-NE activity in the visual cortex is only transiently linked to pupil dilation, and appears to track faster pupil size fluctuations, while BF-ACh activity tracks sustained pupil dilation, especially during locomotion (Reimer et al., 2016). This suggests that dLGN activity modulations from Crombie et al. (2024, Chapter 3) linked to fast pupil size dynamics may be linked to LC-NE input, while those linked to slower pupil dynamics may be more driven by BF-ACh activity. Similarly, activation of the serotonergic dorsal raphe (DR-5HT) causes pupil dilation (Cazettes et al., 2021), but this could also involve the LC-NE system due to reciprocal connectivity between the DR and LC (Kim et al., 2004), and, confusingly, it has been found that 5HT concentration in the dLGN is anti-correlated to pupil size (Reggiani et al., 2022). In addition, at least two “non-modulatory” nuclei have been identified that can control pupil size and receive top-down cognitive signals (Joshi and Gold, 2020). One of these is the superior colliculus, which projects to a sub-section of the dLGN in mice (Kerschensteiner and Guido, 2017), and could thus also simultaneously influence pupil size (Joshi et al., 2016) and dLGN activity. Thus, while pupil size changes are a useful proxy for a certain set of internal signals, they do not provide a direct readout of LC activity (Megemont et al., 2022), nor any other modulatory system.

Behavioural signals

Certain behaviours, such as eye movements, can have direct effects on sensory neurons, often involving the cancellation of inputs caused by self-motion (Crapse and Sommer, 2008). Mice use such saccadic eye movements to explore visual scenes (Zahler et al., 2021; Meyer et al., 2020; Parker et al., 2023). In Crombie et al. (2024, Chapter 3) it was found that saccades were linked to arousal, tending to occur during pupil dilation, but caused a modulation of firing in dLGN neurons that was largely independent of the modulation linked to pupil size dynamics, suggesting a different source. In contrast to arousal, which is often associated with increased neural activity, saccade-related modulation in the visual system is typically described by a peri-saccadic suppression that is thought to limit processing of the visual motion induced by saccades (Wurtz, 2008). Detection of visual motion by circuits in the retina can suppress RGC output (Idrees et al., 2020, 2022), which could also result in a reduction of dLGN activity. In the mouse dLGN, Crombie et al. (2024, Chapter 3) found a cluster of neurons responding with a biphasic modulation – a brief period of suppression embedded within an overall enhancement of activity – consistent with effects measured in the primate LGN (Reppas et al., 2002), and suggesting the presence of a suppressive mechanism for some neurons on sub-second timescales.

However, Crombie et al. (2024, Chapter 3) also demonstrated that the dominant response to saccades in dLGN neurons is a firing rate increase – what can account for this activation? It has been theorized that saccades cause a release from adaptation that increases firing rates and helps decorrelate incoming visual signals (Samonds et al., 2018). Consistent with this theory, Parker et al. (2023) recently found that the rapid, often positive, responses of V1 neurons to eye movements were replaced by an overall suppression in a dark environment where visual input is uniform across the visual field. This mechanism is consistent with a facilitative effect of saccades on visual neurons that is independent of arousal, but it remains to be seen if saccadic facilitation in the dLGN is eliminated in darkness as it is in V1. The mouse dLGN also receives input from the parabigeminal nucleus (Sokhadze et al., 2022), which has been directly linked to eye movements in cats (Cui and Malpeli, 2003; Ma et al., 2013). Although it is unclear whether this projection operates via glutamate or ACh (Sokhadze et al., 2022), both excite dLGN neurons (McCormick, 1992), and are therefore consistent with the peri-saccadic facilitation observed. Notably, either of these proposed mechanisms would be independent of the modulatory inputs typically associated with generalized arousal.

Exploratory behaviours such as saccades often co-occur with other active behaviours like locomotion (Niell and Stryker, 2010; Bennett et al., 2013), thus presenting a potential confound when interpreting modulations linked to one or the other. This could be a factor for simple firing rate changes, but is especially relevant for measures of visual responses such as response reliability across trials, as decreased response reliability during locomotion could reflect changes in input caused by eye movement rather than changing responses to a consistent input. In Spacek et al. (2022, Chapter 2) it was confirmed that trials with locomotion were accompanied by more eye movement, and that the change in eye movement was predictive of the decrease in response reliability during locomotion. However, the amount of variability explained by the change in eye movement was relatively small, indicating that locomotion itself still contributes uniquely to the increase in response variability. Similarly, locomotion and pupil size, are highly correlated – with pupil dilation almost invariably

accompanying bouts of locomotion – but have differing effects on visual sensory areas. For example, neurons in the visual cortex have more depolarized membrane potential and higher firing rates during locomotion, but not pupil-indexed arousal in the absence of locomotion (Reimer et al., 2014; Vinck et al., 2015). In the dLGN, Spacek et al. (2022, Chapter 2) observed a decrease in response reliability during locomotion, but not during pupil dilation. This is consistent with results from Crombie et al. (2024, Chapter 3), where stimulus decoding accuracy was similarly high between states defined by pupil size dynamics. Thus, while pupil-linked arousal may be associated with increased tonic firing in the dLGN, locomotion may specifically induce an increase in response variability.

Information about locomotion speed could be indirectly conveyed to the dLGN via the locomotion-related activity of the BF-ACh system in the cortex (Lee et al., 2014; Nelson and Mooney, 2016; Reimer et al., 2016; Lohani et al., 2022; Neyhart et al., 2023). Interestingly, however, *increased* response reliability in V1 was observed both for sub-threshold responses during locomotion (Bennett et al., 2013) and spiking responses during BF stimulation (Goard and Dan, 2009). This latter study in anaesthetized animals also related BF stimulation to increased response reliability in the dLGN (Goard and Dan, 2009), but investigations in awake animals have found the opposite during locomotion in both the auditory thalamus (MGN; McGinley et al., 2015a) and dLGN (Spacek et al., 2022, Chapter 2). The differing results could thus reflect a more variable behavioural drive in awake animals. Furthermore, the independence of decreased thalamic response reliability from CT-FB (Spacek et al., 2022, Chapter 2) argues against an inheritance of this property from locomotion- or BF-related cortical modulation of response reliability.

The pattern of results outlined above suggests that a modulatory mechanism explaining increased response variability during locomotion should be independent of saccadic modulation and pupil-indexed arousal, and act on the dLGN independently of the cortex. A further observation that dLGN neurons have a variety of specific locomotion speed tuning profiles (Erisken et al., 2014; Roth et al., 2016) indicates that locomotion-related modulation should encode fine-grained locomotion speed, rather than a binary “on” or “off” state-like signal. This run speed tuning could also directly explain the increased response variability during locomotion, as locomotion speed itself is highly variable within bouts of movement (Crombie et al., 2024, Chapter 3). While the dLGN does not directly receive locomotion-related BF input (Sokhadze et al., 2022), it does receive cholinergic input from the PPN (Sokhadze et al., 2022), which is found within the “midbrain locomotor region” (MLR; Lee et al., 2014; Leiras et al., 2022). The MLR is upstream to the BF, and contains neurons whose activity is very tightly correlated to locomotion speed (Lee et al., 2014; Caggiano et al., 2018; Josset et al., 2018). Thus, the PPN-dLGN projection may provide a modulatory channel that specifically confers locomotion speed tuning and increased response variability during locomotion bouts to the dLGN. One caveat to this proposed mechanism, however, is that the work linking PPN activity to fine-grained locomotor control targeted *glutamatergic* neurons of the PPN, and, while they are closely associated to cholinergic neurons, it is currently unknown how much locomotion-related activity is conveyed in the ascending projections of PPN-ACh neurons (Mena-Segovia and Bolam, 2017; Leiras et al., 2022). Nonetheless, the PPN-dLGN projection may provide a modulatory channel that specifically confers increased response variability to the dLGN during

locomotion, independently of saccades, pupil-indexed arousal, and the cortical actions of the BF-ACh system.

Outlook

If any one thing is clear from the discussion above, it is that, although pupil size, locomotion, and eye movements may be correlated, several different mechanisms are consistent with the modulations in the dLGN related to each. It is therefore essential for future research to disentangle the potential contributions of each of the sources implicated above. These investigations should be carried out by manipulating modulatory structures *in vivo*, so as to capture the contributions of the full thalamocortical circuit (e.g. Rodenkirch et al., 2019). However, there is a lack of precise quantitative knowledge of the relationship between endogenous neuromodulatory activity patterns and ongoing behaviours, which is starting to be addressed for the cortex (Reimer et al., 2016; Lohani et al., 2022; Zhu et al., 2023; Collins et al., 2023), but remains unaddressed in the dLGN. Therefore, direct imaging of modulatory projections to the dLGN (e.g. Reggiani et al., 2022) is needed to relate the activity of distinct modulatory projections to behavioural variables. However, in combination with this approach, care should be taken to extract the relevant components of these behavioural variables. A decomposition of behavioural signals, as was done with with pupil size dynamics in Crombie et al. (2024, Chapter 3), will help to disentangle independent events that could be linked to different mechanisms. Furthermore, compensatory and gaze-shifting eye movements (Meyer et al., 2020) have been found to differently effect the activity of visual neurons (Parker et al., 2023), as well as saccade direction (Miura and Scanziani, 2022). Similarly, there is the potential for different modulatory contributions from the PPN based on the specific type of locomotion (Caggiano et al., 2018; Josset et al., 2018). Lastly, it will be necessary to account for diverse effects of modulatory mechanisms across the population of dLGN neurons. In order to measure how single dLGN neurons are affected by specific modulatory channels, the activity of functional clusters of modulatory boutons could be used as predictors in the spline-GLM modelling framework of Schmors et al. (2023, Chapter 4). Regardless of the mechanism, however, the presence of multiple influences on the activity of dLGN neurons is already suggestive that multiple functions impinge on the dLGN, each of which may have distinct effects on visual stimulus encoding.

6.3 Visual processing

Response gain and visual attention

Corticothalamic feedback (CT-FB) in the dLGN has been linked to functions such as attention via increased gain of visual responses (McAlonan et al., 2008; Béhuret et al., 2015). Indeed, Spacek et al. (2022, Chapter 2) robustly linked CT-FB during naturalistic stimulus viewing to multiplicative gain increases in dLGN neurons. As discussed in Spacek et al. (2022, Chapter 2) and Schmors et al. (2023, Chapter 4), one explanation for gain modulation with CT-FB intact could be the increased presence synaptic noise. Indeed, rapid stochastic changes in background synaptic input can enhance the detection of small inputs (Hô and Destexhe, 2000; Stacey and Durand, 2001; Shu et al., 2003), an effect which has been shown explicitly in dLGN neurons (Wolfart et al.,

2005). However, the increased presence of synaptic noise has also been linked to *decreased* gain; reducing spike probability (Wolfart et al., 2005) and response amplitudes (Chance et al., 2002) for above-threshold stimuli. The confusion comes from two distinct notions of gain: the first refers to the slope of the spike probability function, and the second refers to the slope of the spiking response amplitude. Altogether, the pattern of effects linked to synaptic noise in these other studies would, in the context of Spacek et al. (2022, Chapter 2), predict the emergence of novel peaks in the PSTH, while decreasing the amplitude of the larger response peaks. However, CT-FB can confer gain increases to dLGN neurons via mechanisms other than stochastic membrane potential fluctuations. Synaptic noise can cause stochastic activation of T-type calcium channels, resulting in high frequency burst-like spiking (Wolfart et al., 2005; Béhuret et al., 2015), which is consistent with the response gain measured in Spacek et al. (2022, Chapter 2). Cortical feedback can also produce longer-lasting depolarization through recruitment of NMDAR-dependent “plateau potentials” (Augustinaite et al., 2014), and such tonic depolarization has been suggested to be a requisite for gain increases elsewhere in the visual system (Cardin et al., 2008). Thus CT-FB is still well positioned to control response gain in the dLGN in a manner consistent with Spacek et al. (2022, Chapter 2); increasing the detection of sub-threshold stimuli via synaptic noise, and, when combined with non-linear properties of thalamocortical cell membranes, increasing responses to above-threshold stimuli.

It is likely that cortical feedback does not globally increase the gain for all stimulus channels passing through the dLGN, but provides more targeted gain adjustments. Firstly, CT-FB is retinotopically organized, such that V1-L6 neurons anatomically target areas of the dLGN aligned with their own spatial RFs (Tsumoto et al., 1978; Born et al., 2021), conferring a spatially organized influence. In addition, the functional influence of CT-FB has been related to the stimulus tuning properties of V1-L6 neurons, such that dLGN neurons with spatial RFs aligned parallel or perpendicular to the orientation preference of the V1-L6 neuron are most strongly affected (Wang et al., 2006, 2018). Evidence from the macaque also shows that V1-L6 neurons are functionally organized into three distinct groups, following the organization of the monkey visual system into three parallel streams roughly responsible for transmitting fast spatially-imprecise, spatially detailed, and chromatic information respectively (Briggs and Usrey, 2009). However, the separation of visual processing streams through the mouse dLGN as in monkeys and cats is unclear (Piscopo et al., 2013; Denman and Contreras, 2016; Kerschensteiner and Guido, 2017; Seabrook et al., 2017). While it is likely that mouse V1-L6 neurons inherit tuning properties of dLGN neurons via thalamocortical axon collaterals terminating in L6 (Sherman and Guillery, 2004; Ji et al., 2016), but it is unknown if these L6 neurons preferentially project back to dLGN cells with similar tuning properties. Finally, shifts in the balance of excitatory versus inhibitory synaptic noise can shift neuronal response curves bidirectionally in a manner consistent with flexible gain modulation of firing rates (Wolfart et al., 2005). This is interesting given that short-term plasticity in the excitatory-inhibitory balance of the direct and indirect CT-FB pathways depends on the activation strength of cortical L6 neurons (Crandall et al., 2015). The implication is that the activation level of a V1-L6 neuron could determine whether the gain conferred by CT-FB is divisive or multiplicative for a given input (Results released at the time of writing indicate this is indeed the case: Dimwamwa et al., 2023).

Although flexible gain adjustment mediated by CT-FB is a strong candidate mechanism for visual attention (Béhuiret et al., 2015), attention is ultimately defined by improved *behavioural* performance in a task, and thus the effects of CT-FB need to be linked to behaviour. Behavioural improvement associated with attention has been thoroughly linked to feature-specific gain adjustment elsewhere in the visual system (Moran and Desimone, 1985; Spitzer et al., 1988; Treue and Trujillo, 1999; Reynolds and Heeger, 2009), but there has been little investigation of gain control in the dLGN via CT-FB in task performance. Behavioural improvements in a cross-modal attention paradigm have been linked to gain changes in the dLGN-V1 circuit, with the involvement of the TRN implicating CT-FB (McAlonan et al., 2006). While this kind of cross-modal attention was found to involve cortical input to the TRN originating from the prefrontal cortex rather than V1 (Wimmer et al., 2015), gain control in the dLGN and TRN has also been linked to spatial attention in a purely visual task (McAlonan et al., 2008), which could involve CT-FB from V1.

Consistent with this more targeted role for CT-FB from primary sensory cortices to the thalamus, Guo et al. (2017) found that CT-FB manipulation could influence behaviour in an auditory go/no-go task where mice had to discriminate between pure tone frequencies. Activation of L6 of primary auditory cortex (A1) >100 ms prior to sound presentation improved hit rates, but also increased false alarms for foil stimuli that were similar to the target (Guo et al., 2017). This effect was reversed for A1-L6 activation <100 ms prior to sound presentation. The behavioural effects were accompanied by broad gain modulations influencing stimulus selectivity in the MGN and auditory TRN (Guo et al., 2017). This study provides strong evidence that CT-FB can modulate behaviour and thalamic gain in a manner consistent with a role in attention, but highlights several open questions for future research. For example, what is the structure of L6 population activity during directed attention? And would the suppression of endogenous L6 activity as in Spacek et al. (2022, Chapter 2) result in more targeted effects? Lastly, frequency tuning in the auditory system can be considered analogous to spatial tuning in visual system in that this property is inherited from the spatial organization of peripheral sensory neurons, but it is known that V1-L6 neurons can have selectivity for more complex stimulus features (Vélez-Fort et al., 2014; Augustinaite and Kuhn, 2020). So, is the recruitment of CT-FB even more specific in tasks involving complex naturalistic stimuli?

Input selection and arousal

While the dLGN activity changes associated with CT-FB are thought to reflect targeted modulation, arousal-related modulations are typically thought to reflect a global signal, although there are indications that the neuromodulatory systems involved in arousal can have functional specificity on stimulus processing. The global view stems from observations that the neuromodulatory systems involved, such as the ACh system, have coordinated brain-wide activity (Buzsaki et al., 1988; Lohani et al., 2022; Collins et al., 2023), and locomotion and pupil size modulate activity globally (Stringer et al., 2019; Musall et al., 2019; Clancy et al., 2019; Shimaoka et al., 2018). However, there are principled differences in how sensory neurons are influenced by these variables, suggestive of targeted functional consequences for the encoding of visual features. While Crombie et al. (2024, Chapter 3) and Schmors et al. (2023, Chapter 4) found variability in the degree to which dLGN neurons couple

to variables like pupil size, other authors focused on stimulus-tuning properties that might help explain this variability. Imaging the activity of RGC axon terminals in the dLGN, Liang et al. (2020) found that arousal has diverse effects on RGC boutons in the dLGN depending on their stimulus tuning properties and the visual stimulation context. Specifically, *suppression* during arousal was especially strong for all response types during visual stimulation with low spatial frequency, whereas boutons with spatial RFs in the centre of the visual field had *enhanced* responses to high spatial frequency stimuli (Liang et al., 2020). These input modulations could be a factor in the preferential effects of locomotion on dLGN neurons preferring high spatial frequency spatial stimuli (Aydın et al., 2018). More generally, the presence of arousal-related modulation at the pre-synaptic level suggests that, unlike CT-FB, which may operate at the population level by manipulating the gain certain of dLGN neurons over others (Béhuret et al., 2015), arousal-related neuromodulators may achieve specificity by changing the RFs of individual dLGN neurons via input selection.

How would a supposedly global system achieve such fine-grained adjustment? Specificity could be conferred anatomically, by neuromodulatory systems that form synapses in the dLGN (e.g. NE and 5HT: Papadopoulos and Parnavelas, 1990) rather than volume transmission as observed in the cortex (c.f. Neyhart et al., 2023, for BF-ACh transmission in cortex). Serotonin (5HT), has been implicated in pre-synaptic modulation of retinogeniculate transmission (Chen and Regehr, 2003), but it was found to act on a different set of RGC terminals than arousal, and dLGN 5HT levels *in vivo* were anti-correlated to pupil size (Reggiani et al., 2022). Alternatively, ACh is particularly interesting in this respect due to its correlation with arousal, and the formation of synapses participating in the “glomeruli” or “synaptic triads” surrounding retinal synapses onto dLGN neurons (Sherman, 2004). In this position, ACh input could simultaneously depolarize the post-synaptic membrane and reduce inhibition from interneurons in a localized dendritic region surrounding RGC input synapses (McCormick and Pape, 1988; Sherman, 2004). Indeed, local interneurons – which are not found in other sensory thalamic nuclei but comprise 6% of the neural population in the dLGN (Evangelio et al., 2018) – have recently been proposed to play a role in dLGN input selectivity by regulating their inhibitory contributions to synaptic triads (Djama et al., 2024). While this mechanism does not explain the pre-synaptic modulation observed in Liang et al. (2020), it remains an under-explored fact that ACh receptors have been found on mammalian retinal terminals (Prusky and Cynader, 1988), and ACh has been found to have inhibitory pre-synaptic effects in other neural systems (e.g. Valentino and Dingledine, 1981). In combination with the above, RGC input to dLGN principal cells is highly convergent (Morgan et al., 2016; Rompani et al., 2017), but functionally organized (Liang et al., 2018), such that localized modulation could influence a targeted group of input features. Furthermore, many RGC inputs make, on average, relatively small functional contributions to dLGN activity (Rosón et al., 2019). This raises the question: why would neurons in the mouse dLGN would retain seemingly non-functional connections (Litvina and Chen, 2017)? The answer might be: to provide a reservoir of response modes that can be unmasked by certain behavioural states.

Bursting and learning

Taking a broader perspective, it is also likely that modulations associated with behavioural state, such as the prominence of thalamic bursting, have functions beyond online stimulus encoding. Signals having to do with learning, memory consolidation, and retrieval may also be embedded in the activity patterns we observe, but have yet to be studied from the perspective of the sensory thalamus. While plasticity in the visual system was considered to be a predominantly cortical phenomenon, recent results have demonstrated substantial experience-dependent plasticity of retinogeniculate transmission in the dLGN in adult animals (Moore et al., 2011; Jaepel et al., 2017; Rose and Bonhoeffer, 2018).

Thalamocortical oscillatory states occurring during sleep such as delta waves and spindles are thought to orchestrate the plasticity underlying memory consolidation (Steriade, 2001, 2006; Diekelmann and Born, 2010; Rasch and Born, 2013; Girardeau and Lopes-Dos-Santos, 2021). The generation mechanism for these rhythms involves low-threshold bursting in thalamic neurons (Steriade et al., 1993), which has also been hypothesized to contribute to plasticity in these neurons (Crunelli et al., 2018). Thus, in addition to a potential role in stimulus encoding and corticothalamic rhythm generation, bursting may also contribute to learning. Learning during sleep has also been linked to a third oscillatory activity pattern: hippocampal sharp wave ripples, which co-occur with delta waves and spindles (Diekelmann and Born, 2010; Rasch and Born, 2013; Girardeau and Lopes-Dos-Santos, 2021). Sharp wave ripples are thought to promote consolidation of previously learned stimuli by driving the reactivation of activity patterns in sensory cortex (Ji and Wilson, 2007; O’Neill et al., 2010), but activity patterns in the sensory thalamus during these events have not been investigated.

These learning-related patterns of oscillatory activity and cortical reactivation also occur during wakefulness. In humans, periods of task disengagement as short as a few seconds, during which the consolidation-related oscillations described above were observed, are associated with facilitated learning and memory retention (Wamsley, 2022). In other animals, periods of wakeful quiescence surrounding exploration, surprising rewards, salient stimuli, and novel environments involve the occurrence of sharp wave ripples that are thought to promote functions such as memory consolidation and retrieval (Carr et al., 2011). Sharp wave ripples have also been directly associated with periods of low pupil-indexed arousal during wakefulness, and the co-occurrence of low frequency oscillations in the thalamocortical system (McGinley et al., 2015b). Indeed, a distinct low-frequency 4 Hz thalamocortical oscillation in mice that occurs during low arousal (Nestvogel and McCormick, 2022) and disengagement from a task (Jacobs et al., 2020) is a putative homologue of the alpha oscillation (another learning-related oscillatory pattern linked to quiet wakefulness; Crunelli et al., 2018). This “alpha oscillation” has a global organization suggestive of system-level functions such as memory consolidation (Ye et al., 2023), and is strongly linked to rhythmic bursting in the visual thalamus (Nestvogel and McCormick, 2022).

Although clearly not all bursting in the dLGN during wakefulness is rhythmic – stimulus-driven bursts were prominent in Spacek et al. (2022, Chapter 2), for example – the clear presence of 4 Hz rhythmicity in awake dLGN bursting during periods of low arousal (Nestvogel and McCormick, 2022; Crombie et al., 2024) strongly suggests that it plays a role in the processes discussed above. It was recently reported that thalamic relay

nuclei decrease their activity surrounding sharp wave ripples and reactivation of neural ensembles in sensory cortices (Chambers et al., 2022; Jeong et al., 2023). This was interpreted as a decoupling of cortical ensembles from feed-forward sensory inputs to allow for memory processing (Chambers et al., 2022; Jeong et al., 2023), but such a view suggests a lack of coordination between cortical and thalamic plasticity. On the other hand, while neither of these studies explicitly measured thalamic bursting, decreases in overall thalamic activity strongly suggests that bursts are occurring. Thalamic bursting is driven by a whole-cell calcium signal with the strong potential to influence plasticity mechanisms (Leresche and Lambert, 2017; Crunelli et al., 2018). In conclusion, thalamic bursting during wakefulness is linked to periods where “online consolidation” is thought to occur, and provides a strong intracellular signal for plasticity to occur.

Outlook

While the overall effect of behavioural and internal states on visual encoding remains unclear, changes to the receptive fields in the dLGN should serve to meet the information processing requirements of the animal’s behavioural context. Therefore, experimenter control of the behavioural context in the form of a task is essential. Specifically, a task could be used in conjunction with CT-FB manipulation to probe the role feedback in task-relevant stimulus encoding (e.g. Guo et al., 2017). The learning phase of a task could also be used to assess the role of bursting during offline periods in learning. It could be predicted that dLGN bursting should be more prevalent during early phases of learning, which are related to shifts in the neural representation of the visual stimuli (Jurjut et al., 2017). Additionally, shifts in stimulus-reward contingencies could be linked to subsequent bursting in dLGN neurons representing these stimulus features. Here, ethological factors need to be considered. Because mice use vision in naturalistic behaviours (Yilmaz and Meister, 2013; Hoy et al., 2016), it is likely that tasks involving these behaviours and stimuli will best engage the circuitry involved in modulating dLGN stimulus representations. Naturalistic stimuli also differently engage retinal circuits (Karamanlis et al., 2022; Goldin et al., 2022) and visual cortex (e.g. Vinje and Gallant, 2000), altering feed-forward and feedback signalling compared to artificial stimuli, making naturalistic stimulation essential to probe modulations of stimulus encoding (Simoncelli and Olshausen, 2001).

The use of non-parametric stimuli can pose a technical challenge for the analysis of stimulus tuning and receptive fields. Schmors et al. (2023, Chapter 4) showed how the use of a spline-GLM can overcome some of these challenges, and this model could be extended to assess RF changes as a function of task context and behavioural state. For example, interaction terms between the stimulus and CT-FB could be introduced, such that CT-FB has spatially extended stimulus-dependent effects (Schmors et al., 2023, Chapter 4). Similarly, for behavioural state effects, the RF itself could be modelled as an interaction between the stimulus input and a full spatiotemporal modulation kernel, such that effective changes in the RF as a function of behavioural states can be captured. A different approach might be to model the RF as a combination of input modes detected via spike-triggered stimulus clustering (Shah et al., 2020). This approach has been shown to improve response prediction to naturalistic stimuli in the visual system (Shah et al., 2020), and mechanistically matches the structure of RGC input to and neuromodulation of dLGN neurons discussed above. In conjunction with

behavioural state monitoring, this approach would reveal potential differences in spike-eliciting stimulus characteristics across behavioural states. These types of changes can be expected given that Crombie et al. (2024, Chapter 3), by partitioning neural activity by pupil-defined states, found that stimulus decoding performance is penalized across states, suggesting an arousal-dependent shift in the way dLGN neurons encode visual information. As in Liang et al. (2020), where it was found that retinal inputs representing nasotemporal motion were suppressed during high arousal where locomotion is likely to occur, modelled RF differences should be analyzed under the hypothesis that changes should be functionally relevant for the stimulus characteristics induced by certain behaviours (Gibson, 1950; Von Holst and Mittelstaedt, 1950).

6.4 Partitioning neural activity and behaviour

The manuscripts enclosed in this dissertation uncovered a variety of relationships behavioural variables and the activity of dLGN neurons, and the above sections above discussed potential mechanisms for these modulations, as well as the roles that these modulations might play in sensory processing. However, the manuscripts also demonstrate the limitations of trying to use single behavioural variables as proxies for internal states of the brain. The following section leaves behind the mechanics of visual processing and modulations in the dLGN, and instead concerns how these results should be interpreted on the level of the organism and its behaviour. Internal states are not physical entities. Instead, they are concepts that serve to organize non-stationarity in brain-derived observables, and are defined by finding statistical patterns among combinations of several physiological variables (Flavell et al., 2022; McCormick et al., 2020). Importantly, the view is adopted that, instead of reflecting a unified internal state (Robbins, 1997), different types of state-related factors overlap, and simultaneously exert their influence on neural populations (McCormick et al., 2020; Flavell et al., 2022). The result is that the spiking activity of a neural population, or even a single neurons, can contains a multiplexing of several behaviour- and state-related influences (Crombie et al., 2024, Chapter 3), that needs to be parsed and interpreted (Miller et al., 2022).

Differentiated modulatory systems

Supporting the notion that brain states are multifaceted, rather than unified, is the simple observation that more than one neuromodulatory system contributes to modulations in the visual system (discussed above). This notion is furthered by noting diversity in the activity patterns and cell ensembles within these systems. Seminal findings provided a strong link between pupil size and the LC-NE modulatory system, but it was already suggested at the time that LC neurons have two activity patterns with distinct timescales that may also serve distinct functions (Aston-Jones and Cohen, 2005). In “phasic mode”, which typically occurs when the animal is engaged in a task with high utility, baseline LC activity is low, and task events, such as reward-predicting stimuli, elicit large, but transient, increases in LC spiking. When task utility wanes, animals tend to engage in exploration, where task performance is low due to more variable behaviour, and LC neurons switch to “tonic mode” where they display high levels of sustained activity. Thus, transient increases in NE signalling in one state denote important within-task events, while sustained increases in NE signalling promote task

disengagement and exploratory actions. For this reason, some researchers separate pre-trial baseline pupil size from the change in pupil size elicited by in-trial events, finding that these quantities predict different aspects of decision-making (Gilzenrat et al., 2010; Jepma and Nieuwenhuis, 2011; Nassar et al., 2012; van Kempen et al., 2019; van den Brink et al., 2023). Similarly, authors have begun to distinguish the effects of cholinergic signalling at diverse temporal scales (Parikh et al., 2007; Ruivo et al., 2017; Disney and Higley, 2020). Finally, this reasoning extends to a full spectrum of temporal scales, not just a dichotomy, and the nesting of different functions in different timescales of activity has been suggested as an efficient mechanism through which a small group of modulatory neurons can play a role in multiple functions (Totah et al., 2019). To the degree to which one can interpret pupil-linked changes to relate to LC-NE activity, it might be inferred that the modulations observed at diverse temporal scales in Crombie et al. (2024, Chapter 3) reflect the sensory consequences of this spectrum of different functions.

In addition to functional diversity conferred via activity timescales, recent results also emphasize the division of the LC into functionally segregated ensembles (Poe et al., 2020). Observations of broadly global projections and highly branching axons (Swanson and Hartman, 1975; Room et al., 1981; Nagai et al., 1981) have informed discussion of the “homogeneous” LC-NE system exerting its effects via global arousal (Sara and Bouret, 2012). Despite these conjectures, LC-NE neurons have been found to preferentially target certain functional systems (Nagai et al., 1981; Simpson et al., 1997; Berridge and Waterhouse, 2003), and even different structures within the visual system (Waterhouse et al., 1993). Furthermore, LC neurons have generally low synchrony, and form distinct functional ensembles that can have diverse effects on cortical activity (Totah et al., 2018; Noei et al., 2022) and underpin different types of learning (Uematsu et al., 2017). This differentiation could contribute to reports of variable coupling between pupil size and LC activity (Yang et al., 2021; Megemont et al., 2022): any LC activity might lead to an increase in pupil size, while not being reflected across all LC neurons. Consequently, coupling between modulatory indices and activity of sensory systems is also expected to be diverse (Crombie et al., 2024, Chapter 3), and the same goes for the functional consequences for sensory processing. One of the limitations of Crombie et al. (2024, Chapter 3) is that the method used to assess coupling cannot distinguish between uniform versus sporadic coupling. It may be that two dLGN neurons strongly couple to the same component of pupil size dynamics, but intermittently such that they are not co-modulated, suggesting that they are targeted by different modulatory ensembles. Cholinergic systems, such as the PPN, also have roughly segregated projection patterns despite axonal branching (Martinez-Gonzalez et al., 2011; Mena-Segovia and Bolam, 2017). In conjunction, the role of the PPN in the coordination of specific behaviours (Caggiano et al., 2018; Josset et al., 2018; Inagaki et al., 2022) suggests that its ascending outputs to structures like the visual thalamus can carry fine-grained behavioural signals. It is also worth noting the the BF-ACh system, although it projects to the cortex and TRN rather than the dLGN, has targeted projections (as opposed to branching) and fast effects (Sarter et al., 2009). BF-ACH axons also have distinct stimulus tuning properties in sensory regions (Zhu et al., 2023), suggesting that they do not act in unison. Thus, it is likely that a greater degree of functional specificity is conferred by arousal-related neuromodulators than is accounted for in typical analyses of state-related influences.

While the results of Crombie et al. (2024) measured during “spontaneous” activity are consistent with a more nuanced view of state-related modulation, the above considerations point to the need for controlled experiments, such that the effects on sensory can be parsed and interpreted based on known variables manipulated by the experimenters. For example, if faster timescales of neuromodulator activity are linked to attentional re-orientation (Hasselmo and Sarter, 2011; Totah et al., 2019), future work could investigate whether coupling of spiking in the dLGN to rapid pupil dilation reflects selective modulation of neurons representing the attended visual features (Wang and Krauzlis, 2018; McBride et al., 2019; Lehnert et al., 2023). At longer timescales, neuromodulatory activity may reflect learning processes (Totah et al., 2019), with prolonged optogenetic LC stimulation (lasting several minutes) driving enhanced plasticity in the visual system (Jordan and Keller, 2023). It could be that longer timescales of pupil-linked modulation in the dLGN, which does not appear to directly reflect behavioural modulation (Crombie et al., 2024, Chapter 3), reflects processes related to sensory learning. In this scenario, slow modulations in sensory systems would be linked to factors such as uncertainty or shifts in stimulus-reward contingencies, and be preferentially reflected in dLGN neurons representing visual features relevant to a task.

Structure of behavioural encoding in the visual system

It was discussed above how modulations related to changes in state and behaviour may contribute to changes in stimulus encoding in the visual thalamus, but there is a growing body of evidence suggesting that the early visual system of mice might encode actionable combinations of visual stimuli and behaviours (Miller et al., 2022) rather than purely visual features. As an example, the increase in response variability associated with intact CT-FB in (Spacek et al., 2022, Chapter 2) is considered. While Spacek et al. (2022, Chapter 2) implicated synaptic noise conferred via CT-FB in the increased response variability, an alternative hypothesis could be formed: response variability conferred by CT-FB is due to encoding of ongoing behaviour by V1-L6. In contrast to Spacek et al. (2022, Chapter 2), a recent study found that activating CT-FB *in vivo* reduced response variability in the dLGN (Murphy et al., 2021), consistent with earlier *in vitro* findings (Chance et al., 2002). This apparent discrepancy can be explained by two related considerations. Firstly, the *in vitro* study injected synaptic noise generated from a stationary process (Chance et al., 2002). Meanwhile, the *in vivo* study employed optogenetic *activation* of CT-FB, and was performed using anaesthetized animals (Murphy et al., 2021). This combination is likely to also produce a stationary input to the dLGN by artificially clamping the activity of V1-L6 neurons at a constant high value, and eliminating the influence of active behaviours and states that could influence V1-L6 activity. Meanwhile, in the awake and behaving animal, V1-L6 activity could have increased dLGN response variability by explicitly encoding behavioural signals, which are inherently variable and non-stationary during wakefulness. Thus, the increased response variability found in awake animals by (Spacek et al., 2022, Chapter 2) in the presence of CT-FB is hypothesized to derive from representations of behaviours in V1-L6. This hypothesis is consistent with reports that L6 neurons are sensitive to specific behavioural variables such as head rotation direction, locomotion, whisking, and even preparatory motor signals (Vélez-Fort et al., 2018; Augustinaite and Kuhn, 2020; Clayton et al., 2021; Dash et al., 2022).

In fact, the direct encoding of behaviours is ubiquitous throughout the early visual system of mice. Neurons in both V1 and the dLGN are not just broadly modulated by locomotion, but have specific and varied profiles of locomotion speed tuning (Saleem et al., 2013). In addition to full-body locomotion, V1 neurons have been found to represent head movements (Vélez-Fort et al., 2018; Bouvier et al., 2020; Guitchounts et al., 2020), directional eye movements (Parker et al., 2023), combinations of eye and head positions (Parker et al., 2022), and paw movements (Abdolrahmani et al., 2021). Even behaviours that are difficult to directly quantify, such as those extracted via dimensionality reduction techniques, are widely represented across visual cortical areas (Stringer et al., 2019; Mimica et al., 2023). Importantly, these movements were strongly represented even in the presence of a task (Musall et al., 2019; Salkoff et al., 2020), indicating that movement representation is not simply what the visual system does when idle, but is a fundamental part of its function. In all of these cases, there was an interaction between the representation of movements and visual stimuli (Saleem et al., 2013; Vélez-Fort et al., 2018; Stringer et al., 2019; Bouvier et al., 2020; Abdolrahmani et al., 2021; Parker et al., 2022, 2023). Although these types of investigations have mainly been carried out in V1, there are hints that the visual thalamus has similar specificity regarding behavioural encoding. In addition to the fact that dLGN neurons receive inputs from V1-L6 neurons with behavioural tuning, experimenters have directly measured tuning of dLGN neurons to specific locomotion speeds (Erisken et al., 2014; Roth et al., 2016) and body postures (Orlowska-Feuer et al., 2022). Thus, right from the earliest stages of vision, “visual” neurons also have detailed representations of behavioural variables.

So, to what degree are neural representations of state separable from the representation of behaviours that are likely to occur in these states? In the introduction of this dissertation, evidence was given to support the existence of an internal state, arousal, that is distinct from the representation of active behaviours. However, in the investigations presented there (e.g. Vinck et al., 2015; Petty et al., 2021), the set of behaviours actually measured by the experimenters was limited. Similarly, Crombie et al. (2024, Chapter 3) measured pupil-linked modulations in dLGN neurons that appeared to be independent of locomotion and eye movements, but what about other behaviours that were not directly quantified? The behavioural repertoire of rodents is much larger than whisking, locomotion, and saccades; modern computational techniques have been used to extract 50-150 stereotyped motifs (Wiltschko et al., 2015; Marshall et al., 2021), but this number is likely to increase as tracking resolution improves and non-stereotyped behaviours are accounted for (Berman, 2018; Datta et al., 2019), and as the technology is applied to more diverse and ethological behavioural contexts. Is it possible that all of the modulations linked to longer timescale pupil dynamics in (Crombie et al., 2024, Chapter 3) are simply a reflection of behaviour representation in the dLGN together with patterns of behavioural organization spanning longer timescales of seconds and minutes (Marshall et al., 2021)?

While this an extreme position, this type of reasoning could help explain seemingly conflicting results in other parts of the visual system. In the ventral lateral geniculate nucleus (vLGN), Salay and Huberman (2021) and Fratzl et al. (2021) provided convincing evidence that certain vLGN projections provide contextual signal of “safety” to action-coordinating centres like the superior colliculus (SC). However, very recent work has shown the vLGN-SC projection also conveys very specific information about behaviours with consequences for visual

re-afference (Vega-Zuniga et al., 2023). Some of these findings might be reconciled by a behaviour-focused definitions of states like fear/ anxiety and safety. For example, low vLGN activity prior to trials where the animal escapes from a visual threat could reflect the absence of a safety signal (Fratzl et al., 2021), or the fact than in an anxious state the animal is less likely to engage in the exploratory behaviours that seem to drive vLGN activity (Vega-Zuniga et al., 2023). Similarly, decreased threat-induced freezing upon vLGN activation could either result from the activation of a safety signal (Salay and Huberman, 2021), or from an increase in compensatory movements to compensate for artificial corollary discharges induced by vLGN activation (Vega-Zuniga et al., 2023). These examples are not meant to promote one explanation over the other, but are meant to emphasize the point that taking into account the organization of behaviours into potential states can generate hypotheses that bridge the gap between seemingly disparate accounts of visual function. An alternative hypothesis is one of functional multiplexing and pluralistic explanations of neural activity (Miller et al., 2022). In any case, it is clear that a better understanding of how animals organize their behaviour across temporal scales will help in the interpretation of both behaviour-linked modulation of visual signals, and vision-linked modulation of behaviours.

7 References

- Mohammad Abdolrahmani, Dmitry R Lyamzin, Ryo Aoki, and Andrea Benucci. Attention separates sensory and motor signals in the mouse visual cortex. *Cell Reports*, 36(2), 2021. doi: <https://doi.org/10.1016/j.celrep.2021.109377>.
- Edgar Douglas Adrian and Brian HC Matthews. The berger rhythm: potential changes from the occipital lobes in man. *Brain*, 57(4):355–385, 1934.
- GM Alexander, TL Fisher, and DW Godwin. Differential response dynamics of corticothalamic glutamatergic synapses in the lateral geniculate nucleus and thalamic reticular nucleus. *Neuroscience*, 137(2):367–372, 2006. doi: <https://doi.org/10.1016/j.neuroscience.2005.11.012>.
- Henry J Alitto and W Martin Usrey. Corticothalamic feedback and sensory processing. *Current opinion in neurobiology*, 13(4):440–445, 2003. doi: [https://doi.org/10.1016/S0959-4388\(03\)00096-5](https://doi.org/10.1016/S0959-4388(03)00096-5).
- Henry J Alitto, Theodore G Weyand, and W Martin Usrey. Distinct properties of stimulus-evoked bursts in the lateral geniculate nucleus. *Journal of Neuroscience*, 25(2):514–523, 2005. doi: <https://doi.org/10.1523/JNEUROSCI.3369-04.2005>.
- Ian M Andolina, Helen E Jones, Wei Wang, and Adam M Sillito. Corticothalamic feedback enhances stimulus response precision in the visual system. *Proceedings of the National Academy of Sciences*, 104(5):1685–1690, 2007. doi: <https://doi.org/10.1073/pnas.0609318104>.
- Ian M Andolina, Helen E Jones, and Adam M Sillito. Effects of cortical feedback on the spatial properties of relay cells in the lateral geniculate nucleus. *Journal of neurophysiology*, 109(3):889–899, 2013. doi: <https://doi.org/10.1152/jn.00194.2012>.
- Gary Aston-Jones and Jonathan D Cohen. An integrative theory of locus coeruleus-norepinephrine function: adaptive gain and optimal performance. *Annual Reviews Neuroscience*, 28:403–450, 2005. doi: <https://doi.org/10.1146/annurev.neuro.28.061604.135709>.
- Sigita Augustinaite and Bernd Kuhn. Complementary ca²⁺ activity of sensory activated and suppressed layer 6 corticothalamic neurons reflects behavioral state. *Current Biology*, 30(20):3945–3960, 2020. doi: <https://doi.org/10.1016/j.cub.2020.07.069>.
- Sigita Augustinaite, Bernd Kuhn, Paul Johannes Helm, and Paul Heggelund. Nmda spike/plateau potentials in dendrites of thalamocortical neurons. *Journal of Neuroscience*, 34(33):10892–10905, 2014. doi: <https://doi.org/10.1523/JNEUROSCI.1205-13.2014>.
- Çağatay Aydın, João Couto, Michele Giugliano, Karl Farrow, and Vincent Bonin. Locomotion modulates specific functional cell types in the mouse visual thalamus. *Nature communications*, 9(1):4882, 2018. doi: <https://doi.org/10.1038/s41467-018-06780-3>.

- Tom Baden, Philipp Berens, Katrin Franke, Miroslav Román Rosón, Matthias Bethge, and Thomas Euler. The functional diversity of retinal ganglion cells in the mouse. *Nature*, 529(7586):345–350, 2016.
- Horace B Barlow and Richard M Hill. Selective sensitivity to direction of movement in ganglion cells of the rabbit retina. *Science*, 139(3553):412–414, 1963. doi: <https://doi.org/10.1126/science.139.3553.412>.
- Michele A Basso, Martha E Bickford, and Jianhua Cang. Unraveling circuits of visual perception and cognition through the superior colliculus. *Neuron*, 109(6):918–937, 2021. doi: <https://doi.org/10.1016/j.neuron.2021.01.013>.
- Sébastien Béhuret, Charlotte Deleuze, and Thierry Bal. Corticothalamic synaptic noise as a mechanism for selective attention in thalamic neurons. *Frontiers in Neural Circuits*, 9:80, 2015. doi: <https://doi.org/10.3389/fncir.2015.00080>.
- Corbett Bennett, Sergio Arroyo, and Shaul Hestrin. Subthreshold mechanisms underlying state-dependent modulation of visual responses. *Neuron*, 80(2):350–357, 2013. doi: <https://doi.org/10.1016/j.neuron.2013.08.007>.
- Hans Berger. Über das elektroencephalogramm des menschen. *Archiv für psychiatrie und nervenkrankheiten*, 87(1):527–570, 1929.
- Gordon J Berman. Measuring behavior across scales. *BMC Biology*, 16(23), 2018. doi: <https://doi.org/10.1186/s12915-018-0494-7>.
- Craig W Berridge and Barry D Waterhouse. The locus coeruleus–noradrenergic system: modulation of behavioral state and state-dependent cognitive processes. *Brain research reviews*, 42(1):33–84, 2003. doi: [https://doi.org/10.1016/S0165-0173\(03\)00143-7](https://doi.org/10.1016/S0165-0173(03)00143-7).
- Tatiana Bezdudnaya, Monica Cano, Yulia Bereshpolova, Carl R Stoelzel, Jose-Manuel Alonso, and Harvey A Swadlow. Thalamic burst mode and inattention in the awake lgnd. *Neuron*, 49(3):421–432, 2006. doi: <https://doi.org/10.1016/j.neuron.2006.01.010>.
- Martha E Bickford, Arkadiusz Slusarczyk, Emily K Dilger, Thomas E Krahe, Can Kucuk, and William Guido. Synaptic development of the mouse dorsal lateral geniculate nucleus. *Journal of Comparative Neurology*, 518(5):622–635, 2010. doi: <https://doi.org/10.1002/cne.22223>.
- PO Bishop, W Burke, and R Davis. Synapse discharge by single fibre in mammalian visual system. *Nature*, 182(4637):728–730, 1958. doi: <https://doi.org/10.1038/182728b0>.
- Tom Boissonnet, Matteo Tripodi, and Hiroki Asari. Awake responses suggest inefficient dense coding in the mouse retina. *Elife*, 12:e78005, 2023. doi: <https://doi.org/10.7554/eLife.78005>.

- Gregory Born, Felix A Schneider-Soupiadis, Sinem Erisken, Agne Vaiceliunaite, Chu Lan Lao, Milad H Mobarhan, Martin A Spacek, Gaute T Einevoll, and Laura Busse. Corticothalamic feedback sculpts visual spatial integration in mouse thalamus. *Nature neuroscience*, 24(12):1711–1720, 2021. doi: <https://doi-org.emedien.ub.uni-muenchen.de/10.1038/s41593-021-00943-0>.
- Dante S Bortone, Shawn R Olsen, and Massimo Scanziani. Translaminar inhibitory cells recruited by layer 6 corticothalamic neurons suppress visual cortex. *Neuron*, 82(2):474–485, 2014. doi: <https://doi.org/10.1016/j.neuron.2014.02.021>.
- J Bourassa and M Deschênes. Corticothalamic projections from the primary visual cortex in rats: a single fiber study using biocytin as an anterograde tracer. *Neuroscience*, 66(2):253–263, 1995. doi: [https://doi.org/10.1016/0306-4522\(95\)00009-8](https://doi.org/10.1016/0306-4522(95)00009-8).
- Guy Bouvier, Yuta Senzai, and Massimo Scanziani. Head movements control the activity of primary visual cortex in a luminance-dependent manner. *Neuron*, 108(3):500–511, 2020. doi: <https://doi.org/10.1016/j.neuron.2020.07.004>.
- Farran Briggs and W Martin Usrey. Parallel processing in the corticogeniculate pathway of the macaque monkey. *Neuron*, 62(1):135–146, 2009. doi: <https://doi.org/10.1016/j.neuron.2009.02.024>.
- Timothy M Brown, Carlos Gias, Megumi Hatori, Sheena R Keding, Ma’ayan Semo, Peter J Coffey, John Gigg, Hugh D Piggins, Satchidananda Panda, and Robert J Lucas. Melanopsin contributions to irradiance coding in the thalamo-cortical visual system. *PLoS biology*, 8(12):e1000558, 2010. doi: <https://doi.org/10.1371/journal.pbio.1000558>.
- Randy M Bruno and Bert Sakmann. Cortex is driven by weak but synchronously active thalamocortical synapses. *Science*, 312(5780):1622–1627, 2006. doi: <https://doi.org/10.1126/science.1124593>.
- Laura Busse, Jessica A Cardin, M Eugenia Chiappe, Michael M Halassa, Matthew J McGinley, Takayuki Yamashita, and Aman B Saleem. Sensation during active behaviors. *Journal of Neuroscience*, 37(45):10826–10834, 2017. doi: <https://doi.org/10.1523/JNEUROSCI.1828-17.2017>.
- GY Buzsáki, Reginald G Bickford, Greg Ponomareff, LJ Thal, Ronald Mandel, and Fred H Gage. Nucleus basalis and thalamic control of neocortical activity in the freely moving rat. *Journal of neuroscience*, 8(11):4007–4026, 1988. doi: <https://doi.org/10.1523/JNEUROSCI.08-11-04007.1988>.
- György Buzsáki, Costas A Anastassiou, and Christof Koch. The origin of extracellular fields and currents—eeg, ecog, lfp and spikes. *Nature reviews neuroscience*, 13(6):407–420, 2012. doi: <https://doi.org/10.1038/nrn3241>.
- Vittorio Caggiano, Roberto Leiras, Haizea Goñi-Erro, Debora Masini, Carmelo Bellardita, Julien Bouvier, V Caldeira, Gilberto Fisone, and Ole Kiehn. Midbrain circuits that set locomotor speed and gait selection. *Nature*, 553(7689):455–460, 2018. doi: <https://doi.org/10.1038/nature25448>.

- Jessica A Cardin, Larry A Palmer, and Diego Contreras. Cellular mechanisms underlying stimulus-dependent gain modulation in primary visual cortex neurons in vivo. *Neuron*, 59(1):150–160, 2008. doi: <https://doi.org/10.1016/j.neuron.2008.05.002>.
- Margaret F Carr, Shantanu P Jadhav, and Loren M Frank. Hippocampal replay in the awake state: a potential substrate for memory consolidation and retrieval. *Nature neuroscience*, 14(2):147–153, 2011. doi: <https://doi.org/10.1038/nn.2732>.
- Christian Casanova and Leo M Chalupa. The dorsal lateral geniculate nucleus and the pulvinar as essential partners for visual cortical functions. *Frontiers in Neuroscience*, 17, 2023. doi: <https://doi.org/10.3389/fnins.2023.1258393>.
- Fanny Cazettes, Davide Reato, João P Morais, Alfonso Renart, and Zachary F Mainen. Phasic activation of dorsal raphe serotonergic neurons increases pupil size. *Current Biology*, 31(1):192–197, 2021. doi: <https://doi.org/10.1016/j.cub.2020.09.090>.
- Anna R Chambers, Christoffer Nerland Berge, and Koen Vervaeke. Cell-type-specific silence in thalamocortical circuits precedes hippocampal sharp-wave ripples. *Cell reports*, 40(4), 2022. doi: <https://doi.org/10.1016/j.celrep.2022.111132>.
- Frances S Chance, Larry F Abbott, and Alex D Reyes. Gain modulation from background synaptic input. *Neuron*, 35(4):773–782, 2002. doi: [https://doi.org/10.1016/S0896-6273\(02\)00820-6](https://doi.org/10.1016/S0896-6273(02)00820-6).
- Chinfei Chen and Wade G Regehr. Presynaptic modulation of the retinogeniculate synapse. *Journal of Neuroscience*, 23(8):3130–3135, 2003. doi: <https://doi.org/10.1523/JNEUROSCI.23-08-03130.2003>.
- Kelly B Clancy, Ivana Orsolich, and Thomas D Mrsic-Flogel. Locomotion-dependent remapping of distributed cortical networks. *Nature neuroscience*, 22(5):778–786, 2019. doi: <https://doi.org/10.1038/s41593-019-0357-8>.
- Kameron K Clayton, Ross S Williamson, Kenneth E Hancock, Gen-ichi Tasaka, Adi Mizrahi, Troy A Hackett, and Daniel B Polley. Auditory corticothalamic neurons are recruited by motor preparatory inputs. *Current Biology*, 31(2):310–321, 2021. doi: <https://doi.org/10.1016/j.cub.2020.10.027>.
- BG Cleland, MW Dubin, and WR Levick. Simultaneous recording of input and output of lateral geniculate neurones. *Nature New Biology*, 231(23):191–192, 1971. doi: <https://doi.org/10.1038/newbio231191a0>.
- Lindsay Collins, John Francis, Brett Emanuel, and David A McCormick. Cholinergic and noradrenergic axonal activity contains a behavioral-state signal that is coordinated across the dorsal cortex. *Elife*, 12:e81826, 2023. doi: <https://doi.org/10.7554/eLife.81826>.
- Shane R Crandall, Scott J Cruikshank, and Barry W Connors. A corticothalamic switch: controlling the thalamus with dynamic synapses. *Neuron*, 86(3):768–782, 2015. doi: <https://doi.org/10.1016/j.neuron.2015.03.040>.

- Trinity B Crapse and Marc A Sommer. Corollary discharge across the animal kingdom. *Nature Reviews Neuroscience*, 9(8):587–600, 2008. doi: <https://doi.org/10.1038/nrn2457>.
- Francis Crick. Function of the thalamic reticular complex: the searchlight hypothesis. *Proceedings of the National Academy of Sciences*, 81(14):4586–4590, 1984. doi: <https://doi.org/10.1073/pnas.81.14.4586>.
- Sylvain Crochet and Carl CH Petersen. Correlating whisker behavior with membrane potential in barrel cortex of awake mice. *Nature neuroscience*, 9(5):608–610, 2006. doi: <https://doi.org/10.1038/nm1690>.
- Davide Crombie and Laura Busse. Should i stay or should i go? a thalamic circuit for modulating behavioral responses to visual threat. *Neuron*, 109(23):3717–3719, 2021. doi: <https://doi.org/10.1016/j.neuron.2021.11.005>.
- Davide Crombie, Martin A Spacek, Christian Leibold, and Laura Busse. Spiking activity in the visual thalamus is coupled to pupil dynamics across temporal scales. *Plos Biology*, 22(5):e3002614, 2024. doi: <https://doi.org/10.1371/journal.pbio.3002614>.
- V Crunelli, S Lightowler, and CE Pollard. At-type ca²⁺ current underlies low-threshold ca²⁺ potentials in cells of the cat and rat lateral geniculate nucleus. *The Journal of physiology*, 413(1):543–561, 1989. doi: <https://doi.org/10.1113/jphysiol.1989.sp017668>.
- Vincenzo Crunelli and Stuart W Hughes. The slow (< 1 hz) rhythm of non-rem sleep: a dialogue between three cardinal oscillators. *Nature neuroscience*, 13(1):9–17, 2010. doi: <https://doi.org/10.1038/nn.2445>.
- Vincenzo Crunelli, Magor L Lőrincz, William M Connelly, Francois David, Stuart W Hughes, Régis C Lambert, Nathalie Leresche, and Adam C Errington. Dual function of thalamic low-vigilance state oscillations: rhythm-regulation and plasticity. *Nature Reviews Neuroscience*, 19(2):107–118, 2018. doi: <https://doi.org/10.1038/nrn.2017.151>.
- He Cui and Joseph G Malpeli. Activity in the parabigeminal nucleus during eye movements directed at moving and stationary targets. *Journal of neurophysiology*, 89(6):3128–3142, 2003. doi: <https://doi.org/10.1152/jn.01067.2002>.
- Kathleen E Cullen. Sensory signals during active versus passive movement. *Current opinion in neurobiology*, 14(6):698–706, 2004. doi: <https://doi.org/10.1016/j.conb.2004.10.002>.
- Yang Dan, Joseph J Atick, and R Clay Reid. Efficient coding of natural scenes in the lateral geniculate nucleus: experimental test of a computational theory. *Journal of neuroscience*, 16(10):3351–3362, 1996. doi: <https://doi.org/10.1523/JNEUROSCI.16-10-03351.1996>.
- Suryadeep Dash, Dawn M Autio, and Shane R Crandall. State-dependent modulation of activity in distinct layer 6 corticothalamic neurons in barrel cortex of awake mice. *Journal of Neuroscience*, 42(34):6551–6565, 2022. doi: <https://doi.org/10.1523/JNEUROSCI.2219-21.2022>.

- Sandeep Robert Datta, David J Anderson, Kristin Branson, Pietro Perona, and Andrew Leifer. Computational neuroethology: A call to action. *Neuron*, 104(1):11–24, 2019. doi: <https://doi.org/10.1016/j.neuron.2019.09.038>.
- Carmen De Labra, Casto Rivadulla, Kenneth Grieve, Jorge Mariño, Nelson Espinosa, and Javier Cudeiro. Changes in visual responses in the feline dlgn: selective thalamic suppression induced by transcranial magnetic stimulation of v1. *Cerebral Cortex*, 17(6):1376–1385, 2007. doi: <https://doi.org/10.1093/cercor/bhl048>.
- Paul Dean, Peter Redgrave, and GW Max Westby. Event or emergency? two response systems in the mammalian superior colliculus. *Trends in neurosciences*, 12(4):137–147, 1989. doi: [https://doi.org/10.1016/0166-2236\(89\)90052-0](https://doi.org/10.1016/0166-2236(89)90052-0).
- Daniel J Denman and Diego Contreras. Complex effects on in vivo visual responses by specific projections from mouse cortical layer 6 to dorsal lateral geniculate nucleus. *Journal of Neuroscience*, 35(25):9265–9280, 2015. doi: <https://doi.org/10.1523/JNEUROSCI.0027-15.2015>.
- Daniel J Denman and Diego Contreras. On parallel streams through the mouse dorsal lateral geniculate nucleus. *Frontiers in neural circuits*, 10:20, 2016. doi: <https://doi.org/10.3389/fncir.2016.00020>.
- Susanne Diekelmann and Jan Born. The memory function of sleep. *Nature Reviews Neuroscience*, 11(2):114–126, 2010. doi: <https://doi.org/10.1038/nrn2762>.
- Elaida Dimwamwa, Aurelie Pala, Vivek Chundru, Nathaniel C Wright, and Garrett B Stanley. Dynamic corticothalamic modulation of the somatosensory thalamocortical circuit during wakefulness. *bioRxiv*, pages 2023–07, 2023. doi: <https://doi.org/10.1101/2023.07.18.549491>.
- Anita A Disney and Michael J Higley. Diverse spatiotemporal scales of cholinergic signaling in the neocortex. *Journal of Neuroscience*, 40(4):720–725, 2020. doi: <https://doi.org/10.1523/JNEUROSCI.1306-19.2019>.
- Deyl Djama, Florian Zirpel, Zhiwen Ye, Gerald Moore, Charmaine Chue, Christopher Edge, Polona Jager, Alessio Delogu, and Stephen G Brickley. The type of inhibition provided by thalamic interneurons alters the input selectivity of thalamocortical neurons. *bioRxiv*, pages 2024–01, 2024. doi: <https://doi.org/10.1101/2024.01.17.576001>.
- R Becket Ebitz and Tirin Moore. Both a gauge and a filter: Cognitive modulations of pupil size. *Frontiers in neurology*, 9:1190, 2019. doi: <https://doi.org/10.3389/fneur.2018.01190>.
- Gaute T Einevoll and Hans E Plesser. Extended difference-of-gaussians model incorporating cortical feedback for relay cells in the lateral geniculate nucleus of cat. *Cognitive neurodynamics*, 6:307–324, 2012. doi: <https://doi.org/10.1007/s11571-011-9183-8>.
- Gaute T Einevoll, Christoph Kayser, Nikos K Logothetis, and Stefano Panzeri. Modelling and analysis of local field potentials for studying the function of cortical circuits. *Nature Reviews Neuroscience*, 14(11):770–785, 2013. doi: <https://doi.org/10.1038/nrn3599>.

- Alev Erişir, Susan C Van Horn, and S Murray Sherman. Relative numbers of cortical and brainstem inputs to the lateral geniculate nucleus. *Proceedings of the National Academy of Sciences*, 94(4):1517–1520, 1997. doi: <https://doi.org/10.1073/pnas.94.4.1517>.
- Sinem Erisken, Agne Vaiceliunaite, Ovidiu Jurjut, Matilde Fiorini, Steffen Katzner, and Laura Busse. Effects of locomotion extend throughout the mouse early visual system. *Current Biology*, 24(24):2899–2907, 2014. doi: <https://doi.org/10.1016/j.cub.2014.10.045>.
- Marian Evangelio, María García-Amado, and Francisco Clascá. Thalamocortical projection neuron and interneuron numbers in the visual thalamic nuclei of the adult c57bl/6 mouse. *Frontiers in neuroanatomy*, 12:27, 2018. doi: <https://doi.org/10.3389/fnana.2018.00027>.
- Dominic A Evans, A Vanessa Stempel, Ruben Vale, and Tiago Branco. Cognitive control of escape behaviour. *Trends in cognitive sciences*, 23(4):334–348, 2019. doi: <https://doi.org/10.1016/j.tics.2019.01.012>.
- Dirk Eyding, Jeffrey D Macklis, Ute Neubacher, Klaus Funke, and Florentin Wörgötter. Selective elimination of corticogeniculate feedback abolishes the electroencephalogram dependence of primary visual cortical receptive fields and reduces their spatial specificity. *Journal of Neuroscience*, 23(18):7021–7033, 2003. doi: <https://doi.org/10.1523/JNEUROSCI.23-18-07021.2003>.
- Erika E Fanselow, Koichi Sameshima, Luiz A Baccala, and Miguel AL Nicolelis. Thalamic bursting in rats during different awake behavioral states. *Proceedings of the National Academy of Sciences*, 98(26):15330–15335, 2001. doi: <https://doi.org/10.1073/pnas.261273898>.
- Steven W Flavell, Nadine Gogolla, Matthew Lovett-Barron, and Moriel Zelikowsky. The emergence and influence of internal states. *Neuron*, 2022. doi: <https://doi.org/10.1016/j.neuron.2022.04.030>.
- Katrin Franke, Konstantin F Willeke, Kayla Ponder, Mario Galdamez, Na Zhou, Taliah Muhammad, Saamil Patel, Emmanouil Froudarakis, Jacob Reimer, Fabian H Sinz, and Andreas S Tolia. State-dependent pupil dilation rapidly shifts visual feature selectivity. *Nature*, 610(7930):128–134, 2022. doi: <https://doi.org/10.1038/s41586-022-05270-3>.
- Alex Fratzl, Alice M Koltchev, Nicole Vissers, Yu Lin Tan, Andre Marques-Smith, A Vanessa Stempel, Tiago Branco, and Sonja B Hofer. Flexible inhibitory control of visually evoked defensive behavior by the ventral lateral geniculate nucleus. *Neuron*, 109(23):3810–3822, 2021. doi: <https://doi.org/10.1016/j.neuron.2021.09.003>.
- Yu Fu, Jason M Tucciarone, J Sebastian Espinosa, Nengyin Sheng, Daniel P Darcy, Roger A Nicoll, Z Josh Huang, and Michael P Stryker. A cortical circuit for gain control by behavioral state. *Cell*, 156(6):1139–1152, 2014. doi: <https://doi.org/10.1016/j.cell.2014.01.050>.
- Patrick Fuller, David Sherman, Nigel P Pedersen, Clifford B Saper, and Jun Lu. Reassessment of the structural basis of the ascending arousal system. *Journal of Comparative Neurology*, 519(5):933–956, 2011. doi: <https://doi.org/10.1002/cne.22559>.

- James J Gibson. *The perception of the visual world*. Houghton Mifflin, 1950.
- Mark S Gilzenrat, Sander Nieuwenhuis, Marieke Jepma, and Jonathan D Cohen. Pupil diameter tracks changes in control state predicted by the adaptive gain theory of locus coeruleus function. *Cognitive, Affective, & Behavioral Neuroscience*, 10(2):252–269, 2010. doi: <https://doi.org/10.3758/CABN.10.2.252>.
- Gabrielle Girardeau and Vítor Lopes-Dos-Santos. Brain neural patterns and the memory function of sleep. *Science*, 374(6567):560–564, 2021. doi: <https://doi.org/10.1126/science.abi8370>.
- Michael Goard and Yang Dan. Basal forebrain activation enhances cortical coding of natural scenes. *Nature neuroscience*, 12(11):1444–1449, 2009. doi: <https://doi.org/10.1038/nn.2402>.
- Matías A Goldin, Baptiste Lefebvre, Samuele Virgili, Mathieu Kim Pham Van Cang, Alexander Ecker, Thierry Mora, Ulisse Ferrari, and Olivier Marre. Context-dependent selectivity to natural images in the retina. *Nature Communications*, 13(1):5556, 2022. doi: <https://doi.org/10.1038/s41467-022-33242-8>.
- Matthew S Grubb and Ian D Thompson. Quantitative characterization of visual response properties in the mouse dorsal lateral geniculate nucleus. *Journal of neurophysiology*, 90(6):3594–3607, 2003. doi: <https://doi.org/10.1152/jn.00699.2003>.
- William Guido and Theodore Weyand. Burst responses in thalamic relay cells of the awake behaving cat. *Journal of neurophysiology*, 74(4):1782–1786, 1995. doi: <https://doi.org/10.1152/jn.1995.74.4.1782>.
- Grigori Guitchounts, Javier Masis, Steffen BE Wolff, and David Cox. Encoding of 3d head orienting movements in the primary visual cortex. *Neuron*, 108(3):512–525, 2020. doi: <https://doi.org/10.1016/j.neuron.2020.07.014>.
- Wei Guo, Amanda R Clause, Asa Barth-Maron, and Daniel B Polley. A corticothalamic circuit for dynamic switching between feature detection and discrimination. *Neuron*, 95(1):180–194, 2017. doi: <https://doi.org/10.1016/j.neuron.2017.05.019>.
- Divyansh Gupta, Wiktor Młynarski, Anton Sumser, Olga Symonova, Jan Svatoň, and Maximilian Joesch. Panoramic visual statistics shape retina-wide organization of receptive fields. *Nature Neuroscience*, 26(4):606–614, 2023. doi: <https://doi.org/10.1038/s41593-023-01280-0>.
- Bilal Haider, Michael Häusser, and Matteo Carandini. Inhibition dominates sensory responses in the awake cortex. *Nature*, 493(7430):97–100, 2013. doi: <https://doi.org/10.1038/nature11665>.
- Ann E Hallanger, Allan I Levey, Henry J Lee, David B Rye, and Bruce H Wainer. The origins of cholinergic and other subcortical afferents to the thalamus in the rat. *Journal of Comparative Neurology*, 262(1):105–124, 1987. doi: <https://doi.org/10.1002/cne.902620109>.
- Mary E Harrington. The ventral lateral geniculate nucleus and the intergeniculate leaflet: interrelated structures in the visual and circadian systems. *Neuroscience & Biobehavioral Reviews*, 21(5):705–727, 1997. doi: [https://doi.org/10.1016/S0149-7634\(96\)00019-X](https://doi.org/10.1016/S0149-7634(96)00019-X).

- Kenneth D Harris and Alexander Thiele. Cortical state and attention. *Nature reviews neuroscience*, 12(9): 509–523, 2011. doi: <https://doi.org/10.1038/nrn3084>.
- Michael E Hasselmo and Martin Sarter. Modes and models of forebrain cholinergic neuromodulation of cognition. *Neuropsychopharmacology*, 36(1):52–73, 2011. doi: <https://doi.org/10.1038/npp.2010.104>.
- Yasumasa Hayashi and Tetsu Nagata. Receptive field properties of rat ventral lateral geniculate cells projecting to the superior colliculus. *Brain Research*, 226(1-2):298–303, 1981. doi: [https://doi.org/10.1016/0006-8993\(81\)91102-1](https://doi.org/10.1016/0006-8993(81)91102-1).
- Eckhard H Hess and James M Polt. Pupil size as related to interest value of visual stimuli. *Science*, 132(3423): 349–350, 1960. doi: <https://doi.org/10.1126/science.132.3423.349>.
- EH Hess and JM Polt. Pupil size in relation to mental activity during simple problem-solving. *Science*, 143 (3611):1190–1192, 1964. doi: <https://doi.org/10.1126/science.143.3611.1190>.
- Sean Hill and Giulio Tononi. Modeling sleep and wakefulness in the thalamocortical system. *Journal of neurophysiology*, 93(3):1671–1698, 2005. doi: <https://doi.org/10.1152/jn.00915.2004>.
- Akio Hirata and Manuel A Castro-Alamancos. Neocortex network activation and deactivation states controlled by the thalamus. *Journal of neurophysiology*, 103(3):1147–1157, 2010. doi: <https://doi.org/10.1152/jn.00955.2009>.
- Nicolas Hô and Alain Destexhe. Synaptic background activity enhances the responsiveness of neocortical pyramidal neurons. *Journal of neurophysiology*, 84(3):1488–1496, 2000. doi: <https://doi.org/10.1152/jn.2000.84.3.1488>.
- Robert N Holdefer and Barry L Jacobs. Phasic stimulation of the locus coeruleus: effects on activity in the lateral geniculate nucleus. *Experimental brain research*, 79:444–452, 1994. doi: <https://doi.org/10.1007/BF00229184>.
- Jennifer L Hoy, Iryna Yavorska, Michael Wehr, and Cristopher M Niell. Vision drives accurate approach behavior during prey capture in laboratory mice. *Current Biology*, 26(22):3046–3052, 2016. doi: <https://doi.org/10.1016/j.cub.2016.09.009>.
- Jennifer L Hoy, Hannah I Bishop, and Cristopher M Niell. Defined cell types in superior colliculus make distinct contributions to prey capture behavior in the mouse. *Current Biology*, 29(23):4130–4138, 2019. doi: <https://doi.org/10.1016/j.cub.2019.10.017>.
- B Hu, M Steriade, and M Deschênes. The effects of brainstem peribrachial stimulation on neurons of the lateral geniculate nucleus. *Neuroscience*, 31(1):13–24, 1989. doi: [https://doi.org/10.1016/0306-4522\(89\)90027-4](https://doi.org/10.1016/0306-4522(89)90027-4).
- Ziwei Huang, Yanli Ran, Jonathan Oesterle, Thomas Euler, and Philipp Berens. Estimating smooth and sparse neural receptive fields with a flexible spline basis. *Neurons, Behavior, Data Analysis, and Theory*, 2021. doi: <https://doi.org/10.51628/001c.27578>.

- David H Hubel. Single unit activity in lateral geniculate body and optic tract of unrestrained cats. *The Journal of Physiology*, 150(1):91, 1960. doi: <https://doi.org/10.1113/jphysiol.1960.sp006375>.
- Icnelia Huerta-Ocampo, Husniye Hacioglu-Bay, Daniel Dautan, and Juan Mena-Segovia. Distribution of mid-brain cholinergic axons in the thalamus. *ENeuro*, 7(1), 2020. doi: <https://doi.org/10.1523/ENEURO.0454-19.2019>.
- Saad Idrees, Matthias P Baumann, Felix Franke, Thomas A Münch, and Ziad M Hafed. Perceptual saccadic suppression starts in the retina. *Nature communications*, 11(1):1977, 2020. doi: <https://doi.org/10.1038/s41467-020-15890-w>.
- Saad Idrees, Matthias-Philipp Baumann, Maria M Korympidou, Timm Schubert, Alexandra Kling, Katrin Franke, Ziad M Hafed, Felix Franke, and Thomas A Münch. Suppression without inhibition: how retinal computation contributes to saccadic suppression. *Communications Biology*, 5(1):692, 2022. doi: <https://doi.org/10.1038/s42003-022-03526-2>.
- Hidehiko K Inagaki, Susu Chen, Margreet C Ridder, Pankaj Sah, Nuo Li, Zidan Yang, Hana Hasanbegovic, Zhenyu Gao, Charles R Gerfen, and Karel Svoboda. A midbrain-thalamus-cortex circuit reorganizes cortical dynamics to initiate movement. *Cell*, 185(6):1065–1081, 2022. doi: <https://doi.org/10.1016/j.cell.2022.02.006>.
- Kaoru Isa, Thongchai Sooksawate, Kenta Kobayashi, Kazuto Kobayashi, Peter Redgrave, and Tadashi Isa. Dissecting the tectal output channels for orienting and defense responses. *ENeuro*, 7(5), 2020. doi: <https://doi.org/10.1523/ENEURO.0271-20.2020>.
- Elina AK Jacobs, Nicholas A Steinmetz, Andrew J Peters, Matteo Carandini, and Kenneth D Harris. Cortical state fluctuations during sensory decision making. *Current Biology*, 30(24):4944–4955, 2020. doi: <https://doi.org/10.1016/j.cub.2020.09.067>.
- Juliane Jaepel, Mark Hübener, Tobias Bonhoeffer, and Tobias Rose. Lateral geniculate neurons projecting to primary visual cortex show ocular dominance plasticity in adult mice. *Nature neuroscience*, 20(12):1708–1714, 2017. doi: <https://doi.org/10.1038/s41593-017-0021-0>.
- H Jahnsen and R Llinás. Electrophysiological properties of guinea-pig thalamic neurones: an in vitro study. *The Journal of physiology*, 349(1):205–226, 1984. doi: <https://doi.org/10.1113/jphysiol.1984.sp015153>.
- Huijeong Jeong, Vijay Mohan K Namboodiri, Min Whan Jung, and Mark L Andermann. Sensory cortical ensembles exhibit differential coupling to ripples in distinct hippocampal subregions. *Current Biology*, 33(23):5185–5198, 2023. doi: <https://doi.org/10.1016/j.cub.2023.10.073>.
- Marieke Jepma and Sander Nieuwenhuis. Pupil diameter predicts changes in the exploration–exploitation trade-off: Evidence for the adaptive gain theory. *Journal of cognitive neuroscience*, 23(7):1587–1596, 2011. doi: <https://doi.org/10.1162/jocn.2010.21548>.

- Daoyun Ji and Matthew A Wilson. Coordinated memory replay in the visual cortex and hippocampus during sleep. *Nature neuroscience*, 10(1):100–107, 2007. doi: <https://doi.org/10.1038/nn1825>.
- Xu-ying Ji, Brian Zingg, Lukas Mesik, Zhongju Xiao, Li I Zhang, and Huizhong W Tao. Thalamocortical innervation pattern in mouse auditory and visual cortex: laminar and cell-type specificity. *Cerebral cortex*, 26(6):2612–2625, 2016. doi: <https://doi.org/10.1093/cercor/bhv099>.
- Barbara E Jones. Activity, modulation and role of basal forebrain cholinergic neurons innervating the cerebral cortex. *Progress in brain research*, 145:157–169, 2004. doi: [https://doi.org/10.1016/S0079-6123\(03\)45011-5](https://doi.org/10.1016/S0079-6123(03)45011-5).
- Edward G Jones, Brahim Tighilet, Bich-Van Tran, and Molly M Huntsman. Nucleus-and cell-specific expression of nmda and non-nmda receptor subunits in monkey thalamus. *Journal of Comparative Neurology*, 397(3):371–393, 1998.
- Helen E Jones, Ian M Andolina, Bashir Ahmed, Stewart D Shipp, Jake TC Clements, Kenneth L Grieve, Javier Cudeiro, Thomas E Salt, and Adam M Sillito. Differential feedback modulation of center and surround mechanisms in parvocellular cells in the visual thalamus. *Journal of Neuroscience*, 32(45):15946–15951, 2012. doi: <https://doi.org/10.1523/JNEUROSCI.0831-12.2012>.
- Rebecca Jordan and Georg B Keller. The locus coeruleus broadcasts prediction errors across the cortex to promote sensorimotor plasticity. *Elife*, 12:RP85111, 2023. doi: <https://doi.org/10.7554/eLife.85111.3>.
- Siddhartha Joshi and Joshua I Gold. Pupil size as a window on neural substrates of cognition. *Trends in cognitive sciences*, 24(6):466–480, 2020. doi: <https://doi.org/10.1016/j.tics.2020.03.005>.
- Siddhartha Joshi, Yin Li, Rishi M Kalwani, and Joshua I Gold. Relationships between pupil diameter and neuronal activity in the locus coeruleus, colliculi, and cingulate cortex. *Neuron*, 89(1):221–234, 2016. doi: <https://doi.org/10.1016/j.neuron.2015.11.028>.
- Nicolas Josset, Marie Roussel, Maxime Lemieux, David Lafrance-Zoubga, Ali Rastqar, and Frederic Bretzner. Distinct contributions of mesencephalic locomotor region nuclei to locomotor control in the freely behaving mouse. *Current Biology*, 28(6):884–901, 2018. doi: <https://doi.org/10.1016/j.cub.2018.02.007>.
- Ovidiu Jurjut, Petya Georgieva, Laura Busse, and Steffen Katzner. Learning enhances sensory processing in mouse v1 before improving behavior. *Journal of Neuroscience*, 37(27):6460–6474, 2017. doi: <https://doi.org/10.1523/JNEUROSCI.3485-16.2017>.
- Daniel Kahneman and Jackson Beatty. Pupil diameter and load on memory. *Science*, 154(3756):1583–1585, 1966. doi: <https://doi.org/10.1126/science.154.3756.1583>.
- Dimokratis Karamanlis, Helene Marianne Schreyer, and Tim Gollisch. Retinal encoding of natural scenes. *Annual Review of Vision Science*, 8:171–193, 2022. doi: <https://doi.org/10.1146/annurev-vision-100820-114239>.

- Daniel Kerschensteiner. Feature detection by retinal ganglion cells. *Annual review of vision science*, 8:135–169, 2022. doi: <https://doi.org/10.1146/annurev-vision-100419-112009>.
- Daniel Kerschensteiner and William Guido. Organization of the dorsal lateral geniculate nucleus in the mouse. *Visual neuroscience*, 34:E008, 2017. doi: <https://doi.org/10.1017/S0952523817000062>.
- Juhyun Kim, Chanel J Matney, Aaron Blankenship, Shaul Hestrin, and Solange P Brown. Layer 6 corticothalamic neurons activate a cortical output layer, layer 5a. *Journal of Neuroscience*, 34(29):9656–9664, 2014. doi: <https://doi.org/10.1523/JNEUROSCI.1325-14.201>.
- Myung-A Kim, Hyun S Lee, Beob Y Lee, and Barry D Waterhouse. Reciprocal connections between subdivisions of the dorsal raphe and the nuclear core of the locus coeruleus in the rat. *Brain research*, 1026(1): 56–67, 2004. doi: <https://doi.org/10.1016/j.brainres.2004.08.022>.
- T Kim, N Shen, J-C Hsiang, KP Johnson, and D Kerschensteiner. Dendritic and parallel processing of visual threats in the retina control defensive responses. *Science advances*, 6(47):eabc9920, 2020. doi: <https://doi.org/10.1126/sciadv.abc9920>.
- Megan A Kirchgessner, Alexis D Franklin, and Edward M Callaway. Context-dependent and dynamic functional influence of corticothalamic pathways to first-and higher-order visual thalamus. *Proceedings of the National Academy of Sciences*, 117(23):13066–13077, 2020. doi: <https://doi.org/10.1073/pnas.2002080117>.
- Christian Kolmac and John Mitrofanis. Organization of brain stem afferents to the ventral lateral geniculate nucleus of rats. *Visual Neuroscience*, 17(2):313–318, 2000. doi: <https://doi.org/10.1017/S0952523800002108>.
- Rylan S Larsen and Jack Waters. Neuromodulatory correlates of pupil dilation. *Frontiers in neural circuits*, 12:21, 2018. doi: <https://doi.org/10.3389/fncir.2018.00021>.
- A Moses Lee, Jennifer L Hoy, Antonello Bonci, Linda Wilbrecht, Michael P Stryker, and Christopher M Niell. Identification of a brainstem circuit regulating visual cortical state in parallel with locomotion. *Neuron*, 83(2):455–466, 2014. doi: <https://doi.org/10.1016/j.neuron.2014.06.031>.
- Seung-Hee Lee and Yang Dan. Neuromodulation of brain states. *Neuron*, 76(1):209–222, 2012. doi: <https://doi.org/10.1016/j.neuron.2012.09.012>.
- Jonas Lehnert, Kuwook Cha, Jamie Halperin, Kerry Yang, Daniel F Zheng, Anmar Khadra, Erik P Cook, and Arjun Krishnaswamy. Visual attention to features and space in mice using reverse correlation. *Current Biology*, 33(17):3690–3701, 2023. doi: <https://doi.org/10.1016/j.celrep.2021.109377>.
- Roberto Leiras, Jared M Cregg, and Ole Kiehn. Brainstem circuits for locomotion. *Annual review of neuroscience*, 45:63–85, 2022. doi: <https://doi.org/10.1146/annurev-neuro-082321-025137>.
- Nathalie Leresche and Régis C Lambert. T-type calcium channels in synaptic plasticity. *Channels*, 11(2): 121–139, 2017. doi: <https://doi.org/10.1080/19336950.2016.1238992>.

- Nicholas A Lesica and Garrett B Stanley. Encoding of natural scene movies by tonic and burst spikes in the lateral geniculate nucleus. *Journal of Neuroscience*, 24(47):10731–10740, 2004. doi: <https://doi.org/10.1523/JNEUROSCI.3059-04.2004>.
- Liang Liang, Alex Fratzl, Glenn Goldey, Rohan N Ramesh, Arthur U Sugden, Josh L Morgan, Chinfei Chen, and Mark L Andermann. A fine-scale functional logic to convergence from retina to thalamus. *Cell*, 173(6):1343–1355, 2018. doi: <https://doi.org/10.1016/j.cell.2018.04.041>.
- Liang Liang, Alex Fratzl, Jasmine DS Reggiani, Omar El Mansour, Chinfei Chen, and Mark L Andermann. Retinal inputs to the thalamus are selectively gated by arousal. *Current Biology*, 30(20):3923–3934, 2020. doi: <https://doi.org/10.1016/j.cub.2020.07.065>.
- Olle Lindvall, Anders Björklund, Anders Nobin, and Ulf Stenevi. The adrenergic innervation of the rat thalamus as revealed by the glyoxylic acid fluorescence method. *Journal of comparative Neurology*, 154(3):317–347, 1974. doi: <https://doi.org/10.1002/cne.901540307>.
- Elizabeth Y Litvina and Chinfei Chen. An evolving view of retinogeniculate transmission. *Visual neuroscience*, 34:E013, 2017. doi: <https://doi.org/10.1017/S0952523817000104>.
- Margaret S Livingstone and David H Hubel. Effects of sleep and arousal on the processing of visual information in the cat. *Nature*, 291(5816):554–561, 1981. doi: <https://doi.org/10.1038/291554a0>.
- Rodolfo R Llinás and Mircea Steriade. Bursting of thalamic neurons and states of vigilance. *Journal of neurophysiology*, 95(6):3297–3308, 2006. doi: <https://doi.org/10.1152/jn.00166.2006>.
- Sweyta Lohani, Andrew H Moberly, Hadas Benisty, Boris Landa, Miao Jing, Yulong Li, Michael J Higley, and Jessica A Cardin. Spatiotemporally heterogeneous coordination of cholinergic and neocortical activity. *Nature Neuroscience*, pages 1–8, 2022. doi: <https://doi.org/10.1038/s41593-022-01202-6>.
- Shao-Ming Lu, William Guido, and S Murray Sherman. The brain-stem parabrachial region controls mode of response to visual stimulation of neurons in the cat’s lateral geniculate nucleus. *Visual neuroscience*, 10(4):631–642, 1993. doi: <https://doi.org/10.1017/S0952523800005332>.
- Rui Ma, He Cui, Sang-Hun Lee, Thomas J Anastasio, and Joseph G Malpeli. Predictive encoding of moving target trajectory by neurons in the parabrachial nucleus. *Journal of neurophysiology*, 109(8):2029–2043, 2013. doi: <https://doi.org/10.1152/jn.01032.2012>.
- Alan Mackay-Sim, Ann Jervie Sefton, and Paul R Martin. Subcortical projections to lateral geniculate and thalamic reticular nuclei in the hooded rat. *Journal of comparative neurology*, 213(1):24–35, 1983. doi: <https://doi.org/10.1002/cne.902130103>.
- Valerio Mante, Vincent Bonin, and Matteo Carandini. Functional mechanisms shaping lateral geniculate responses to artificial and natural stimuli. *Neuron*, 58(4):625–638, 2008. doi: <https://doi.org/10.1016/j.neuron.2008.03.011>.

- Jesse D Marshall, Diego E Aldarondo, Timothy W Dunn, William L Wang, Gordon J Berman, and Bence P Ölveczky. Continuous whole-body 3d kinematic recordings across the rodent behavioral repertoire. *Neuron*, 109(3):420–437, 2021. doi: <https://doi.org/10.1016/j.neuron.2020.11.016>.
- Emily M Martersteck, Karla E Hirokawa, Mariah Evarts, Amy Bernard, Xin Duan, Yang Li, Lydia Ng, Seung W Oh, Benjamin Ouellette, Joshua J Royall, et al. Diverse central projection patterns of retinal ganglion cells. *Cell reports*, 18(8):2058–2072, 2017. doi: <https://doi.org/10.1016/j.celrep.2017.01.075>.
- Cristina Martinez-Gonzalez, J Paul Bolam, and Juan Mena-Segovia. Topographical organization of the pedunculo-pontine nucleus. *Frontiers in neuroanatomy*, 5:22, 2011. doi: <https://doi.org/10.3389/fnana.2011.00022>.
- Richard H Masland. The neuronal organization of the retina. *Neuron*, 76(2):266–280, 2012. doi: <https://doi.org/10.1016/j.neuron.2012.10.002>.
- Sebastiaan Mathôt. Tuning the senses: How the pupil shapes vision at the earliest stage. *Annual Review of Vision Science*, 6:433–451, 2020. doi: <https://doi.org/10.1146/annurev-vision-030320-062352>.
- Kerry McAlonan, James Cavanaugh, and Robert H Wurtz. Attentional modulation of thalamic reticular neurons. *Journal of Neuroscience*, 26(16):4444–4450, 2006. doi: <https://doi.org/10.1523/JNEUROSCI.5602-05.2006>.
- Kerry McAlonan, James Cavanaugh, and Robert H Wurtz. Guarding the gateway to cortex with attention in visual thalamus. *Nature*, 456(7220):391–394, 2008. doi: <https://doi.org/10.1038/nature07382>.
- Ethan G McBride, Su-Yee J Lee, and Edward M Callaway. Local and global influences of visual spatial selection and locomotion in mouse primary visual cortex. *Current Biology*, 29(10):1592–1605, 2019. doi: <https://doi.org/10.1016/j.cub.2018.01.038>.
- Robert W McCarley, Odile Benoit, and German Barrionuevo. Lateral geniculate nucleus unitary discharge in sleep and waking: state-and rate-specific aspects. *Journal of neurophysiology*, 50(4):798–818, 1983. doi: <https://doi.org/10.1152/jn.1983.50.4.798>.
- David A McCormick. Neurotransmitter actions in the thalamus and cerebral cortex and their role in neuromodulation of thalamocortical activity. *Progress in neurobiology*, 39(4):337–388, 1992. doi: [https://doi.org/10.1016/0301-0082\(92\)90012-4](https://doi.org/10.1016/0301-0082(92)90012-4).
- David A McCormick and Hans-Christian Pape. Acetylcholine inhibits identified interneurons in the cat lateral geniculate nucleus. *Nature*, 334(6179):246–248, 1988. doi: <https://doi.org/10.1038/334246a0>.
- David A McCormick and Hans-Christian Pape. Properties of a hyperpolarization-activated cation current and its role in rhythmic oscillation in thalamic relay neurones. *The Journal of physiology*, 431(1):291–318, 1990. doi: <https://doi.org/10.1113/jphysiol.1990.sp018331>.

- David A McCormick and Marcus von Krosigk. Corticothalamic activation modulates thalamic firing through glutamate" metabotropic" receptors. *Proceedings of the National Academy of Sciences*, 89(7):2774–2778, 1992. doi: <https://doi.org/10.1073/pnas.89.7.2774>.
- David A McCormick, Matthew J McGinley, and David B Salkoff. Brain state dependent activity in the cortex and thalamus. *Current opinion in neurobiology*, 31:133–140, 2015. doi: <https://doi.org/10.1016/j.conb.2014.10.003>.
- David A McCormick, Dennis B Nestvogel, and Biyu J He. Neuromodulation of brain state and behavior. *Annual review of neuroscience*, 43:391–415, 2020. doi: <https://doi.org/10.1146/annurev-neuro-100219-105424>.
- Matthew J McGinley, Stephen V David, and David A McCormick. Cortical membrane potential signature of optimal states for sensory signal detection. *Neuron*, 87(1):179–192, 2015a. doi: <https://doi.org/10.1016/j.neuron.2015.05.038>.
- Matthew J McGinley, Martin Vinck, Jacob Reimer, Renata Batista-Brito, Edward Zagher, Cathryn R Cadwell, Andreas S Tolias, Jessica A Cardin, and David A McCormick. Waking state: rapid variations modulate neural and behavioral responses. *Neuron*, 87(6):1143–1161, 2015b. doi: <https://doi.org/10.1016/j.neuron.2015.09.012>.
- James T McKenna, Chun Yang, Serena Franciosi, Stuart Winston, Kathleen K Abarr, Matthew S Rigby, Yuchio Yanagawa, Robert W McCarley, and Ritchie E Brown. Distribution and intrinsic membrane properties of basal forebrain gabaergic and parvalbumin neurons in the mouse. *Journal of Comparative Neurology*, 521(6):1225–1250, 2013. doi: <https://doi.org/10.1002/cne.23290>.
- Rebecca A Mease, Patrik Krieger, and Alexander Groh. Cortical control of adaptation and sensory relay mode in the thalamus. *Proceedings of the National Academy of Sciences*, 111(18):6798–6803, 2014. doi: <https://doi.org/10.1073/pnas.1318665111>.
- Rebecca A Mease, Thomas Kuner, Adrienne L Fairhall, and Alexander Groh. Multiplexed spike coding and adaptation in the thalamus. *Cell Reports*, 19(6):1130–1140, May 2017. doi: [10.1016/j.celrep.2017.04.050](https://doi.org/10.1016/j.celrep.2017.04.050).
- Marine Megemont, Jim McBurney-Lin, and Hongdian Yang. Pupil diameter is not an accurate real-time readout of locus coeruleus activity. *Elife*, 11:e70510, 2022. doi: <https://doi.org/10.7554/eLife.70510>.
- Juan Mena-Segovia and J Paul Bolam. Rethinking the pedunculopontine nucleus: from cellular organization to function. *Neuron*, 94(1):7–18, 2017. doi: <https://doi.org/10.1016/j.neuron.2017.02.027>.
- Arne F Meyer, John O’Keefe, and Jasper Poort. Two distinct types of eye-head coupling in freely moving mice. *Current Biology*, 30(11):2116–2130, 2020. doi: <https://doi.org/10.1016/j.cub.2020.04.042>.
- Cory T Miller, David Gire, Kim Hoke, Alexander C Huk, Darcy Kelley, David A Leopold, Matthew C Smear, Frederic Theunissen, Michael Yartsev, and Cristopher M Niell. Natural behavior is the language of the brain. *Current Biology*, 32(10):R482–R493, 2022. doi: <https://doi.org/10.1016/j.cub.2022.03.031>.

- Bartul Mimica, Tuçe Tombaz, Claudia Battistin, Jingyi Guo Fuglstad, Benjamin A Dunn, and Jonathan R Whitlock. Behavioral decomposition reveals rich encoding structure employed across neocortex in rats. *Nature Communications*, 14(1):3947, 2023. doi: <https://doi.org/10.1038/s41467-023-39520-3>.
- Satoru K Miura and Massimo Scanziani. Distinguishing externally from saccade-induced motion in visual cortex. *Nature*, 610(7930):135–142, 2022. doi: <https://doi.org/10.1038/s41586-022-05196-w>.
- Vicente M Montero. Attentional activation of the visual thalamic reticular nucleus depends on ‘top-down’ inputs from the primary visual cortex via corticogeniculate pathways. *Brain research*, 864(1):95–104, 2000. doi: [https://doi.org/10.1016/S0006-8993\(00\)02182-X](https://doi.org/10.1016/S0006-8993(00)02182-X).
- Bartlett D Moore, Caitlin W Kiley, Chao Sun, and W Martin Usrey. Rapid plasticity of visual responses in the adult lateral geniculate nucleus. *Neuron*, 71(5):812–819, 2011. doi: <https://doi.org/10.1016/j.neuron.2011.06.025>.
- Robert Y Moore, Angelos E Halaris, and Barbara E Jones. Serotonin neurons of the midbrain raphe: ascending projections. *Journal of Comparative Neurology*, 180(3):417–438, 1978. doi: <https://doi.org/10.1002/cne.901800302>.
- Robert Y Moore, Roger Weis, and Margaret M Moga. Efferent projections of the intergeniculate leaflet and the ventral lateral geniculate nucleus in the rat. *Journal of Comparative Neurology*, 420(3):398–418, 2000.
- Jeffrey Moran and Robert Desimone. Selective attention gates visual processing in the extrastriate cortex. *Science*, 229(4715):782–784, 1985. doi: <https://doi.org/10.1126/science.4023713>.
- Josh Lyskowski Morgan, Daniel Raimund Berger, Arthur Willis Wetzel, and Jeff William Lichtman. The fuzzy logic of network connectivity in mouse visual thalamus. *Cell*, 165(1):192–206, 2016. doi: <https://doi.org/10.1016/j.cell.2016.02.033>.
- Lawrence P Morin and Keith M Studholme. Retinofugal projections in the mouse. *Journal of Comparative Neurology*, 522(16):3733–3753, 2014. doi: <https://doi.org/10.1002/cne.23635>.
- Giuseppe Moruzzi and Horace Winchell Magoun. Brain stem reticular formation and activation of the eeg. *Electroencephalography and clinical neurophysiology*, 1(1-4):455–473, 1949. doi: [https://doi.org/10.1016/0013-4694\(49\)90219-9](https://doi.org/10.1016/0013-4694(49)90219-9).
- Matthias HJ Munk, Pieter R Roelfsema, Peter König, Andreas K Engel, and Wolf Singer. Role of reticular activation in the modulation of intracortical synchronization. *Science*, 272(5259):271–274, 1996. doi: <https://doi.org/10.1126/science.272.5259.271>.
- Allison J Murphy, Luke Shaw, J Michael Hasse, Robbe LT Goris, and Farran Briggs. Optogenetic activation of corticogeniculate feedback stabilizes response gain and increases information coding in lgn neurons. *Journal of computational neuroscience*, 49(3):259–271, 2021. doi: <https://doi.org/10.1007/s10827-020-00754-5>.

- Simon Musall, Matthew T Kaufman, Ashley L Juavinett, Steven Gluf, and Anne K Churchland. Single-trial neural dynamics are dominated by richly varied movements. *Nature neuroscience*, 22(10):1677–1686, 2019. doi: <https://doi.org/10.1038/s41593-019-0502-4>.
- T Nagai, K Satoh, K Imamoto, and T Maeda. Divergent projections of catecholamine neurons of the locus coeruleus as revealed by fluorescent retrograde double labeling technique. *Neuroscience letters*, 23(2):117–123, 1981. doi: [https://doi.org/10.1016/0304-3940\(81\)90027-6](https://doi.org/10.1016/0304-3940(81)90027-6).
- Matthew R Nassar, Katherine M Rumsey, Robert C Wilson, Kinjan Parikh, Benjamin Heasley, and Joshua I Gold. Rational regulation of learning dynamics by pupil-linked arousal systems. *Nature neuroscience*, 15(7):1040–1046, 2012. doi: <https://doi.org/10.1038/nn.3130>.
- Anders Nelson and Richard Mooney. The basal forebrain and motor cortex provide convergent yet distinct movement-related inputs to the auditory cortex. *Neuron*, 90(3):635–648, 2016. doi: <https://doi.org/10.1016/j.neuron.2016.03.031>.
- Garrett T Neske. The slow oscillation in cortical and thalamic networks: mechanisms and functions. *Frontiers in neural circuits*, 9:88, 2016. doi: <https://doi.org/10.3389/fncir.2015.00088>.
- Dennis B Nestvogel and David A McCormick. Visual thalamocortical mechanisms of waking state dependent activity and alpha oscillations. *Neuron*, 1(5):120–138.e4, 2022. doi: <https://doi.org/10.1016/j.neuron.2021.10.005>.
- Erin Neyhart, Na Zhou, Brandon R Munn, Robert G Law, Cameron Smith, Zakir H Mridha, Francisco A Blanco, Guochuan Li, Yulong Li, Matthew J McGinley, James M Shine, and Jacob Reimer. Simultaneously-recorded cholinergic axons and cortical acetylcholine are highly correlated with pupil size and locomotion under spontaneous conditions. *bioRxiv*, pages 2023–11, 2023. doi: <https://doi.org/10.1101/2023.11.14.567116>.
- Miguel AL Nicolelis and Erika E Fanselow. Thalamocortical optimization of tactile processing according to behavioral state. *Nature neuroscience*, 5(6):517–523, 2002. doi: <https://doi.org/10.1038/nn0602-517>.
- Cristopher M Niell and Michael P Stryker. Modulation of visual responses by behavioral state in mouse visual cortex. *Neuron*, 65(4):472–479, 2010. doi: <https://doi.org/10.1016/j.neuron.2010.01.033>.
- Shahryar Noei, Ioannis S Zouridis, Nikos K Logothetis, Stefano Panzeri, and Nelson K Totah. Distinct ensembles in the noradrenergic locus coeruleus are associated with diverse cortical states. *Proceedings of the National Academy of Sciences*, 119(18):e2116507119, 2022. doi: <https://doi.org/10.1073/pnas.2116507119>.
- Shawn R Olsen, Dante S Bortone, Hillel Adesnik, and Massimo Scanziani. Gain control by layer six in cortical circuits of vision. *Nature*, 483(7387):47–52, 2012. doi: <https://doi.org/10.1038/nature10835>.

- Patrycja Orlowska-Feuer, Aghileh S Ebrahimi, Antonio G Zippo, Rasmus S Petersen, Robert J Lucas, and Riccardo Storchi. Look-up and look-down neurons in the mouse visual thalamus during freely moving exploration. *Current Biology*, 32(18):3987–3999, 2022. doi: <https://doi.org/10.1016/j.cub.2022.07.049>.
- Joseph O’Neill, Barty Pleydell-Bouverie, David Dupret, and Jozsef Csicsvari. Play it again: reactivation of waking experience and memory. *Trends in neurosciences*, 33(5):220–229, 2010. doi: <https://doi.org/10.1016/j.tins.2010.01.006>.
- Janelle MP Pakan, Scott C Lowe, Evelyn Dylida, Sander W Keemink, Stephen P Currie, Christopher A Coutts, and Nathalie L Rochefort. Behavioral-state modulation of inhibition is context-dependent and cell type specific in mouse visual cortex. *Elife*, 5:e14985, 2016. doi: <https://doi.org/10.7554/eLife.14985>.
- Georgios C Papadopoulos and John G Parnavelas. Distribution and synaptic organization of serotonergic and noradrenergic axons in the lateral geniculate nucleus of the rat. *Journal of Comparative Neurology*, 294(3):345–355, 1990. doi: <https://doi.org/10.1002/cne.902940304>.
- Vinay Parikh, Rouba Kozak, Vicente Martinez, and Martin Sarter. Prefrontal acetylcholine release controls cue detection on multiple timescales. *Neuron*, 56(1):141–154, 2007. doi: <https://doi.org/10.1016/j.neuron.2007.08.025>.
- Philip RL Parker, Elliott TT Abe, Emmalyn SP Leonard, Dylan M Martins, and Cristopher M Niell. Joint coding of visual input and eye/head position in v1 of freely moving mice. *Neuron*, 110(23):3897–3906, 2022. doi: <https://doi.org/10.1016/j.neuron.2022.08.029>.
- Philip RL Parker, Dylan M Martins, Emmalyn SP Leonard, Nathan M Casey, Shelby L Sharp, Elliott TT Abe, Matthew C Smear, Jacob L Yates, Jude F Mitchell, and Cristopher M Niell. A dynamic sequence of visual processing initiated by gaze shifts. *Nature Neuroscience*, pages 1–11, 2023. doi: <https://doi.org/10.1038/s41593-023-01481-7>.
- James T Pearson and Daniel Kerschensteiner. Ambient illumination switches contrast preference of specific retinal processing streams. *Journal of neurophysiology*, 114(1):540–550, 2015. doi: <https://doi.org/10.1152/jn.00360.2015>.
- Gordon H Petty, Amanda K Kinnischtzke, Y Kate Hong, and Randy M Bruno. Effects of arousal and movement on secondary somatosensory and visual thalamus. *Elife*, 10:e67611, 2021. doi: <https://doi.org/10.7554/eLife.67611>.
- Didier Pinault. The thalamic reticular nucleus: structure, function and concept. *Brain research reviews*, 46(1):1–31, 2004. doi: <https://doi.org/10.1016/j.brainresrev.2004.04.008>.
- Denise M Piscopo, Rana N El-Danaf, Andrew D Huberman, and Cristopher M Niell. Diverse visual features encoded in mouse lateral geniculate nucleus. *Journal of Neuroscience*, 33(11):4642–4656, 2013. doi: <https://doi.org/10.1523/JNEUROSCI.5187-12.2013>.

- Gina R Poe, Stephen Foote, Oxana Eschenko, Joshua P Johansen, Sebastien Bouret, Gary Aston-Jones, Carolyn W Harley, Denise Manahan-Vaughan, David Weinschenker, Rita Valentino, Craig Berridge, Daniel J Chandler, Barry Waterhouse, and Susan J Sara. Locus coeruleus: a new look at the blue spot. *Nature Reviews Neuroscience*, 21(11):644–659, 2020. doi: <https://doi.org/10.1038/s41583-020-0360-9>.
- Pierre-Olivier Polack, Jonathan Friedman, and Peyman Golshani. Cellular mechanisms of brain state-dependent gain modulation in visual cortex. *Nature neuroscience*, 16(9):1331–1339, 2013. doi: <https://doi.org/10.1038/nn.3464>.
- James FA Poulet and Carl CH Petersen. Internal brain state regulates membrane potential synchrony in barrel cortex of behaving mice. *Nature*, 454(7206):881–885, 2008. doi: <https://doi.org/10.1038/nature07150>.
- James FA Poulet, Laura MJ Fernandez, Sylvain Crochet, and Carl CH Petersen. Thalamic control of cortical states. *Nature neuroscience*, 15(3):370–372, 2012. doi: <https://doi.org/10.1038/nn.3035>.
- Glen T Prusky and Max S Cynader. [3h] nicotine binding sites are associated with mammalian optic nerve terminals. *Visual neuroscience*, 1(2):245–248, 1988. doi: <https://doi.org/10.1017/S095252380001504>.
- J Rajkowski, P Kubiak, and G Aston-Jones. Locus coeruleus activity in monkey: phasic and tonic changes are associated with altered vigilance. *Brain research bulletin*, 35(5-6):607–616, 1994. doi: [https://doi.org/10.1016/0361-9230\(94\)90175-9](https://doi.org/10.1016/0361-9230(94)90175-9).
- Eion J Ramcharan, James W Gnadt, and S Murray Sherman. Burst and tonic firing in thalamic cells of unanesthetized, behaving monkeys. *Visual neuroscience*, 17(1):55–62, 2000. doi: <https://doi.org/10.1017/S0952523800171056>.
- Santiago Ramón Y Cajal, DR Azoulay, Neely Swanson, and Larry W Swanson. *Histology Of The Nervous System: Of Man And Vertebrates*. Oxford University Press, 1995.
- Björn Rasch and Jan Born. About sleep’s role in memory. *Physiological Reviews*, 2013. doi: <https://doi.org/10.1152/physrev.00032.2012>.
- Daniel L Rathbun, David K Warland, and W Martin Usrey. Spike timing and information transmission at retinogeniculate synapses. *Journal of Neuroscience*, 30(41):13558–13566, 2010. doi: <https://doi.org/10.1523/JNEUROSCI.0909-10.2010>.
- Jasmine DS Reggiani, Qiufen Jiang, Melanie Barbini, Andrew Lutas, Liang Liang, Jesseba Fernando, Fei Deng, Jinxia Wan, Yulong Li, Chinfei Chen, and Mark L Andermann. Brainstem serotonin neurons selectively gate retinal information flow to thalamus. *Neuron*, 2022. doi: <https://doi.org/10.1016/j.neuron.2022.12.006>.
- Jacob Reimer, Emmanouil Froudarakis, Cathryn R Cadwell, Dimitri Yatsenko, George H Denfield, and Andreas S Tolia. Pupil fluctuations track fast switching of cortical states during quiet wakefulness. *Neuron*, 84(2):355–362, 2014. doi: <https://doi.org/10.1016/j.neuron.2014.09.033>.

- Jacob Reimer, Matthew J McGinley, Yang Liu, Charles Rodenkirch, Qi Wang, David A McCormick, and Andreas S Tolia. Pupil fluctuations track rapid changes in adrenergic and cholinergic activity in cortex. *Nature communications*, 7(1):13289, 2016. doi: <https://doi.org/10.1038/ncomms13289>.
- Pamela Reinagel, Dwayne Godwin, S Murray Sherman, and Christof Koch. Encoding of visual information by lgn bursts. *Journal of neurophysiology*, 81(5):2558–2569, 1999. doi: <https://doi.org/10.1152/jn.1999.81.5.2558>.
- Kimberly Reinhold, Arbora Resulaj, and Massimo Scanziani. Brain state-dependent modulation of thalamic visual processing by cortico-thalamic feedback. *Journal of Neuroscience*, 43(9):1540–1554, 2023. doi: <https://doi.org/10.1523/JNEUROSCI.2124-21.2022>.
- John B Reppas, W Martin Usrey, and R Clay Reid. Saccadic eye movements modulate visual responses in the lateral geniculate nucleus. *Neuron*, 35(5):961–974, 2002. doi: [https://doi.org/10.1016/S0896-6273\(02\)00823-1](https://doi.org/10.1016/S0896-6273(02)00823-1).
- John H Reynolds and David J Heeger. The normalization model of attention. *Neuron*, 61(2):168–185, 2009. doi: <https://doi.org/10.1016/j.neuron.2009.01.002>.
- Foster Rieke and Denis A Baylor. Single-photon detection by rod cells of the retina. *Reviews of Modern Physics*, 70(3):1027, 1998. doi: <https://doi.org/10.1103/RevModPhys.70.1027>.
- Trevor W Robbins. Arousal systems and attentional processes. *Biological psychology*, 45(1-3):57–71, 1997. doi: [https://doi.org/10.1016/S0301-0511\(96\)05222-2](https://doi.org/10.1016/S0301-0511(96)05222-2).
- Charles Rodenkirch, Yang Liu, Brian J Schriver, and Qi Wang. Locus coeruleus activation enhances thalamic feature selectivity via norepinephrine regulation of intrathalamic circuit dynamics. *Nature neuroscience*, 22(1):120–133, 2019. doi: <https://doi.org/10.1038/s41593-018-0283-1>.
- Robert W Rodieck. Quantitative analysis of cat retinal ganglion cell response to visual stimuli. *Vision research*, 5(12):583–601, 1965. doi: [https://doi.org/10.1016/0042-6989\(65\)90033-7](https://doi.org/10.1016/0042-6989(65)90033-7).
- Santiago B Rompani, Fiona E Muellner, Adrian Wanner, Chi Zhang, Chiara N Roth, Keisuke Yonehara, and Botond Roska. Different modes of visual integration in the lateral geniculate nucleus revealed by single-cell-initiated transsynaptic tracing. *Neuron*, 93(4):767–776, 2017. doi: <https://doi.org/10.1016/j.neuron.2017.01.028>.
- Peter Room, Folkert Postema, and Jakob Korf. Divergent axon collaterals of rat locu demonstration by a fluorescent double labeling technique. *Brain Research*, 221(2):219–230, 1981. doi: [https://doi.org/10.1016/0006-8993\(81\)90773-3](https://doi.org/10.1016/0006-8993(81)90773-3).
- Tobias Rose and Tobias Bonhoeffer. Experience-dependent plasticity in the lateral geniculate nucleus. *Current Opinion in Neurobiology*, 53:22–28, 2018. doi: <https://doi.org/10.1016/j.conb.2018.04.016>.

- Miroslav Román Rosón, Yannik Bauer, Ann H Kotkat, Philipp Berens, Thomas Euler, and Laura Busse. Mouse dlgn receives functional input from a diverse population of retinal ganglion cells with limited convergence. *Neuron*, 102(2):462–476, 2019. doi: <https://doi.org/10.1016/j.neuron.2019.01.040>.
- Morgane M Roth, Johannes C Dahmen, Dylan R Muir, Fabia Imhof, Francisco J Martini, and Sonja B Hofer. Thalamic nuclei convey diverse contextual information to layer 1 of visual cortex. *Nature neuroscience*, 19(2):299–307, 2016. doi: <https://doi.org/10.1038/nn.4197>.
- Leonor M Teles-Grilo Ruivo, Keeley L Baker, Michael W Conway, Peter J Kinsley, Gary Gilmour, Keith G Phillips, John TR Isaac, John P Lowry, and Jack R Mellor. Coordinated acetylcholine release in prefrontal cortex and hippocampus is associated with arousal and reward on distinct timescales. *Cell reports*, 18(4):905–917, 2017. doi: <https://doi.org/10.1016/j.celrep.2016.12.085>.
- Yuri B Saalman and Sabine Kastner. Cognitive and perceptual functions of the visual thalamus. *Neuron*, 71(2):209–223, 2011. doi: <http://dx.doi.org/10.1016/j.neuron.2011.06.027>.
- Ubadah Sabbagh, Gubbi Govindaiah, Rachana D Somaiya, Ryan V Ha, Jessica C Wei, William Guido, and Michael A Fox. Diverse gabaergic neurons organize into subtype-specific sublaminae in the ventral lateral geniculate nucleus. *Journal of neurochemistry*, 159(3):479–497, 2021. doi: <https://doi.org/10.1111/jnc.15085>.
- Lindsey D Salay and Andrew D Huberman. Divergent outputs of the ventral lateral geniculate nucleus mediate visually evoked defensive behaviors. *Cell Reports*, 37(1), 2021. doi: <https://doi.org/10.1016/j.celrep.2021.109792>.
- Aman B Saleem, Aslı Ayaz, Kathryn J Jeffery, Kenneth D Harris, and Matteo Carandini. Integration of visual motion and locomotion in mouse visual cortex. *Nature neuroscience*, 16(12):1864–1869, 2013. doi: <https://doi.org/10.1038/nn.3567>.
- David B Salkoff, Edward Zagher, Erin McCarthy, and David A McCormick. Movement and performance explain widespread cortical activity in a visual detection task. *Cerebral Cortex*, 30(1):421–437, 2020. doi: <https://doi.org/10.1093/cercor/bhz206>.
- Jason M Samonds, Wilson S Geisler, and Nicholas J Priebe. Natural image and receptive field statistics predict saccade sizes. *Nature neuroscience*, 21(11):1591–1599, 2018. doi: <https://doi.org/10.1038/s41593-018-0255-5>.
- Susan J Sara and Sebastien Bouret. Orienting and reorienting: the locus coeruleus mediates cognition through arousal. *Neuron*, 76(1):130–141, 2012. doi: <https://doi.org/10.1016/j.neuron.2012.09.011>.
- Martin Sarter, Vinay Parikh, and W Matthew Howe. Phasic acetylcholine release and the volume transmission hypothesis: time to move on. *Nature Reviews Neuroscience*, 10(5):383–390, 2009. doi: <https://doi.org/10.1038/nrn2635>.

- Thomas E Scammell, Elda Arrigoni, and Jonathan O Lipton. Neural circuitry of wakefulness and sleep. *Neuron*, 93(4):747–765, 2017. doi: <https://doi.org/10.1016/j.neuron.2017.01.014>.
- HE Scharfman, SM Lu, W Guido, PR Adams, and SM Sherman. N-methyl-d-aspartate receptors contribute to excitatory postsynaptic potentials of cat lateral geniculate neurons recorded in thalamic slices. *Proceedings of the National Academy of Sciences*, 87(12):4548–4552, 1990. doi: <https://doi.org/10.1073/pnas.87.12.4548>.
- Lisa Schmors, Ann H Kotkat, Yannik Bauer, Ziwei Huang, Davide Crombie, Lukas S Meyerollbersleben, Sacha Sokoloski, Philipp Berens, and Laura Busse. The combination of stimulus-driven and modulatory inputs in visual thalamus depend on visual responsiveness and stimulus type. *bioRxiv*, pages 2023–10, 2023. doi: <https://doi.org/10.1101/2023.10.18.562960>.
- Tania A Seabrook, Timothy J Burbridge, Michael C Crair, and Andrew D Huberman. Architecture, function, and assembly of the mouse visual system. *Annual review of neuroscience*, 40:499–538, 2017. doi: <https://doi.org/10.1146/annurev-neuro-071714-033842>.
- Nishal P Shah, Nora Brackbill, Colleen Rhoades, Alexandra Kling, Georges Goetz, Alan M Litke, Alexander Sher, Eero P Simoncelli, and EJ Chichilnisky. Inference of nonlinear receptive field subunits with spike-triggered clustering. *Elife*, 9, 2020. doi: <https://doi.org/10.7554/eLife.45743>.
- Congping Shang, Zhihui Liu, Zijun Chen, Yingchao Shi, Qian Wang, Su Liu, Dapeng Li, and Peng Cao. A parvalbumin-positive excitatory visual pathway to trigger fear responses in mice. *Science*, 348(6242):1472–1477, 2015. doi: <https://doi.org/10.1126/science.aaa8694>.
- S Murray Sherman. Tonic and burst firing: dual modes of thalamocortical relay. *Trends in neurosciences*, 24(2):122–126, 2001. doi: [https://doi.org/10.1016/S0166-2236\(00\)01714-8](https://doi.org/10.1016/S0166-2236(00)01714-8).
- S Murray Sherman. Interneurons and triadic circuitry of the thalamus. *Trends in neurosciences*, 27(11):670–675, 2004. doi: <https://doi.org/10.1016/j.tins.2004.08.003>.
- S Murray Sherman and RW Guillery. On the actions that one nerve cell can have on another: distinguishing “drivers” from “modulators”. *Proceedings of the National Academy of Sciences*, 95(12):7121–7126, 1998. doi: <https://doi.org/10.1073/pnas.95.12.7121>.
- S Murray Sherman and RW Guillery. The role of the thalamus in the flow of information to the cortex. *Philosophical Transactions of the Royal Society of London. Series B: Biological Sciences*, 357(1428):1695–1708, 2002. doi: <https://doi.org/10.1098/rstb.2002.1161>.
- SM Sherman and RW Guillery. The visual relays in the thalamus. In *The visual neurosciences*, volume 1, pages 565–591. MIT Press Cambridge, 2004.
- Daisuke Shimaoka, Kenneth D Harris, and Matteo Carandini. Effects of arousal on mouse sensory cortex depend on modality. *Cell reports*, 22(12):3160–3167, 2018. doi: <https://doi.org/10.1016/j.celrep.2018.02.092>.

- Yousheng Shu, Andrea Hasenstaub, Mathilde Badoual, Thierry Bal, and David A McCormick. Barrages of synaptic activity control the gain and sensitivity of cortical neurons. *Journal of Neuroscience*, 23(32):10388–10401, 2003. doi: <https://doi.org/10.1523/JNEUROSCI.23-32-10388.2003>.
- Joshua H Siegle, Xiaoxuan Jia, Séverine Durand, Sam Gale, Corbett Bennett, Nile Graddis, Gregory Heller, Tamina K Ramirez, Hannah Choi, Jennifer A Luviano, et al. Survey of spiking in the mouse visual system reveals functional hierarchy. *Nature*, 592(7852):86–92, 2021. doi: <https://doi.org/10.1038/s41586-020-03171-x>.
- Eero P Simoncelli and Bruno A Olshausen. Natural image statistics and neural representation. *Annual review of neuroscience*, 24(1):1193–1216, 2001. doi: <https://doi.org/10.1146/annurev.neuro.24.1.1193>.
- Kimberly L Simpson, Daniel W Altman, Li Wang, Michael L Kirifides, Rick C-S Lin, and Barry D Waterhouse. Lateralization and functional organization of the locus coeruleus projection to the trigeminal somatosensory pathway in rat. *Journal of Comparative Neurology*, 385(1):135–147, 1997.
- Lawrence C Sincich, Daniel L Adams, John R Economides, and Jonathan C Horton. Transmission of spike trains at the retinogeniculate synapse. *Journal of Neuroscience*, 27(10):2683–2692, 2007. doi: <https://doi.org/10.1523/JNEUROSCI.5077-06.2007>.
- Guela Sokhadze, Kyle L Whyland, Martha E Bickford, and William Guido. The organization of cholinergic projections in the visual thalamus of the mouse. *Journal of Comparative Neurology*, 530(7):1081–1098, 2022. doi: <https://doi.org/10.1002/cne.25235>.
- Martin A Spacek, Davide Crombie, Yannik Bauer, Gregory Born, Xinyu Liu, Steffen Katzner, and Laura Busse. Robust effects of corticothalamic feedback and behavioral state on movie responses in mouse dlgn. *Elife*, 11:e70469, 2022. doi: <https://doi.org/10.7554/eLife.70469>.
- Hedva Spitzer, Robert Desimone, and Jeffrey Moran. Increased attention enhances both behavioral and neuronal performance. *Science*, 240(4850):338–340, 1988. doi: <https://doi.org/10.1126/science.3353728>.
- William C Stacey and Dominique M Durand. Synaptic noise improves detection of subthreshold signals in hippocampal ca1 neurons. *Journal of Neurophysiology*, 86(3):1104–1112, 2001. doi: <https://doi.org/10.1152/jn.2001.86.3.1104>.
- M Steriade. Grouping of brain rhythms in corticothalamic systems. *Neuroscience*, 137(4):1087–1106, 2006. doi: <https://doi.org/10.1016/j.neuroscience.2005.10.029>.
- Mircea Steriade. Impact of network activities on neuronal properties in corticothalamic systems. *Journal of neurophysiology*, 86(1):1–39, 2001. doi: <https://doi.org/10.1152/jn.2001.86.1.1>.
- Mircea Steriade, David A McCormick, and Terrence J Sejnowski. Thalamocortical oscillations in the sleeping and aroused brain. *Science*, 262(5134):679–685, 1993. doi: [10.1126/science.8235588](https://doi.org/10.1126/science.8235588).
- Mircea M Steriade and Robert W McCarley. *Brainstem control of wakefulness and sleep*. Springer Science & Business Media, 1990.

- Carl R Stoelzel, Yulia Bereshpolova, Jose-Manuel Alonso, and Harvey A Swadlow. Axonal conduction delays, brain state, and corticogeniculate communication. *Journal of Neuroscience*, 37(26):6342–6358, 2017. doi: <https://doi.org/10.1523/JNEUROSCI.0444-17.2017>.
- Carsen Stringer, Marius Pachitariu, Nicholas Steinmetz, Charu Bai Reddy, Matteo Carandini, and Kenneth D Harris. Spontaneous behaviors drive multidimensional, brainwide activity. *Science*, 364(6437):eaav7893, 2019. doi: <https://doi.org/10.1126/science.aav7893>.
- Sofie Charlotte Sundberg, Sarah Helen Lindström, Gonzalo Manuel Sanchez, and Björn Granseth. Cre-expressing neurons in visual cortex of ntsr1-cre gn220 mice are corticothalamic and are depolarized by acetylcholine. *Journal of Comparative Neurology*, 526(1):120–132, 2018.
- Harvey A Swadlow and Alexander G Gusev. The impact of 'bursting' thalamic impulses at a neocortical synapse. *Nature neuroscience*, 4(4):402–408, 2001. doi: <https://doi.org/10.1038/86054>.
- LW Swanson and BK Hartman. The central adrenergic system. an immunofluorescence study of the location of cell bodies and their efferent connections in the rat utilizing dopamine-b-hydroxylase as a marker. *Journal of Comparative Neurology*, 163(4):467–505, 1975. doi: <https://doi.org/10.1002/cne.901630406>.
- Alex M Thomson. Neocortical layer 6, a review. *Frontiers in neuroanatomy*, 4:1339, 2010. doi: <https://doi.org/10.3389/fnana.2010.00013>.
- Jonathan N Tinsley, Maxim I Molodtsov, Robert Prevedel, David Wartmann, Jofre Espigulé-Pons, Mattias Lauwers, and Alipasha Vaziri. Direct detection of a single photon by humans. *Nature communications*, 7(1):12172, 2016. doi: <https://doi.org/10.1038/ncomms12172>.
- Nelson K Totah, Ricardo M Neves, Stefano Panzeri, Nikos K Logothetis, and Oxana Eschenko. The locus coeruleus is a complex and differentiated neuromodulatory system. *Neuron*, 99(5):1055–1068, 2018. doi: <https://doi.org/10.1016/j.neuron.2018.07.037>.
- Nelson KB Totah, Nikos K Logothetis, and Oxana Eschenko. Noradrenergic ensemble-based modulation of cognition over multiple timescales. *Brain Research*, 1709:50–66, 2019. doi: <https://doi.org/10.1016/j.brainres.2018.12.031>.
- Stefan Treue and Julio C Martinez Trujillo. Feature-based attention influences motion processing gain in macaque visual cortex. *Nature*, 399(6736):575–579, 1999. doi: <https://doi.org/10.1038/21176>.
- T Tsumoto, OD Creutzfeldt, and CR Legendy. Functional organization of the corticofugal system from visual cortex to lateral geniculate nucleus in the cat: With an appendix on geniculo-cortical mono-synaptic connections. *Experimental Brain Research*, 32:345–364, 1978. doi: <https://doi.org/10.1007/BF00238707>.
- Akira Uematsu, Bao Zhen Tan, Edgar A Ycu, Jessica Sulkes Cuevas, Jenny Koivumaa, Felix Junyent, Eric J Kremer, Ilana B Witten, Karl Deisseroth, and Joshua P Johansen. Modular organization of the brainstem

- noradrenaline system coordinates opposing learning states. *Nature neuroscience*, 20(11):1602–1611, 2017. doi: <https://doi.org/10.1038/nn.4642>.
- W Martin Usrey, John B Reppas, and R Clay Reid. Specificity and strength of retinogeniculate connections. *Journal of neurophysiology*, 82(6):3527–3540, 1999. doi: <https://doi.org/10.1152/jn.1999.82.6.3527>.
- RJ Valentino and R Dingledine. Presynaptic inhibitory effect of acetylcholine in the hippocampus. *Journal of Neuroscience*, 1(7):784–792, 1981. doi: <https://doi.org/10.1523/JNEUROSCI.01-07-00784.1981>.
- Ruud L van den Brink, Keno Hagen, Niklas Wilming, Peter R Murphy, Joshua Calder-Travis, Jürgen Finsterbusch, Christian Büchel, and Tobias H Donner. Brainstem arousal systems adaptively shape large-scale cortical interactions for flexible decision-making. *bioRxiv*, pages 2023–12, 2023. doi: <https://doi.org/10.1101/2023.12.05.570327>.
- Susan C Van Horn, Alev Erişir, and S Murray Sherman. Relative distribution of synapses in the a-laminae of the lateral geniculate nucleus of the cat. *Journal of Comparative Neurology*, 416(4):509–520, 2000.
- Jochem van Kempen, Gerard M Loughnane, Daniel P Newman, Simon P Kelly, Alexander Thiele, Redmond G O’Connell, and Mark A Bellgrove. Behavioural and neural signatures of perceptual decision-making are modulated by pupil-linked arousal. *Elife*, 8:e42541, 2019. doi: <https://doi.org/10.7554/eLife.42541>.
- Tomas Vega-Zuniga, Anton Sumser, Olga Symonova, Peter Koppensteiner, Florian H Schmidt, and Maximilian Joesch. A thalamic hub of action cues coordinates early visual processing and perception. *bioRxiv*, pages 2023–12, 2023. doi: <https://doi.org/10.1101/2023.12.23.573221>.
- Mateo Vélez-Fort, Charly V Rousseau, Christian J Niedworok, Ian R Wickersham, Ede A Rancz, Alexander PY Brown, Molly Strom, and Troy W Margrie. The stimulus selectivity and connectivity of layer six principal cells reveals cortical microcircuits underlying visual processing. *Neuron*, 83(6):1431–1443, 2014. doi: <https://doi.org/10.1016/j.neuron.2014.08.001>.
- Mateo Vélez-Fort, Edward F Bracey, Sepiedeh Keshavarzi, Charly V Rousseau, Lee Cossell, Stephen C Lenzi, Molly Strom, and Troy W Margrie. A circuit for integration of head-and visual-motion signals in layer 6 of mouse primary visual cortex. *Neuron*, 98(1):179–191, 2018. doi: <https://doi.org/10.1016/j.neuron.2018.02.023>.
- Martin Vinck, Renata Batista-Brito, Ulf Knoblich, and Jessica A Cardin. Arousal and locomotion make distinct contributions to cortical activity patterns and visual encoding. *Neuron*, 86(3):740–754, 2015. doi: <https://doi.org/10.1016/j.neuron.2015.03.028>.
- William E Vinje and Jack L Gallant. Sparse coding and decorrelation in primary visual cortex during natural vision. *Science*, 287(5456):1273–1276, 2000. doi: <https://doi.org/10.1126/science.287.5456.1273>.
- Erich Von Holst and Horst Mittelstaedt. Das reafferenzprinzip: wechselwirkungen zwischen zentralnervensystem und peripherie. *Naturwissenschaften*, 37(20):464–476, 1950. doi: <https://doi.org/10.1007/BF00622503>.

- Erin J Wamsley. Offline memory consolidation during waking rest. *Nature Reviews Psychology*, 1(8):441–453, 2022. doi: <https://doi.org/10.1038/s44159-022-00072-w>.
- Lupeng Wang and Richard J Krauzlis. Visual selective attention in mice. *Current Biology*, 28(5):676–685, 2018. doi: <https://doi.org/10.1016/j.cub.2018.01.038>.
- Wei Wang, Helen E Jones, Ian M Andolina, Thomas E Salt, and Adam M Sillito. Functional alignment of feedback effects from visual cortex to thalamus. *Nature neuroscience*, 9(10):1330–1336, 2006. doi: <https://doi.org/10.1038/nm1768>.
- Wei Wang, Ian M Andolina, Yiliang Lu, Helen E Jones, and Adam M Sillito. Focal gain control of thalamic visual receptive fields by layer 6 corticothalamic feedback. *Cerebral cortex*, 28(1):267–280, 2018. doi: <https://doi.org/10.1093/cercor/bhw376>.
- Barry D Waterhouse, Barbara Border, Linda Wahl, and Gregory A Mihailoff. Topographic organization of rat locus coeruleus and dorsal raphe nuclei: distribution of cells projecting to visual system structures. *Journal of Comparative Neurology*, 336(3):345–361, 1993. doi: <https://doi.org/10.1002/cne.903360304>.
- Shijun Weng, Wenzhi Sun, and Shigang He. Identification of on-off direction-selective ganglion cells in the mouse retina. *The Journal of physiology*, 562(3):915–923, 2005. doi: <https://doi.org/10.1113/jphysiol.2004.076695>.
- Theodore G Weyand, Michael Boudreaux, and William Guido. Burst and tonic response modes in thalamic neurons during sleep and wakefulness. *Journal of neurophysiology*, 85(3):1107–1118, 2001. doi: <https://doi.org/10.1152/jn.2001.85.3.1107>.
- Courtney Michelle Whilden, Maxime Chevée, Seong Yeol An, and Solange Pezon Brown. The synaptic inputs and thalamic projections of two classes of layer 6 corticothalamic neurons in primary somatosensory cortex of the mouse. *Journal of Comparative Neurology*, 529(17):3751–3771, 2021. doi: <https://doi.org/10.1002/cne.25163>.
- Ross S Williamson, Kenneth E Hancock, Barbara G Shinn-Cunningham, and Daniel B Polley. Locomotion and task demands differentially modulate thalamic audiovisual processing during active search. *Current Biology*, 25(14):1885–1891, 2015. doi: <https://doi.org/10.1016/j.cub.2015.05.045>.
- JR Wilson, N Bose, and SM Sherman. Fine structural morphology of identified x-and y-cells in the cat’s lateral geniculate nucleus. *Proceedings of the Royal society of London. Series B. Biological sciences*, 221(1225):411–436, 1984. doi: <https://doi.org/10.1098/rspb.1984.0042>.
- Alexander B Wiltschko, Matthew J Johnson, Giuliano Iurilli, Ralph E Peterson, Jesse M Katon, Stan L Pashkovski, Victoria E Abaira, Ryan P Adams, and Sandeep Robert Datta. Mapping sub-second structure in mouse behavior. *Current Biology*, 88:1121–1135, 2015. doi: <http://dx.doi.org/10.1016/j.neuron.2015.11.031>.

- Ralf D Wimmer, L Ian Schmitt, Thomas J Davidson, Miho Nakajima, Karl Deisseroth, and Michael M Halassa. Thalamic control of sensory selection in divided attention. *Nature*, 526(7575):705–709, 2015. doi: <https://doi.org/10.1038/nature15398>.
- Jakob Wolfart, Damien Debay, Gwendal Le Masson, Alain Destexhe, and Thierry Bal. Synaptic background activity controls spike transfer from thalamus to cortex. *Nature neuroscience*, 8(12):1760–1767, 2005. doi: <https://doi.org/10.1038/nn1591>.
- Robert H Wurtz. Neuronal mechanisms of visual stability. *Vision research*, 48(20):2070–2089, 2008. doi: <https://doi.org/10.1016/j.visres.2008.03.021>.
- Min Xu, Shinjae Chung, Siyu Zhang, Peng Zhong, Chenyan Ma, Wei-Cheng Chang, Brandon Weissbourd, Noriaki Sakai, Liqun Luo, Seiji Nishino, and Dan Yang. Basal forebrain circuit for sleep-wake control. *Nature neuroscience*, 18(11):1641–1647, 2015. doi: <https://doi.org/10.1038/nm.4143>.
- Hongdian Yang, Bilal A Bari, Jeremiah Y Cohen, and Daniel H O’Connor. Locus coeruleus spiking differently correlates with s1 cortex activity and pupil diameter in a tactile detection task. *Elife*, 10:e64327, 2021. doi: <https://doi.org/10.7554/eLife.64327>.
- Ya-Chin Yang, Chun-Chang Hu, and Yi-Chen Lai. Non-additive modulation of synaptic transmission by serotonin, adenosine, and cholinergic modulators in the sensory thalamus. *Frontiers in Cellular Neuroscience*, 9:60, 2015. doi: <https://doi.org/10.3389/fncel.2015.00060>.
- Zhiwen Ye, Matthew S Bull, Anna Li, Daniel Birman, Tanya L Daigle, Bosiljka Tasic, Hongkui Zeng, and Nicholas A Steinmetz. Brain-wide topographic coordination of traveling spiral waves. *bioRxiv*, pages 2023–12, 2023. doi: <https://doi.org/10.1101/2023.12.07.570517>.
- Melis Yilmaz and Markus Meister. Rapid innate defensive responses of mice to looming visual stimuli. *Current Biology*, 23(20):2011–2015, 2013. doi: <https://doi.org/10.1016/j.cub.2013.08.015>.
- Edward Zagha and David A McCormick. Neural control of brain state. *Current opinion in neurobiology*, 29:178–186, 2014. doi: <https://doi.org/10.1016/j.conb.2014.09.010>.
- Sebastian H Zahler, David E Taylor, Joey Y Wong, Julia M Adams, and Evan H Feinberg. Superior colliculus drives stimulus-evoked directionally biased saccades and attempted head movements in head-fixed mice. *Elife*, 10:e73081, 2021. doi: <https://doi.org/10.7554/eLife.73081>.
- Xinyu Zhao, Mingna Liu, and Jianhua Cang. Visual cortex modulates the magnitude but not the selectivity of looming-evoked responses in the superior colliculus of awake mice. *Neuron*, 84(1):202–213, 2014. doi: <https://doi.org/10.1016/j.neuron.2014.08.037>.
- Mu Zhou, Feixue Liang, Xiaorui R Xiong, Lu Li, Haifu Li, Zhongju Xiao, Huizhong W Tao, and Li I Zhang. Scaling down of balanced excitation and inhibition by active behavioral states in auditory cortex. *Nature neuroscience*, 17(6):841–850, 2014. doi: <https://doi.org/10.1038/nm.3701>.

Fangchen Zhu, Sarah Elnozahy, Jennifer Lawlor, and Kishore V Kuchibhotla. The cholinergic basal forebrain provides a parallel channel for state-dependent sensory signaling to auditory cortex. *Nature neuroscience*, pages 1–10, 2023. doi: <https://doi.org/10.1038/s41593-023-01289-5>.

8 Appendix

8.1 List of publications

Zuo, X., Honey, C. J., Barense, M. D., **Crombie, D.**, Norman, K. A., Hasson, U., & Chen, J. (2020). Temporal integration of narrative information in a hippocampal amnesic patient. *NeuroImage*, 213, 116658. DOI: <https://doi.org/10.1016/j.neuroimage.2020.116658>.

Crombie, D., & Busse, L. (2021). Should I stay or should I go? A thalamic circuit for modulating behavioral responses to visual threat. *Neuron*, 109(23), 3717-3719. DOI: <https://doi.org/10.1016/j.neuron.2021.11.005>.

Spacek, M. A., **Crombie, D.**, Bauer, Y., Born, G., Liu, X., Katzner, S., & Busse, L. (2022). Robust effects of corticothalamic feedback and behavioral state on movie responses in mouse dLGN. *Elife*, 11, e70469. DOI: <https://doi.org/10.7554/eLife.70469>.

Crombie, D., Spacek, M. A., Leibold, C., & Busse, L. (2024). Spiking activity in the visual thalamus is coupled to pupil dynamics across temporal scales. *Plos Biology*, 22(5), e3002614. DOI: <https://doi.org/10.1371/journal.pbio.3002614>

Schmors, L., Kotkat, A. H., Bauer, Y., Huang, Z., **Crombie, D.**, Meyerrolbersleben, L., Sokoloski, S., Berens, P., & Busse, L. (2024). The combination of stimulus-driven and modulatory inputs in visual thalamus depend on visual responsiveness and stimulus type. *bioRxiv*, 2023.10.18.562960. DOI: <https://doi.org/10.1101/2023.10.18.562960>.

8.2 Curriculum vitae

Not included in online version.

8.3 Author contributions

Martin A Spacek, **Daive Crombie**, Yannik Bauer, Gregory Born, Xinyu Liu, Steffen Katzner, Laura Busse (2022). Robust effects of corticothalamic feedback and behavioral state on movie responses in mouse dLGN. *Elife*, 11, e70469. DOI: <https://doi.org/10.7554/eLife.70469>.

Author contributions

The study was conceptualized by MAS and LB. MAS and YB performed the experiments, with the assistance of XL. The data was curated by MAS, DC, GB, SK, and LB. The methodology was developed by MAS and DC. The formal statistical analysis was performed by SK. MAS, DC, YB, XL, and SK all contributed to developing the software infrastructure supporting the investigation. Data visualization was performed by MAS, YB, GB, and SK. GB and LB wrote the original draft. MAS, DC, SK, and LB contributed to reviewing and editing the manuscript. LB was responsible for project administration, supervision, and funding acquisition. DC, YB, and GB contributed equally to the work.

Personal contributions

DC wrote the software used to perform video-based eye tracking and curated the eye tracking data that was used in Figure 1 – supplement 2, Figure 1 – supplement 6, Figure 5 – supplement 1, and Figure 5 – supplement 2. The code for the analyses involving eye tracking data in Figure 5 – supplement 1h and i, and Figure 5 – supplement 2 was written by DC. DC also contributed substantially to developing the software infrastructure supporting the investigation. Furthermore, DC regularly participated in project meetings to decide on methodology, wrote the methods section pertaining to eye tracking, and contributed to the editing and review process.

Munich, 27.02.2024

Place, Date

MARTIN A SPACEK

Munich, 27.02.2024

Place, Date

LAURA BUSSE

Davide Crombie, Martin A Spacek, Christian Leibold, Laura Busse (2024). Spiking activity in the visual thalamus is coupled to pupil dynamics across temporal scales. bioRxiv, 2021.04.30.442134. DOI: <https://doi.org/10.1101/2021.04.30.442134>.

Author contributions

The study was conceptualized by DC, CL and LB. MAS performed the experiments. The data was curated by DC and MAS. The methodology was developed by DC, CL, and LB. The formal analysis was performed by DC. DC and MAS contributed to developing the software infrastructure supporting the investigation. Data visualization was performed by DC. DC, CL, and LB wrote the original draft. DC, CL, and LB contributed to reviewing and editing the manuscript. CL and LB were responsible for project administration and supervision. Funding for the project was acquired by CD, CL, and LB.

Personal contributions

The code for all analyses and data visualizations was written by DC. DC also contributed substantially to developing the software infrastructure supporting the investigation. Furthermore, DC regularly made decisions regarding methodology, wrote the majority of the methods and results sections, collaborated with the co-authors in producing the introduction and discussions sections, as well as the editing and review process. The funding for the first year of the project was acquired by DC with the supervision of LB and CL through the “SmartStart2” fellowship program administered by the Berstein Center for Computational Neuroscience.

Munich, 27.02.2024

Place, Date

LAURA BUSSE

Lisa Schmors, Ann H Kotkat, Yannik Bauer, Ziwei Huang, **Daive Crombie**, Lukas Meyerolbersleben, Sacha Sokoloski, Philipp Berens, Laura Busse (2023). Effects of non-retinal inputs in visual thalamus depend on visual responsiveness and stimulus context. bioRxiv, 2023.10.18.562960. DOI: <https://doi.org/10.1101/2023.10.18.562960>.

Author contributions

The study was conceptualized by LB, PB, and SS. YB, AK, and LM performed the experiments. LS, AK, YB, LM, and DC all contributed to the data curation. The methodology was developed by LS, YB, AK, ZH, DC, PB, SS and LB. The formal analysis was performed by LS, AK, and YB. LS, AK, YB, ZH, and DC all contributed to developing the software infrastructure supporting the investigation. Data visualization was performed by LS, AK, and YB. LB, LS, AK, and YB wrote the original draft, and all authors contributed to reviewing and editing the manuscript. Supervision was provided by LB, PB, and SS. LB and PB were responsible for project administration, funding acquisition, and provided the resources necessary to carry out the study.

Personal contributions

DC wrote the software used to perform video-based eye tracking and curated the eye tracking data, which was then used as input to the spline-GLM model. DC also contributed substantially to the software infrastructure used to support the investigation. DC further participated in early discussions on how behavioural variables might be included in the model, and contributed to reviewing and editing the manuscript.

Munich, 27.02.2024

Place, Date

LISA SCHMORS

Munich, 27.02.2024

Place, Date

LAURA BUSSE

Davide Crombie, Laura Busse (2021). Should I stay or should I go? A thalamic circuit for modulating behavioral responses to visual threat. *Neuron*, 109(23), 3717-3719. DOI: <https://doi.org/10.1016/j.neuron.2021.11.005>.

Author contributions

The original draft writing, editing, and reviewing was performed equally by DC and LB. The invitation to produce the work was acquired by LB.

Personal contributions

DC contributed equally to writing the original draft and reviewing and edition, and produced the figure presented in the article.

Munich, 27.02.2024

Place, Date

LAURA BUSSE

8.4 Affidavit

Eidesstattliche Versicherung/Affidavit

Hiermit versichere ich an Eides statt, dass ich die vorliegende Dissertation “Contextual modulation of stimulus processing in the mouse visual thalamus” selbstständig angefertigt habe, mich außer der angegebenen keiner weiteren Hilfsmittel bedient und alle Erkenntnisse, die aus dem Schrifttum ganz oder annähernd übernommen sind, als solche kenntlich gemacht und nach ihrer Herkunft unter Bezeichnung der Fundstelle einzeln nachgewiesen habe.

I hereby confirm that the dissertation “Contextual modulation of stimulus processing in the mouse visual thalamus” is the result of my own work and that I have only used sources or materials listed and specified in the dissertation.

Munich, 27.02.2024

Davide Crombie

Place, Date

DAVIDE CROMBIE